# Automated image-based planning of left atrial interventions

**Pedro André Gonçalves Morais**

September, 2018

# Automated image-based planning of left atrial interventions

Thesis submitted in partial fulfillment of the requirements for the degree of Doctor (Doctoral thesis under co-supervision) in Biomedical Engineering by the Faculdade de Engenharia da Universidade do Porto and for the degree of Doctor (Doctoral thesis under co-supervision) in Biomedical Sciences by the Doctoral School of Biomedical Sciences of KU Leuven.

Pedro André Gonçalves Morais
Master in Biomedical Engineering from the University of Minho

**Doctoral thesis prepared under supervision of:**

Professor João Manuel Ribeiro da Silva Tavares (Supervisor)
Professor Associado com Agregação no Departamento de Engenharia Mecânica
Faculdade de Engenharia da Universidade do Porto

Professor João Luís Araújo Martins Vilaça (Co-supervisor)
Associate Professor of the Department of Technologies
School of Technologies, Polytechnic Institute of Cávado and Ave

Professor Jan D'hooge (Supervisor at the KU Leuven)
Professor of the Department of Cardiovascular Sciences
Faculty of Medicine of KU Leuven

*To find yourself, think for yourself.*

- Socrates-

## Acknowledgements/Agradecimentos

With the conclusion of this PhD thesis, I would like to manifest my esteemed gratitude to everyone who contributed directly or indirectly to the success of this work.

First of all, I would like to thank all my supervisors, Professors Jan D'hooge, João Manuel R. S. Tavares, and João L. Vilaça, for their availability through all the endless meetings to discuss the project, for the motivation and all the precious advice throughout the last four years. You share with me all your extensive scientific experience and teach me how to be an excellent researcher. This thesis would not be possible without your effort and contribution.

I thank the contribution of the remaining co-authors of the studies published or prepared during this PhD, namely the members from ICVS/3B's (Fernando Veloso, Pedro L. Rodrigues, Sandro Queirós), KU Leuven (KUL)/UZLeuven (Joris Ector, Pieter De Meester and Werner Budts), German Heart Center Muniche (Felix Bourier and Isabel Deisenhofer) and Careggi University Hospital Florence (Alberto Marchi). You provided the clinical input and the required technical support to validate and develop all methods described in this thesis. Especialmente ao Sandro, agradeço por toda a amizade ao longo dos últimos anos, por toda a disponibilidade diária para a discussão de ideias, na preparação de documentos, na escrita de códigos e por todas as sugestões úteis para potenciar todo o trabalho desta tese. A special thanks to Brecht Heyde and Daniel Barbosa, for all their support at the beginning of my work as a researcher.

Aos restantes membros do ICVS/3B's (António Moreira, Bruno Oliveira, Helena Torres, João Fonseca, Nuno Rodrigues) agradeço por todo o companheirismo, por todas as discussões de ideais e críticas ao longo do trabalho. To KUL/MIRC members (Alejandra Ortega, Bidisha Chakraborty, João Pedrosa, Mahdi Tabassian, Natalia Ilyina, Nuno Almeida, Pedro Santos and Vangjush Komini), I thank for all your support during my period in Belgium and for all knowledge sharing. A special thanks to Professor Jan Bogaert (KUL), for sharing with me all your vast knowledge and experience, and for all your availability to discuss and explain several clinical aspects. I learned so much from you, you are a reference for me.

I would like to acknowledge the support of the secretariat and the board of directors of the institutes/universities that contributed in this thesis, INEGI (University of Porto, UP), MIRC (KUL), ICVS/3B's (University of Minho) and 2Ai (IPCA). A special thanks to the directors of the doctoral program in Biomedical Engineering (UP) and Health and Technologies (KUL). I also acknowledge the Fundação para a Ciência e a Tecnologia, in Portugal, for my PhD grant.

À Cristiana Fernandes e à Joana Meneses agradeço por toda a amizade, paciência, disponibilidade e bons conselhos ao longo destes últimos anos. Especialmente à Joana,

agradeço também por toda a confiança demonstrada, por todo o apoio em todos os momentos, por todas as aventuras, pela ótima companhia em todas as situações, particularmente nas mais diversas provas e infinitos treinos, por todas as descobertas e, acima de tudo, por todos os ensinamentos. És um dos meus maiores exemplos, parceira.

O meu último, e maior, agradecimento vai para a minha família, pais (José Morais e Joaquina Gonçalves), irmão (Jorge Morais) e cunhada (Catarina Moreira), pelo apoio incondicional em tudo. Dedico ainda esta tese aos meus avós, por todos os ensinamentos ao longo da vida, e aos meus sobrinhos (Gonçalo Morais e Rodrigo Morais), que esta seja um exemplo ao longo do vosso grande e promissor futuro, meus pequeninhos.

Thank you. Dank u wel. Obrigado a todos,

Pedro Morais

(11/07/2018)

The present work was possible thanks to the financial support provided by FCT – "Fundação para a Ciência e a Tecnologia" (Portugal), and the European Social Fund, through the "Programa Operacional Capital Humano" (POCH), in the scope of the PhD grant SFRH/BD/95438/2013; by funds from the European Regional Development Fund (FEDER) through the Operational Programme Competitiveness Factors (COMPETE) and by National Funds through FCT under the projects POCI-01-0145-FEDER-007038; and by the project NORTE-01-0145-FEDER-000013, NORTE-01-0145-FEDER-000022 and NORTE-01-0145-FEDER-024300, supported by Northern Portugal Regional Operational Programme (Norte2020), under the Portugal 2020 Partnership Agreement, through FEDER.

## Summary

Nowadays, minimally invasive cardiac interventions are widely performed to treat several pathologies, given their high success rate, low complication rate, superior outcome, reduced procedural time and costs. Particularly, percutaneous left atrial (LA) interventions are quite common, and they are performed daily to treat pathologies such as atrial fibrillation, mitral valve diseases, left atrial appendage (LAA) occlusion, among others. Nevertheless, since no direct percutaneous access route is available to the LA, an extra procedure, termed transseptal puncture (TSP), is typically required to gain access to the LA by puncturing the inter-atrial septal (IAS) wall using a catheter inserted into the right atrium. In this sense, the intervention is not only hampered by the particularities of the LA, but also by the transseptal access used. Thus, in order to achieve high success rate in these atrial interventions, experienced operators, multiple technological solutions and appropriate planning are mandatory.

This PhD thesis focused on the planning stage of LA interventions. As such, automated and fast image-based solutions were developed to improve this stage, by reducing the observer variability and the analysis time, and even by facilitating medical decisions, namely in less experienced centers. The added-value of an improved planning stage using the developed solutions was validated in two specific interventions, namely TSP and LAA occlusion.

Starting with the TSP, an initial literature review was performed to evaluate the recent technological solutions applied in this intervention. While several researchers presented improved surgical instruments and guidance techniques, only a few works focused on the planning stage, warranting further research. As such, a novel strategy to generate patient-specific atrial phantom models was initially presented. At this point, realistic anatomies (including the IAS wall) were generated from pre-procedural images, producing flexible and ultrasound-compatible cardiac walls through a mold-cast approach. Later, this phantom was used in an experimental scenario to evaluate the performance of a novel concept for an interventional framework, which may ease TSP intervention, by fusing intra-procedural data with pre-procedural models. To automate the pre-procedural planning stage of this framework, a fully automatic atrial region segmentation in computed tomographic images was later presented. In contrast to previous methods, this novel approach used a competitive strategy to correctly segment the atrial region and their thin inter-atrial walls. Finally, the accurate atrial region models were used to automatically identify relevant anatomical landmarks, namely the fossa ovalis (FO), *i.e.* the thinnest region of the IAS wall. Since the FO represents the optimal

access region for TSP, accurate evaluation of this region is required to detect the optimal puncture position, improving therefore the traditional interventional routine.

Regarding the LAA occlusion, a novel fast automatic LAA segmentation in 3D transesophageal echocardiographic images was described. The proposed method uses a semi-automatic approach, requiring a manual definition of a centerline to initialize a standard deformable model. To reduce the computational time, the B-spline Explicit Active Surface (BEAS) framework was applied. However, due to the complex LAA anatomical shape, a novel blind-ended model was developed, by combining different topological spaces, improving the BEAS performance to segment more complex shapes. Then, to facilitate and speed up the device selection stage, an automated and fast method to estimate the relevant clinical indicators from the obtained 3D surface was also presented.

The developed methods were validated in multiple clinical databases and even in specific online benchmarks, demonstrating a high accuracy and robustness, with a performance comparable to other state-of-the-art solutions. In addition, the described methods typically presented appealing computational time and allow the extraction of unique and novel anatomical features (e.g. thin atrial walls, fossa ovalis and relevant clinical measurements in the LAA), which are relevant to the abovementioned LA interventions.

Overall, the solutions/methodologies developed throughout the current PhD thesis proved their added-value for the planning of minimally invasive LA interventions, making them more accurate, simpler, faster and more reproducible between observers.

**Keywords:** Left atrial interventions; Transseptal puncture; Left atrial appendage occlusion; Image segmentation; Pre-procedural planning.

## Resumo

Atualmente, intervenções minimamente invasivas são amplamente realizadas para tratar diversas patologias cardíacas. Estas apresentam elevada taxa de sucesso, baixa taxa de complicações, resultado cosmético superior e custos e tempo de intervenção reduzidos. Particularmente, intervenções percutâneas à aurícula esquerda (AE) são realizadas diariamente para tratar patologias como a fibrilação auricular, doenças da válvula mitral, oclusão do apêndice auricular esquerdo (AAE), entre outras. Contudo, devido à ausência anatómica de uma via de acesso percutânea para a AE, é necessário realizar um procedimento extra designado de punção transeptal (PT). Para tal, um cateter é inserido até à aurícula direita, puncionado depois o septo interauricular (SIA) para aceder a AE. Desta forma, a dificuldade da intervenção não está apenas relacionada com a anatomia da AE, mas também com a posição escolhida para o acesso transeptal. Assim, estas intervenções exigem operadores com elevada experiência, diferentes soluções tecnológicas e correto planeamento da intervenção.

A presente tese de doutoramento é focada na fase de planeamento das intervenções da AE. Para tal, novas soluções baseadas em processamento de imagem foram desenvolvidas para melhorar esta fase. Estas soluções, sendo automatizadas e rápidas, permitem uma redução da variabilidade entre observadores e do tempo de análise, além de apresentarem o potencial para facilitar alguns processos médicos, principalmente em centros menos especializados. Ao longo da tese, as vantagens de um planeamento otimizado usando as soluções desenvolvidas foram validadas em duas intervenções específicas, nomeadamente na PT e oclusão do AAE.

Relativamente à PT, inicialmente foi realizada uma análise da literatura para identificar as soluções tecnológicas mais recentes. Enquanto múltiplos investigadores apresentaram novas agulhas cirúrgicas e formas de navegação, apenas um baixo número de estudos se focam no planeamento. Assim, uma nova estratégia para gerar modelos *phantom* específicos da anatomia do paciente foi desenvolvida. Anatomias realistas (principalmente do SIA) foram geradas a partir de imagens obtidas durante o planeamento e construídas com materiais flexíveis e compatíveis com aquisição por ultrassons. Este *phantom* foi mais tarde utilizado num cenário experimental para validar a performance de um novo conceito que visa facilitar o procedimento da PT. Aqui foi usada uma ferramenta de navegação para a intervenção, o qual combina dados obtidos durante o procedimento com modelos pré-intervenção. De forma a automatizar o estágio de planeamento desta ferramenta, uma estratégia de segmentação totalmente automática aplicada em imagens pré-operativas de tomografia computorizada foi desenvolvida. Contrariamente aos métodos de estado da arte, esta nova solução utilizou uma estratégia

competitiva para segmentar corretamente a região auricular e as paredes interauriculares. Por fim, uma estratégia para identificar pontos de referência anatómicos (nomeadamente a região mais fina do SIA, designada como *fossa ovalis* - FO) foi desenvolvida, utilizando para tal os modelos tridimensionais obtidos. Uma vez que FO representa a região ótima para a PT, uma avaliação precisa da sua extensão é exigida, de forma a detetar corretamente o ponto de punção ótimo, melhorando assim o procedimento atual.

De forma a potenciar o planeamento da oclusão do AAE, foi desenvolvida uma nova estratégia automatizada e rápida para a segmentação desta estrutura em imagens tridimensionais de ecocardiografia transesofágica. O método desenvolvido usa uma estratégia semiautomática, necessitando da definição manual do eixo central do AAE. Todo o processo de segmentação foi implementado utilizando a ferramenta *B-spline Explicit Active Surface* (BEAS), a qual demonstrou, previamente, alta precisão na segmentação de diferentes estruturas cardíacas aliada a um baixo custo computacional. Contudo, devido à elevada complexidade anatómica do AAE, foi desenvolvido um novo modelo BEAS, designado de *blind-ended*. Assim diferentes espaços topológicos são combinados, aumentando a capacidade desta ferramenta para segmentar estruturas mais complexas. Depois, para facilitar o passo de identificação do dispositivo de oclusão ótimo, foi apresentado uma estratégia automatizada para calcular os indicadores clínicos relevantes a partir das superfícies segmentadas.

Todos os métodos desenvolvidos foram validados em múltiplas bases de dados clínicas e em *benchmarks*, onde demonstraram a sua alta precisão e robustez, e uma performance comparável às soluções de estado da arte. Para além disso, as soluções propostas apresentam um baixo custo computacional e permitem a extração de características anatómicas únicas (por exemplo, as paredes finas entre aurículas, a *fossa ovalis* e indicadores clínicos para a oclusão do AAE), os quais são relevantes para as intervenções acima citadas.

De forma geral, as soluções/metodologias desenvolvidas durante esta tese provaram o seu potencial para o planeamento de intervenções minimamente-invasivas da AE, tornando este processo mais preciso, simples, rápido e reprodutível entre observadores.

**Palavras-chave:** Intervenções da aurícula esquerda; Punção transeptal; Oclusão do apêndice auricular esquerdo; Planeamento da Intervenção.

# Contents

## List of Abbreviations

| | |
|---|---|
| 2D | Two-dimensional |
| 3D | Three-dimensional |
| 4D | Four-dimensional |
| 95HS | 95$^{th}$ percentile of Hausdorff distance |
| AAE | "Apêndice auricular esquerdo" |
| AE | "Aurícula esquerda" |
| AF | Atrial fibrillation |
| AM | Animal model |
| ANOVA | Analysis of variance |
| Ao | Aortic tract |
| ASD | Atrial septal defect |
| Auto | Automatic |
| BEAS | B-spline Explicit Active Surface |
| BRK | Brockenbrough |
| C | Number of Complications |
| CA | Circumflex artery |
| CAD | Computer-aided design |
| CBEAS | Competitive B-spline Explicit Active Surface |
| CHD | Congenital Heart Disease |
| COMPETE | Competitiveness Factors Operational Programme |
| CPE | Centroid position error |
| CPU | Central processing unit |
| CS | Coronary sinus |
| CT | Computed Tomography |
| CTS | Coaxial transseptal |
| Dat. | Dataset |
| DC | Dice coefficient |
| DOF | Degrees of freedom |
| EAM | Electroanatomical mapping |
| EC | Cropped Version |
| ECG | Electrocardiogram |
| EF | Entire Surface |
| Electro. | Electrocautery |
| EM | Electromagnetic |
| F | Number of Failures |
| FA | Fully automatic |
| FC | Fluoroscopy |
| FCT | "Fundação para a Ciência e a Tecnologia" |
| FEDER | "Fundo Europeu de Desenvolvimento Regional" |
| FO | Fossa Ovalis |

| | |
|---|---|
| FOV | Field of view |
| GPU | Graphics processing unit |
| GW | Guidewire |
| HU | Hounsfield |
| IAS | Inter-atrial septum |
| ICE | Intracardiac echocardiography |
| ICP | Iterative closest point |
| IF | Image fusion |
| Inter | Inter-observer variability |
| Intra | Intra-observer variability |
| IOV | Inter-observer variability |
| IVC | Inferior vena cava |
| IP | Intracardiac potential |
| KUL | KU Leuven |
| LA | Left atrium |
| LAA | Left atrial appendage |
| LAO | Left anterior oblique |
| LAx | Long-axis view |
| LOA | Limits of agreement |
| LV | Left ventricle |
| LVOT | Left ventricular outflow tract |
| LZ | Landing zone |
| MITK | Medical Imaging Interaction Toolkit |
| MR | Magnetic Resonance |
| MRI | Magnetic Resonance Imaging |
| MV | Mitral valve |
| MVD | Mitral valve diseases |
| NbT | Number of transseptal punctures |
| NVAF | Non-valvular atrial fibrillation |
| Obs | Observer |
| P2Pl | Point-to-plane |
| P2S | Point-to-surface |
| PA | Pulmonary artery |
| Pat. | Patients |
| PFO | Patent foramen ovale |
| Ph | Phantom |
| PM | Planning method |
| POCH | “Programa Operacional Capital Humano” |
| PT | “Punção transeptal” |
| PV | Pulmonary veins |
| PVA | Polyvinyl alcohol |
| PVA-C | Polyvinyl alcohol cryogel |

| | |
|---|---|
| RA | Right atrium |
| RAA | Right atrial appendage |
| RAO | Right anterior oblique |
| RF | Radio-frequency |
| ROI | Region of interest |
| RotAng | Rotational Angiography |
| RP | Repeated procedure |
| RV | Right Ventricle |
| SA | Semi-automatic |
| SAx | Short-axis view |
| SIA | “Septo interauricular” |
| SLY | Signed local Yezzi |
| stl | Stereolitrography |
| SVC | Superior vena cava |
| TA | Transaortic |
| TEE | Transesophageal echocardiography |
| th | Threshold |
| TSP | Transseptal puncture |
| TTE | Transthoracic echocardiography |
| TV | Tricuspid valve |
| UP | University of Porto |
| US | Ultrasound |
| V | Validation |
| VC | Vena cava |
| VTK | Visualization Toolkit |

## List of Figures

## List of Tables

# Chapter 1

## Introduction

The current PhD thesis focused on the development of novel automated image-based solutions to improve the planning of left atrial minimally invasive interventions. This initial chapter introduces the main clinical aspects related to the thesis' topics, presenting a general overview of the heart anatomy (with specific emphasis on the atria and the inter-atrial septal wall), cardiac function and most common atrial pathologies. Then, the concept of transcatheter cardiac interventions is introduced, briefly describing the different steps of two specific interventions/procedures. The relevance of the different medical imaging modalities is highlighted for each intervention, later presenting some medical image processing solutions that have been developed for each. The final part of this chapter describes the motivation, aims and contributions of this PhD thesis.

**Contents**

## 1.1. The heart

The heart is a double intermittent side by side pump that propels the blood into the vessels, transporting it to the body (Figure 1.1) (Davies *et al.*, 2001). Both pumps work in an almost synchronous way. The right heart pump ejects deoxygenated blood to the lungs through the pulmonary circulation, later returning to the left heart pump as oxygenated blood and pumped to the entire body via the systemic circulation (Boron and Boulpaep, 2008). The walls of the heart are mainly composed of cardiac muscle (the myocytes), termed as the myocardium, which is an autonomous striated muscle (Davies *et al.*, 2001). Electrical pulses are propagated through these cardiac muscles, controlling the contraction and relaxation moment of each of them, creating thereby the cardiac cycle (Martini, 2018). Two main periods must be emphasized in this cycle, the contraction (known as systole) and the relaxation (known as diastole). During systole[1], the volume of each cardiac chamber decreases with an increase of the pressure inside the cavity, pushing the blood to other compartments or to the pulmonary/systemic system. In

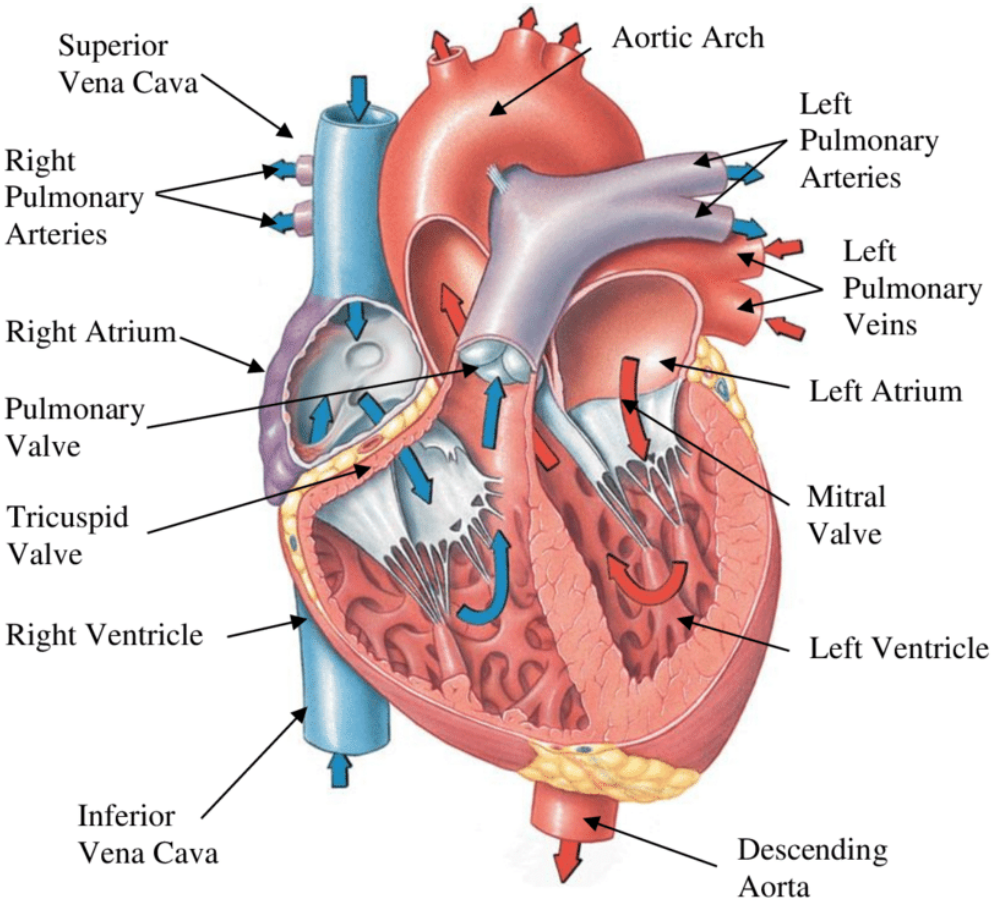


**Figure 1.1 - Illustration of the cardiac anatomy.**
Reprinted by permission of Pearson Education, Inc., New York, New York (Martini, 2018).

[1] Note that systole and diastole are terms more commonly used to describe the left ventricular function, which implies that the atrial volume is maximum and minimum at these stages, respectively.

opposition, during diastole[1], the chambers' volume increases with a decrease of the pressure, allowing the blood filling process (Davies *et al.*, 2001; Martini, 2018).

### 1.1.1. Cardiac anatomy and function

The heart is composed by four chambers (Figure 1.1): the left and right ventricle (LV and RV) and the left and the right atria (LA and RA) (Boron and Boulpaep, 2008). The LA and LV constitute the left heart pump, while the right pump relies on the RA and RV cavities (Boron and Boulpaep, 2008). Both atria collect blood from the circulatory system and eject it into the ventricles. They are anatomically smaller than the ventricles and they are composed by thin muscular walls, making them highly expandable chambers (Hall, 2006; Martini, 2018). In contrast, the ventricles are responsible to pump the blood to the body (*i.e.* the RV to the lungs and the LV to the remaining body), showing larger volume and thicker muscular walls (Davies *et al.*, 2001; Martini, 2018). Two atrioventricular valves (Figure 1.1), which open passively, are used to control the blood circulation and to prevent backflow between atria and ventricles, namely the mitral valve (MV, also known as the bicuspid valve) and the tricuspid valve (TV) for the left and right heart, respectively. Moreover, two semilunar valves are found between ventricles and the remaining body. The aortic valve (AV) controls the blood flow between the LV and the main great vessel (or artery) of the human body (the aorta), while the pulmonary valve (second great vessel) is found between the RV and the pulmonary artery (PA) (Davies *et al.*, 2001; Martini, 2018; Silverthorn *et al.*, 2009).

The cardiac function, through each heartbeat, is an involuntary dynamic process maintained by a complex electrical activity (Davies *et al.*, 2001; Hall, 2006; Martini, 2018). This is a complex and fast process (approximately 70 times per minute), which is repeated throughout life. Since the entire activity is controlled by electrical pulses, it can be registered through an electrocardiogram (ECG) (Davies *et al.*, 2001; Martini, 2018; Rhoades and Bell, 2012). The heartbeat is divided into four phases (Figure 1.2): 1) isovolumetric ventricular contraction; 2) ejection; 3) isovolumetric ventricular relaxation (Davies *et al.*, 2001); and 4) ventricular filling. Stage 1 starts with the depolarization of both ventricles (QRS complex in the ECG), and its contraction (*i.e.* ventricular systole). Since the pressure inside the ventricles starts increasing (while reducing the ventricular volume), the atrioventricular valves are closed (*i.e.* pressure inside ventricles is higher than the atria) (Davies *et al.*, 2001). This phase ends when the ventricular pressure exceeds the pressure inside the aorta and the pulmonary artery. Then, the semilunar valves open (stage 2), and the blood flows through the great vessels. At stage 3 (beginning of the ventricular diastole), the ventricular pressure starts reducing while increasing

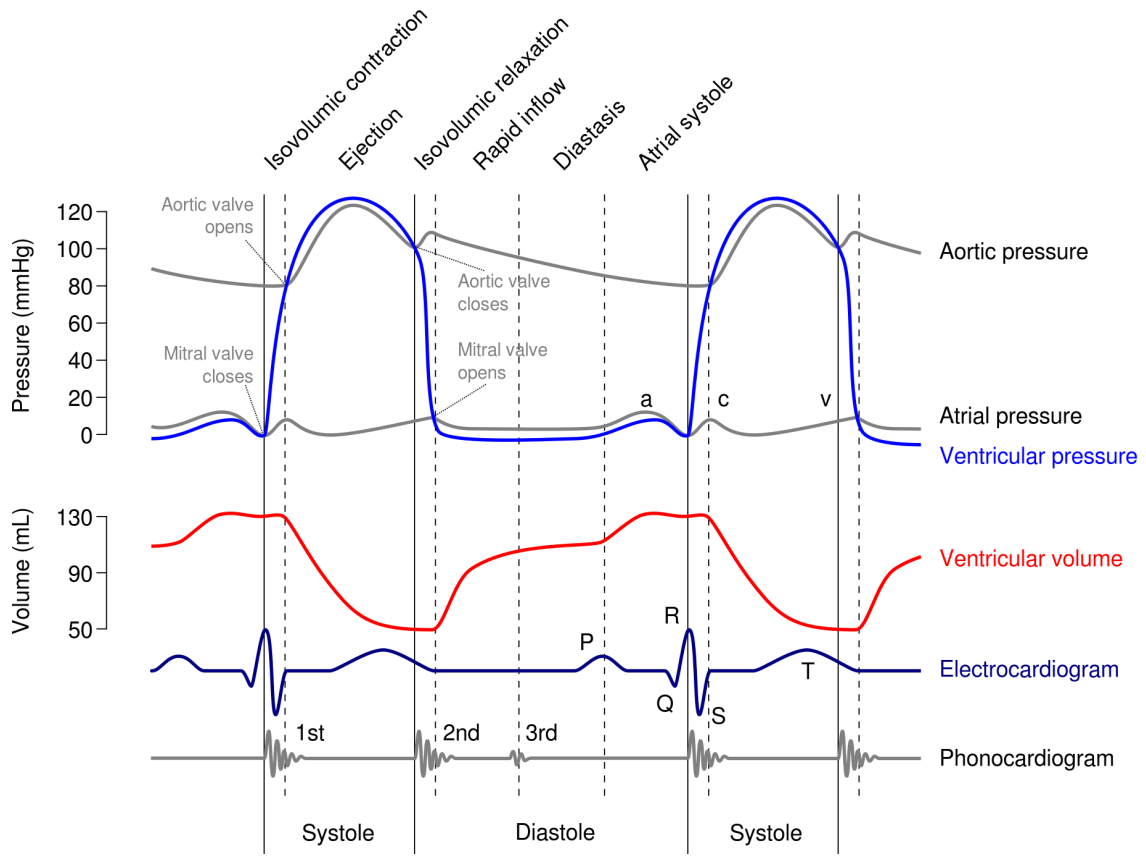


**Figure 1.2 - Wiggers diagram summarizing the key events (and associated traces) during the cardiac cycle.** Reproduced with permission via Wikimedia Commons.

the ventricular volume. A closure of the semilunar valves is observed. Simultaneously, blood starts flowing into the atria, increasing their pressure. When the atrial pressures are higher than the ventricular ones, the atrioventricular valves opens, inducing blood flow and thereby filling both ventricles, starting therefore stage 4 (*i.e.* the ventricular filling). This stage is divided into three sequential moments, namely: the rapid inflow, the diastasis and the atrial systole. The first occurs while the ventricles are relaxing (*i.e.* ventricular relaxation), allowing fast filling of the ventricles. Then, at diastasis, a slowdown of the ventricular filling is registered, due to the continuous expansion of the ventricles, which makes them less compliant. At the end of this stage, atrial depolarization (detected in the ECG as the P wave) triggers atrial systole, defining the ventricular diastolic period, and the cycle starts over (Davies *et al.*, 2001; Rhoades and Bell, 2012).

### 1.1.2. The atria

Anatomically, the RA is larger than the LA with thinner walls (Figure 1.3) (Standring, 2008). It has an irregular ellipsoid shape and it is superiorly delimited by the superior vena cava (SVC) and the right atrial appendage (RAA) (Martini, 2018; Standring, 2008). Inferiorly, the

RA is delimited by the inferior vena cava (IVC) and the tricuspid valve (Figure 1.3). Both SVC and IVC are used to return blood (from the upper body and the lower body, respectively) to the heart through a low-pressure route (Martini, 2018). The RAA is a small sac connected to the RA, being broad and triangular with a wide junction (Al-Saady *et al.*, 1999). Moreover, the coronary sinus (CS), which corresponds to a set of vessels that collect blood from the myocardium draining into the RA, is usually located between the IVC and the TV. The sinoatrial node (SA, the pacemaker of the heart), which spontaneously initializes the cardiac electric activity, is positioned laterally to the SVC ostia (Anderson *et al.*, 1999; Standring,

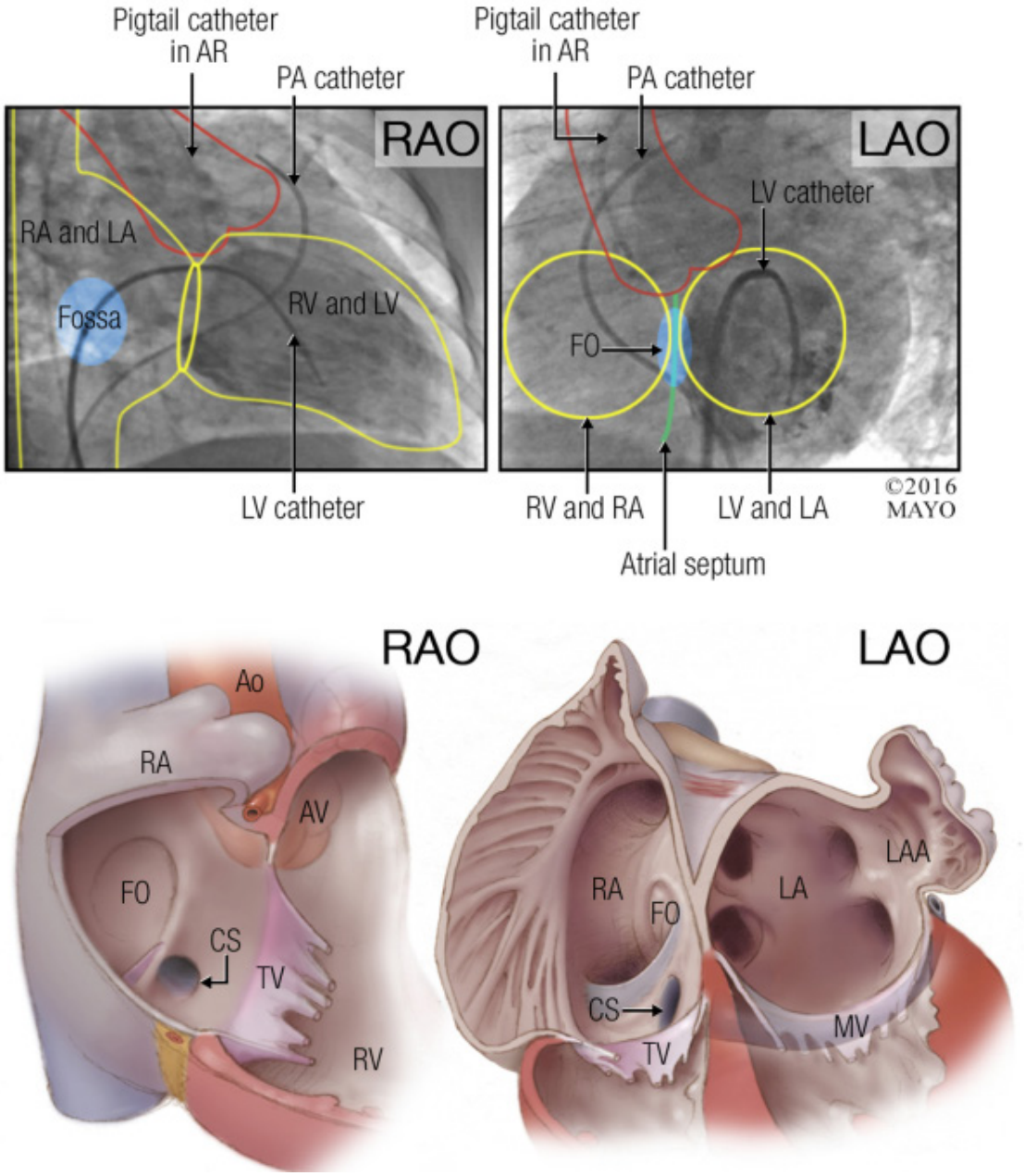


**Figure 1.3 - Schematic of the atrial anatomy and the inter-atrial septal wall at the X-ray projections.** X-ray projections: left anterior oblique (LAO) and right anterior oblique (RAO). Reproduced with permission from Alkhouli *et al.* (2016).

2008). Regarding the LA, it has a cuboidal shape (Figure 1.3), it is delimited superiorly by four main pulmonary veins (PV, which drain blood to the LA from the lungs) and the left atrial appendage (LAA), and inferiorly by the MV (Standring, 2008). Similar to the RAA, the LAA is a small sac that represents the remnant of the original embryonic LA. Nevertheless, the LAA has a highly variable anatomy, being usually a long, tubular and blind-ended structure (Al-Saady *et al.*, 1999; Wunderlich *et al.*, 2015). Externally, both atria are surrounded by several vital structures, namely the aorta, the pulmonary artery and the esophagus (Ho *et al.*, 2011).

Both atria are physically separated by a thin small membrane, termed as inter-atrial septal wall (IAS, Figure 1.3). The IAS is formed from the fusion of the thin septum primum (LA septum) and the thicker septum secundum (RA septum) (Babaliaros *et al.*, 2008; Faletra *et al.*, 2017; Standring, 2008), and it can be divided into three regions: 1) the muscular part – fusion of septum secundum and septum primum; 2) the limbus – the immediate surrounding margins of the muscular rim; and 3) the fossa ovalis (FO) – a thin flap valve at the middle of the limbus formed mainly by the septum primum. The FO is the thinnest region of the IAS and it is mainly composed of fibrous tissue (Babaliaros *et al.*, 2008; Faletra *et al.*, 2017; Standring, 2008). When assessed from the right heart, it is described as a depression with an oval or circular shape. It presents an expected area between 1.5-2.4 $cm^2$ and it is situated at the lower part of the septum, between the IVC and the CS (Babaliaros *et al.*, 2008). Beyond the FO, the His bundle is also positioned at the inferior IAS wall, and it is composed by a set of myocardial cells specialized for the electrical conduction of the cardiac activity (Standring, 2008).

### 1.1.3. Left atrial pathologies

Left atrial pathologies are characterized by an abnormal function or morphology of the LA and its remnant structures. Since the heart is divided into several chambers which interact between them, categorization of the cardiovascular diseases as an LA pathology is not straightforward. Indeed, several LA pathologies are often caused by a disorder of the main left heart chamber, *i.e.* the LV, which negatively affect the LA function, blocking the normal blood flow or even hampering the LA contraction. The opposite situation (*i.e.* the LV is affected by the abnormal LA activity) is also common. Overall, the main LA pathologies can be categorized as: 1) disorders of cardiac conduction (namely, arrhythmias), 2) shunted flow (e.g. atrial septal defects, ASD); 3) obstruction of flow (e.g. mitral valve stenosis and blood clots/thrombus formation); and 4) regurgitation flow (e.g. mitral valve regurgitation) (Kumar *et al.*, 2014). The different pathologies typically manifest through abnormal heart electrical activity,

morphological modifications (e.g. LA enlargement), chest pain, palpitations, among others (Kirchhof *et al.*, 2016; Sanchis-Gomar *et al.*, 2017).

Atrial fibrillation (AF) is the most common arrhythmia and it is described as an abnormal heart rhythm, with a fast and irregular beating of the atria (Sanchis-Gomar *et al.*, 2017). It affects more than 30 million persons worldwide and it shows a prevalence of one in every four middle-aged adults in Europe (Kirchhof *et al.*, 2016; Sanchis-Gomar *et al.*, 2017). It can result in atrial dilation, valvular heart diseases and congestive heart failure. Moreover, it is one of the major causes of stroke and sudden death.

Atrial septal defect is a congenital heart disease that is described as an abnormal communication route between the LA and RA (through the IAS). It is the third most common congenital heart disease, with an incidence of 56 per 100 000 live births (approximately 7% of all congenital heart diseases) (Akagi, 2015; Geva *et al.*, 2014). Three types of ASD are typically described, being the most common the secundum defects. This condition can lead to right-sided heart failure, arrhythmia and pulmonary hypertension (Akagi, 2015; Geva *et al.*, 2014).

Blood clot formation can occlude the normal function of specific structures into the heart, may prevent the blood flow and the correct oxygenation of the different cardiac anatomies (Kumar *et al.*, 2014). Moreover, it can affect specific vessels or arteries, which may result in complications, such as ischemia or even stroke. Currently, it is known that the LAA is one of the major sources of thromboembolism in the left heart. This situation is aggravated in patients with non-valvular atrial fibrillation (NVAF), where 90% of thrombi are located in this appendage, usually requiring treatment to reduce the risk of thromboembolism (Meier *et al.*, 2014; Wunderlich *et al.*, 2015). Indeed, this increased risk for thromboembolism formation is explained by a reduction of the LAA contractibility due to AF (Beigel *et al.*, 2014). If untreated, stroke is the most common result. Moreover, embolization of lower extremities is also possible.

Mitral valve diseases (MVD) represent all pathologies related to MV function and morphology. It is the most common valvular heart disease, with a prevalence of more than 10% in people older than 75 years (Nishimura *et al.*, 2012). Mitral regurgitation and mitral stenosis are the MVD with higher incidence, with a prevalence of 1.7% and 0.1% in the USA. The former is characterized by an incomplete closure of the valve, allowing blood's back flow throughout the cardiac cycle. It can be caused by an abnormality of the MV apparatus or even result from other cardiac pathology (e.g. endocarditis). The latter is a result of a partial/total immobility of the valve leaflets, which partially narrows the annular valve orifice, influencing therefore the blood flow and the blood pressure between atria and ventricles. The most common cause is rheumatic carditis, which may cause leaflet thickening and calcification, commissural

fusional or even chordal fusion (Motiwala and Delling, 2015). Congenital malformations are also possible but rare (Nishimura *et al.*, 2012).

Different treatments are currently available and performed for the abovementioned pathologies. Although in the initial stages, medical treatment is preferred, cardiac interventions or even cardiac surgery is applied in severe cases. Indeed, due to its advantages for the patient (*i.e.* small incision, fast recovery period), minimally invasive cardiac interventions (through transcatheter approaches) are being widely explored and applied to treat LA pathologies. A description of LA transcatheter cardiac interventions is presented in the next section.

## 1.2. Left atrial transcatheter cardiac interventions

Transcatheter cardiac interventions cover the minimally invasive procedures where access to the heart is performed via the circulatory system. Instead of the traditional open-chest surgery that requires large incisions in the chest wall to access the target organ, minimally invasive interventions use only a small hole through the skin to access the vascular system and, consequently, to access the heart. Nowadays, a high number of cardiac procedures are performed using this approach, such as mitral valve replacement (Baldus *et al.*, 2012), atrial septal defect closure (Akagi, 2015), catheter ablation for atrial fibrillation (Kirchhof *et al.*, 2016), left atrial appendage occlusion (Wunderlich *et al.*, 2015), among others.

Since vascular access is used, a direct visualization of the target is not possible and manipulation of surgical instruments is difficult. Thus, several kinds of equipment are required to guarantee a safe medical procedure, namely imaging modalities to guide the expert throughout the entire procedure and transcatheter surgical tools (e.g. electrocautery needles, guidewire, dilators, sheaths, contrast-injection tools) to ease the instruments manipulation.

Several advantages are associated with these minimally invasive techniques, namely: less postoperative pain, reduced procedural time, improved cosmetic result, less blood loss, lower costs and shorter hospital stay (Rosengart *et al.*, 2008). However, these techniques require experienced operators and high-level of equipment. Moreover, interventional complications can result in open-chest surgery and failures are possible.

In the next sub-sections, a detailed description of two specific LA interventions will be presented. The first one is termed transseptal puncture (TSP) and it is clinically used to gain access to the LA body (Figure 1.4). The second intervention is the LAA occlusion, where an occluding device, inserted transseptally, is implanted at the LAA orifice, preventing/reducing the risk of thromboembolism. It might be noted that although the technical contributions of the

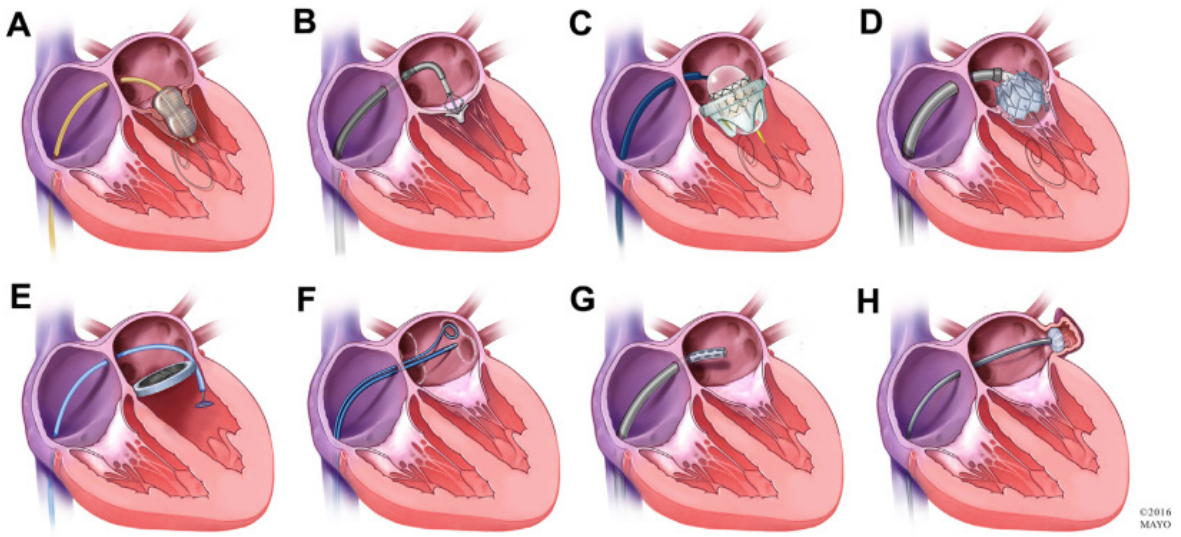


**Figure 1.4 – Illustration of the various transseptal cardiac interventions.**
(A) Percutaneous mitral balloon valvuloplasty; (B) Transcatheter mitral valve repair; (C) Mitral valve-in-valve implantation; (D) Transcatheter mitral valve replacement; (E) Mitral paravalvular leak closure; (F) Pulmonary vein isolation; (G) Percutaneous left ventricular assist device placement and (H) Left atrial appendage closure. Reproduced with permission from Alkhouli *et al.* (2016).

current thesis are mainly demonstrated in these two LA interventions, its application or even extension for some of the remaining LA interventions is also feasible.

### 1.2.1. Transseptal puncture

Since no direct percutaneous access route to the LA is anatomically available, a transseptal route is traditionally used. For that, the TSP procedure is widely applied, where a catheter is inserted until the RA, through which a needle is moved forward to puncture the IAS wall and access the LA body.

In short, the procedure relies on the following steps (Figure 1.5):

1) a guidewire is inserted into the vena cava using a femoral vein access;

2) a dilator and sheath are positioned at the SVC using the guidewire (Figure 1.5A);

3) the guidewire is removed and replaced by a transseptal needle (Figure 1.5B-C). This needle is kept inside the sheath to prevent procedural complications;

4) the full assembly (dilator, sheath and needle) is rotated to 4-5 o'clock, pulled-down and then aligned with the FO region (Figure 1.5C-E). While moving the assembly, two movements will be detected, namely the entrance into the RA body (Figure 1.5D) and the depression of the IAS wall (*i.e.* the FO, Figure 1.5E). It might be noted that since the FO is the thinnest region of the IAS wall and due to its anatomical spatial location, the FO is clinically accepted as the optimal puncture region;

5) alignment between the assembly and the FO is confirmed using medical images;

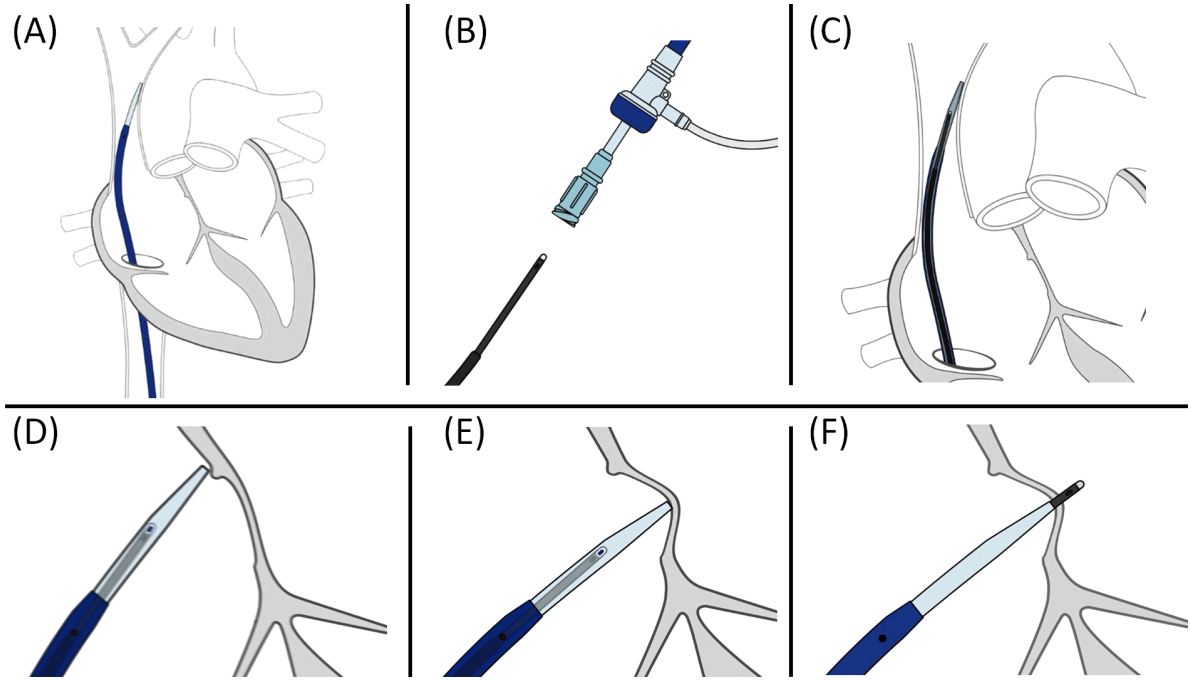


**Figure 1.5 - Transseptal puncture technique.**
(A) A dilator and sheath are placed into the SVC using a guidewire; (B) a needle is inserted into the dilator until (C) the SVC. The needle is pull-down and two movements are detected: (D) entrance into the RA and (E) entrance into the FO. (F) Then, the puncture is performed. © Baylis Medical Company Inc., 2014. Used with permission. Baylis does not endorse the research or claims made herein.

6) the IAS wall is punctured by the transseptal needle (Figure 1.5F);

7) confirmation of a successful puncture using medical images.

### 1.2.2. Left atrial appendage occlusion

The LAA occlusion consists of the percutaneous implantation of a foldable device at the LAA orifice, obstructing it and interrupting the communication between the LA body and the LAA (Figure 1.6) (Meier *et al.*, 2014; Wunderlich *et al.*, 2015). Similar to the majority of the LA interventions, the initial access to the LA is performed via a transseptal route. Then, after puncturing the IAS wall, a pigtail catheter is advanced into the LAA and later exchanged by a stiff guidewire for the delivery sheath (Figure 1.6a) (Meier *et al.*, 2014). At this point, anatomical evaluation of the LAA is performed and relevant clinical indicators are estimated to identify the optimal occluding device. The different measurements are normally computed using medical images (Saw and Lempereur, 2014; Song *et al.*, 2016; Wunderlich *et al.*, 2015). Contrast-agents are usually injected to enhance the particularities of the LAA anatomy, easing the estimation of these measurements. Regarding the occluding devices, a high number of devices with different specifications (e.g. shape, size) are produced by independent companies (Saw and Lempereur, 2014). The most common ones are the Watchman (Boston Scientific, Natick, Massachusetts), the Amulet (St. Jude Medical, St. Paul, Minnesota) and the WaveCrest

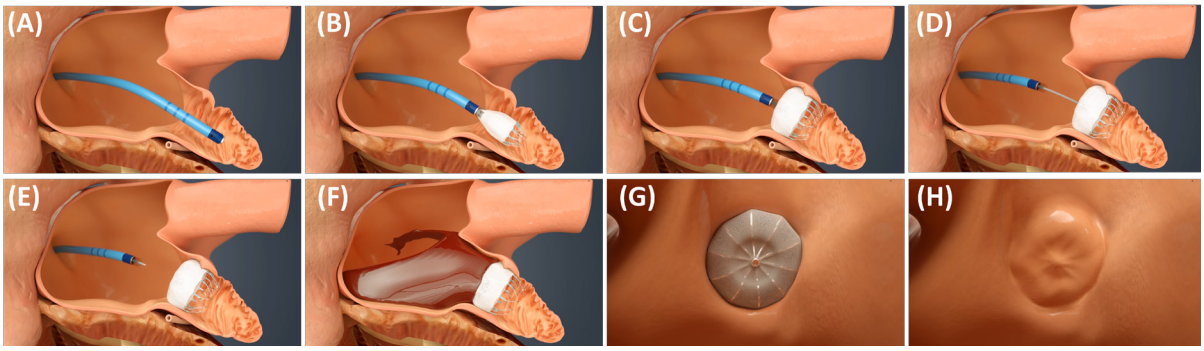


**Figure 1.6 – Left atrial appendage occlusion intervention.**
(A) A catheter is advanced into the LAA; (B) The device is released at the optimal location (C). (D) The expert evaluates the level of anchorage of the device and then release it (E). (F, G) The device occludes the communication between the LA body and the LAA. (H) After a few months, it is covered by a biological tissue, increasing the long-term fixation of the device.
Adapted from: https://www.youtube.com/watch?v=K-RZM6sG-pc&t=4s (accessed at 13/07/2018).

(Coherex Medical Inc., Salt Lake City, Utah) (Wunderlich *et al.*, 2015). Therefore, the expert should be familiarized with the specifications and limitations of each device before implanting it. Further details on devices' specifications can be found in (Meier *et al.*, 2014).

After implanting the device (Figure 1.6B-C), the expert must confirm the correct positioning and anchorage of the device to the anatomy (Figure 1.6D). As such, while keeping the delivery device connected to the occluder, the entire unit is pulled-back, evaluating its anchorage level. Ideally, this device must be slightly compressed by the LAA walls, reducing the risk of device embolization (Meier *et al.*, 2014). Moreover, the expert should be aware that residual leaks, due to sub-optimal occlusion, are common and must be evaluated. Such evaluation is performed using two-dimensional (2D) and three-dimensional (3D) intra-procedural images with contrast agents or even Doppler evaluation. While small residual leaks are not catastrophic to the patient (width <3 mm), large ones can still result in severe complications, namely thromboembolism. Although the first case does not require a modification of the procedure, the second one requires the implantation of a larger device. Finally, after confirming all these points, the device can be delivered (Figure 1.6E) and post-procedural medical images are used to confirm correct device implantation, again confirming the device position/shape (Bertrand *et al.*, 2014) and possible leaks. Later, the occluding device will be covered by biological tissue, generated thanks to an endothelization process, closing completely the interface between LA body and the occluder, improving therefore the long-term fixation of the device (Figure 1.6F-H) (Camm *et al.*, 2014).

In alternative to the LAA occlusion (*i.e.* endoluminal technique), an external exclusion approach through the LAA ligation device (termed LARIAT suture device) was also described. Although such technique was widely used in the past, it is currently known that the LARIAT

procedure can results on serious complications, such as pericardial effusion and major bleeding, making the endoluminal approach more attractive for clinical practice (Meier *et al.*, 2014; Saw and Lempereur, 2014; Stone *et al.*, 2015). Nevertheless, it should be taken into consideration that LAA occlusion is complex, requiring high operator's expertise.

## 1.3. Cardiac medical imaging

The success of cardiac minimally invasive interventions is highly dependent on the medical images used in the different procedural stages, namely: pre-procedural planning, intra-procedural guidance and post-procedural evaluation. Currently, a multitude of different imaging modalities is available, presenting advantages and limitations for the different stages. In the next sub-sections, an overview of the medical images typically applied in each of the abovementioned stages is described (section 1.3.1). Moreover, a description of recent technological advances to enhance relevant anatomical landmarks in these images is also presented (section 1.3.2). For further details on technical principles of each imaging modality, the reader is kindly directed to Suetens (2017).

### 1.3.1. Procedural stages

#### A. Pre-procedural planning

At this stage, high-resolution images are used to evaluate the cardiac anatomy, to confirm the initial diagnosis, to detect abnormal anatomies, to evaluate the percutaneous access route and to estimate relevant clinical measurements/landmarks (Bourier *et al.*, 2016; Christiaens *et al.*, 2010; Di Biase *et al.*, 2012; Pellegrino *et al.*, 2016; Schernthaner *et al.*, 2013; Verma *et al.*, 2011; Wagdi and Alkadhi, 2012). Computed tomography (CT) (Di Biase *et al.*, 2012; Pellegrino *et al.*, 2016), magnetic resonance imaging (MRI) (Meier *et al.*, 2014; Tobon-Gomez *et al.*, 2015) and ultrasound (US) acquisitions (namely, transthoracic, TTE, or transesophageal echocardiography, TEE) are paramount at this initial stage (Figure 1.7) (Meier *et al.*, 2014; Schernthaner *et al.*, 2013). While the first two modalities allow high-detailed 3D acquisitions, cardiac function assessment is limited and the acquisition protocol is complex, being time-consuming (mainly MRI) and requiring radiation exposure (for CT acquisition only) or even contrast agents in specific cases (Achenbach *et al.*, 2008; Libby, 2008; Schroeder *et al.*, 2007). The US acquisition shows a high temporal resolution (*i.e.* high frame rate) and it does not present any serious disadvantage to the patient health (Dandel and Hetzer, 2009; Klein *et al.*, 2001; Lang *et al.*, 2006). Nevertheless, the field of view (FOV) is limited and the resulting image is highly affected by artifacts (Noble and Boukerroui, 2006; Pedrosa *et al.*, 2016).

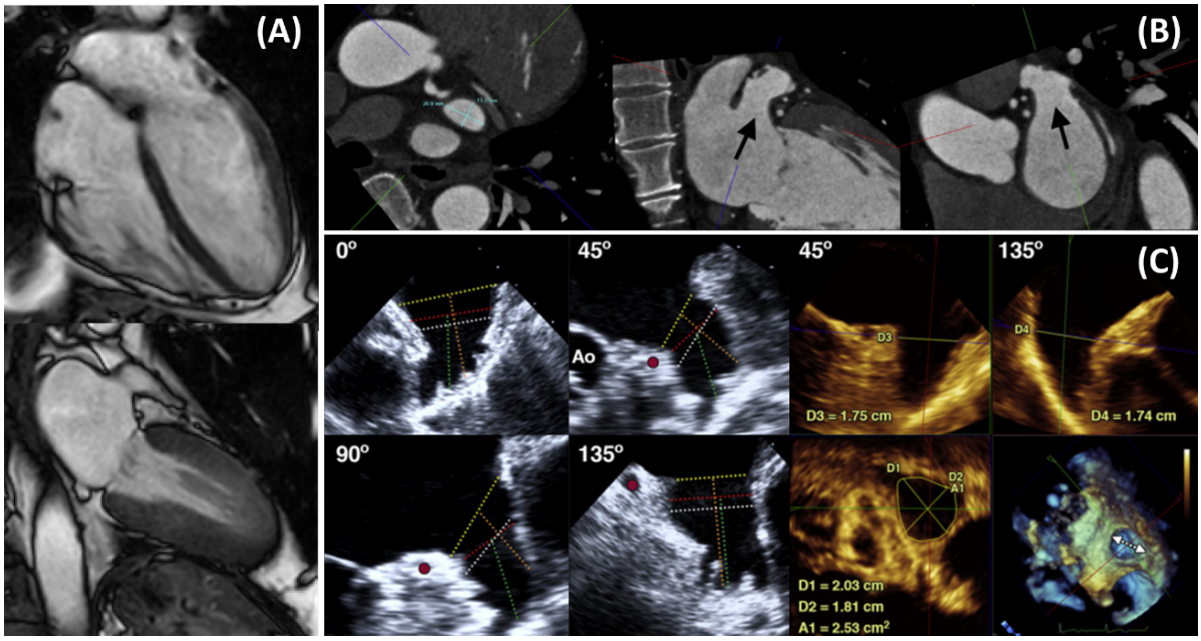


**Figure 1.7 - Pre-procedural medical images.**
(A) Magnetic Resonance Imaging; (B) Computed Tomography (reproduced with permission from Kwong and Troupis (2015)) and (C) Ultrasound imaging, namely transesophageal echocardiography. Reproduced with permission from Wunderlich *et al.* (2015).

Ultimately, US is dependent on the operator expertise. The 2D US is mainly acquired in normal clinical practice, due to the simple acquisition and superior image quality (Meier *et al.*, 2014). Notwithstanding, specialized centers corroborated the added-value of the volumetric ultrasound acquisition (Faletra *et al.*, 2011; Faletra *et al.*, 2014a).

Particularly for the TSP, CT and TEE acquisitions have proved their added-value for the evaluation of the IAS wall and prediction of the procedural feasibility by identifying abnormal situations (Schernthaner *et al.*, 2013; Verma *et al.*, 2011; Wagdi and Alkadhi, 2012). While CT is interesting to study the integrity of the IAS wall, to confirm the FO position and even to detect the optimal puncture location (Bourier *et al.*, 2016; Verma *et al.*, 2011; Wagdi and Alkadhi, 2012), TEE imaging shows its potential for the detection of specific pathologies using Doppler function (e.g. atrial septal defect), as well as to evaluate the flexibility of the IAS wall throughout the cardiac cycle (Schernthaner *et al.*, 2013). Regarding the LAA occlusion, taking into consideration the guidelines (Meier *et al.*, 2014), pre-procedural TEE acquisition is mandatory to evaluate the entire LAA anatomy and to confirm the absence of LAA thrombi (Meier *et al.*, 2014). Moreover, more recently, different researchers suggested the usage of CT to identify the optimal occluding device (Rajwani *et al.*, 2016; Wang *et al.*, 2016a).

### B. Intra-procedural guidance

The intra-operative images are vital to: 1) guide the different surgical tools (*i.e.* catheters, needles, guidewire); 2) estimate the device to be implanted; 3) identify relevant

landmarks (e.g. the fossa ovalis); 4) ensure correct position of the occluding device; and 5) identify and predict possible complications or failures.

The X-ray 2D fluoroscopy is the standard imaging modality to guide cardiac minimally invasive interventions (Figure 1.8A-C) (Babaliaros *et al.*, 2008; Earley, 2009). It allows a real-time acquisition with a high spatial resolution of any region of the human body, and it shows unique properties to visualize surgical instruments/devices. Moreover, it presents a large FOV, allowing an exceptional view of the full extent of the surgical catheters, increasing therefore the spatial perception of the operator (Cleary and Peters, 2010; Houston and Davis, 2001). Nevertheless, since soft-tissues are not easily detected, fluoroscopy does not provide relevant anatomical information. Moreover, 3D spatial perception is not straightforward. As a solution, contrast-agents are commonly injected and multiple views are acquired, instantly enhancing the cardiac borders and providing "limited" tridimensional information. Nonetheless, application of contrast agents can be harmful to specific patients and the multiple view acquisition increases the procedural time and radiation dose exposure (Cleary and Peters, 2010; Linte *et al.*, 2010b; Mah *et al.*, 2014; Nguyen *et al.*, 2013). To increase the spatial information throughout the intervention, fluoroscopy is typically complemented with 3D TEE (Figure 1.8D-F) (Chierchia *et al.*, 2008) or 3D intra-cardiac echocardiography (3D-ICE) (Biermann *et al.*, 2012; Russo *et*

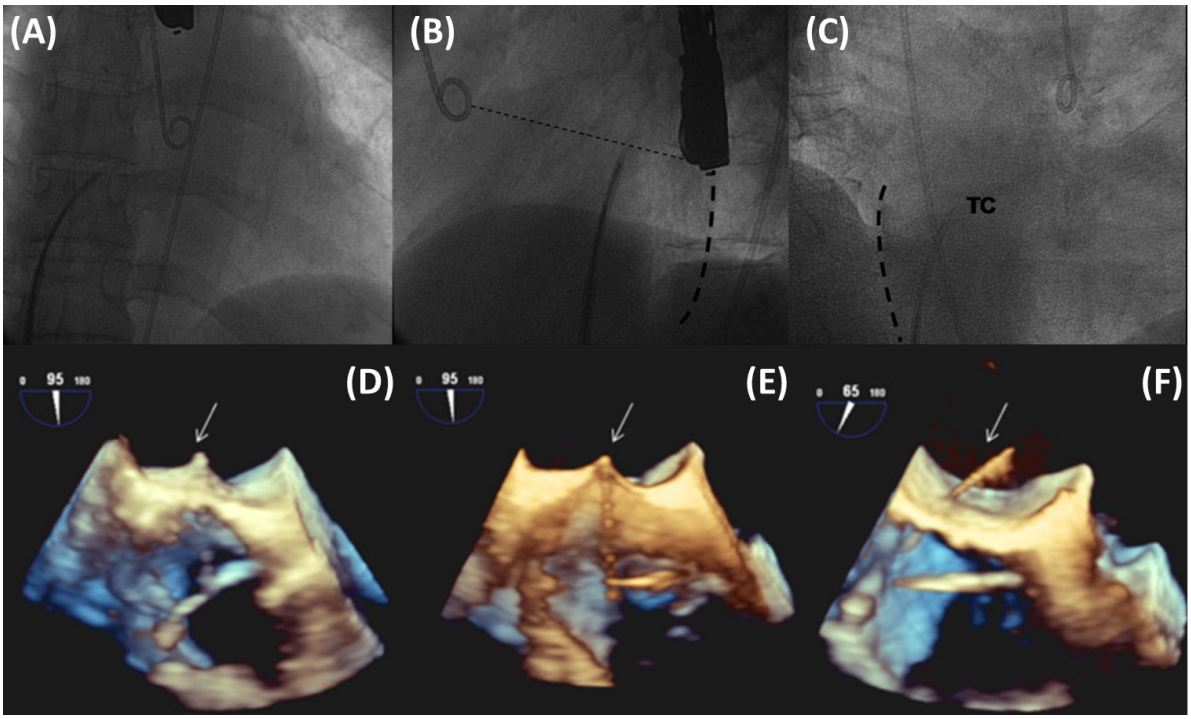


**Figure 1.8 – Intra-procedural medical images in transseptal puncture.**
(A-C) X-ray fluoroscopy image (reproduced with permission from Babaliaros *et al.* (2008)) and (D-F) transesophageal echocardiography (reproduced with permission from Vahanian and Brochet (2017)). Note that (D), (E) and (F) represents the tenting phase, the puncture and the crossing of the inter-atrial septal wall by a transseptal needle, respectively. TC – transseptal dilator.

*al.*, 2013). Nevertheless, both imaging modalities are typically acquired independently, making its interpretation hard. More recently, rotational angiography was also proposed, allowing a fast acquisition of multiple 3D volumes throughout the intervention (Koektuerk *et al.*, 2016).

Taken into consideration the abovementioned LA interventions, fluoroscopy is mandatory to guide the catheter inserted into the femoral vein until the RA (Babaliaros *et al.*, 2008; Earley, 2009). Then, the puncture of the IAS wall is typically performed by combining both fluoroscopy and TEE images (Chierchia *et al.*, 2008; Faletra *et al.*, 2011). At the TEE images, correct alignment between the needle and the FO is confirmed, while the fluoroscopy is used to manipulate all surgical instruments (Babaliaros *et al.*, 2008; Chierchia *et al.*, 2008; Faletra *et al.*, 2011). The correct puncture attempt is confirmed through TEE (Figure 1.8D-F) (Faletra *et al.*, 2011). After puncturing the IAS wall, access to the LAA cavity is performed through fluoroscopy. The optimal occluding device is selected based on images acquired throughout the intervention (termed peri-procedural images) (Meier *et al.*, 2014; Wunderlich *et al.*, 2015). Due to the high anatomical variability of the LAA (Figure 1.9), both fluoroscopy (by injecting contrast in multiple views) and 3D TEE are acquired and evaluated at this stage.

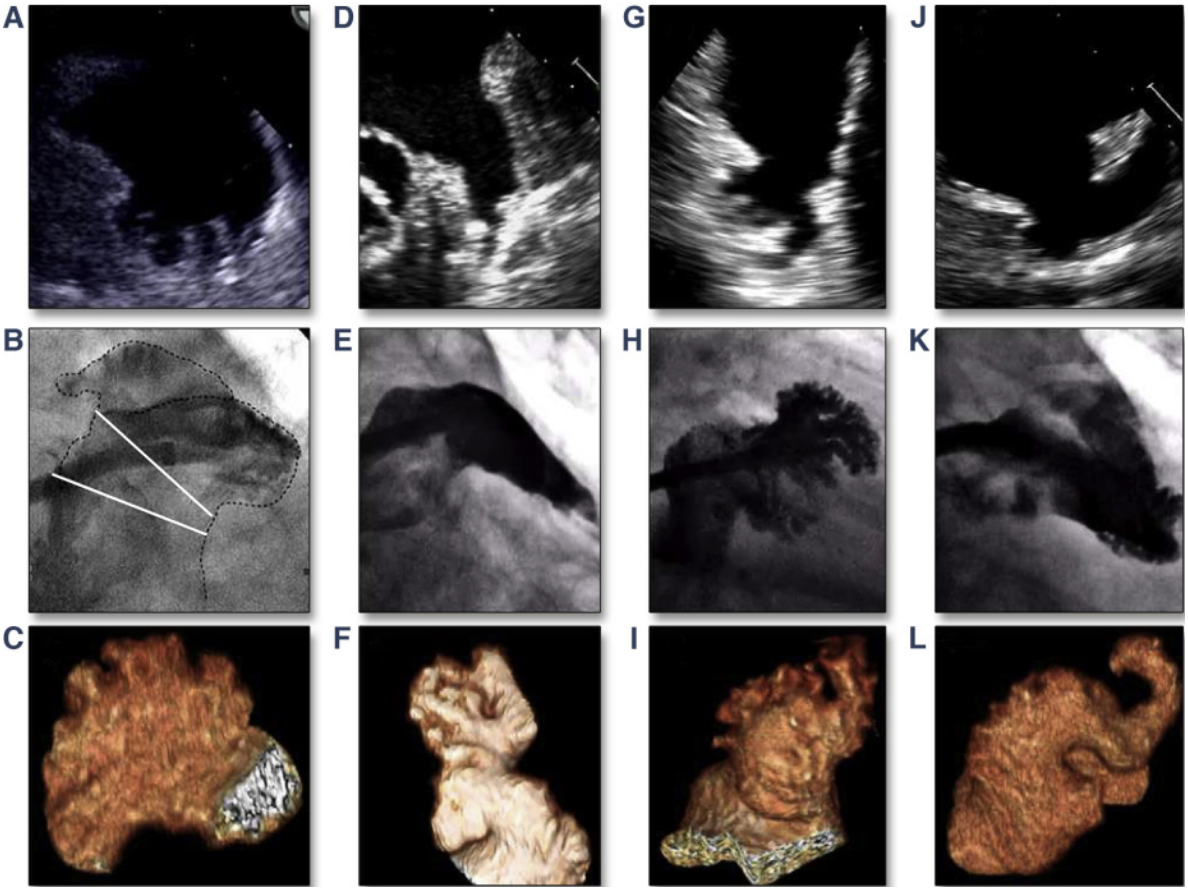


**Figure 1.9 - Intra-procedural medical images in the LAA occlusion.**
The first line shows examples of transesophageal echocardiographic images, while the second line shows examples of X-ray fluoroscopic images. The last line shows 3D reconstructions. Each column represents the same patient. Reproduced with permission from Beigel *et al.* (2014).

Correct device delivery is again confirmed using both modalities, and possible residual leaks are assessed through Doppler imaging and contrast injection (Meier *et al.*, 2014).

**C. Post-procedural evaluation**

This final stage evaluates the intervention outcome, namely: confirmation of correct device position, presence/size of residual leaks (through flow analysis) and assessment of the integrity of the IAS wall. Although TEE is considered the most revealing technique at this stage (allows anatomical and function assessment), TTE, X-ray or even CT are also viable solutions (Meier *et al.*, 2014). This evaluation is performed at different periods, namely: 1) immediate after the intervention; 2) 45 days; 3) 6 months and 4) 1 year following implantation. It might be noted that these periods are not fixed and may vary between centers.

### 1.3.2. Medical image processing

A multitude of automated solutions were proposed to enhance and process the clinical medical images at different procedural stages. Such solutions make the image analysis process faster and more reproducible (removing or minimizing the inter- and intra-observer variability), presenting clear advantages to the normal clinical practice.

Starting with the pre-procedural planning stage, several researchers presented fully automated solutions to 3D segment the different cardiac chambers in CT images (Figure 1.10) (Ecabert *et al.*, 2008; Ecabert *et al.*, 2011; Kirişli *et al.*, 2010; Shahzad *et al.*, 2017; Zheng *et al.*, 2008; Zuluaga *et al.*, 2013). The obtained contours are used to evaluate relevant cardiac indices (e.g. the volume of each chamber) (Ecabert *et al.*, 2011), to assess the cardiac anatomy (Ecabert *et al.*, 2011; Tobon-Gomez *et al.*, 2015) and even to enhance the intra-procedural images through image-fusion strategies (Bourier *et al.*, 2016). Pure image-based (Tobon-Gomez *et al.*, 2015), deformable models (Ecabert *et al.*, 2008; Ecabert *et al.*, 2011), machine learning (Zheng *et al.*, 2008) and atlas-based techniques (Kirişli *et al.*, 2010; Shahzad *et al.*, 2017; Zuluaga *et al.*, 2013) were mainly applied. Interestingly, the deformable technique described by Ecabert *et al.* (2011) and the machine learning approach of Zheng *et al.* (2008)

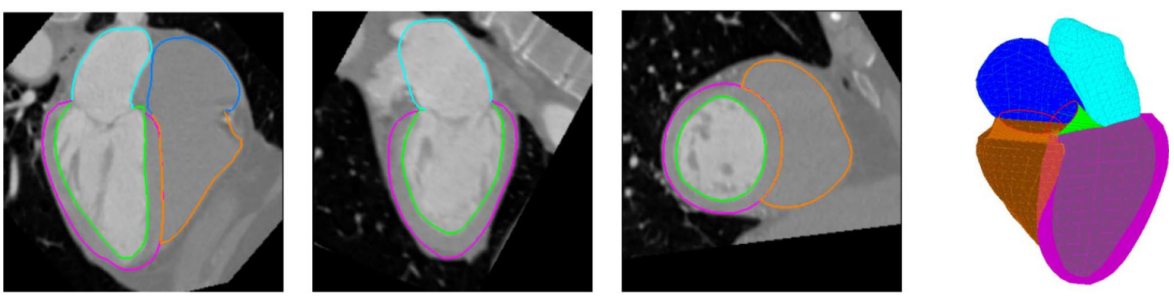

**Figure 1.10 – Example result of a fully automatic four-chamber heart model segmentation approach.** Reproduced with permission from Zheng *et al.* (2008).

proved their added-value for fast automatic segmentation (requiring a few seconds) of all cardiac chambers plus great vessels. The atlas-based technique proved its robustness in large clinical databases (Kirişli *et al.*, 2010; Shahzad *et al.*, 2017). Nevertheless, due to its long computational cost (several hours), its application in the clinical practice is limited. Automated solutions to segment specific cardiac chambers in MRI and ultrasound-based images (*i.e.* TEE and TTE) were also presented (Almeida *et al.*, 2016; Pedrosa *et al.*, 2016; Queirós *et al.*, 2016; Tobon-Gomez *et al.*, 2015). In a different way, simulation strategies to predict optimal puncture location were also described (Jayender *et al.*, 2011). For that, anatomical models were combined with a mechanical model of the transseptal needle, estimating the optimal puncture position that guarantees maximum catheter dexterity at the left heart.

Focusing on the LAA occlusion, patient-specific phantom models were developed, proving its potential for the identification of the optimal occluding device (Liu *et al.*, 2016; Pellegrino *et al.*, 2016). In detail, the patient anatomy is extracted from medical images (using manual or semi-automatic segmentation strategies) and physically constructed using 3D printing technologies. Then, multiple occluding devices are tested in the physically constructed model, allowing an accurate identification of the optimal one. Moreover, few studies describing automated strategies to segment the LAA in CT images were also presented (Grasland-Mongrain *et al.*, 2010; Jin *et al.*, 2018). Nevertheless, although 3D surfaces were accurately extracted, relevant clinical measurements were not estimated, requiring manual interaction. Moreover, such approaches are quite recent and require further validation.

Regarding the intra-operative stage, strategies to enhance fluoroscopy images by fusing it, with other image modalities were described (Basman *et al.*, 2017; Biaggi *et al.*, 2015; Cleary and Peters, 2010), namely TEE-fluoroscopy (Figure 1.11) (Afzal *et al.*, 2017; Faletra *et al.*, 2017; Gao *et al.*, 2012a; Lang *et al.*, 2011), fluoroscopy-CT (Bourier *et al.*, 2016; Liao *et al.*, 2013) and TEE-fluoroscopy-CT approaches (Housden *et al.*, 2013a). The majority of these approaches use the spatial location of the scanner/probe to fuse both modalities (Gao *et al.*, 2012a) or even through rigid pre-calibrations (Bourier *et al.*, 2016). While the fluoroscopy allows accurate visualization of the catheter's position, the remaining modalities add the relevant 3D anatomical information (Figure 1.11). Moreover, these image-fusion approaches transfer the pre-planning models (e.g. anatomical models from CT) to the interventional world (Bourier *et al.*, 2016) easing the identification of relevant landmarks (e.g. FO can be estimated in TEE images and transferred to the fluoroscopy) (Faletra *et al.*, 2017). Tracking/localization of the surgical instruments was also explored (Cleary and Peters, 2010), by detecting it using image-based approaches (Brost *et al.*, 2010; De Buck *et al.*, 2009; Kozlowski *et al.*, 2017) or

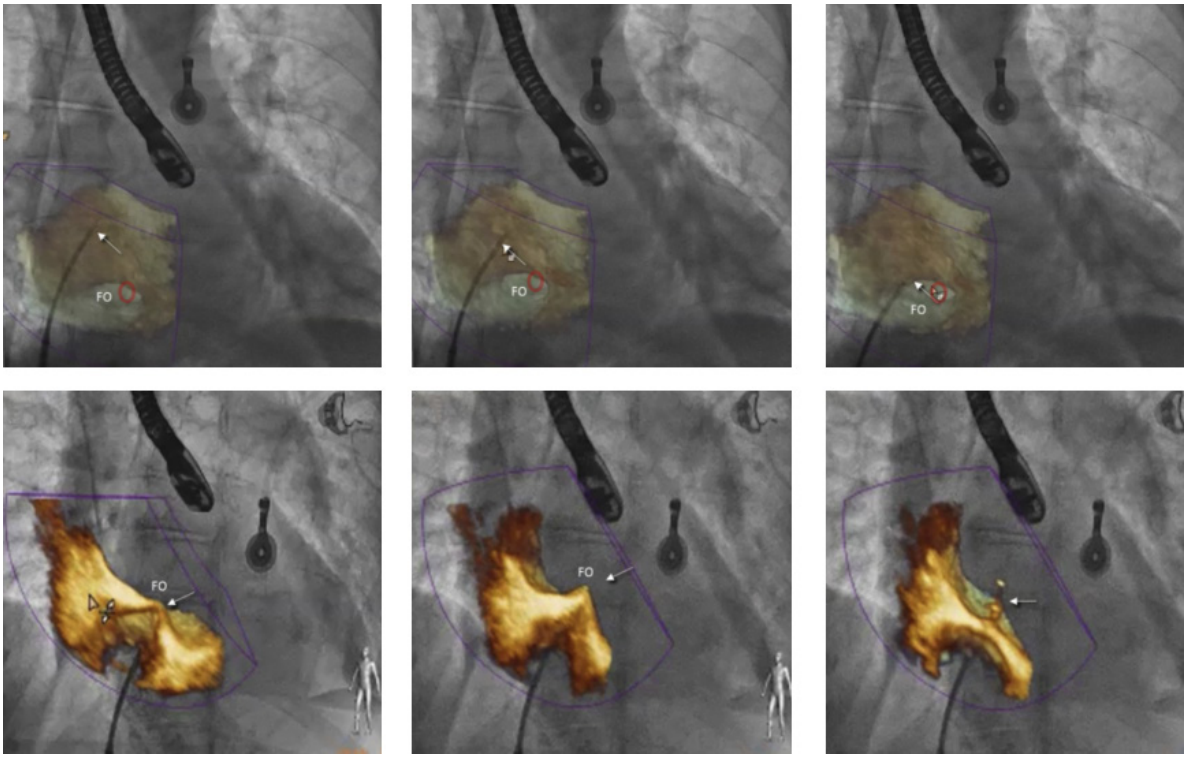


**Figure 1.11 – Fusion of X-ray fluoroscopy and TEE images to guide transseptal puncture.**
Reproduced with permission from Faletra *et al.* (2017).

through external electromagnetic sensors (Ballesteros *et al.*, 2017; Mansour *et al.*, 2015), corroborating its potential to reduce the radiation dose used during the guidance.

Finally, for the post-procedural evaluation stage, a few works focused on specific interventions were presented. Particularly for TSP and LAA occlusion, no relevant works were described. However, focusing on other LA interventions, strategies to quantify the amount of regurgitated flow after MV replacement intervention were described (Tan *et al.*, 2016).

## 1.4. Motivation

Minimally invasive left atrial interventions are routinely performed in normal clinical practice, showing a high application rate worldwide. Indeed, specific atrial pathologies show high prevalence typically requiring a percutaneous intervention to correct the abnormal cardiac anatomy or function. For instance, prevalence studies proved that, in 2010, 8.8 million of people in the European Union had atrial fibrillation and a notable increase is expected until 2060 (Krijthe *et al.*, 2013). Moreover, recent reports indicated that LAA is the major source of thromboembolism in patients with NVAF, showing a high risk of stroke (Meier *et al.*, 2014; Wunderlich *et al.*, 2015). To treat both pathologies, catheter ablation for atrial fibrillation and even LAA occlusion are usually applied, respectively. While the first is performed at the pulmonary veins, correcting the abnormal heart electrical pulses (Haegeli and Calkins, 2014),

the second intervention blocks the blood flow between LA body and LAA (Meier *et al.*, 2014; Wunderlich *et al.*, 2015). Both interventions require a transseptal access, which is commonly achieved through a TSP procedure (Alkhouli *et al.*, 2016; Earley, 2009). In fact, the majority of the LA interventions are performed using a transseptal access, corroborating the high application rate of this procedure (Alkhouli *et al.*, 2016).

Taking into consideration the high technological dependence of the minimally invasive atrial interventions (e.g. requiring medical images, specific catheters), a multitude of novel efficient solutions were proposed and validated during the last decade. Specifically for TSP, multiple researchers proposed novel guidance techniques (Bayrak *et al.*, 2012; Elagha *et al.*, 2008; Faletra *et al.*, 2017; Ferguson *et al.*, 2009; Mahmoud *et al.*, 2015; Mansour *et al.*, 2015; Nijenhuis *et al.*, 2017; Pavlović *et al.*, 2014; Ruisi *et al.*, 2013; Saliba *et al.*, 2008; Thiagalingam *et al.*, 2008) and improved surgical tools (Capulzini *et al.*, 2010; Fromentin *et al.*, 2011; Giudici *et al.*, 2015; Hsu *et al.*, 2013; Jauvert *et al.*, 2015; Knecht *et al.*, 2008a). The majority of these approaches proved their added-value for clinical routine (Capulzini *et al.*, 2010; Knecht *et al.*, 2008a; Mahmoud *et al.*, 2015), reducing the procedural time (Giudici *et al.*, 2015; Hsu *et al.*, 2013; Mahmoud *et al.*, 2015), the number of complications (Bayrak *et al.*, 2012; Faletra *et al.*, 2017; Jauvert *et al.*, 2015; Knecht *et al.*, 2008a; Mahmoud *et al.*, 2015; Saliba *et al.*, 2008) and/or the radiation dose (Elagha *et al.*, 2008; Mansour *et al.*, 2015; Pavlović *et al.*, 2014). Notwithstanding, focusing on the pre-procedural stage, few studies were presented (Bourier *et al.*, 2016; Jayender *et al.*, 2011; Schernthaner *et al.*, 2013; Verma *et al.*, 2011; Wagdi and Alkadhi, 2012), keeping the traditional technique sub-optimal to detect abnormal anatomies, to define safe routes and to recognize the optimal puncture location. A small number of strategies to estimate the optimal puncture location based on finite elements models (Jayender *et al.*, 2011) and to estimate the relevant anatomical landmarks (Bourier *et al.*, 2016; Schernthaner *et al.*, 2013; Verma *et al.*, 2011) were described. Nevertheless, both strategies rely on manual approaches to accurately extract the atrial contours and even the fossa ovalis region (Bourier *et al.*, 2016; Jayender *et al.*, 2011; Schernthaner *et al.*, 2013; Verma *et al.*, 2011). Despite such approach being extremely time-consuming (hampering its routine application in normal clinical practice), it also showed high intra- and inter-observer variability, being still a sub-optimal approach. Similarly, the majority of the technical advances in the LAA occlusion intervention focused on the development of novel and more efficient occluding devices (Meier *et al.*, 2014; Wunderlich *et al.*, 2015). Only a few works have focused on the pre-planning stage, describing strategies to segment the LAA anatomy or to generate mock models. Nevertheless, such approaches were mainly applied on high-detailed pre-procedural images (namely CT)

(Grasland-Mongrain *et al.*, 2010; Jin *et al.*, 2018), neglecting possible anatomical variations of the complex LAA shape at the intervention time and failing to estimate the relevant clinical measurements to identify the optimal occluding device. In this sense, in normal clinical practice, the optimal occluding device is usually identified during the intervention (using peri-procedural images) through a totally manual approach, which increases the procedural time, the radiation exposure dose and thus the procedural cost.

## 1.5. Aims

By evaluating the literature, it was clear that medical images are crucial in all interventional stages. Nevertheless, in particular for the pre-procedural planning stage, automatic strategies to process medical images are limited, and the available solutions usually require high user interaction, making them highly dependent on the user expertise, and being time demanding. As such, to improve the traditional pre-procedural planning procedures, the following aims were defined for this PhD project:

- To prepare an exhaustive literature review of novel technological solutions applied in transseptal-based left atrial interventions, describing the main contributions for each of the abovementioned procedural stages and assessing the application rate of this technique worldwide. Moreover, current limitations and possible future solutions will be highlighted.
- To improve, or even enhance, the planning of different LA interventions by proposing novel technological solutions, e.g. software solutions or patient models. The proposed solutions must be applied in normal clinical data (*i.e.* CT for the TSP and TEE for the LAA occlusion), not demanding any notable modification of normal clinical routine.
- To develop fully automatic, or at least semi-automatic, solutions for the abovementioned clinical applications, reducing/removing the inter- and intra-observer variability and potentially facilitating the medical decision, particularly in less specialized centers. Moreover, taking into consideration the time requirements for medical decision in some specific cases (e.g. device selection for LAA occlusion), the developed solutions must be computationally efficient.
- To evaluate the feasibility of the developed methods in different and novel scenarios, corroborating their versatility/potential for future applications.
- To study the application of the novel planning techniques in real interventions, through the development of novel integrated interventional frameworks.

The current PhD thesis intended to develop novel solutions to improve the planning stage of LA interventions, namely the TSP and LAA occlusion interventions. In this sense, novel approaches for construction of patient-specific phantom models from pre-procedural data for simulation and medical training on specific atrial interventions were developed. Moreover, initial concepts to improve the guidance of LA interventions by fusing pre-procedural and intra-procedural data were presented. Finally, automated software solutions, based on image segmentation techniques, were also pursued throughout this PhD thesis to accurately and quickly extract the relevant anatomical models, landmarks and clinical indicators, reducing the analysis time and increasing the reproducibility of the analysis, ultimately facilitating the medical clinical routines.

## 1.6. Brief description of the developed work

In this sub-section, a brief description of each chapter is presented, indicating the aim and the relevant contributions and results of each one.

The current thesis is divided into two parts, describing developments for the TSP (Part I) and the LAA occlusion (Part II) interventions, respectively.

In Part I, Chapter 2 starts by reviewing the literature, showing the recent technological solutions applied to the TSP. This review addressed three major development fields, namely: pre-procedural planning techniques, guidance approaches and surgical tools. Finally, taken into consideration the current limitations in the literature, a future trends section was also included, showing the authors view for the next years. Then, taking into consideration the focus of this thesis, a novel patient-specific atrial phantom model with correct modeling of the thin atrial walls was developed (Chapter 3). This phantom model can be used to improve the planning stage and even to improve the current medical training. The manufacturing process of this strategy was evaluated proving its high accuracy. Additionally, the resulting intra-procedural image was also evaluated, allowing correct identification of the different anatomies. This model was later used as a validation scenario in a novel concept for an interventional framework for TSP intervention (Chapter 4), which may improve the current TSP intervention. Nevertheless, this interventional framework required high user interaction, hampering its application in normal clinical practice. In this sense, a novel semi-automatic strategy to segment the atrial region with correct delineation of the thin mid atrial walls in pro-procedural data was presented (Chapter 5). The feasibility of this novel method was tested in both CT and MR datasets, showing a performance similar to other state-of-the-art methods in terms of segmentation metrics but with a clearly superior performance at the thin wall regions. As a clear novelty, this

work introduced a competitive segmentation formulation, which uses the spatial position of the different contours to improve the robustness of the method and to correctly delineate the mid thin atrial walls. This competitive strategy was expanded to a fully automatic one in Chapter 6 using a fast global atlas-based technique, and later applied to estimate relevant anatomical landmarks of the IAS wall, namely the fossa ovalis region (Chapter 6). The results corroborated the high accuracy of this fully automatic approach, with a performance comparable to the inter-observer variability for both atrial region segmentation and fossa ovalis identification.

Part II focuses on the image-based planning of LAA occlusions. In this sense, we started by proposing a novel strategy to segment the LAA in 3D peri-procedural images (TEE) using a novel blind-ended model (Chapter 7). This initial algorithm was semi-automatic requiring a manual definition of the LAA centerline, through a small number of clicks, to initialize the model. Nevertheless, the 3D result was obtained in a few seconds, allowing its application in peri-procedural images. Overall, the proposed segmentation solutions proved its high accuracy against manual contouring and significantly improved the reproducibility between observers for the estimation of required clinical indicators. Furthermore, it allowed the 3D assessment of the LAA shape during the intervention, which might be a relevant feature to improve the traditional intervention. To (semi-) automatically estimate the optimal occluding device using 3D data, a novel algorithm to compute the relevant clinical measurements using the segmented surface was developed (Chapter 8). This method proved its low computational time and high reproducibility in a clinical database, showing a performance similar (or superior in specific cases) to the difference between two observers, corroborating the potential and the added-value of this solution for normal clinical routine.

## 1.7. Contributions

In the current thesis, automated solutions to improve the planning of two specific left atrial interventions are described, reducing the observer expertise dependence, making it faster and attractive for the clinical practice. As a summary, the following contributions were pursued (Figure 1.12):

1. A systematic review of recent planning and guidance methods and novel surgical instruments applied in TSP intervention (Chapter 2);
2. A novel patient-specific atrial phantom model with correct modeling of the inter-atrial septal wall, allowing its application for realistic simulation of inter-atrial interventions (Chapter 3);

3. A preliminary validation of a novel concept for the development of an integrated interventional guidance framework for improved TSP (Chapter 4);
4. A novel semi-automatic strategy to segment the atrial region in CT/MR images with correct delineation of the mid thin atrial walls through a competitive deformable model approach (Chapter 5);
5. A fully automatic version of the competitive atrial region segmentation method with accurate estimation of relevant landmarks for the planning of the TSP (Chapter 6);
6. A novel semi-automatic strategy to segment the LAA in 3D TEE images using a blind-ended deformable model (Chapter 7);
7. A novel approach to automate the estimation of the clinical measurements for the identification of the occluding device in LAA occlusion intervention (Chapter 8).

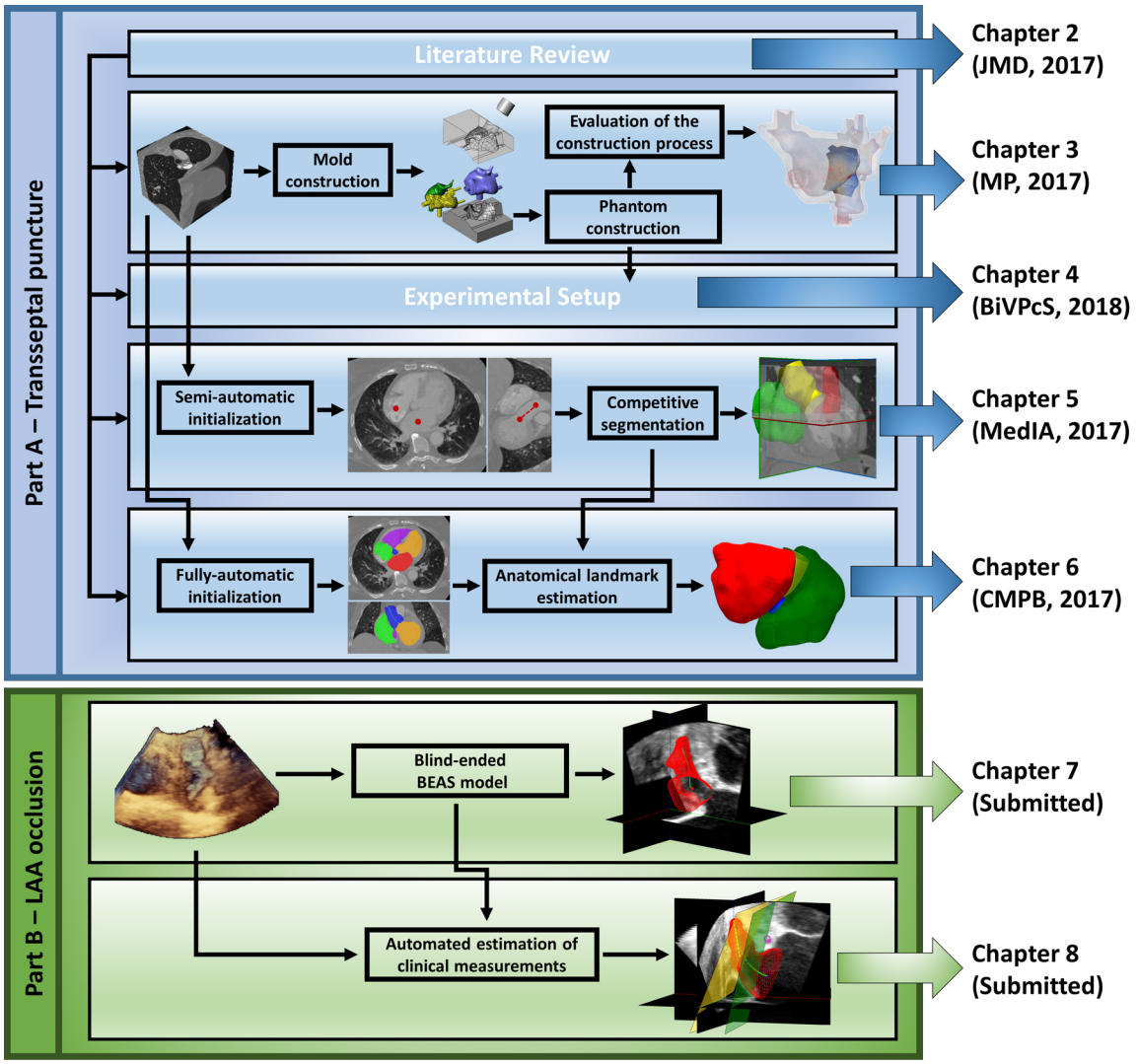


**Figure 1.12 - Overview of the main contribution of this PhD thesis.**
The associated international journal articles or conference proceedings are indicated between parenthesis as (abbreviated journal title, year).

The thesis contributions were published in four international journal articles ((Morais *et al.*, 2017a), (Morais *et al.*, 2017b), (Morais *et al.*, 2017c), (Morais *et al.*, 2018a)) and as a proceeding of one international conference (*MICCAI 2018 Workshop on Bio-Imaging and Visualization for Patient-Customized Simulations, (Morais et al., 2018b)*). Moreover, three extra publications are currently under revision.

## 1.8. Organization of the Thesis

This initial chapter introduces relevant clinical aspects, context and structure of the thesis, aims and contributions of the thesis. The remaining two parts (focused on the TSP and LAA occlusion interventions) are composed of eight articles (Chapter 2 to 8), currently accepted or submitted to international journals and conferences, written/developed throughout the PhD project. In this sense, Part I is composed by the following articles:

Chapter 2 - Pedro Morais, João L. Vilaça, Joris Ector, Jan D'hooge, João Manuel R. S. Tavares, "Novel solutions applied in transseptal puncture: a systematic review", *Journal of Medical Devices*, vol. 11, p. 010801, 2017.

Chapter 2 (Appendix) – Pedro Morais, João L. Vilaça, Jan D'hooge, João Manuel R. S. Tavares, "Novel solutions applied in transseptal puncture: a systematic review – Update to 2018", *submitted to an international journal (2018).*

Chapter 3 - Pedro Morais, João Manuel R. S. Tavares, Sandro Queirós, Fernando Veloso, Jan D'hooge, João L. Vilaça, "Development of a patient-specific atrial phantom model for planning and training of inter-atrial interventions", *Medical Physics*, vol. 44, pp. 5638-5649, 2017.

Chapter 4 - Pedro Morais, João L. Vilaça, Sandro Queirós, Pedro L. Rodrigues, João Manuel R. S. Tavares, Jan D'hooge, "A novel interventional guidance framework for transeptal puncture in left atrial interventions", *in MICCAI 2018 Workshop on Bio-Imaging and Visualization for Patient-Customized Simulations*. *Lecture Notes in Computer Sciences (LNCS), Springer,* September 16-20 2018, Granada, 2018.

Chapter 5 - Pedro Morais, João L. Vilaça, Sandro Queirós, Felix Bourier, Isabel Deisenhofer, João Manuel R. S. Tavares, Jan D'hooge, "A competitive strategy for atrial and aortic tract segmentation based on deformable models", *Medical Image Analysis*, vol. 42, pp. 102-116, 2017.

Chapter 6 - Pedro Morais, João L. Vilaça, Sandro Queirós, Alberto Marchi, Felix Bourier, Isabel Deisenhofer, Jan D'hooge, João Manuel R. S. Tavares, "Automated segmentation of the atrial region and fossa ovalis towards computer-aided planning of inter-

atrial interventions", *Computer Methods and Programs in Biomedicine*, vol. 161, pp. 73-84, 2018.

Part II is composed by the following articles:

Chapter 7 - Pedro Morais, Sandro Queirós, Pieter De Meester, Werner Budts, João L. Vilaça, João Manuel R. S. Tavares, Jan D'hooge, "Fast segmentation of the Left Atrial Appendage in 3D Transesophageal Echocardiographic Images", *submitted to an international journal (2018).*

Chapter 8 - Pedro Morais, João L. Vilaça, Sandro Queirós, Pieter De Meester, Werner Budts, João Manuel R. S. Tavares, Jan D'hooge, "Semi-Automatic image-based planning of Left Atrial Appendage Occlusion in 3D Transesophageal Echocardiographic Images", *submitted to an international journal (2018).*

Finally, in the last chapter (chapter 9), the main conclusions, contributions and future perspectives of the current PhD thesis are presented and discussed.

# Part I

## Transseptal puncture

This part focuses on the development and validation of novel image-based planning solutions for transseptal puncture procedure. Moreover, a state-of-the-art of current technological solutions applied in this intervention and a novel concept for an integrated interventional framework is also presented.

**Contents**

# Chapter 2

## Novel solutions applied in transseptal puncture: a systematic review

This chapter has been published in *Journal of Medical Devices*: **Pedro Morais**, João L. Vilaça, Joris Ector, Jan D'hooge, João Manuel R. S. Tavares, "Novel solutions applied in transseptal puncture: a systematic review", *Journal of Medical Devices*, vol. 11, p. 010801, 2017. It presents a systematic review of recent technological advances in transseptal puncture procedure. All relevant articles published between 2008 and April 2015 were considered and analyzed. Only minor changes to the original publication have been performed. The figures and sections numbers were updated with the chapter title and all references were combined in a common final section. A final appendix evaluating the most recent publications (*i.e.* between April 2015 and January 2018) on this topic was also added. This appendix was recently submitted to an international journal (currently, under review).

**Keywords:** Transseptal puncture; Left atrium access; Systematic review; Optimal puncture position.

**Contents**

## Abstract

Access to the left atrium is required for several minimally invasive cardiac interventions in the left heart. For this purpose, transseptal puncture (TSP) technique is often performed, perforating the atrial septum under fluoroscopic or/and ultrasound imaging guidance. Although this approach has been used for many years, complications/failures are not uncommon mainly in patients with abnormal atrial anatomy and repeated TSP. Thus, this study presents an overview of methods and techniques that have been proposed to increase the safety and feasibility of the TSP. A systematic review of literature was conducted through the analysis of the articles published between 2008 and 2015. The search was performed in PubMed, Scopus and ISI Web of Knowledge using the expression "transseptal puncture". A total of 354 articles were retrieved from the databases, and 64 articles were selected for this review. Moreover, these 64 articles were divided into four categories, namely: 1) incidence studies; 2) intra-procedural guidance techniques; 3) pre-procedural planning methods and 4) surgical instruments. A total of 36 articles focused on incidence studies, 24 articles suggested novel intra-procedural guidance techniques, 5 works focused on pre-procedural planning strategies and 21 works proposed surgical instruments. The novel 3D guidance techniques, radio-frequency surgical instruments and pre-interventional planning approaches showed potential to overcome the main procedural limitations/complications, through the reduction of the intervention time, radiation, number of failures and complications.

## 2.1. Introduction

Percutaneous access of the left atrium (LA) is required in a large number of minimally invasive procedures, such as catheter ablation for atrial fibrillation, paravalvular leakage repair, percutaneous mitral valve replacement and left atrial appendage closure (Babaliaros *et al.*, 2008; Matsumoto and Kar, 2013). These procedures are frequently performed (Table 2.1) being a preferred practice to the traditional open-chest surgery, due to the lower costs and lower complication rate. Nonetheless, these procedures are not free of risks being highly dependent of physician experience and medical devices/instruments used (Earley, 2009).

Two techniques are commonly used to gain access to the LA, namely: transaortic (TA) and transseptal puncture (TSP). In TA, a catheter inserted in the femoral artery is retrogradely advanced through the aortic valve towards the left ventricle (LV). Subsequently, the catheter is rotated 180° and advanced through the mitral valve (MV) into the LA chamber. In contrast, in TSP a catheter is inserted into the right-atrium (RA) via the venous system, through which a needle can be moved forward, in order to puncture the interatrial septum (IAS) and

**Table 2.1 – Application rate of different percutaneous procedures that require TSP**

| Procedure | Application rate |
|---|---|
| Catheter ablation for atrial fibrillation | In 2010, 8.8 million of patients had atrial fibrillation in the Europe Union. A projection study estimated a total of 17.9 million of patients at 2060 (Krijthe *et al.*, 2013). |
| Paravalvular leakage repair | Affects 5%-17% of all implanted prosthetic heart valves (Taramasso *et al.*, 2014). |
| Percutaneous mitral valve replacement | Mitral valve diseases present an estimated prevalence of 7% in subjects ≥75 years old (Baldus *et al.*, 2012). |
| Left atrial appendage closure | Left atrial appendage is the primary source of the thromboemboli in non-valvular atrial fibrillation patients (Reddy *et al.*, 2011). |

consequently gain access to the LA. Yet, the puncture should be performed through the thinnest region of the IAS wall, termed fossa ovalis (FO). Thus, the TSP technique establishes a "more direct" access route, when compared with TA approach. Nevertheless, in complex situations TSP can result in serious complications, such as perforation of large vessels (Earley, 2009).

Despite the similar safety between the two techniques (Earley, 2009; Schwagten *et al.*, 2010), the TA route requires a 180° rotation of the catheter, hampering its manipulation and the procedure. Moreover, the TA uses an access route through the high-pressure arterial system. Contrarily, TSP uses simple routes and enters into the LA using the low-pressure venous system. As such, in the last years, a higher number of procedures based on TSP were suggested (Earley, 2009). However, determining the optimal puncturing site is not straightforward, as not only the ease of puncturing depends on the location, but also the target site to be reached in the LA has to be taken into account, as crossing the septum limits the maneuverability of the catheters and, thus, their ability to reach the LA target sites. To date, this decision is entirely based on the physician's experience and secondary punctures are usually required as the first one turns out inadequate (Earley, 2009).

New strategies have been proposed to overcome the main-complications of the TSP, through the inclusion of novel guidance approaches, planning methods and surgical instruments. In this study an overview of these new strategies and their advantages is presented.

Briefly, the current work introduces four novelties, namely: 1) an incidence study about the TSP; 2) a review of the recent guidance methods applied in TSP; 3) a review of intra-procedural planning methods for safe puncture zone recognition; and 4) an overview of novel surgical instruments recently used to puncture the IAS wall.

The current article is divided into six main sections: 1) description of the traditional TSP procedure (section 2.1.1); 2) method used to identify the relevant studies for this review (section

2.2); 3) aims and main conclusions of the selected articles (section 2.3); 4) discussion of the relevant articles, presenting their advantages and main drawbacks (section 2.4); 5) future trends (section 2.5) and 6) conclusions (section 2.6).

### 2.1.1. Traditional transseptal puncture procedure

The TSP has been widely addressed in literature (Babaliaros *et al.*, 2008; Earley, 2009; Ross, 2008), reporting the guidance equipment and catheters used to safely puncture the IAS wall. This is typically guided using bi-dimensional fluoroscopy and is performed using a mechanical Brockenbrough needle (BRK, St. Jude Medical, Minneapolis) (Earley, 2009). Furthermore, several auxiliary catheters are used to prevent puncture of vital structures. For instance, catheters at the aorta, coronary sinus (CS) and His bundle are commonly used. Regarding the procedural time, 1 to 15 minutes are frequently reported (Fromentin *et al.*, 2011; Hsu *et al.*, 2013; Lakkireddy *et al.*, 2008; Mitchell-Heggs *et al.*, 2010; Yao *et al.*, 2013).

The procedure starts with the insertion of a guidewire (0.032-0.035 inch) into the inferior vena cava using the right femoral vein access (Figure 2.1a). The guidewire defines a safe route between the femoral vein and the superior vena cava (SVC). It should be noticed that some works presented a variant of the TSP, where the needle is inserted via right internal jugular vein until SVC (Lim *et al.*, 2009). A dilator and sheath are also positioned into the SVC using the guidewire. At this stage, the guidewire is replaced by the BRK needle, maintaining it inside the sheath to prevent inadvertent punctures. Then, the assembly (needle-sheath-dilator) is positioned at the FO. The assembly is rotated to 4-5 o'clock position and posteriorly pulled-down. Two movements will be detected: the first indicates the entrance of the assembly into the RA (Figure 2.1b); and the second, which is less perceptible, occurs when the assembly is inside the FO (Figure 2.1c). Since puncture outside the FO increases the risk of perforating vital structures and limits the maneuverability of the catheter in the LA, confirmation of the needle

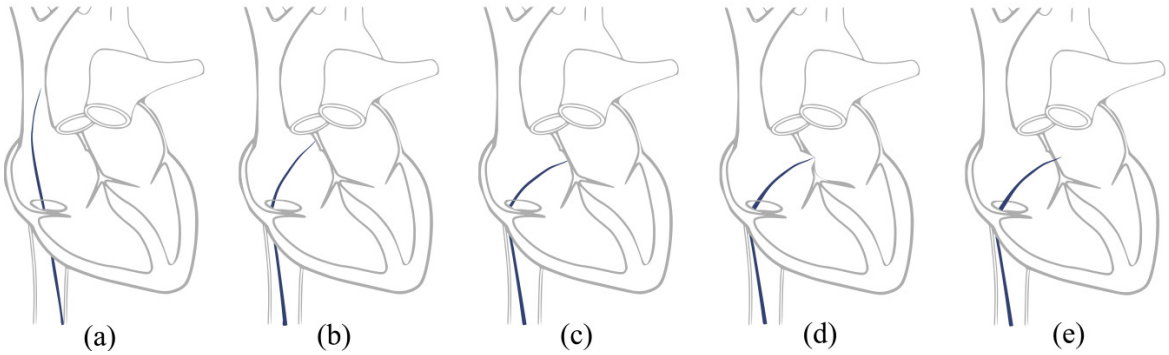


**Figure 2.1 - Transseptal puncture traditional technique**.
(a) A catheter (blue) is placed into the SVC; the catheter is pull-down and two movements are detected, namely: (b) entrance into the RA and (c) into FO, (d) after FO identification the puncture is performed (e).

position should be performed (Figure 2.1d-e). Furthermore, a confirmation of the actual position of the aorta, CS and His bundle is required to ensure safety of the puncture.

Finally, the puncture can be performed (Figure 2.1e) and the surgical tool can be introduced into the LA. The position of the needle is confirmed using the LA pressure variation or contrast agents. It should be noted that a repetition of the procedure is required when the assembly is not aligned with the FO or when the expert has doubts about the assembly position.

As a final remark, during the entire procedure the expert should be aware of the possible anatomical variations that hamper the identification of the puncture position. An overview of the most common ones are presented in Table 2.2. A different access site is required when an abnormal anatomy is identified, being this recognition only performed based on the physician's experience. Note that these modifications are crucial to ensure the maximum safety of the procedure and reduce the number of complications (Knecht *et al.*, 2008d).

## 2.2. Materials and Methods

In this section, we report the criteria used to identify the relevant works for the review performed. We followed the PRISMA statement for the design, implementation, analysis and reporting of the results (Moher *et al.*, 2010).

**Table 2.2 – Overview of the main anatomical variations of the atria**

| Anatomic variations | Description | Difficulties | Solution |
|---|---|---|---|
| **Patent foramen ovale (PFO)** | - A direct route between the RA and the LA (Rana *et al.*, 2010).<br>- LA access without any puncture (Rana *et al.*, 2010). | - Since the PFO is located at the anterior superior part of the IAS, access to the pulmonary veins are hampered (Knecht *et al.*, 2008d; Rana *et al.*, 2010). | - TSP procedure should be used, even in the presence of PFO (Knecht *et al.*, 2008d). |
| **Left atrium dilation** | - LA dilation results in a posterior position of the FO (Gard *et al.*, 2011). | - Higher risk of puncture an adjacent structure (Gard *et al.*, 2011). | - A different TSP position should be used (Gard *et al.*, 2011). |
| **Abnormal mechanical properties of the IAS** | - Heart diseases can result in aneurysmal, elastic or thickened IAS wall (Fromentin *et al.*, 2011).<br>- Patients with previous TSP procedure, present a thickened IAS wall (Hsu *et al.*, 2013). | - TSP can result in serious complications for the patient, such as atrial roof puncture or aortic route puncture. (Fromentin *et al.*, 2011). | - Application of radio-frequency needles (Fromentin *et al.*, 2011). |
| **Abnormal position of the FO** | - A superior position of the FO is detected (Ho *et al.*, 2011). | - Superior LA access reduces the maneuverability of catheters in pulmonary veins and mitral valve procedures (Ho *et al.*, 2011). | - Puncture the inferior part of the FO (Ho *et al.*, 2011). |

### 2.2.1. Selection method

A search was performed on PubMed, Scopus and ISI Web of Sciences databases between 9 and 10 of April 2015. The search used the exact expression "transseptal puncture". Only works published between January of 2008 and April of 2015 were considered. A total of distinct 354 articles were obtained and evaluated.

### 2.2.2. Data collection and processing

The identification of the relevant works was performed through a double-stage strategy, as explained below and previously reported in PRISMA guidelines (Moher *et al.*, 2010).

First, the title and the abstract of all 354 articles obtained during section 2.2.1 were analyzed by the first author of the current study. All the works with aims different of the main topic of this review were removed, resulting in a total of 141 articles eligible for this study. It should be noticed that works not written in English and patents were automatically discarded.

Second, the obtained 141 articles were completely read and analyzed, and the following criteria were used to identify the relevant studies: 1) the selected studies should focus on novel technical innovations of the TSP procedure, discarding small case-to-case adaptations of the traditional approach due to difficult intervention or strange anatomies; 2) incidence studies about the current TSP technique were also considered as valid for this review; 3) short clinical reports about difficult procedure, letters between editor, author or reader and short communications without technical description were discarded; and 4) previously presented reviews about TSP and similar topics were also rejected. Table 2.3 presents an overview of the excluded reviews. As such, a total of 64 articles were selected for the review. Note that, the identification of the relevant works was done by the first author of this review.

**Table 2.3 – Topics addressed in different reviews published between 2008 and April 2015**

| Authors | Aims |
|---|---|
| Matsumoto and Kar (2013) | Recent advances in transseptal left heart interventions. |
| Kautzner and Peichl (2012) | Review of imaging techniques used in LA procedures. |
| Sy *et al.* (2011) | Overview of difficulties and possible solutions throughout TSP procedure. |
| Tzeis *et al.* (2010) | An exhaustive review of TSP procedure and overview of tips and caveats with relevant value for safe TSP. |
| Earley (2009) | Review of TSP procedure complications and possible solutions. |
| Babaliaros *et al.* (2008) | Review of novel techniques used in TSP intervention and emerging indications of this intervention. |
| Ross (2008) | Overview of transseptal left heart catheterization procedures. |

### 2.2.3. Data analysis

The 64 selected articles were analyzed and classified into different categories: incidence studies, intra-procedural guidance techniques, pre-procedural planning methods and surgical instruments (Figure 2.2). Each publication could be included in more than one category.

## 2.3. Results

In this section, an overview of the topic addressed by the selected articles is presented.

### 2.3.1. Study characteristics

Thirty-six articles reported TSP previous experience, describing the technique applied and the complication rate achieved. Regarding the novel strategies proposed to improve TSP, twenty-four studies suggested new intra-procedural guidance techniques, five studies focused on pre-procedural planning and twenty-one works presented novel surgical equipments.

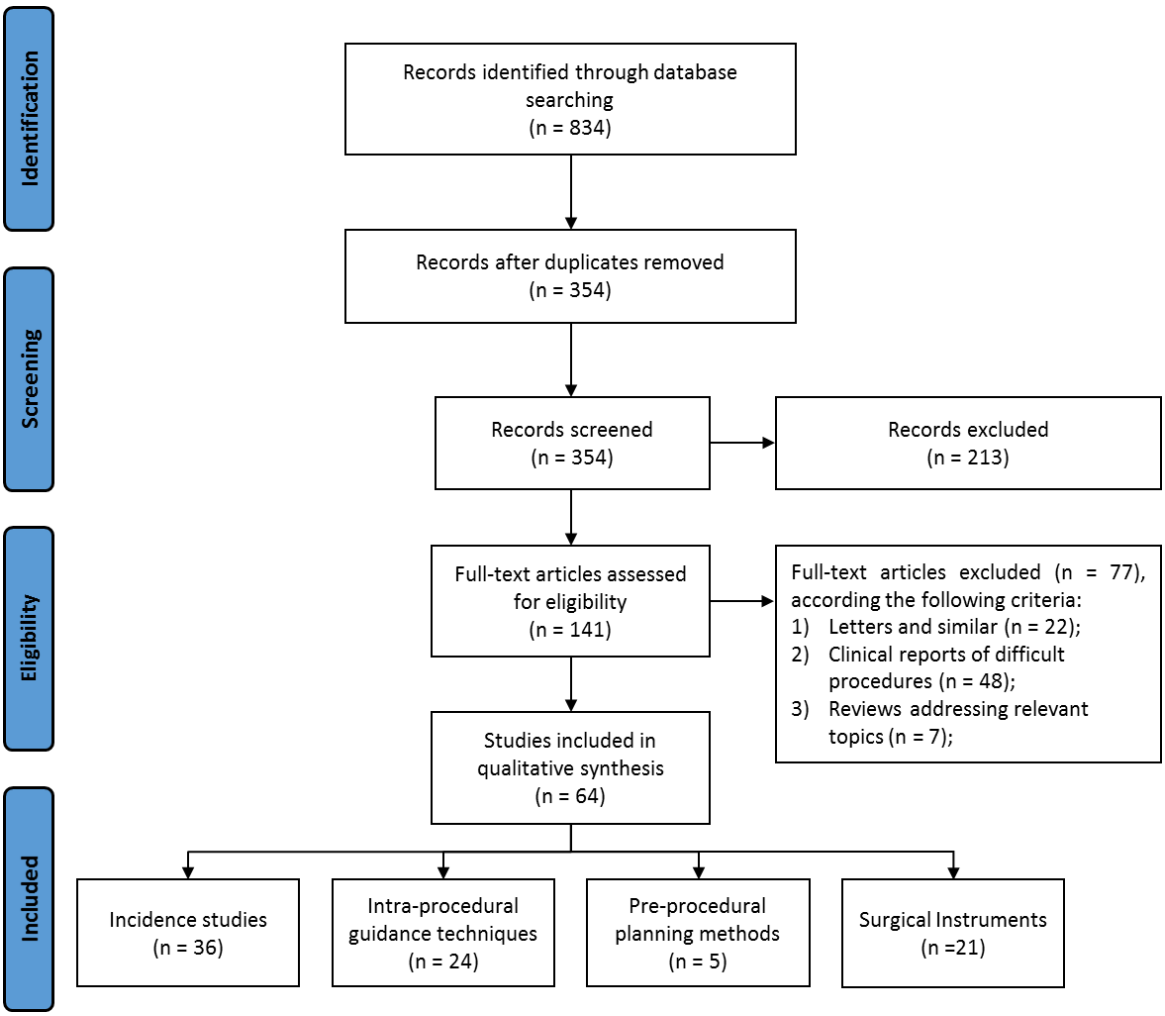


**Figure 2.2 – Overview of the methodology used to select the relevant articles for this review.**
The identification of the relevant works was performed using Prisma Statement (Moher *et al.*, 2010).

### 2.3.2. Incidence study

Table 2.4 presents a review of the number of TSP performed between 2008 and April of 2015. Several studies use heterogeneous populations, which includes: children's (Clark *et al.*, 2008; Elayi *et al.*, 2011; von Alvensleben *et al.*, 2014), abnormal anatomy (Bayrak *et al.*, 2012; Jauvert *et al.*, 2015; Lakkireddy *et al.*, 2008; Miyazaki *et al.*, 2011; Mulder *et al.*, 2012; Tang *et al.*, 2014; Wadehra *et al.*, 2011; Wieczorek *et al.*, 2010; Yao *et al.*, 2012; Zellerhoff *et al.*, 2014) and patients with previous TSP (Esch *et al.*, 2013; Fromentin *et al.*, 2011; Hsu *et al.*, 2013; Knecht *et al.*, 2008a; Lehrmann *et al.*, 2014; Smelley *et al.*, 2010; Tomlinson *et al.*, 2008). The number of puncture attempts, failures and complications were registered. The results show that approximately 12% of the procedures require more than one puncture attempt, and complications/failures rate are lower than 1%. Note that, since studies with different operator's expertise (*i.e.* expert and trainee), heterogeneous populations and multiple equipment were included in this analysis, high variation of complication and failure rate was found.

### 2.3.3. Intra-procedural guidance techniques

In order to overcome the limitations of the procedures only guided by fluoroscopy, several researchers exploited the application of new imaging modalities in TSP (Table 2.5),

**Table 2.4 – Number of TSP (NbT), percentage of repeated procedures (RP), failures (F), and complications (C) reported between 2008 and April 2015**

| Authors | NbT | RP (%) | F | C | Authors | NbT | RP (%) | F | C |
|---|---|---|---|---|---|---|---|---|---|
| Jauvert *et al.* (2015) | 225 | 5.78 | 5 | 3 | Winkle *et al.* (2011) | 1550 | - | 13 | 9 |
| von Alvensleben *et al.* (2014) | 365 | - | 0 | 8 | Elayi *et al.* (2011) | 13 | 15.38 | 0 | 0 |
| Koermendy *et al.* (2014) | 147 | - | 4 | 20 | Capulzini *et al.* (2010) | 162 | 11.73 | | 0 |
| Lehrmann *et al.* (2014) | 678 | - | 0 | 0 | Haegeli *et al.* (2010) | 269 | - | 0 | 8 |
| Tang *et al.* (2014) | 3452 | - | 0 | 10 | Mitchell-Heggs *et al.* (2010) | 79 | - | 0 | 9 |
| Unnithan *et al.* (2014) | 54 | - | 0 | 1 | Schwagten *et al.* (2010) | 11 | - | 1 | 0 |
| Zellerhoff *et al.* (2014) | 39 | - | 0 | 1 | Smelley *et al.* (2010) | 41 | 31.70 | 1 | 2 |
| Chierchia *et al.* (2013) | 103 | - | 0 | 9 | Wieczorek *et al.* (2010) | 158 | 4.44 | 0 | 0 |
| Esch *et al.* (2013) | 10 | - | 1 | 0 | Ferguson *et al.* (2009) | 21 | - | 0 | 0 |
| Hsu *et al.* (2013) | 72 | - | 10 | 2 | Chierchia *et al.* (2008) | 24 | 0 | 0 | 0 |
| Katritsis *et al.* (2013) | 393 | - | 0 | 5 | Clark *et al.* (2008) | 10 | - | 0 | 0 |
| Yao *et al.* (2013) | 120 | 14.17 | 5 | 0 | Hu *et al.* (2008) | 29 | - | 0 | 0 |
| Bayrak *et al.* (2012) | 205 | 46.34 | 1 | 3 | Knecht *et al.* (2008a) | 269 | 4.47 | 0 | 0 |
| Wang *et al.* (2012) | 4443 | - | 0 | 27 | Knecht *et al.* (2008d) | 154 | - | 0 | 0 |
| Yao *et al.* (2012) | 539 | 1.11 | 0 | 0 | Lakkireddy *et al.* (2008) | 90 | - | 1 | 4 |
| Abed *et al.* (2012) | 543 | 1.84 | 10 | 10 | Saliba *et al.* (2008) | 40 | - | 2 | 1 |
| Fromentin *et al.* (2011) | 241 | - | 0 | 2 | Wu *et al.* (2008) | 468 | 27.1 | 0 | 1 |
| Miyazaki *et al.* (2011) | 114 | - | - | 1 | Tomlinson *et al.* (2008) | 42 | - | 0 | 4 |
| Wadehra *et al.* (2011) | 210 | 18.57 | 5 | 0 | **Mean** | | **12.07** | **0.51** | **0.88** |

namely: transesophageal echocardiography (TEE) (Bayrak *et al.*, 2012; Chierchia *et al.*, 2008; Faletra *et al.*, 2011; Faletra *et al.*, 2014a; Gafoor *et al.*, 2015; Stec *et al.*, 2011; Wu *et al.*, 2008), intracardiac echocardiography (ICE) (Biermann *et al.*, 2012; Ferguson *et al.*, 2009; Liang *et al.*, 2010; Mitchell-Heggs *et al.*, 2010; Ruisi *et al.*, 2013; Russo *et al.*, 2013), real-time magnetic resonance (MR) (Elagha *et al.*, 2008) and direct color visualization (Thiagalingam *et al.*, 2008). Furthermore, needle tracking based on electromagnetic sensors (Jeevan *et al.*, 2014) and electroanatomic mapping (EAM) (Clark *et al.*, 2008; Mah *et al.*, 2014; Nguyen *et al.*, 2013; Pavlović *et al.*, 2014; Saliba *et al.*, 2008; Shepherd *et al.*, 2008; Unnithan *et al.*, 2014) were also presented. These novel guidance techniques increase the safety of the TSP procedure (Faletra *et al.*, 2011; Ferguson *et al.*, 2009; Mitchell-Heggs *et al.*, 2010; Unnithan *et al.*, 2014), reduce or completely eliminate the radiation from the procedure (Clark *et al.*, 2008; Ferguson *et al.*, 2009; Jeevan *et al.*, 2014; Liang *et al.*, 2010; Shepherd *et al.*, 2008) and remove the contrast injection to confirm correct LA access (Liang *et al.*, 2010). Moreover, faster procedures were performed (Liang *et al.*, 2010) and higher success rates in difficult situations were achieved (Faletra *et al.*, 2011; Mitchell-Heggs *et al.*, 2010).

### 2.3.4. Pre-procedural planning techniques

Some researchers proposed pre-interventional planning techniques, namely: identification of a safe zone for TSP (Schernthaner *et al.*, 2013; Tomlinson *et al.*, 2008; Verma *et al.*, 2011; Wagdi and Alkadhi, 2012) and recognition of the optimal puncture position, which guarantee maximum catheter dexterity inside the LA (Jayender *et al.*, 2011). This planning step relies on pre-interventional image acquisitions, namely, by: CT (Jayender *et al.*, 2011; Verma *et al.*, 2011; Wagdi and Alkadhi, 2012), MR (Jayender *et al.*, 2011) or TEE (Schernthaner *et al.*, 2013; Tomlinson *et al.*, 2008). The researchers agreed that these novel planning methods allow accurate planning of the TSP therefore, increasing the safety of TSP and reducing complication/failures rate (Jayender *et al.*, 2011; Wagdi and Alkadhi, 2012).

Table 2.6 presents the aims, validation and conclusion of these novel studies.

### 2.3.5. Surgical instruments

A high number of studies focused on the traditional BRK needle. This crosses the septum using a mechanical process, by applying pressure on FO. Nonetheless, in abnormal septal wall high pressure can result in inadvertent puncture and consequently, intervention complication (Fromentin *et al.*, 2011). As such, novel needles were proposed, specifically: RF

**Table 2.5 - Novel intra-procedural guidance techniques applied in TSP procedure between 2008 and April 2015 (Part 1)**

| | | Authors | Aims | Guidance technique | V | Conclusion |
|---|---|---|---|---|---|---|
| **Image-based** | **Ultrasound image** | Gafoor *et al.* (2015) | Use of EchoNavigator in TSP. | TEE with FC. | - | This strategy eased the identification of the relevant anatomical structures and showed potential for TSP. |
| | | Faletra *et al.* (2014a) | Application of 3D TEE in TSP. | 3D TEE. | - | 3D TEE eased TSP when compared with remaining guidance approaches, such as 2D TEE or fluoroscopy. |
| | | Ruisi *et al.* (2013) | Application of ICE in TSP. | ICE. | - | ICE allows an accurate visualization of RA anatomy and can be used to guide TSP. |
| | | Russo *et al.* (2013) | Application of ICE in TSP. | ICE. | - | ICE contributed to improve the efficacy of TSP. |
| | | Bayrak *et al.* (2012) | Application of 2D TEE in TSP. | TEE and FC. | 105 pat. | TEE proved to be useful to guide TSP even when performed by unexperienced operators. |
| | | Biermann *et al.* (2012) | Application of ICE in TSP. | ICE. | - | ICE contributed to improving the efficacy of TSP. |
| | | Faletra *et al.* (2011) | Advantages of 3D TEE in TSP. | 3D TEE. | - | 3D TEE eased the identification of the FO. |
| | | Stec *et al.* (2011) | Application of micro-TEE in TSP. | Micro-TEE probe. | 12 pat. | Micro-TEE can guide TSP in non-sedated patients. |
| | | Liang *et al.* (2010) | Comparison of mechanical vs. phased-array ICE probes in TSP. | ICE. | 6 pat. | Mechanical ICE allows a better image of the FO region, being therefore more adequate to perform TSP. |
| | | Mitchell-Heggs *et al.* (2010) | Advantages of ICE-TEE in TSP. | ICE via an esopaghus route. | 79 pat. | This technique is safe and it is done without sedation. |
| | | Ferguson *et al.* (2009) | Application of ICE in TSP. | ICE. | 21 pat. | Correct TSP using ICE guidance was possible. |
| | | Chierchia *et al.* (2008) | Application of 3D TEE in TSP. | 3D TEE. | 24 pat. | TEE facilitated TSP, with lower procedural time. |
| | | Wu *et al.* (2008) | Application of TEE in TSP. | TEE. | 468 pat. | TEE eased the identification of the optimal puncture position. |
| | **Other** | Yao *et al.* (2013) | Validation of a new TSP strategy. | FC. | 120 pat. | This method was simple, safe and economic. |
| | | Elagha *et al.* (2008) | Application of real-time MRI in TSP. | Real-time MRI. | 7 AM | MRI-guided can be used to perform safe TSP procedure. |
| | | Thiagalingam *et al.* (2008) | Full-color visualization of FO. | Fiber optic + FC. | 6 swine | Direct full-color visualization can be used to identify FO. |

AM – Animal model; FC – Fluoroscopy; FO – Fossa Ovalis; IAS – Interatrial septum; ICE – Intracardiac echocardiography; LA – Left atrium; MRI – Magnetic Resonance Imaging; pat. – patients; RotAng – Rotational Angiography; V – validation; TEE - transesophageal echocardiography; TSP – Transseptal puncture.

**Table 2.5. (cont.) – Novel intra-procedural guidance techniques applied in TSP procedure between 2008 and April 2015 (Part 2)**

| | Authors | Aims | Guidance technique | V | Conclusion |
|---|---|---|---|---|---|
| Electroanatomic mapping (EAM) | Mah *et al.* (2014) | EAM with ICE can ease TSP. | EAM with ICE. | 25 pat. | The system reduced the radiation exposure and time. |
| | Pavlović *et al.* (2014) | Simple reaccess of FO without radiation. | EAM (Carto 3). | 25 pat. | A radiation-free recrossing of the IAS wall was achieved. |
| | Unnithan *et al.* (2014) | Simple reaccess of FO without radiation. | EAM (3D NavX). | 54 pat. | The method reduced the time that the catheter dwells in LA. |
| | Nguyen *et al.* (2013) | Strategy to manual or automatic reaccess of FO without radiation. | EAM (NavX). | 5 pat. | Manual and automatic reaccess of the LA is viable and fast. Radiation was removed. |
| | Clark *et al.* (2008) | EAM with TEE can be used to perform TSP. | EAM with TEE. | 10 pat. | This method can eliminate the FC used throughout TSP procedure. |
| | Saliba *et al.* (2008) | Combination of EAM-ICE in TSP. | EAM and ICE. | 40 pat. | This system ensured safe TSP procedure. |
| | Shepherd *et al.* (2008) | Application of EAM in TSP. | EAM (NavX). | - | EAM can reduce the fluoroscopy time. |
| Other | Jeevan *et al.* (2014) | Validation of a new method for radiation-free TSP. | EM sensor with MRI. | 1 ph. | This system reduced the procedural time, had no learning curve and reduced the complication rate. |

EAM – Electroanatomical mapping; EM – Electromagnetic sensors; FC – Fluoroscopy; FO – Fossa Ovalis; IAS – Interatrial septum; ICE – Intracardiac echocardiography; LA – Left atrium; MRI – Magnetic Resonance Imaging; pat. – patients; ph – phantom; V – Validation; TEE - transesophageal echocardiography;

(radio-frequency) rigid NRG (Baylis Medical) (Crystal *et al.*, 2010; Esch *et al.*, 2013; Feld *et al.*, 2011; Fromentin *et al.*, 2011; Hsu *et al.*, 2013; Karagöz *et al.*, 2014; Smelley *et al.*, 2010; Winkle *et al.*, 2011), RF flexible Toronto (Baylis Medical) (Jauvert *et al.*, 2015), electrocautery (Abed *et al.*, 2012; Capulzini *et al.*, 2010; Greenstein *et al.*, 2012; Knecht *et al.*, 2008a; Mcwilliams and Tchou, 2009) and coaxial transseptal (CTS) needles (Uchida *et al.*, 2011).

Furthermore, some researchers proposed novel solutions for the remaining surgical equipment, particularly: dilator, guidewire and catheters. Thereby, a new dilator approach (Wang *et al.*, 2012), a laser catheter and a nitinol guidewire with "J" shape (Giudici *et al.*, 2015; Wadehra *et al.*, 2011; Wieczorek *et al.*, 2010) were suggested.

A robotic remote navigation system was also suggested to perform safe interventions. This system was applied on TSP and catheter ablation for atrial fibrillation (Saliba *et al.*, 2008).

Table 2.7 presents an overview of these novel equipment's.

## 2.4. Discussion

### 2.4.1. Incidence study

Between 2008 and 2015, an average complication and failure rate lower than 1% was reported (Table 2.4). These results are in accordance with previous studies (Earley, 2009),

**Table 2.6 - Pre-procedural planning methods applied in TSP procedure between 2008 and April 2015**

| | Authors | Aims | PM | V | Conclusion |
|---|---|---|---|---|---|
| **Richly detailed images** | Wagdi and Alkadhi (2012) | Identification of a "safe zone" for TSP. | CT. | 20 pat. | CT can be used to predict the feasibility of TSP intervention. |
| | Verma *et al.* (2011) | Identification of the FO region in CT. | CT. | 49 pat. | It was possible to detect FO in CT. |
| | Jayender *et al.* (2011) | Identification of the optimal puncture site. | MR/CT. | 1 dat. | A safe puncture position with high catheter dexterity was achieved. |
| **Ultrasound images** | Schernthaner *et al.* (2013) | TEE images can be used to detect abnormal anatomies. | TEE. | 100 pat. | Pre-planning images provided accurate information on the patient anatomy. |
| | Tomlinson *et al.* (2008) | FO thickness is a predictor of difficult TSP. | TEE. | 42 pat. | No relation was found between difficult TSP and FO thickness. |

CT – Computed Tomography; dat. – dataset; FO – Fossa Ovalis, MR – Magnetic Resonance, TEE - transesophageal echocardiography, pat. – patient; PM – Planning method; V – Validation;

proving that TSP is a safe and feasible technique in clinical practice. Nevertheless, since TSP is required as an intermediate step for several procedures, a high number of patients with complications still being reported.

Multiple studies proved that cardiac tamponade is the major complication of the TSP procedure, being also common transient ischemic attack and transient ST elevation (Earley, 2009; Jauvert *et al.*, 2015; Katritsis *et al.*, 2013; Koermendy *et al.*, 2014; Zellerhoff *et al.*, 2014). Furthermore, we investigated the number of situations where a second attempt was required to access the LA. This analysis is interesting to assess the feasibility of the current guidance techniques and instruments used. Approximately 12% of the procedures required more than one puncture attempt, which increases the procedural time and the radiation exposure (Abed *et al.*, 2012; Bayrak *et al.*, 2012; Elayi *et al.*, 2011; Jauvert *et al.*, 2015; Knecht *et al.*, 2008a; Wadehra *et al.*, 2011; Wieczorek *et al.*, 2010; Yao *et al.*, 2013; Yao *et al.*, 2012). This last result indicates that FO recognition/puncture is not straightforward, claiming for novel guidance strategies and smart equipment (Chierchia *et al.*, 2013; Katritsis *et al.*, 2013; von Alvensleben *et al.*, 2014).
In 2012, Yao *et al.* (2012) published a clinical experience article about TSP. A total of 539 punctures were reported, with success of 100% and first attempt puncture of 98.9%. Similarly, von Alvensleben *et al.* (2014) and Elayi *et al.* (2011) proved that TSP can be safely applied on children with a low complication rate (2%). Yao *et al.* (2013) and Bayrak *et al.* (2012) discussed the difficulties of TSP on unexperienced hands, proving that higher failure rate and higher procedural times are achieved by trainees. Moreover, Schwagten *et al.* (2010) presented a comparison between LA access through TSP and TA approach. Twenty-two patients were used in this experiment and similar complication/failure rate was achieved by the two strategies.

**Table 2.7 – Surgical instruments used in various TSP works between 2008 and April 2015 (Part 1)**

| | | Authors | Aims | Instruments/Methods | V | Conclusion |
|---|---|---|---|---|---|---|
| **Needles** | **Radio-frequency (RF)** | Jauvert *et al.* (2015) | Evaluation of the safety of a RF powered flexible needle. | RF powered flexible needle and BRK needle. | 125 pat. | The flexible needle was safer and more efficient than BRK needle. |
| | | Karagöz *et al.* (2014) | Advantages of NRG needle. | NRG and BRK needle. | 3 pat. | NRG needle eased the TSP procedure in patients with pulmonary hypertension. |
| | | Esch *et al.* (2013) | Usage of RF needle in patients with CHD. | NRG and BRK needle. | 10 pat. | NRG needle can be used to access the LA in patients with congenital heart disease, even when BRK needle failed. |
| | | Hsu *et al.* (2013) | Comparison of needles. | NRG and BRK needle. | 72 pat. | NRG needle allowed shorter procedure time and lower failure rate. |
| | | Feld *et al.* (2011) | Comparison of needles. | NRG RF and BRK needle. | In vitro. | NRG needle appeared to be safer than the traditional needle, presenting a more adequate shape that reduces the risk of embolization. |
| | | Fromentin *et al.* (2011) | Comparison of needles. | NRG RF and BRK needle. | 241 pat. | NRG needle showed superior performance than BRK. |
| | | Winkle *et al.* (2011) | Comparison of needles. | NRG RF and BRK needle. | 1167 pat. | NRG needle showed superior performance than BRK, with reduced procedural time and superior performance. |
| | | Crystal *et al.* (2010) | Validation of NRG needle. | NRG needle. | AM. | RF needle eased TSP procedure, presenting newer devices and shapes to improve the LA access technique. |
| | | Smelley *et al.* (2010) | Validation of NRG needle. | NRG needle. | 41 pat. | NRG needle was safe with low failure rate. |
| | | Greenstein *et al.* (2012) | The difference of tissue coring between needles. | Electrocautery and BRK needles. | AM. | A similar number of tissue coring was achieved by the two techniques. |
| | | Abed *et al.* (2012) | Comparison of needles. | Electrocautery and BRK needles. | 10 pat. | Electrocautery method was safe and cost-effective when compared with the traditional one. |
| | | Capulzini *et al.* (2010) | Comparison of needles. | Electrocautery and BRK needless. | 162 pat. | Electrocautery method is a safe and reproducible technique, particularly in patients with abnormal anatomy. |
| | | Mcwilliams and Tchou (2009) | Comparison of needles. | Electrocautery and BRK needless. | 350 proc. | The electrocautery technique showed potential to facilitate TSP. |
| | | Knecht *et al.* (2008a) | Usage of electrocautery needles in TSP. | Electrocautery needle. | 269 proc. | Electrocautery provided simple and safe LA access, even in situations where BRK needle failed. |
| | **Other** | Uchida *et al.* (2011) | Validation of a novel CTS needle. | CTS needle. | AM. | CTS needle performed safe TSP in animal model, even in difficult situations where the BRK needle failed; |

AM – Animal model; BRK – Brockenbrough needle; CHD – Congenital Heart disease; CTS – Coaxial Transseptal Needle; NRG – RF needle designed by (Baylis medical); pat. – patient; proc. – procedure; V – Validation;

**Table 2.7. (cont.) - Surgical instruments used in various TSP works between 2008 and April 2015 (Part 2)**

| | | Authors | Aims | Instruments/ Methods | V | Conclusion |
|---|---|---|---|---|---|---|
| Other instruments | Guidewire | Giudici *et al.* (2015) | Validation of a novel nitinol guidewire. | Nitinol guidewire. | 100 pat. | This method is simple, inexpensive and safe. |
| | | Wadehra *et al.* (2011) | Assess the safety of a novel TSP method. | Nitinol guidewire and BRK needle. | 210 pat. | The new method showed a high success rate, showing potential to improve TSP. |
| | | De Ponti *et al.* (2010) | Comparison of a novel transseptal guidewire with the traditional method. | Nitinol guidewire. | 19 pat. | This novel guidewire eased TSP procedure. |
| | | Wieczorek *et al.* (2010) | Validation of a novel nitinol guidewire in TSP. | Nitinol guidewire and BRK needle. | 158 pat. | This approach is safe and effective in difficult situations. |
| | Other | Wang *et al.* (2012) | Comparison of a novel dilator method with the traditional strategy. | New dilator method and traditional TSP. | 2292 pat. | The new technique was safer than the traditional one. |
| | | Saliba *et al.* (2008) | Robotic remote steerable sheath system to perform TSP puncture. | Robotic remote navigation system. | 40 pat. | The robotic system was safe with results comparable to the traditional approach. |

BRK – Brockenbrough needle; CTS – Coaxial transseptal needle; NRG – RF needle designed by (Baylis medical); pat. – patient; V - Validation;

Several researchers focused on clinical studies to identify the main complications and limitations of the TSP (Chierchia *et al.*, 2013; Hu *et al.*, 2008; Katritsis *et al.*, 2013; Knecht *et al.*, 2008d; Koermendy *et al.*, 2014; Lehrmann *et al.*, 2014; Tang *et al.*, 2014; Zellerhoff *et al.*, 2014). The researchers reported that:

1) Any consensus was found between LA access through patent foramen ovale (PFO) or TSP procedure. Lehrmann *et al.* (2014) and Knecht *et al.* (2008d) agreed that TSP procedure results in lower complication rate and allow simple maneuverability of the catheter inside the LA when compared with PFO access. However, Koermendy *et al.* (2014) and Miyazaki *et al.* (2011) published clinical reports proving that LA access through PFO is safe with higher success rate and lower complication rate when compared with TSP;

2) Repeated TSP presented higher complication rate and higher number of puncture attempts (Hu *et al.*, 2008) when compared with patients without any previous procedure;

3) Anterior, medial and posterior FO are the optimal puncture position, with equal complication rate and maximum catheter dexterity (Chierchia *et al.*, 2013).

In order to ease left heart procedures, multiple catheters placed through double TSP was suggested (Haegeli *et al.*, 2010; Lakkireddy *et al.*, 2008). Haegeli *et al.* (2010) performed 269 procedures using double puncture with a low complication rate (approximately 3%). Similarly, Lakkireddy *et al.* (2008) applied the same technique in 90 patients with only one failure and a

complication rate of 4%. Thus, the researchers agreed that double TSP increases the maneuverability of the catheters inside the LA and it is a feasible in normal clinical practice.

Finally, a high number of studies focused on novel TSP techniques and its comparison against the traditional technique (Abed *et al.*, 2012; Chierchia *et al.*, 2008; Clark *et al.*, 2008; Esch *et al.*, 2013; Ferguson *et al.*, 2009; Fromentin *et al.*, 2011; Haegeli *et al.*, 2010; Hsu *et al.*, 2013; Jauvert *et al.*, 2015; Mitchell-Heggs *et al.*, 2010; Saliba *et al.*, 2008; Smelley *et al.*, 2010; Unnithan *et al.*, 2014; Wadehra *et al.*, 2011; Wang *et al.*, 2012; Wieczorek *et al.*, 2010; Winkle *et al.*, 2011). The novel methods reduced the number of complications, failure rate, procedural time and radiation exposure.

### 2.4.2. Intra-procedural guidance techniques

Several researchers proposed novel guidance techniques, based on TEE or ICE, to overcome the main limitations of the fluoroscopy-based procedures, namely: 1) two-dimensional acquisition with low contrast between the relevant structures and the neighbors, and 2) continuous radiation exposure.

Wu *et al.* (2008) and Chierchia *et al.* (2008) suggested the application of 2D and 3D TEE, respectively, in TSP to correct the alignment between the needle and FO. The researchers validated this novel image guidance approach in humans. A low complication rate and no failures were reported, proving therefore the safety and feasibility of the new method in clinical practice. Furthermore, lower procedural time was reported (Chierchia *et al.*, 2008; Wu *et al.*, 2008). Faletra *et al.* presented extended reports about atrial anatomy interpretation in 3D TEE (Faletra *et al.*, 2011; Faletra *et al.*, 2014a). They proposed that TEE is useful in pre-procedural planning step and during the TSP, due to the clear definition of the "true" septum border. Moreover, Bayrak *et al.* (2012) proved that TEE allows simple recognition of the anatomical structures, namely FO, and it is essential to safe TSP in unexperienced hands. Finally, Gafoor *et al.* (2015) recently proposed the application of the novel EchoNavigator system (Philips Inc., Netherlands) on the TSP procedure. The EchoNavigator automatically combines 3D TEE image with fluoroscopy, which allows simple catheter guidance until the target site. Note that TEE and fluoroscopy ease FO recognition and instruments tracking/identification, respectively. As such, the physician can introduce landmarks on the image obtained from TEE (e.g. FO position) and accurately visualize them in the fluoroscopic image. Although this system presented promising results, no validation study was reported (Gafoor *et al.*, 2015).

Since TEE generally requires high level of sedation with high costs to facilitate the manipulation of the thick TEE probe, micro-TEE probe was suggested. Stec *et al.* (2011)

applied the novel method in 12 non-sedated patients without failures. Moreover, a clear image of IAS wall was achieved, proving that this guidance approach can be safely used in TSP.

Similarly, ICE imaging was also proposed as a solution for safe TSP. Instead the esophageal route required for TEE imaging (which requires anesthesia to increase the patient comfort during the long-period of the intervention) an intravascular route is used, consequently removing the need of high sedation levels. Since ICE provides a clear definition of the IAS wall in real-time, identification of the FO position is facilitated. Ferguson *et al.* (2009) proved that ICE guaranteed safe TSP, through the application of this technique in 21 situations without any complication. Liang *et al.* (2010) compared two ICE techniques in order to identify the optimal strategy for TSP, namely mechanical ICE and phased-array ICE. Mechanical ICE uses a non-flexible catheter, with a bidimensional image generated perpendicularly to the catheter. In contrast, phased-array ICE uses a flexible catheter, shows color Doppler functions and uses multiple transducers controlled electronically to produce a wedge shaped image. Both methods showed a clear image of the IAS and FO. However, since mechanical ICE has a better near field view, needle guidance inside the RA is simpler. Additionally, mechanical ICE is a lower cost strategy. Finally, some researchers presented interesting extended reports about ICE image guidance during TSP procedures, where a detailed explanation about atrial anatomy interpretation in ICE is presented (Biermann *et al.*, 2012; Ruisi *et al.*, 2013; Russo *et al.*, 2013).

Mitchell-Heggs *et al.* (2010) proposed a different guidance technique, where the ICE probe (smaller than TEE probe) is used through the esophageal route instead of the traditional intravascular one. The researchers reported that this new strategy, termed ICE-TEE, reduces the risks associated with femoral hematoma (common in traditional ICE), ease the catheter manipulation and facilitate the identification of the relevant anatomical structures. The technique was successfully in 79 patients with a complication rate of 11%.

Elagha *et al.* (2008) and Thiagalingam *et al.* (2008) proposed different image-guidance strategies based on real-time MRI and direct full color visualization, respectively. Regarding the first strategy, the researchers applied interactive, multi-slice real-time MRI using steady free precession pulse sequences. Since the patient is positioned inside the MRI machine, some equipment (e.g. catheters) were modified. As a result, the researchers proved that the transseptal needle and FO can be accurately identified with this imaging technique. Moreover, fast identification of possible complications was easily observed, namely perforation of aorta and of atrial free wall. The method was tested successfully (100%) in animal models (Elagha *et al.*, 2008). Thiagalingam *et al.* (2008) proposed direct visualization of the IAS through a fiber optic catheter. A real-time visualization of IAS was achieved through a connection between the fiber

optic and a monitor. Moreover, a pressurized bag of saline solution, connected to the fiber optic, was used to clean the blood from the top of the camera. TSP was performed in animal models without any complication. Furthermore, post-mortem analysis showed a high correlation between puncture site and real FO. However, although these methodologies presented large potential to a safe and quick TSP, human validation is missing.

Instead of novel image guidance methods, Yao *et al.* (2013) proposed a modification of the traditional TSP. Similarly to the traditional approach, this new method is also guided by fluoroscopy, being therefore an inexpensive solution. Nevertheless, in this solution, a distal CS catheter is positioned on the lateral marginal of the heart, consequently defining the level of FO at posterior-anterior projection of fluoroscopy. Thus, after an initial alignment between the needle and FO, using the normal procedure, a confirmation of the needle site is performed using the CS catheter site. In this confirmation, the physician verifies if the TSP needle is positioned between the distal CS catheter and the peak posterior margin of the LA at right anterior oblique direction of fluoroscopy. Finally, the needle can safely puncture the FO until LA. Three trainee and one expert applied this method in 120 patients with a mean failure rate of 4%.

Several studies proposed novel guidance methodologies based on EAM (Clark *et al.*, 2008; Mah *et al.*, 2014; Saliba *et al.*, 2008; Shepherd *et al.*, 2008) and electromagnetic sensors (Jeevan *et al.*, 2014), respectively. The researchers suggested that fluoroscopy time can be reduced (Mah *et al.*, 2014; Shepherd *et al.*, 2008) or removed (Clark *et al.*, 2008) from TSP, presenting clear advantages for the physician and the patient. Shepherd *et al.* (2008) used the EAM technique to generate a 3D model of the atria and to guide the transseptal needle until the FO. Nonetheless, no clinical validation was performed. Moreover, since EAM technique does not provide real-time geometries, a sub-optimal guidance approach was achieved. As such, Mah *et al.* (2014) suggested the combination of EAM and ICE to reduce the fluoroscopy exposure time. This approach was applied in the clinical practice, where a reduction of the fluoroscopy dose/time was observed. Saliba *et al.* (2008) applied the same technique in a robotic remote navigation system to perform the TSP procedure. This framework was tested in 40 patients, showing similar complication/failure results when compared with the traditional approach.

Instead of ICE imaging, Clark *et al.* (2008) presented a novel system where EAM data is fused with TEE. The optimal puncture is performed in two steps: 1) identification of the optimal puncture position using the RA geometry generated by EAM; 2) confirmation of the correct alignment between the needle and puncture site using TEE. The system was applied in 10 patients without any complication or failure. Furthermore, fluoroscopy time and exposure was not required. Finally, Jeevan *et al.* (2014) proposed a different strategy to guide TSP. In

this strategy, an electromagnetic sensor was positioned on the tip of the catheter and it was rigidly aligned with a patient specific atrial model obtained from a pre-interventional MRI. This alignment was performed through a set of fiducial markers positioned on the real and virtual model, being the FO also represented by a fiducial marker. As such, during the intervention the electromagnetic system indicates the optimal trajectory until the puncture site. The system was tested using one phantom, being the procedure performed quickly and without complications. However, it was only tested using a static model being far from being applied in real situations.

Recent studies suggested that left-sided catheter dwelling time appears to be associated with bleeding, clotting, endothelial dysfunction or char particle embolization (Unnithan *et al.*, 2014). As such, repeated/multiple LA access through TSP is required to reduce the catheter dwelling time in the LA, and consequently reduce these complications (Medi *et al.*, 2013; Unnithan *et al.*, 2014). However, multiple LA access is time-consuming, frustrating, require large radiation dose and can originate serious complications (Nguyen *et al.*, 2013). Interesting solutions to quick and safe LA reaccess without any radiation were proposed in (Nguyen *et al.*, 2013; Pavlović *et al.*, 2014; Unnithan *et al.*, 2014). All the strategies use EAM to generate geometry of the atrial region and create a marker of the TSP site. Unnithan *et al.* (2014) and Pavlović *et al.* (2014) validated this methodology in 10 and 5 patients, respectively. Quick access (approximately 14 seconds) with low complication rate was reported. Additionally, Nguyen *et al.* proposed a new remote magnetic catheter navigator system that allows "manual" and "automatic" LA reaccess Nguyen *et al.* (2013). The automatic remote navigator system relies on 8 electromagnetics positioned along the patient. These electromagnetics modify the magnetic field applied when a correction of needle position or pose is required to achieve the target site. This technique was applied with success in 5 patients, taking 6.2 ± 8.1 and 30.4 ± 28.4 seconds in automatic and manual operation mode, respectively (Nguyen *et al.*, 2013).

### 2.4.3. Pre-procedural planning techniques

The novel pre-procedural planning methods for TSP focused on pre-interventional imaging, specifically: CT (Jayender *et al.*, 2011; Wagdi and Alkadhi, 2012), MR (Jayender *et al.*, 2011) or TEE (Schernthaner *et al.*, 2013; Tomlinson *et al.*, 2008). Wagdi and Alkadhi (2012) reported that TSP is challenging in situations where larger device sizes (e.g. amplatzer) have been applied to close an IAS defect. As such, they suggested the analysis of CT datasets to define a "safe zone" for TSP. This study was performed on 20 patients, and the results proved that CT data can predict the feasibility and safety of TSP. Similarly, Schernthaner *et al.* (2013) used TEE to predict the feasibility of TSP, proving that TEE can be used to identify patients

with abnormal IAS wall anatomy. Tomlinson *et al.* (2008) suggested that FO thickness is a predictor of the difficulty of TSP procedure. Thus, during the pre-procedural stage, 42 patients were assessed by TEE and classified as difficult or not difficult procedure. It should be noted that wall thickness can be easily observed in TEE. This initial classification was subsequently compared with the difficulty of the real procedure, where no correlation was found between the pre-procedural classification and the difficulty of the procedure. Finally, Jayender *et al.* (2011) proposed a novel approach for optimal puncture location estimation. This strategy combines pre-interventional anatomical models with a mechanical model of the catheter to simulate the TSP. As such, a finite element method was used to estimate the optimal puncturing site based on the thickness of the septal wall and the mechanical maneuverability of the catheter at all positions of the LA. The current system was only tested in one offline dataset, missing application in clinical practice.

### 2.4.4. Surgical instruments

New surgical instruments have also been presented to increase the performance of the TSP, with a notable focus on the needles. Although the mechanical needle appears to be safe in non-complex procedures, the same is not observed in abnormal atrial anatomy or in patients with previous procedure. As such, NRG (Crystal *et al.*, 2010; Esch *et al.*, 2013; Feld *et al.*, 2011; Fromentin *et al.*, 2011; Hsu *et al.*, 2013; Jauvert *et al.*, 2015; Smelley *et al.*, 2010; Winkle *et al.*, 2011) and electrocautery needles (Abed *et al.*, 2012; Capulzini *et al.*, 2010; Greenstein *et al.*, 2012; Knecht *et al.*, 2008a; Mcwilliams and Tchou, 2009) were proposed.

NRG is a rigid needle that uses RF energy to diminish the septal wall resistance, reducing therefore the force required for FO puncture. This needle presents a novel design, with an oval tip to prevent inadvertent puncture. Furthermore, a radiopaque marker was incorporated inside this equipment to simplify needle guidance in fluoroscopy-based methods (Feld *et al.*, 2011). Regarding the clinical practice, no relevant modification of the traditional procedure is required, therefore facilitating the introduction of this instrument (Fromentin *et al.*, 2011).

In 2010, some researchers demonstrated that NRG needles can be used to perform safe TSP, principally in difficult procedures (Crystal *et al.*, 2010; Smelley *et al.*, 2010). The method was validated in: 1) animal model (Crystal *et al.*, 2010), and 2) 35 patients (Smelley *et al.*, 2010). Although animals with complex anatomy were used, no complications were found (Crystal *et al.*, 2010). Regarding the clinical validation, only one failure was registered. Thus, the results showed that the NRG needle can be used to perform safe TSP even in difficult cases (Crystal *et al.*, 2010; Smelley *et al.*, 2010).

Subsequently, several researchers presented large clinical studies where a comparison between the NRG needle and the conventional one is performed (Esch *et al.*, 2013; Feld and Yao, 2014; Fromentin *et al.*, 2011; Hsu *et al.*, 2013; Jauvert *et al.*, 2015; Karagöz *et al.*, 2014; Winkle *et al.*, 2011). The researchers agreed that NRG needle reduces the procedural time, the complication/failure rate, and facilitates the procedure in presence of complex anatomies when compared with the traditional strategy (Esch *et al.*, 2013; Fromentin *et al.*, 2011; Karagöz *et al.*, 2014; Winkle *et al.*, 2011). Additionally, randomized single blinded studies have also been used to validate these conclusions (Hsu *et al.*, 2013). Moreover, Feld *et al.* (2011) proved that BRK needle can introduce plastic particles into the circulatory system of the patient, which can be the origin of microinfarcts and left ventricular dysfunction. These particles are created due to a process of skiving when the needle is advanced along the plastic dilator. The NRG needle was also tested and no plastic particles were found. Although the NRG needle appeared to present a superior performance when compared with the traditional equipment, several theoretical risks should be considered, particularly: 1) inadvertent cardiac puncture using RF can result in more serious complications; 2) puncture site is less likely to close spontaneously; and 3) the RF puncture can be more traumatic for the FO (Smelley *et al.*, 2010).

Recently, a novel RF powered flexible needle, termed Toronto needle was proposed (Jauvert *et al.*, 2015). The advantage of this new tool is the specific shape of the instrument, where a flexible catheter with large "J" shaped distal curve is used, consequently preventing inadvertent punctures. Moreover an RF system is used to ease TSP (Hsu *et al.*, 2013). Jauvert *et al.* (2015) compared the Toronto and BRK needle in humans. 125 punctures were performed with Toronto needle, and 100 punctures with the traditional approach. The results demonstrated that the Toronto needle has a superior performance, lower number of failures (5% for BRK and 0% for Toronto) and lower complication rate (3% for BRK and 0% for Toronto).

An electrocautery pen combined with traditional BRK needle was also proposed to ease septal wall crossing (Abed *et al.*, 2012; Capulzini *et al.*, 2010; Greenstein *et al.*, 2012; Knecht *et al.*, 2008a; Mcwilliams and Tchou, 2009). In this method, the traditional TSP is initially performed to align the needle with the FO region. Subsequently, the cautery pen is applied on the proximal portion of the needle (Capulzini *et al.*, 2010; Mcwilliams and Tchou, 2009), cauterizing the FO and reducing the pressure required to perform the FO crossing. Similarly to the NRG and Toronto needles, this novel approach reduced the complication/failure rates when compared with the BRK needle, mainly in highly elastic, aneurysmal, or fibrotic septal walls (Abed *et al.*, 2012; Capulzini *et al.*, 2010; Knecht *et al.*, 2008a; Mcwilliams and Tchou, 2009). Finally, Greenstein *et al.* (2012) compared both techniques to verify the incidence of tissue

coring into the needle tip. It should be noticed that coring of the septal wall can result in complications, such as systemic embolization. The study was performed in animal models and the results showed a similar number of tissues coring (~35% of the punctures) with both approaches, raising questions about the real safety of the TSP.

In opposition, Uchida *et al.* (2011) proposed a novel mechanical needle, termed CTS needle. This needle was longer than the traditional one, showing high safety (100%) and feasibility in 10 animals. Note that TSP was not successfully with the BRK needle due to the particular anatomy of the animal.

Although several researchers proposed and validated novel needles to safely perform TSP, novel solutions were also presented for the remaining equipment: nitinol guidewires (De Ponti *et al.*, 2010; Giudici *et al.*, 2015; Wadehra *et al.*, 2011; Wieczorek *et al.*, 2010) and laser catheters (Elagha *et al.*, 2008). Nitinol guidewire (SafeSeptTM, Pressure Products Inc., San Pedro, USA) presented a "J" preformed with 0.014″ wire and a sharp-distal tip. This novel equipment was positioned inside the needle assuming two different shapes: 1) a straight shape when the guidewire is completely positioned inside the needle, and 2) a "J" shape when the guidewire is outside of the needle. The straight guidewire shape facilitates catheter manipulation and the "J" guidewire shape prevents inadvertent punctures. Furthermore, this novel guidewire has a radiopaque marker at the guidewire tip, facilitating instrument identification in fluoroscopy. This novel solution was compared with the traditional TSP strategies in humans, showing a high success rate even in difficult procedures (De Ponti *et al.*, 2010; Giudici *et al.*, 2015; Wadehra *et al.*, 2011; Wieczorek *et al.*, 2010). Moreover, Wadehra *et al.* (2011) suggested that the nitinol guidewire is a safe and useful alternative for the expensive TSP procedures based on 3D image guidance.

Elagha *et al.* (2008) proposed a laser catheter for TSP guided by real-time MRI. A receiver coil, positioned at the catheter tip, was used to generate a bright spot that can be detected on MRI. This new system was validated in animal models, proving that the laser catheter can be accurately detected in real-time MRI. Furthermore, the novel system proved to be feasible, with a success rate of 100%.

Some researchers suggested that robotic remote navigation system can be used in TSP. The robotic system allows better catheter stability, precise positioning of the surgical equipment and simple catheter maneuverability, increasing therefore the safety of the procedures. Clinical validation was reported, being reported only one complication (Saliba *et al.*, 2008).

Finally, Wang *et al.* (2012) proposed a different TSP strategy, where a different surgical tool configuration is used. This strategy, termed dilator method, presented the following

modifications: 1) the outer sheath was removed from the procedure, being only required the dilator and a transseptal needle; and 2) the needle was kept inside the dilator during the entire guidance procedure. As such, the identification of the lip edge of the FO was performed using the dilator. Since the dilator presents a blunt tip, the FO identification was eased. A comparison between the novel method and the traditional one was performed in a total of 4443 patients. The results suggested that the dilator technique is much safer than the traditional approach, with a reduction of the complication rate. Nevertheless, an increase of the procedure time and radiation time was registered (Wang *et al.*, 2012).

## 2.5. Future Trends

Several studies explored the major technical limitations of the traditional TSP approach, specifically: 1) incorrect visualization of IAS; 2) difficulty in identifying the surgical tools; 3) incorrect estimation of the puncture position, mainly in patients with PFO; 4) inadequate needles for patients with abnormal anatomy; and 5) difficulty in confirming successful puncture or even procedural complications.

In this sense, multiple improvements were introduced to the traditional technique, namely: 1) new guidance approaches through real-time imaging modalities or electromagnetic tracking sensors; 2) new pre-planning strategies based on CT or MRI; and 3) new surgical instruments, mostly new TSP needles. In particular, RF needles and puncture guidance using 3D ultrasound showed its added-value to the current TSP technique, mainly in difficult anatomies. The first one uses RF energy to reduce the septal wall resistance, facilitating the puncture in patients with thick (caused by repeated procedures) or aneurismal walls. While the second one relies on a radiation-free imaging technique that allows real-time visualization of the 3D anatomy, being typically used to confirm the correct alignment between the transseptal needle and the fossa ovalis. However, large randomized and comparative studies between the aforementioned imaging modalities are still missing. Furthermore, TSP merely guided through ultrasound imaging is not typically used, due to the difficulty to understand the anatomy and to visualize the surgical instruments. As such, ultrasound combined with fluoroscopy is applied.

Although some planning solutions have been proposed to accurately identify the puncture position and the optimal needle trajectory, extensive validations of the available technique still missing, hampering its application in the real clinical practice. Furthermore, several studies are not tested in patients with abnormal anatomy, consequently not proving the adequacy of the proposed technique in challenging cases. As such, the current clinical practice still being largely dependent on physician experience. As a result, sub-optimal locations that

reduce the catheter dexterity at the left heart or even multiple puncture attempts, which increase the procedural time (and thus costs) and radiation exposure, are often used.

In the near future, the development of integrated image guidance tools that combine pre-procedural planning with intra-procedural imaging appears as an attractive solution to guide the physician until the optimal puncture position. Due to the high anatomic detail obtained with pre-planning imaging (such as CT and MR), accurate identification and planning of the optimal puncture position based on the target position at the left heart and septal wall thickness can be performed. Moreover, accurate simulation of the optimal puncture position and measurement of the catheter dexterity through computational simulation methods (e.g. finite element modeling) are important tools to plan the entire intervention. Then, the entire pre-procedural stage can be transported for the real interventional world, through image fusion solutions between CT/MR and 3D ultrasound imaging. This stage is vital, since all the annotations generated during the planning stage are superimposed on the patient anatomy (obtained in real-time by US), easing the identification of the optimal puncture position, consequently facilitating the puncture (enhancing several anatomic structures such as IAS and fossa ovalis) and increasing the level of confidence of the physician. Note that, ultrasound imaging seems as an interesting solution to align the intra and pre-procedural stages, due to the 3D acquisition of the cardiac anatomy in real-time and also due to the clear definition of the IAS wall and cardiac chambers. Moreover, since this imaging modality is currently integrated in the operating room and traditionally is required to confirm correct alignment of the needle with fossa ovalis, simple integration of this new system in the current surgical setup is possible. Finally, the fused 3D world should be aligned with biplane fluoroscopy imaging, in order to accurately identify the needle (and remaining surgical instruments) position. Although, needle tracking through ultrasound imaging or external sensors appears as an interesting solution with clear advantages for the patient and the medical team, robust solutions with high accuracy are still a research topic, failing to prove its advantages in the real clinical scenario. Moreover, long learning curves and significant modifications of the traditional clinical procedure are required, hampering its application in the near future. In this sense, the synergy between richly-detailed models and anatomic references obtained from CT/MR data, live anatomic information extracted from US and accurate catheter tracking obtained from fluoroscopy, appears as a potential optimal strategy to perform TSP, increasing the procedural safety, avoiding procedural complications and removing the need for secondary punctures due to low catheter dexterity. Furthermore, the integrated guidance tool can decrease the interventional time (and thus cost) and radiation dose exposition.

## 2.6. Conclusions

An overview of novel techniques recently applied in TSP procedure was presented. TSP is safe and feasible in clinical practice, with complication and failure rate lower than 1% of the total number of interventions. Nonetheless, the traditional procedure uses radiation and it is highly dependent of the physician's experience.

During the last years, the novel RF needles and the 3D TEE/ICE imaging guidance approaches showed a notable reduction of procedural time and radiation exposure time. A lower number of procedural complications/failures were also reported even in the presence of complex atrial anatomy, proving the advantages of these novel methodologies. Furthermore, pre-procedural planning based on high-resolution imaging showed potential to predict the feasibility of the TSP procedure and to identify a safe puncture zone that guarantees maximum catheter dexterity throughout the remaining LA intervention. Nevertheless, integrated guidance tools able to fuse pre-procedural with intra-procedural planning still not being described. Moreover, the current needles are only adequate for fluoroscopy guidance, being required several modifications in order to allow/ease intervention guidance without radiation.

## 2.7. Appendixes

### Appendix A – Update to 2018

The previous review was extended to include the relevant studies published between April 2015 and January 2018. For that, the abovementioned selection method (section 2.2.1), data collection and processing (section 2.2.2) and data analysis (section 2.2.3) strategies were reapplied. In this sense, a total of 30 novel articles were included in this appendix. An overview of the selection method is presented in Figure 2.A.1. Again, the selected articles were divided into four main groups, namely: 21 articles for the incidence study, 15 for intra-procedural guidance techniques, 1 for pre-procedural planning methods and 3 for surgical instruments. As previously stated, one work can be included in more than one group. In the next sub-sections, a description of the major contributions of each work and a discussion of them is presented.

Results

The current analysis was performed for each pre-defined group independently, namely: incidence study, intra-procedural guidance techniques, pre-procedural planning techniques and surgical instruments. As a remark, an overview of the published reviews between April 2015 and January 2018 is presented in Table 2.A.1.

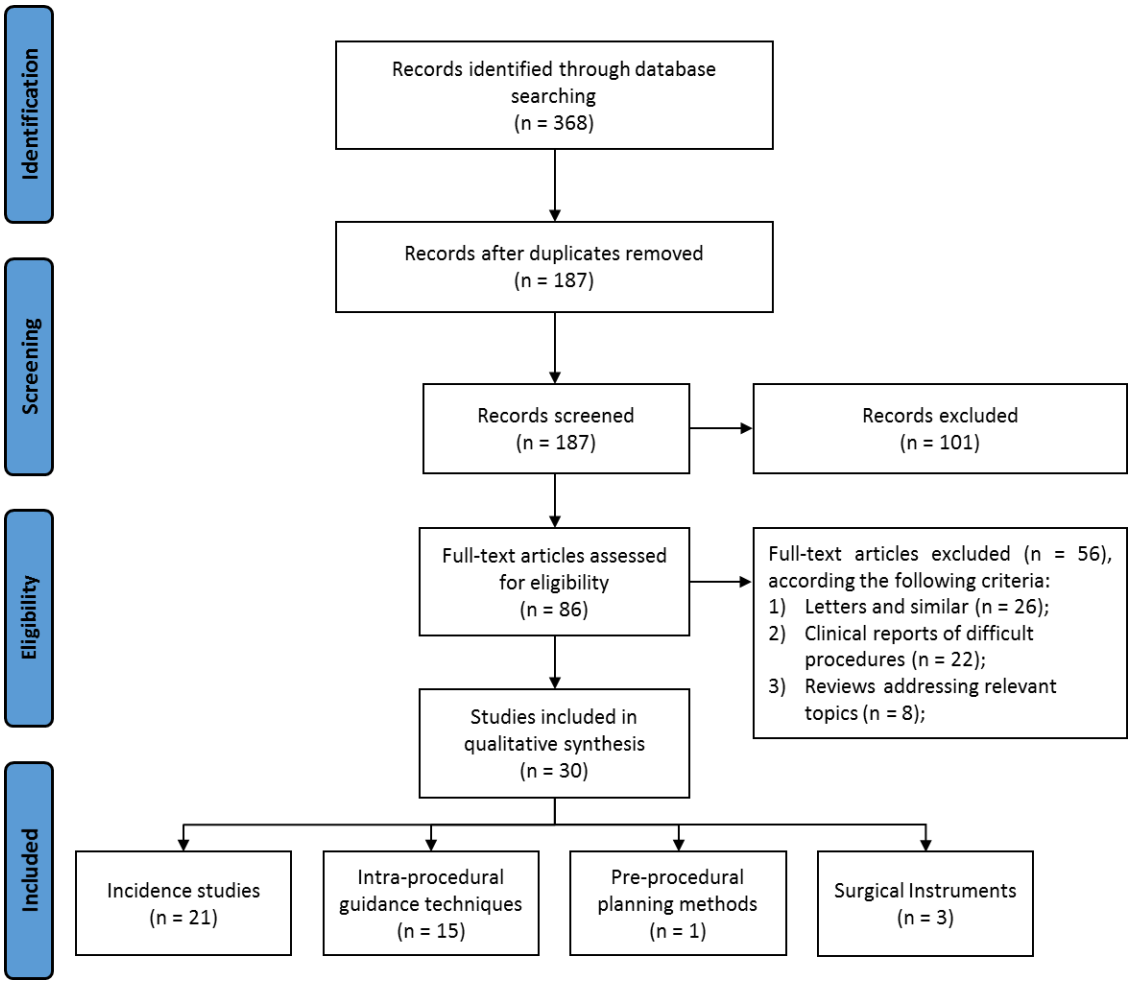


**Figure 2.A.1 - Overview of the methodology used to select the relevant articles for this appendix.**
The identification of the relevant works was performed using Prisma Statement (Moher *et al.*, 2010).

*Incidence study:* Between April 2015 and January 2018 several clinical validations of novel techniques (Afzal *et al.*, 2017; Ballesteros *et al.*, 2017; Bourier *et al.*, 2016; Dong *et al.*, 2015; Gowda *et al.*, 2017; Knadler *et al.*, 2017; Koektuerk *et al.*, 2016; Mansour *et al.*, 2015; Matoshvili *et al.*, 2017; Radinovic *et al.*, 2016; Sharma *et al.*, 2017; Wang *et al.*, 2016c; Yuan *et al.*, 2017) or performance reports (Wasmer *et al.*, 2017) using children (Ehrlinspiel *et al.*,

**Table 2.A.1 – Topics addressed in different reviews published between April 2015 and January 2018**

| Authors | Aims |
|---|---|
| O'Brien *et al.* (2017) | Overview of novel surgical devices, relevant anatomy for TSP and main complications/challenges of the technique. |
| Salghetti *et al.* (2017) | Overview of main complications of TSP and description of the strategies/equipment to reduce the number of complications. |
| Vahanian and Brochet (2017) | Review of complications, applications and possible solutions in the near future for TSP procedure. |
| Alkhouli *et al.* (2016) | A step-by-step description of challenging transseptal access and procedural complications. |

2017; Gowda *et al.*, 2017; Knadler *et al.*, 2017; Yoshida *et al.*, 2015), patients with abnormal anatomy (Aksu *et al.*, 2017; Kataria *et al.*, 2017; Sharma *et al.*, 2017) and previous TSP (Arkles *et al.*, 2015) were reported (Table 2.A.2). During this period, a total of 14175 TSP was considered, with a complication and failure rate of 0.37% and 0.59%, respectively. Moreover, repeated TSP was required in 9.87% of the cases. Finally, by combining both evaluated period (*i.e.* 2008 to April 2015, and April 2015 to January 2018), a global complication and failure rates of 0.44% and 0.76% was registered. Repeated TSP was required in 11.54% of the cases.

*Intra-procedural guidance techniques:* Recently, a high number of novel image-guided techniques were described (Table 2.A.3). These new strategies focused on novel imaging modalities or strategies, namely: the rotational angiography acquisition (Koektuerk *et al.*, 2016) and image-fusion strategies (Afzal *et al.*, 2017; Basman *et al.*, 2017; Biaggi *et al.*, 2015; Bourier *et al.*, 2016; Faletra *et al.*, 2017). In detail, image-fusion systems, combining fluoroscopy and TEE (Afzal *et al.*, 2017; Faletra *et al.*, 2017) or fluoroscopy with CT (Bourier *et al.*, 2016), were developed and applied to guide TSP interventions. Differently, one team suggested the use of intracardiac potentials obtained from surgical tools as a helpful information to increase the safety of TSP (Heinroth *et al.*, 2017). In contrast, some researchers still explore the potential of previous described guidance techniques, namely fluoroscopy (Dong *et al.*, 2015; Wang *et al.*, 2016c), TEE (Nijenhuis *et al.*, 2017), EAM (Clark *et al.*, 2017; Yuan *et al.*, 2017) and electromagnetic systems (Ballesteros *et al.*, 2017; Mansour *et al.*, 2015).

*Pre-procedural planning techniques:* One contribution focusing on CT-based intervention planning using manually delineated anatomical models (Bourier *et al.*, 2016) was found during the selected period (Table 2.A.4).

**Table 2.A.2 – Number of TSP (NbT), percentage of repeated procedures (RP), failures (F), and complications (C) reported between April 2015 and January 2018**

| Authors | NbT | RP (%) | F | C | Authors | NbT | RP (%) | F | C |
|---|---|---|---|---|---|---|---|---|---|
| Afzal *et al.* (2017) | 88 | - | 0 | 0 | Yuan *et al.* (2017) | 40 | - | 0 | 0 |
| Aksu *et al.* (2017) | 213 | 5.16 | 0 | 0 | Bourier *et al.* (2016) | 65 | - | 0 | 0 |
| Ballesteros *et al.* (2017) | 62 | - | 2 | 3 | Erden *et al.* (2016) | 62 | - | 0 | 25 |
| Ehrlinspiel *et al.* (2017) | 157 | - | 1 | 0 | Koektuerk *et al.* (2016) | 271 | - | 7 | 2 |
| Gowda *et al.* (2017) | 54 | - | 1 | 2 | Radinovic *et al.* (2016) | 6 | - | 0 | 0 |
| Kataria *et al.* (2017) | 384 | 17.71 | 0 | 0 | Wang *et al.* (2016c) | 2820 | - | 0 | 8 |
| Knadler *et al.* (2017) | 220 | - | 5 | 1 | Arkles *et al.* (2015) | 251 | - | 20 | 6 |
| Matoshvili *et al.* (2017) | 4690 | - | 14 | 34 | Dong *et al.* (2015) | 376 | 4.52 | 0 | 0 |
| Sharma *et al.* (2017) | 52 | - | 3 | 0 | Mansour *et al.* (2015) | 16 | - | 0 | 0 |
| Wasmer *et al.* (2017) | 4305 | - | 0 | 2 | Yoshida *et al.* (2015) | 43 | - | 0 | 1 |
| | | | | | **Mean** | | **9.87** | **0.37** | **0.59** |

**Table 2.A.3 – Novel intra-procedural guidance techniques applied in TSP procedures between 2008 and January 2018**

| | | Authors | Aims | Guidance technique | V | Conclusion |
|---|---|---|---|---|---|---|
| Image-based | US | Nijenhuis *et al.* (2017) | Use of micro-TEE probe in TSP. | Micro-TEE probe. | 49 pat. | This approach is feasible to perform safe TSP. |
| | | Mahmoud *et al.* (2015) | Use of a specific anatomical view. | 3D TEE. | 20 pat. | This novel strategy is feasible and reduces the procedural time. |
| | IF | Afzal *et al.* (2017) | Validation of the Echonavigator in TSP. | TEE + FC. | 88 pat. | The system proved to be safe to perform TSP. |
| | | Basman *et al.* (2017) | Use of IF techniques in TSP. | CT, TEE, FC. | - | IF approaches have potential to improve TSP. |
| | | Faletra *et al.* (2017) | Validation of the Echonavigator in TSP. | TEE + FC. | - | This system showed potential to facilitate TSP. |
| | | Bourier *et al.* (2016) | Validation of a CT-FC approach in TSP. | CT + FC. | 65 pat. | This approach proved its added-value in abnormal situations. |
| | | Biaggi *et al.* (2015) | Advantages of IF in TSP. | CT, TEE, FC. | - | Image-fusion approaches have benefits for TSP. |
| | Other | Koektuerk *et al.* (2016) | Validation of a new image modality in TSP. | RotAng. | 271 pat. | TSP guided by this modality is a safe and effective method. |
| | | Wang *et al.* (2016c) | Validation of a novel TSP strategy. | FC. | 2820 pat. | This approach showed potential to reduce the need of atriography and unexpected cardiac perforation. |
| | | Dong *et al.* (2015) | Validation of a new TSP strategy. | FC. | 17 pat. | This novel technique is simple and safe. |
| Not purely image-based | EAM | Clark *et al.* (2017) | Validation of a EAM-ICE approach for TSP. | EAM + ICE. | 9 pat. | This approach was applied successfully in pediatric cases. |
| | | Yuan *et al.* (2017) | Safety of EAM in TSP. | EAM. | 48 pat. | This technique can guide safely TSP procedure. |
| | EM | Ballesteros *et al.* (2017) | Use of the MediGuide tracking system in TSP. | EM with FC. | 62 pat. | This technique is safe and can be performed with low radiation exposure. |
| | | Mansour *et al.* (2015) | Use of the MediGuide tracking system in TSP. | EM with FC. | 16 pat. | This technique can be successfully applied in TSP. |
| | Other | Heinroth *et al.* (2017) | IP from surgical tools can improve TSP. | IP. | 31 pat. | IP signals show specific patterns and can be used to increase the safety of TSP. |

CT – Computed tomography; EAM – Electroanatomical mapping; EM – Electromagnetic sensors; FC – Fluoroscopy; ICE – Intracardiac echocardiography; IF – Image fusion; IP – Intracardiac potentials; pat. – patients; V – Validation; TEE - transesophageal echocardiography; US – Ultrasound;

*Surgical Instruments:* Some works focused on the surgical tools (Table 2.A.5), mainly the needles, *i.e.* the NRG RF (Sharma *et al.*, 2017) and the electrocautery needle (Gowda *et al.*, 2017). For the remaining tools, a wafer-thin inner stylet (Kataria *et al.*, 2017) was presented.

**Table 2.A.4 – Pre-procedural planning methods applied in TSP between April 2015 and January 2018**

| | Authors | Aims | PM | V | Conclusion |
|---|---|---|---|---|---|
| Richly detailed images | Bourier *et al.* (2016) | Planning of TSP using specific patient models from CT. | CT. | 65 pat. | The improved planning proved its added-value in abnormal situations. |

CT – Computed Tomography; pat. – patient; PM – Planning method; V – Validation;

**Table 2.A.5 – Surgical instruments used in various TSP works between April 2015 and January 2018**

| | | Authors | Aims | Instruments | V | Conclusion |
|---|---|---|---|---|---|---|
| Needles | RF | Sharma *et al.* (2017) | Evaluation of the spatial accuracy of surgical needles. | NRG RF and BRK needle. | 52 pat. | No statistically significant differences were found between both needles. However, RF proved its added-value in abnormal cases. |
| | Electro. | Gowda *et al.* (2017) | Validation of an electrocautery needle. | Electrocautery needle. | 55 pat. | Electrocautery needle is feasible and effective for TSP procedure. |
| Other | GW | Knadler *et al.* (2017) | Validation of a novel nitinol guidewire. | Nitinol guidewire. | 220 pat. | This instrument is safe and feasible for TSP. |

BRK – Brockenbrough; Electro. – Electrocautery; GW – Guidewire; RF – Radiofrequency; V – Validation;

Discussion

*Incidence study:* During the selected period, relevant studies were presented to corroborate the safety of the TSP in different scenarios. Wasmer *et al.* (2017) evaluated the total number of inadvertent aortic puncture during TSP in a period of 10 years. A total of 4305 TSP were performed with only two cases of inadvertent aortic puncture. Matoshvili *et al.* (2017) described its clinical performance in a total of 4690 consecutive TSP, obtaining a complication and failure rate of 0.72% and 0.30%, respectively. Again, different researchers corroborated the safety of TSP in children's, with a low complication rate (<4%) (Gowda *et al.*, 2017) and a low failure rate (<1%) (Ehrlinspiel *et al.*, 2017; Knadler *et al.*, 2017). Aksu *et al.* (2017) suggested that TSP should be performed during a deep inspiration. Since the chest wall expand and the diaphragm descends during a deep inspiration, a more negative intrapleural pressure will be found, moving the IAS to the right side and easing therefore the TSP. Indeed, such approach proved its added-value in abnormal anatomical situations, mainly in cases where the conventional approach failed.

Regarding repeated TSP cases, Arkles *et al.* (2015) addressed this issue by comparing patients with and without previous TSP. The researchers concluded that repeated TSP can be difficult in specific situations, but feasible in the majority of cases.

Finally, multiple researchers proved the added-value of the novel intra-procedural guidance techniques, planning strategies and recent surgical instruments. Overall, such solutions reduced the procedural time and radiation dose exposure and improved the safety of the procedure (Afzal *et al.*, 2017; Ballesteros *et al.*, 2017; Bourier *et al.*, 2016; Erden *et al.*, 2016; Kataria *et al.*, 2017; Knadler *et al.*, 2017; Koektuerk *et al.*, 2016; Mansour *et al.*, 2015; Radinovic *et al.*, 2016; Sharma *et al.*, 2017; Wang *et al.*, 2016c; Yuan *et al.*, 2017).

*Intra-procedural guidance techniques:* Starting with guidance techniques using TEE images, Erden *et al.* (2016) corroborated this approach added-value in the TSP procedure, showing a reduction of the fluoroscopy time, procedural time and even of the complication rate when compared with the traditional approach (*i.e.* only fluoroscopy). Mahmoud *et al.* (2015) proposed the "RATLe-90" maneuver for the guidance of TSP. Specifically, after selecting 3D zoom in the echocardiographic system, a rotation anticlockwise of 90º around the Z-axis was applied, followed by a tilt left of 90º around the Y-axis. As such, an anatomical oriented view of the IAS from the RA was achieved, easing the guidance of the catheter towards the optimal puncture site. This approach was tested on 20 patients, proving to be safe, simple and quick (reducing the fluoroscopy time and minimizing US probe manipulations). Similarly, micro-TEE probes were again tested, showing a performance (in terms of image quality and procedural result) similar to standard US approaches (Nijenhuis *et al.*, 2017). Instead of TEE-guided interventions, which typically require large expertise from the medical team due to the poor image quality and due to the presence of artifacts, Koektuerk *et al.* (2016) studied the advantages of rotational angiography acquisition for the TSP procedure. In detail, the atrial region was captured in 3D using a circular arc acquisition - a specific configuration of the fluoroscopic system, being latter reconstructed and 3D segmented using computer-aided tools. The segmented surfaces were subsequently evaluated to detect abnormal anatomies and to identify the optimal puncture site. Then, they are superimposed on the traditional bidimensional fluoroscopic image, enhancing the relevant anatomical structures and easing the entire procedure. It might be noted that since both rotational angiography and bidimensional fluoroscopic images were acquired using the same setup, a fixed spatial relationship was achieved, allowing an accurate alignment between both images. This novel guidance approach was tested on 271 patients with a success rate >97%, corroborating the added-value and safety of this technique (Koektuerk *et al.*, 2016).

Nowadays, a particular focus on minimally invasive cardiac interventions guided by image fusion systems has been observed. Several researchers presented clinical validations and descriptions of TSP procedures guided by the EchoNavigator (Philips Inc., Netherlands) (Afzal *et al.*, 2017; Basman *et al.*, 2017; Biaggi *et al.*, 2015; Faletra *et al.*, 2017). Specifically, this system automatically superimposes the 3D TEE image on the fluoroscopy, based on the spatial location of the TEE probe in both images. Thus, while the fluoroscopy allows simple catheter identification and guidance until the target site, TEE introduces the relevant anatomical information of the cardiac structures, enhancing the intra-procedural images and possibly reducing the number of procedural complications. As such, the physician can introduce

landmarks (e.g. FO position) on the anatomical image, *i.e.* TEE, and accurately visualize them in the fluoroscopic image. Nevertheless, the current setup still presents some limitations, namely: 1) the added landmarks are static and not tracked throughout the cardiac cycle; and 2) a restricted rotation of the C-arm is found, preventing fusion of both images in specific and relevant clinical orientations. Afzal *et al.* (2017) tested the current system in 44 patients without complications or procedural failures, reinforcing the added-value of this approach. It might be noted that the EchoNavigator system has shown its potential for the majority of the left heart interventions, as discussed in (Faletra *et al.*, 2017). In contrast, other researchers enhanced the fluoroscopy image using pre-procedural data, namely high-resolution CT images. Bourier *et al.* (2016) generated multiple surfaces (namely, cardiac chambers, fossa ovalis, ascending aorta, pulmonary artery, coronary sinus and thoracic spine) of relevant anatomies using CT data and then transferred the entire planning stage to the intra-procedural space using the CARTO UNIVU module (Biosense Webster, Diamond Bar, USA). Note that the initial spatial alignment between fluoroscopy and CT images was achieved through an x-ray compatible registration marker (performed at the beginning of the intervention). The current setup was applied in 65 patients without complications or procedural failures, corroborating the potential of 3D-augmented interventions to facilitate and increase the safety of TSP, particularly in difficult/abnormal situations. Inspired by a similar focus, Basman *et al.* (2017) described the potential of HeartNavigator system (Philips Inc, Netherlands) to guide minimally invasive cardiac interventions. Again, CT-extracted information (e.g. relevant surfaces) is fused with fluoroscopic images by using contrast aortography or by detecting radiopaque markers. Nevertheless, although all the image fusion setups have theoretical advantages against the traditional practice, further clinical validation studies to exhaustively assess its real added-value are missing and are expected in the near future.

As previously observed, some researchers improved the guidance of TSP by adding new protocols/procedures (*i.e.* identification of specific views or anatomical landmarks) to the fluoroscopy, instead of adding new imaging modalities. In detail, Wang *et al.* (2016c) and Dong *et al.* (2015) proposed novel guidance techniques based on the manual identification of anatomical landmarks and even evaluation of the target anatomy on pre-defined fluoroscopic views, respectively. Initially, the researchers studied (*in offline)* a high number of pre-procedural CT images, identifying main landmarks and even relevant spatial measurements that ease the recognition of the optimal puncture route. Then, the proposed strategies were tested on clinical databases with 2820 (Wang *et al.*, 2016c) and 17 patients (Dong *et al.*, 2015), corroborating its safety.

Taken into consideration the previous interest demonstrated by the research community in EAM-based technique for TSP, Clark *et al.* (2017) and Yuan *et al.* (2017) corroborated the added-value of this technique in normal clinical practice, including in pediatric cases (Clark *et al.*, 2017), with a reduction of the procedural time and the radiation dose exposure.

To facilitate the tracking of surgical instruments, some researchers validated novel electromagnetic systems, namely the MediGuide Tracking system (St. Jude Medical, St. Paul, Minnesota, USA). Specifically, this system combines a pre-recorded cine loop of fluoroscopy images from the patient with two electromagnetic sensors (one coupled at the needle tip and the second one at the patient's chest) and one transmitter. While the acquired images are maintained "static" during the intervention, which do not require extra radiation, catheters/needles positions are updated based on the electromagnetic system. Moreover, the anatomical variations caused by respiratory motions are compensated thanks to the sensor coupled at the patient's chest. Mansour *et al.* (2015) and Ballesteros *et al.* (2017) presented clinical validation of this setup, registering a safety and complication rate comparable to other techniques, but with a reduction of the radiation dose throughout the intervention.

Finally, based on a different concept, Heinroth *et al.* (2017) suggested the assessment of intracardiac potentials obtained from multiple surgical tools (namely, sheath-transseptal-needle/guidewire) as a complementary strategy for the guidance of TSP, increasing the safety of the technique. The researchers found specific patterns and changes in the amplitude of each signal throughout the different stages of the intervention (e.g. puncture of the fossa ovalis). Moreover, they proved that these patterns/variations were reproducible, demonstrating its adequacy for the guidance of the TSP.

*Pre-procedural planning techniques:* Bourier *et al.* (2016) used a semi-automatic segmentation strategy, which involves the providing of a few clicks, from Carto3 (Biosense Webster, Diamond Bar, USA) to generate 3D surfaces of the different cardiac cavities and the FO. Moreover, other relevant structures such as ascending aorta, coronary sinus and thoracic spine were also reconstructed. The entire planning was later transferred to the intra-procedural images, based on an image fusion strategy, enhancing the anatomical properties of the low contrasted fluoroscopic image. The researchers agreed that by applying these models, a simple identification of the optimal puncture route was possible, improving the safety of the TSP.

*Surgical Instruments:* Focusing on the transseptal needles, Sharma *et al.* (2017) evaluated the spatial accuracy of the NRG RF needle by comparing it with the traditional mechanical needle (BRK) using two independent patient groups. No statistically significant

differences in terms of spatial accuracy were found between groups. Nevertheless, RF needles proved its added-value in abnormal cases, not presenting procedural complications (3 complications were found for the traditional one). Moreover, the identification of the optimal puncture location was quicker with this RF needle (Sharma *et al.*, 2017). Similarly, (Gowda *et al.*, 2017) validated the advantages of the electrocautery needle for pediatric cases, successfully applying it in 55 cases.

Finally, for the remaining surgical instruments, Kataria *et al.* (2017) described the use of a wafer-thin inner stylet through the conventional transseptal needle as a strategy to ease the TSP. This novel strategy was termed "mosquito" (MOSQ-TSP). In detail, the novel stylet is inserted through the BRK needle, helping to puncture stretched septums. The current preliminary study corroborated the safety and effectiveness of this approach in a total of 34 patients. Moreover, this approach can reduce the procedural time and it does not require extra guidance techniques (e.g. TEE) (Kataria *et al.*, 2017).

Final Remarks

During the last years, the majority of the researchers focused on the development and validation of novel image-fusion strategies for cardiac interventions, including transseptal puncture. Although such solutions improved the intervention, by enhancing relevant anatomical structures in the intra-procedural image, it still presents some limitations, which are expected to be improved in the near future, namely: 1) the superimposed anatomical models/landmarks are typically static, not adapting throughout the cardiac cycle; 2) pre-procedural information, e.g. anatomical models or simulation information of the optimal puncture location, is limited or not used; and 3) the surgical tools are typically not tracked, requiring X-ray images and, thus, radiation exposure to detect it. Regarding the remaining evaluated field, few works were detected. While between 2008 and 2015 (first review period addressed in Chapter 2), a high number of studies describing improved TSP needles were presented, only two novel works were found between 2015 and 2018. Indeed, this notable reduction can possibly be explained by the high performance of the current RF and electrocautery needles, which clearly proved its added-value (and validated it in different scenarios) for difficult TSP cases, mainly for abnormal cases or repeated TSP. Finally, the planning stage is still the less explored field. Since the current clinical methods are typically manual, time-consuming, tedious and not reproducible between observers, its normal application in clinical routine is hampered. Nevertheless, automated solutions are expected to be presented in the next few years, increasing the clinical interest of such solutions to improve TSP intervention.

# Chapter 3

## Development of a patient-specific atrial phantom model for planning and training of inter-atrial interventions

This chapter has been published in *Medical Physics*: **Pedro Morais**, João Manuel R. S. Tavares, Sandro Queirós, Fernando Veloso, Jan D'hooge, João L. Vilaça, "Development of a patient-specific atrial phantom model for planning and training of inter-atrial interventions", *Medical Physics*, vol. 44, pp. 5638-5649, 2017. Only minor changes to the original publication have been performed. The figures and sections numbers were updated with the chapter title and all references were combined in a common final section.

**Keywords:** 3D-printing; Cardiac Atria; Inter-atrial septal wall; Patient-specific phantom models; Ultrasound-compatible phantom model.

**Contents**

## Abstract

Several researchers have presented cardiac phantoms to mimic the particularities of the heart, making it suitable for medical training and surgical planning. Although the initial models were mainly focused on the ventricles, personalized phantoms of the atria were recently presented. However, such models are typically rigid, the atrial wall is not realistic and they are not compatible with ultrasound (US), being sub-optimal for planning/training of several interventions. In this work, we propose a strategy to construct a patient-specific atrial model. Specifically, the target anatomy is generated using a computed tomography (CT) dataset and then constructed using a mold-cast approach. An accurate representation of the inter-atrial wall (IAS) was ensured during the model generation, allowing its application for IAS interventions. Two phantoms were constructed using different flexible materials (silicone and polyvinyl alcohol cryogel, PVA-C), which were then compared to assess their appropriateness for US acquisition and for the generation of complex anatomies. Two experiments were set up to validate the proposed methodology. First, the accuracy of the manufacturing approach was assessed through the comparison between a post-production CT and the virtual references. The results proved that the silicone-based model was more accurate than the PVA-C-based one, with an error of 1.68 ± 0.79, 1.36 ± 0.94, 1.45 ± 0.77 mm for the left (LA) and right atria (RA) and IAS, respectively. Secondly, an US acquisition of each model was performed and the obtained images quantitatively and qualitatively assessed. Both models showed a similar performance in terms of visual evaluation, with an easy detection of the LA, RA and the IAS. Furthermore, a moderate accuracy was obtained between the atrial surfaces extracted from the US and the ideal reference, and again a superior performance of the silicone-based model against the PVA-C phantom was observed. The proposed strategy proved to be accurate and feasible for the correct generation of complex personalized atrial models.


## 3.1. Introduction

During the last two decades, multiple researchers focused on the development of three-dimensional (3D) models, typically termed as phantoms, of multiple human organs (e.g., liver, heart, brain, kidney) (Estevez *et al.*, 2010; Preece *et al.*, 2013). Computational and physical models were initially presented and compared, with the physical models, showing several advantages (e.g. easy to understand and simple to learn the anatomy) when compared with the virtual ones (Preece *et al.*, 2013). In this sense, the physical models were applied to characterize the anatomical shape, to study physiological mechanisms and as a surgical learning tool (Sugand *et al.*, 2010). Nevertheless, mean/standard shape models were used, while patient-

specific models could be beneficial. Furthermore, such mean models are not necessarily adequate in non-healthy patients, where abnormal anatomies are typically found. As such, some researchers presented patient-specific models, where the anatomical particularities of each patient are taken into account during the model construction stage. The patient anatomy is extracted from a high-resolution imaging acquisition (e.g., computed tomography – CT), post-processed and then used to create the model (Carton *et al.*, 2011; Rengier *et al.*, 2010; Sodian *et al.*, 2007; Winder and Bibb, 2005). Besides allowing a correct patient-specific anatomy assessment, these personalized models also improve surgical planning strategies and surgical training techniques (Matsumoto *et al.*, 2015; Spottiswoode *et al.*, 2013; Tam *et al.*, 2013). Moreover, these realistic models can be used as a validation scenario (Huang *et al.*, 2009; Jeevan *et al.*, 2014; Linte *et al.*, 2010a).

Specifically for the heart, multiple researchers developed left ventricular models to study the dynamic behavior of this cardiac chamber (Heyde *et al.*, 2012; Lesniak-Plewinska *et al.*, 2010; Vannelli *et al.*, 2015). Initially, simple models (e.g., a cylinder) were used (Olszewski *et al.*, 2012), while recent ones are more realistic and complex (Vannelli *et al.*, 2015). The heartbeat is simulated through water or air pumps (Heyde *et al.*, 2012; Linte *et al.*, 2010a), with functional parameters similar to the expected physiological ones. Recently, some researchers focused on atrial phantom models (Jeevan *et al.*, 2014; Rettmann *et al.*, 2014). These models were mainly used for training and planning of cardiac ablations (Rettmann *et al.*, 2014; Sun *et al.*), presenting the atrial body and the proximal part of the pulmonary veins. Nevertheless, these solutions were either rigid (Rettmann *et al.*, 2014) or not appropriate for ultrasound (US) acquisition (Jeevan *et al.*, 2014), being therefore sub-optimal to simulate minimally invasive cardiac interventions. Furthermore, the thin and complex inter-atrial wall was not correctly modeled (Bourier *et al.*, 2015; Sun *et al.*), hampering the identification of the atrial anatomy. Finally, the accuracy of the manufacturing technique was rarely assessed (*i.e.* the error between the virtually designed model and the physical one).

In this work, we present a strategy to construct a patient-specific phantom model of the cardiac atrial region. This is modeled from a high-resolution CT acquisition and then constructed by a mold-cast approach using a flexible and ultrasound-compatible material. Moreover, a correct representation of the atrial wall is ensured, particularly for the inter-atrial wall, improving the identification of this region and allowing its application as training and validation scenario in several inter-atrial wall interventions, such as transseptal puncture or atrial septal defect closure.

This work is structured as follow. In section 3.2, a description of the strategy applied to construct the patient-specific atrial phantom model is presented. The experimental scenario used to validate the proposed method is described in section 3.3, and the results obtained presented in section 3.4. Section 3.5 discusses the performance of the proposed method. Finally, the conclusions of this work are presented in section 3.6.

## 3.2. Methods

An overview of the proposed technique is presented in Figure 3.1. The patient-specific atrial model is constructed from a 3D CT acquisition of the patient (Figure 3.1a), by manual delineation of the left and right atria (LA, RA) and atrial wall (Figure 3.1b). Multiple 2D slices are manually segmented and then 3D reconstructed (Figure 3.1c). These 3D surfaces are required to generate a mold (as a negative of the target shapes) using a computer-aided design (CAD) software package (Figure 3.1d) and finally physically constructed using a 3D-printer (Figure 3.1e). The final model is composed by inner structures (red molds in Figure 3.1e), which represents the hollow cavities of the atrial bodies, and an external mold (blue mold in Figure 3.1e), with the external shape of the target anatomy. The flexible phantom is finally created through the pouring of a flexible material inside the mold (Figure 3.1f), followed by the elimination of the inner rigid structures (red parts, Figure 3.1g). Each of these steps are described in detail in the following sections. Furthermore, a step-by-step description of the mold construction is presented in Appendix 3.7.A.

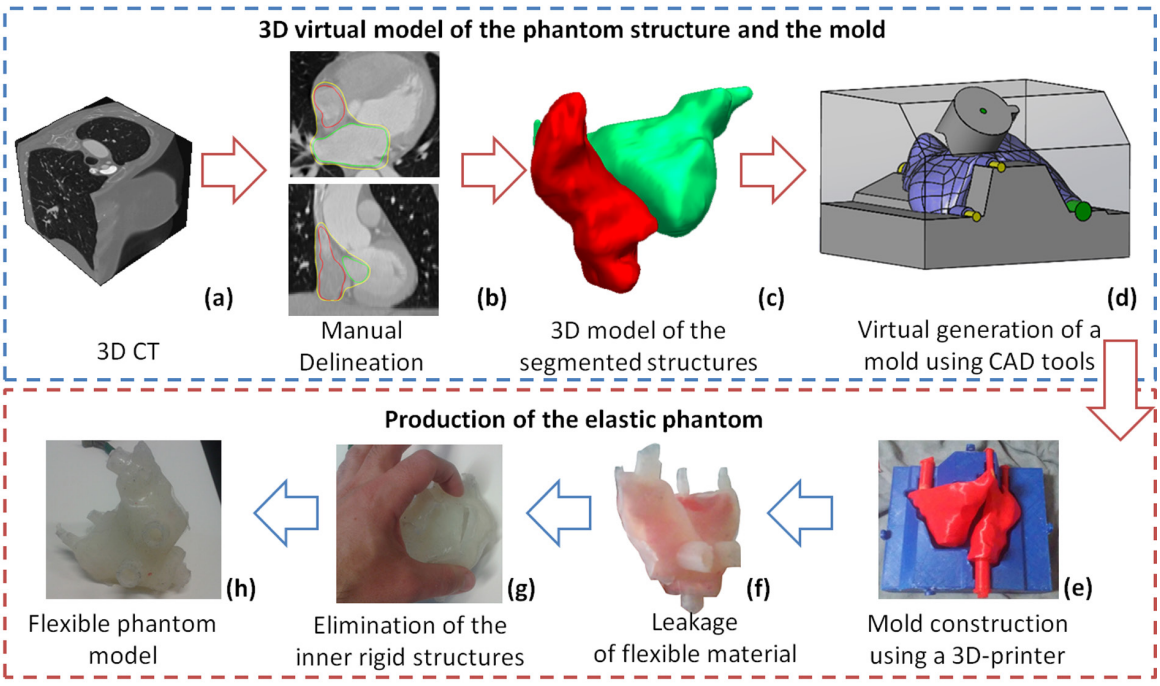


**Figure 3.1 - Overview of the proposed method to construct patient-specific atrial phantom models.**

### 3.2.1. Data acquisition

The 3D CT of the anatomy was acquired with a Sensation 64 (Siemens Medical Solutions, Erlangen, Germany). The acquisition was performed with 64 rows, rotation time 0.36 ms, gantry angle of ± 30 degrees. One hundred and twenty milliliter (ml) of iodinated contrast agent (Omnnipaque 350; GE Healthcare, Waukesha, WI) was injected at 5 ml/s. A matrix size of 512 x 512 x 96 with an isotropic voxel spacing of 0.4 mm and a slice thickness of 1 mm were used. The dataset was reconstructed at the ventricular end-diastole phase, with a convolution kernel B20f. The patient was enrolled in this study with indications for left atrial pathology, but with normal anatomy. Because of the retrospective nature of this study, no written informed consent was obtained from the patient.

### 3.2.2. Manual delineation

The manual delineation was initially performed for the atrial cavities, followed by the atrial outer wall. No pre-processing stage was used, using directly the real information of the image. All delineations were performed by one experienced observer using the Medical Imaging Interactive Toolkit (MITK) (Wolf *et al.*, 2005) software and its specific interactive segmentation menu. Specifically, a few 2D slices were manually segmented and then used as anchors points to reconstruct the final 3D surface. The reconstructed surface was assessed and extra corrections were performed if needed.

The LA and RA contours relied on the atrial body region, with both left and right atrial appendage being excluded (Figure 3.2). Moreover, only the proximal parts of the pulmonary veins (PV) and the vena cava (VC) were included. The mitral (MV) and tricuspid valves (TV) regions were identified by a plane. This plane was used to separate the target atrial region from

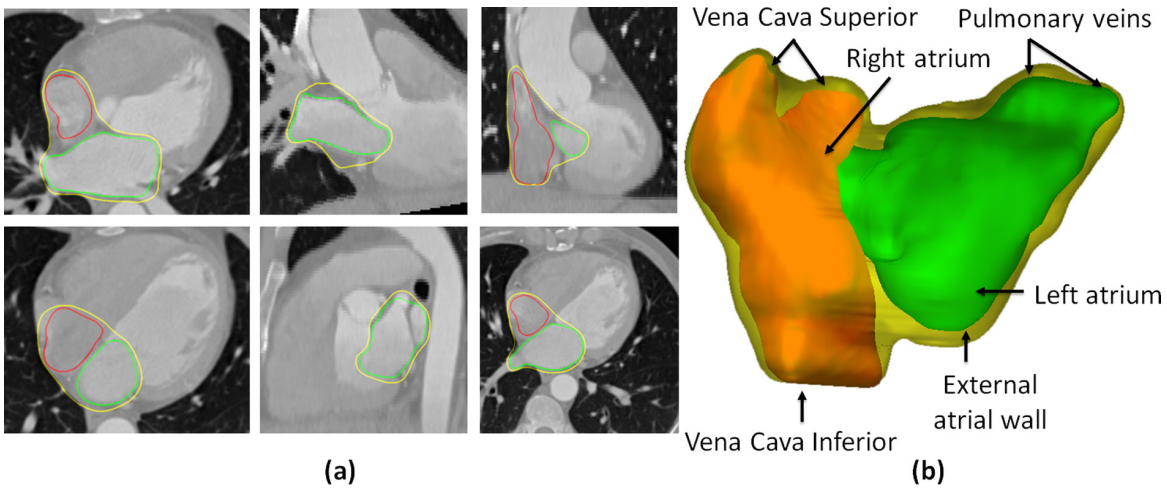


**Figure 3.2 - Manual delineation strategy.**
a) Multiple 2D slices; and b) 3D representation of the atrial shape. Yellow – External atrial wall, Green – Left Atrium, Red – Right Atrium.

the ventricular cavities. Multiple access points were defined for each atrium, namely: two for the PV, two for the VC (*i.e.* inferior and superior) and one for each ventricle. The size and orientation of each access point were defined with a specific contouring label. Since the current phantom model is intended to be used for surgical planning/training, realistic access points (*i.e.* similar used for planning/training multiple surgeries to the real input and output orifices of the human atria) are required.

The external atrial wall was defined using the aforementioned LA and RA regions as references. Indeed, it was initially defined as a dilated version of the LA and RA with a constant thickness (approximately 3 mm). Then, multiple refinements were manually performed to guarantee maximum adaptation between the contour and the anatomy. It should be noted that intermediate atrial regions (*i.e.* inter-atrial septal wall) were merged. Moreover, free wall regions (e.g., mitral valve and tricuspid valve regions) were not refined and the constant thickness was kept.

### 3.2.3. Virtual modeling of the phantom mold

To manufacture the segmented anatomy, a cast-mold strategy is used (Figure 3.3). The entire design was performed on a CAD software package (SolidWorks, Dassault Systèmes S.A, Vélizy-Villacoublay, France) using multiple solids of the obtained segmentations (*i.e.* LA, RA and external atrial wall). The abovementioned solids were generated using GeoMagic (3D Systems, South Carolina), obtaining, as output, a compact representation of each contour (*i.e.* the contour and its inner region are a unique solid without hollow regions).

Specifically, the patient-specific mold is designed through a two-steps strategy, namely:

1) generation of the cardiac wall solid (see Figure 3.3a), through the intersection between the external atrial wall and the negative of both LA and RA solids. Since the external atrial wall solid is a compact component that includes both LA and RA solids and with an outer surface shape described as the external atrial anatomy (manually delineated in section 3.2.2), its intersection with the atrial bodies results in a new solid (*i.e.* cardiac wall solid) with hollow cavities (see Figure 3.3a), that represents the desired phantom anatomy.
2) design of the target mold as the negative of the cardiac wall solid generated in step (1). Due to the complexity of the atrial anatomy, three external (gray molds in Figure 3.3b) and two internal molds (yellow and green mold in Figure 3.3b) are required. The external molds are the negative of the atrial wall, and the internal molds are the LA and RA solids themselves (see Figure 3.3b). Multiple external molds are needed

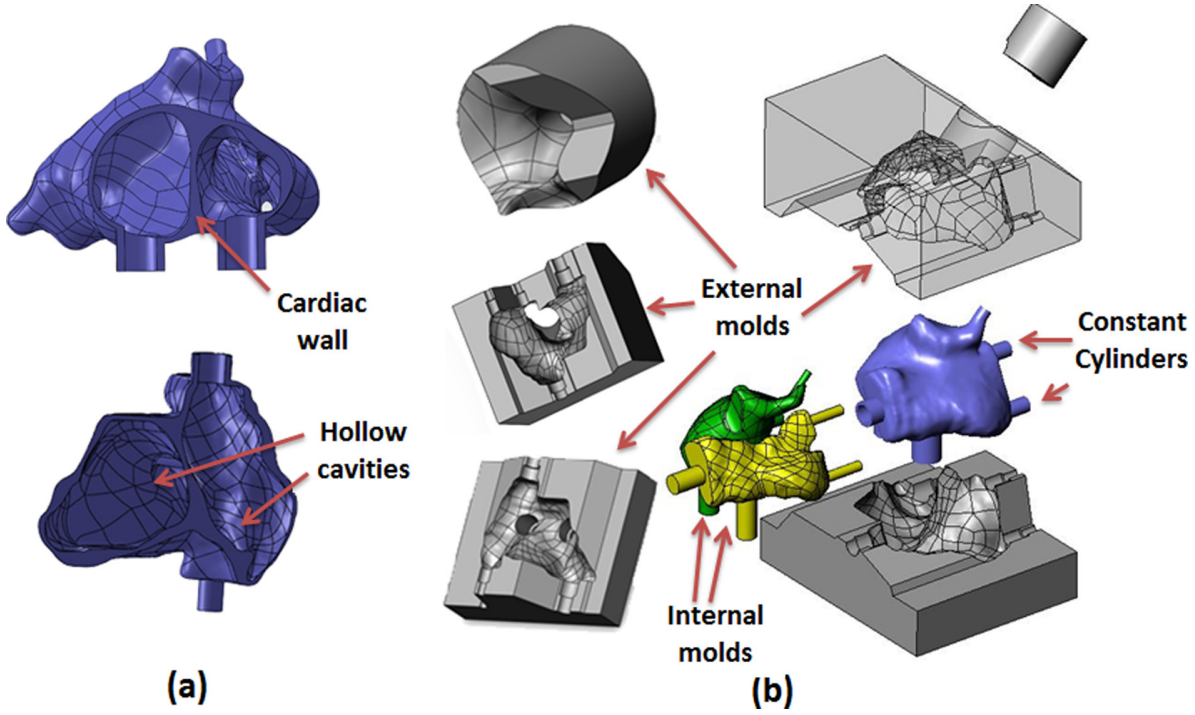


**Figure 3.3 - Technique used to create the phantom mold.**
(a) Three different solids (LA, RA and external atrial wall) are combined. (b) Using the combined solid, internal and external molds representing the negative of their shape were designed.

to allow correct positioning of the internal parts, reduce manufacturing costs and consequently allow multiple usages of the same mold. As a result, after final mold construction through the combination of the different external and internal parts, a compact structure with a small cavity (*i.e.* empty space) is obtained. A schematic (with dimensions) of the phantom wall is presented in Appendix 3.7.B.

Regarding the different access points (*i.e.* PV, VC, MV and TV), these are designed and constructed as constant cylinders with specific diameter and thickness (Figure 3.3b and dimensions in Appendix 3.7.B). The cylinder orientation and positions are defined based on the user labeling done in section 3.2.2. Moreover, these cylinders are detachable to allow the pouring of material through multiple mold orifices, while guaranteeing the correct position of the inner molds relatively to the external mold. As a final remark, the authors would like to emphasize that these 'adapted' orifices can be used to develop a dynamic phantom by connecting hydraulic tubes to these cylinders, simulating therefore the blood circulation into de atria (see one schematic of the dynamic phantom model in Appendix 3.7.C).

### 3.2.4. Construction of the phantom mold using a 3D printer

The designed molds are converted into G-code format using the Cura software (Ultimaker, Geldermalsen, Netherlands) and 3D-printed using an Ultimaker II (Ultimaker,

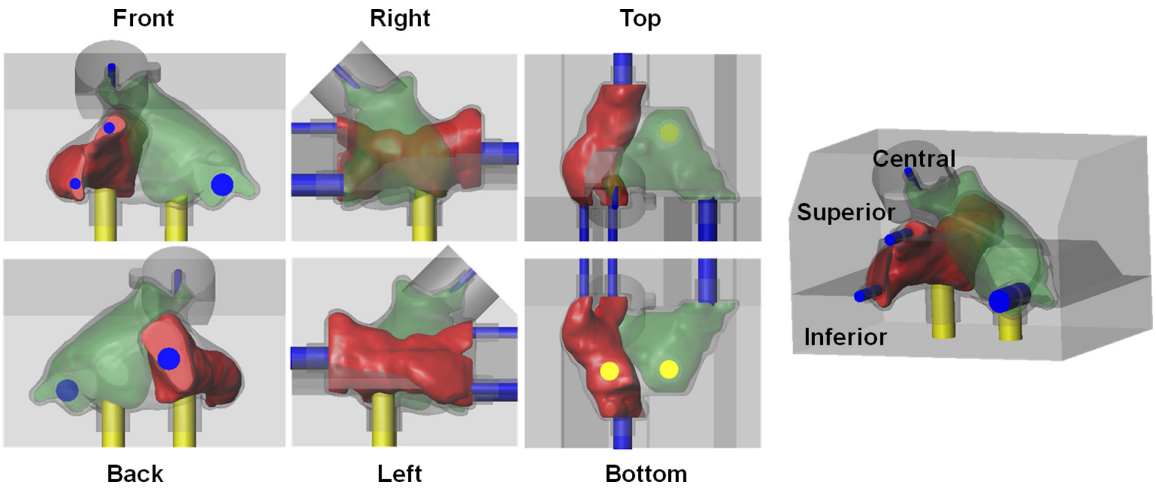


**Figure 3.4 - Illustration of the assembled 3D printed-molds.**
Red and green structures are the inner molds of the right atrium and left atrium, respectively. Blue and yellow cylinders are the support structures to the pulmonary veins/vena cava and ventricles, respectively. The external mold (gray mold) is composed of three independent components, *i.e.* the inferior, superior and central.

Netherlands). Polylactic acid (PLA) was used (filament of 2.85 mm, Ultimaker, Geldermalsen, Netherlands). The following parameters were applied during the 3D-printing: speed of 60%, nozzle temperature of 225 °C, build-plate temperature of 60 °C, material flow at 100% and fan speed at 50%. An in-plane resolution (X-Y) of 0.25 mm with a layer height of 0.06 mm (resolution in Z) was used.

The printed mold is assembled as illustrated in Figure 3.4. We start by connecting the multiple cylinders (yellow for the ventricle region, and blue for the PV and VC) with the inner mold of the RA (green structure) and LA (red structure). Then, the obtained component (LA/RA plus cylinders) is positioned on the inferior part of the external mold (see gray mold in Figure 3.4). Note that, the yellow and blue cylinders provide support and guarantee correct positioning of the inner molds. Finally, the mold is closed with the superior and central part of the external mold. As abovementioned, to pour the flexible material, each cylinder is detached (one at a time) and used as an access point.

### 3.2.5. Fexible materials

Two different materials were used to produce the flexible phantom, namely: silicone and polyvinyl alcohol cryogel (PVA - C, Figure 3.5).

The silicone is an additive HB FLEX 5513 A+B transparent (HBQuimica, Porto, Portugal). It presents a Young's modulus of approximately 720 kPa, linear contraction <0.05% and stretching until breaking of 450 %. The flexible material was prepared by mixing 75 g of both part A and B. Then, the material was poured into the mold. After 24 hours, the external

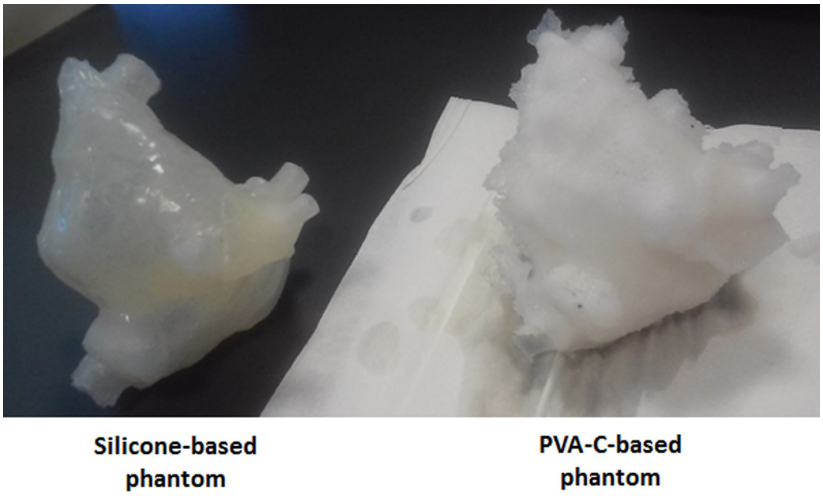


**Figure 3.5 - Final silicone-based and PVA-C-based phantoms.**

molds were removed. Regarding the internal molds, one small incision was done to remove them, followed by the addition of silicone on the small incision region to close it.

The PVA relies on Mowiol 10-98 (Kuraray Europe GmbH, Hattersheim am Maim, Germany) with a molecular weight of 61,000 $u$, 98-98.8 mol% hydrolysis, ~14000 polymerization, 1.1-1.9% of impurities, viscosity of 9-11mPa.s, 4% in H20 (20 °C) and ester number of 15-25. Initially, the PVA powder was milled and mixed with water (temperature 80 °C, during 2 hours), creating a viscous solution. This solution was subsequently poured into the mold. Then, two thaw-freeze cycles were performed, resulting in a compact and flexible wall with a Young's Modulus of near 110 kPa and Poisson's ratio of 0.45 (Fromageau *et al.*, 2007; Leśniak-Plewińska *et al.*). Each cycle consisted of 12-h freezing period in a freezer at -20 °C, followed by a 24h thawing period. At the end of the freezing stage, the freezer was turned off and the temperature slowly increased until the environment temperature. Finally, after 3 days, the external mold was removed and two incisions were made to remove the internal molds. The viscous material was used to cover the incision site, and a third freeze/thaw cycle (12 hours freezing and 24 hours thawing) was performed.

## 3.3. Experiments

Two experiments were performed to validate the proposed phantom model, namely: (i) evaluation of the accuracy of the proposed phantom production technique and (ii) qualitative and quantitative assessment of the resulting ultrasound image of each phantom model.

### 3.3.1. Accuracy of the proposed production technique

After phantom production, we assessed the accuracy of the proposed production technique through the comparison between the resulting phantom models and the original

virtual design (henceforward referred as ideal model). In this sense, a high-resolution CT image was acquired for each constructed model (*i.e.* PVA-C and silicone), using a Somatom Force CT (Siemens Medical Solutions, Erlangen, Germany). A total of 2 x 192 rows, with a collimator width of 0.6 mm, a rotation time of 250 ms and a convolution kernel Ur73u was used. Furthermore, a matrix size of 512 x 512 x 437 with an isotropic pixel spacing of 0.35 mm and a slice thickness of 0.3 mm was used.

The obtained images were manually delineated using MITK. A threshold-based strategy followed by manual corrections was applied to generate the 3D surfaces of the LA and RA bodies and cardiac wall (Figure 3.6). To compare the post-production meshes with the pre-production one (*i.e.* ideal model), a surface-to-surface alignment using the iterative closest point algorithm (ICP) (Besl and McKay, 1992) was applied. Specifically, a set of landmarks were manually selected in each model (see Figure 3.6b), allowing to initially align both models with a similar orientation and position, which was subsequently refined using a rigid ICP strategy. An overview of the selected landmarks is presented in Figure 3.6b, in which we can observe that the model's extremities were used to obtain a robust initialization. The initial transformation was computed through a least square solution between the reference (pre-production model) and target (post-production model) landmarks. The optimal rigid transformation (initialization plus ICP) was finally applied to each surface (*i.e.* LA, RA and cardiac wall), consequently aligning the pre- and post-production models.

The differences between pre- and post-production surfaces (*i.e.* LA, RA and cardiac wall) were assessed through three metrics, namely absolute point-to-surface (P2S) distance,

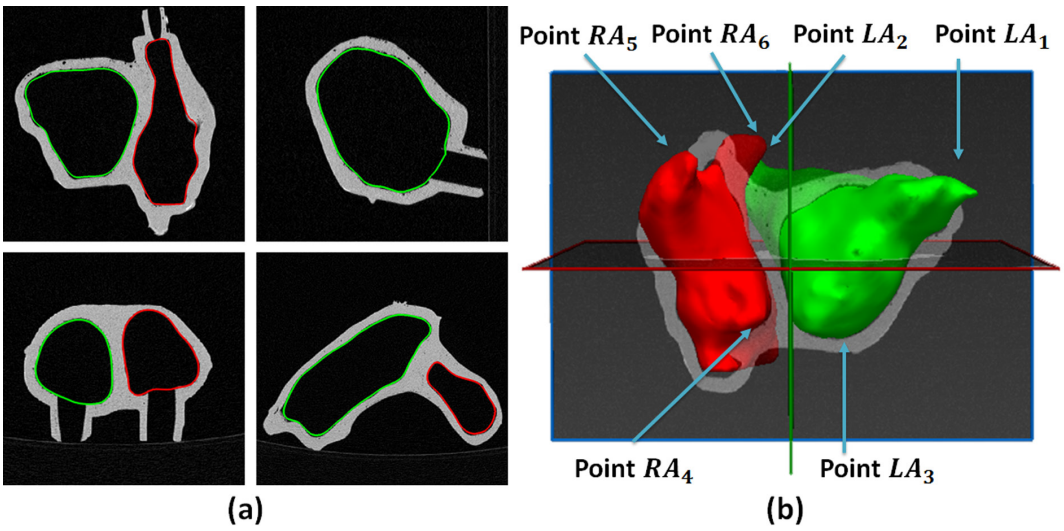


**Figure 3.6 – Post-production evaluation strategy.**
(a) CT image with manual delineated contours. (b) 3D surface of the left and right atrium and representation of the manual landmarks required to perform the surface alignment. Green – Left atrium, Red – Right atrium.

Dice and 95$^{th}$ percentile of the Hausdorff distance. The volume of each chamber was also computed and compared. Furthermore, we evaluated the accuracy of the method for thin walls (in this specific case, the inter-atrial septal wall). In this sense, a small region of interest (ROI) was created around the thin wall region. This ROI was defined as the largest connected region with a thickness lower than 5 mm. The abovementioned threshold (*i.e.* 5 mm) was selected based on the expected thickness of the thinner region, as previously described in literature (Reig *et al.*, 1997).

### 3.3.2. Qualitative and quantitative evaluation of the phantom model in ultrasound imaging

Both phantom models (*i.e.* silicone or PVA-C) were submerged in a large water tank (water at room temperature and tank dimension of 45.5x35x25 cm$^3$) and the resulting ultrasound images were evaluated. The acquisition was performed with a transesophageal echocardiography (TEE) ultrasound probe (Vivid E9 Breakthrough 2012, General Electrics, Connecticut, USA) connected to a 4D ultrasound system (Vivid E9, General Electrics, Connecticut, USA). The maximum image depth was 18 mm and the image resolution was 0.07x0.07x1 mm$^3$. The frequency of the transducer was set to 4 MHz. The differences in terms of image appearance were visually evaluated by one observer.

Next, to compare the resulting ultrasound images of each phantom model with the ideal reference, we applied a strategy similar to section 3.3.1. In detail, we started by manually segmenting the LA and RA in each US image (for each model), identifying subsequently multiple landmarks to initialize the alignment strategy (see Figure 3.6b). A final refinement through a rigid ICP was applied to improve the alignment of both US and reference surfaces. Finally, the differences between each surface were quantitatively assessed using the absolute P2S, Dice and 95$^{th}$ of the Hausdorff distance. Moreover, the volume of each surface extracted from the US was computed and compared with the ideal value.

## 3.4. Results

Table 3.1 shows the shape differences between the final post-production silicone-based and PVA-C-based phantom models (through a CT acquisition) when compared with the ideal model. The errors' spatial distribution is presented in Figure 3.7, presenting the high accuracy of the production technique for the real atrial body. A superior performance was found for the silicone-based phantom. Moreover, Figure 3.8 shows the errors' spatial distribution for the thin-

**Table 3.1 - Assessment of the proposed production technique.**
The evaluation was performed in terms of volume (ml), point-to-surface error (P2S, mm), Dice (%) and 95$^{th}$ percentile of the Hausdorff distance (mm). The study is performed independently for the left atrium (LA), right atrium (RA), cardiac wall and thin walls

| Structure | Model | Volume (ml) | P2S (mm) | Dice (%) | 95$^{th}$ perc. Hausdorff (mm) |
|---|---|---|---|---|---|
| **LA** | Silicone | 71.89 | 1.68±0.79 | 88.50 | 2.97 |
| | PVA-C | 71.39 | 1.70±1.34 | 87.85 | 4.41 |
| | Virtual model | 77.83 | - | - | - |
| **RA** | Silicone | 43.50 | 1.36±0.94 | 86.50 | 3.35 |
| | PVA-C | 41.20 | 1.32±1.11 | 88.21 | 3.56 |
| | Virtual model | 49.51 | - | - | - |
| **Cardiac wall** | Silicone | - | 1.59±1.20 | - | 4.20 |
| | PVA-C | - | 1.90±1.60 | - | 5.25 |
| **Thin walls** | Silicone | - | 1.45±0.77 | - | 2.85 |
| | PVA-C | - | 1.53±1.18 | - | 4.00 |

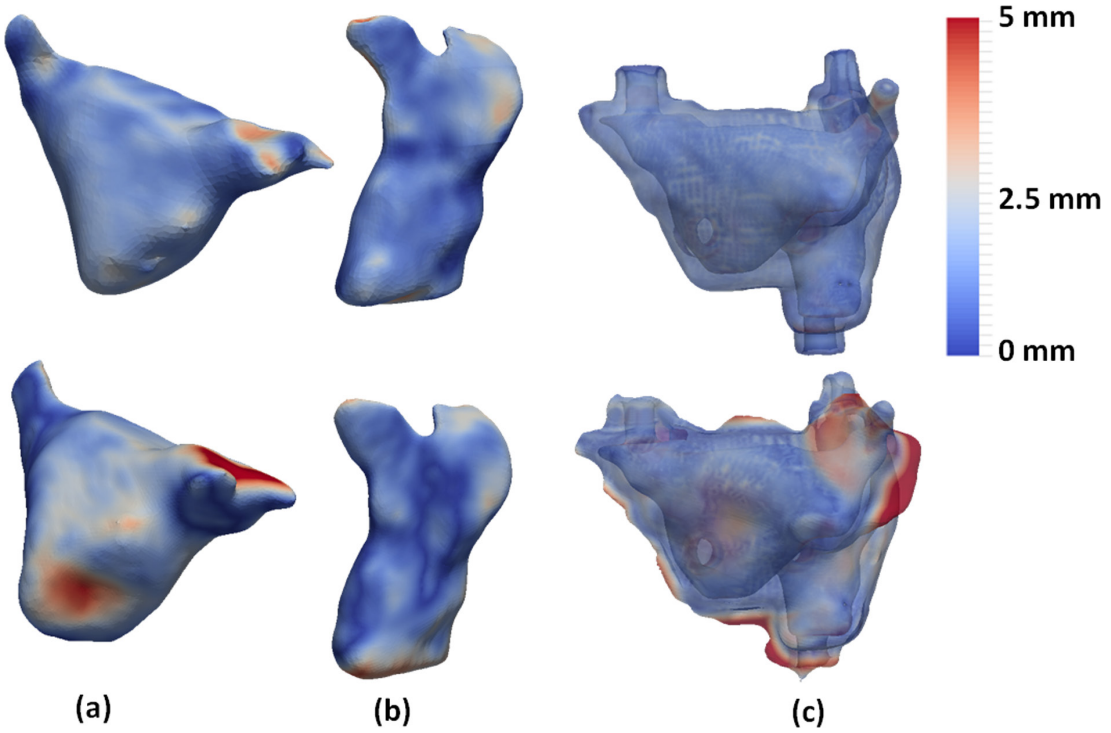


**Figure 3.7 - Accuracy of the proposed production technique.**
(a) Left atrium, (b) right atrium, (c) cardiac wall. First row represents the silicone-based phantom, with the second row being the PVA-C-based phantom.

wall, *i.e.* the inter-atrial septal wall, with both models showing high accuracy with a mean error around 1.5 mm and a maximum error of 2.8 mm.

Figure 3.9 presents the ultrasound image appearance of each phantom model. Both chambers (LA, RA) and inter-atrial wall are easily visible. Furthermore, the final 3D shape observed in US was visually compared with the ideal model (Figure 3.10), showing a high similarity. Table 3.2 quantitatively compares the data extracted from the resulting US image and the ideal model, showing a moderate accuracy of the proposed method.

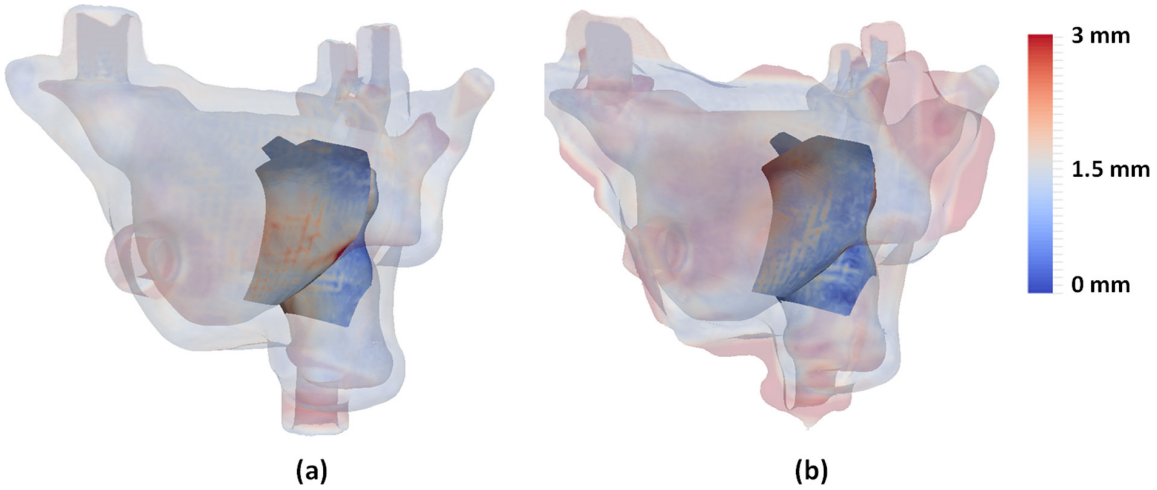


**Figure 3.8 - Accuracy of the proposed production technique for thin walls.**
(a) Silicone-based and (b) PVA-C-based phantoms.

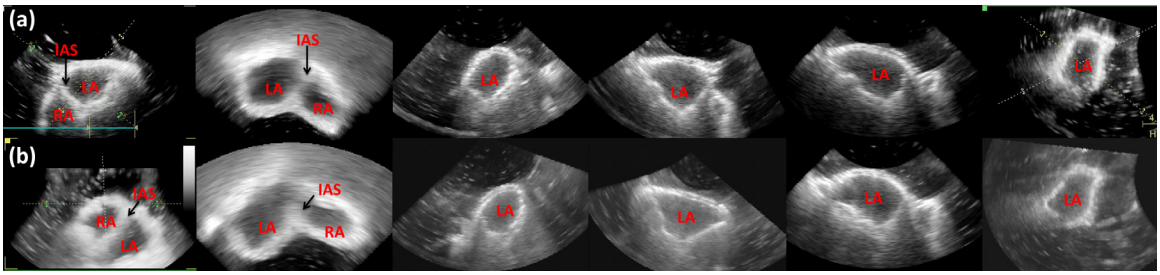


**Figure 3.9 - Resulting ultrasound image for (a) silicone-based and (b) PVA-C-based phantom.**
LA- Left atrium, RA – Right Atrium, IAS – Inter-atrial septal wall.

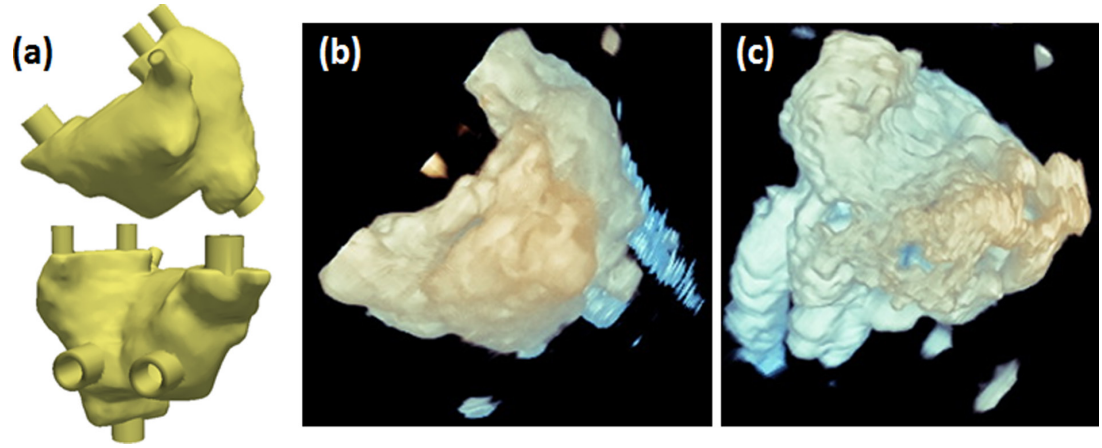


**Figure 3.10 - 3D visualization of the proposed phantom model in 3D US images.**
(a) Ideal model, b) Silicone-based and (c) PVA-C-based phantom model.

## 3.5. Discussion

In the current study, we present and assess the accuracy of a phantom production technique. The proposed strategy generates realistic and patient-specific models using as a reference a high-resolution medical acquisition based on CT. Besides the accurate representation of the atrial anatomy (*i.e.* LA and RA), a correct modeling of the inter-atrial wall

**Table 3.2 - Comparison of the atrial surfaces extracted from ultrasound images and the ideal models.** The comparison was performed in terms of volume (ml), point-to-surface error (P2S, mm), Dice (%) and 95$^{th}$ percentile of the Hausdorff distance (mm)

| Structure | Model | Volume (ml) | P2S (mm) | Dice (%) | 95$^{th}$ perc. Hausdorff (mm) |
|---|---|---|---|---|---|
| **LA** | Silicone | 68.26 | 2.77±2.10 | 83.74 | 6.51 |
| | PVA-C | 67.89 | 2.91±2.36 | 82.15 | 7.43 |
| | Virtual model | 77.83 | - | - | - |
| **RA** | Silicone | 40.43 | 2.49±2.20 | 81.77 | 6.34 |
| | PVA-C | 40.97 | 2.54±2.39 | 81.20 | 6.57 |
| | Virtual model | 49.51 | - | - | - |

was also pursued, improving the realism of the proposed model. Indeed, particular attention was given to the design of the inter-atrial wall, consequently showing the particular interest of this phantom for simulation of atrial wall interventions, specifically transseptal puncture (Morais *et al.*, 2017b) and atrial septal defect closure (Faletra *et al.*, 2014b). To the author's best knowledge, no patient-specific phantom model with correct representation of the mid atrial wall was previously presented, being a clear novelty of this work.

Regarding the phantom construction, it relies on four main stages: 1) accurate anatomical model generation using pre-procedural image acquisition, 2) virtual and 3) physical construction of the phantom mold and 4) pouring of the flexible and ultrasound-compatible material inside the mold. The first stage is applied to obtain an accurate representation of the patient anatomical details with a particular interest in the design of the atrial boundaries at the inter-atrial septum region. Previous works have used a similar approach to generate the phantom model for catheter ablation simulation (Laing *et al.*, 2017; Rettmann *et al.*, 2014; Sun *et al.*). Nevertheless, they failed to correctly generate the entire inter-septal wall (Rettmann *et al.*, 2014; Sun *et al.*). Secondly (*i.e.* stage 2), the atrial and wall surfaces are exported into a CAD tool, virtually generating a mold that represents the target anatomy. Due to software (CAD) limitations with extreme irregular shapes, smoothed atrial surfaces were used (obtained through MITK), decimating the detailed mesh and making it suitable for the CAD software. Although this smoothing process slightly modifies the patient's anatomy, it only represents a mean error of approximately 0.3 mm. Note that this error is lower than the CT voxel size (0.4 mm), which ultimately limits the resolution of the construction process, or even the errors caused by the remaining stages of the production technique. During the remaining phantom construction stages (stage 3 and 4), rigid and outer molds are constructed using recent 3D-printer technology (stage 3) and the atrial anatomy generated by leaking flexible material inside the mold (stage

4). Although such strategy allows a fast and accurate generation of complex anatomies, in particular of the inter-atrial walls, the usage of rigid inner molds hampers the inclusion of the atrial appendages and the pulmonary veins. However, and although direct 3D-printing of the phantom walls (instead of a mold approach) could be an interesting solution to mimic the complex atrial shape, ultrasound-compatible 3D printing flexible materials are not available, hampering its application for the simulation of the real intervention (Laing *et al.*, 2017). Notwithstanding, the proposed phantom construction through rigid inner molds is a sub-optimal approach, namely due to the latter incision done on the final phantom model. Indeed, in order to improve the extraction stage, a 3D printing material with a dissolvable support solution or even a highly flexible inner mold (which could be extracted by the virtually generated entry points) could be interesting solutions. Nevertheless, further studies are required to prove the real advantages of any of these techniques.

In order to evaluate the accuracy of the described phantom production technique, we start by comparing a post-production CT acquisition of each model with the ideal reference. Both models showed high accuracy (P2S always lower than 2 mm), being the errors found explained by several intrinsic limitations of the proposed technique, such as: material tolerance during 3D printing of the mold; flexible material retraction after cooling; reagent addition process; small errors linked to the delineation and errors caused by sub-optimal surface alignment through ICP. When comparing both models, a superior performance was found for the silicone-based phantom, which is clearly supported by the different metrics assessed in Table 3.1 and through the errors' spatial map (Figure 3.7). The low performance found for the PVA-C-based phantom is related with the low viscosity of the material, which hampers the material pouring and the incision closing stage. Furthermore, and contrary to the silicone-based phantom, the PVA-C-one required storage in a controlled environment (*i.e.* water tank with water at a specific temperature) and an inherent small shrinking of the material throughout the time was observed, which again can explain the lower accuracy of this model.

Due to the particular interest on the inter-atrial wall, we also assessed the technique accuracy at this specific region (Figure 3.8). Again, a mean error of approximately 1.5 mm was obtained for the silicone and PVA-C-based phantom at the selected ROI, corroborating their accuracy and applicability for the simulation/training of the aforementioned interventions. Interestingly, it is possible to observe that the lower errors (Figure 3.8) were found at the central position of the selected region, being the highest errors detected on the limits of the ROI. This result is explained by the anatomy of the inter-atrial wall, being thin and straight at the central part and presenting a more complex shape in the peripheries (Anderson *et al.*, 1999; Reig *et al.*,

1997). Thus, the proposed construction technique was able to accurately generate the straight inter-atrial wall, presenting a sub-optimal performance on the remaining regions. Nevertheless, the authors would like to emphasize that the majority of the inter-atrial interventions focus on the straight inter-atrial wall (e.g. transseptal puncture) (Morais *et al.*, 2017b).

To evaluate the adequacy of the proposed phantom model for atrial interventions, we also assessed the resulting model appearance on a traditional intra-procedural image modality, namely ultrasound. The acquired ultrasound images (Figure 3.9) proved that the different cardiac chambers (*i.e.* LA and RA) can be easily observed and identified in both phantom models (*i.e.* silicone-based and PVA-C-based). Similar to the expected and observed in normal clinical practice, a double chamber view was easily obtained for both models. A 3D analysis of the obtained ultrasound model (Figure 3.10) showed a high similarity when compared with the pre-production one. Moreover, a clear definition/identification of the inter-atrial septal wall was also achieved, reinforcing the appropriateness of this phantom model for inter-atrial wall interventions. Although gelatin-based phantom models have been widely described for different scenarios (Gerstenmaier *et al.*, 2013; Richardson *et al.*, 2015), its application for this specific model was not possible due to its mechanical properties (high viscoelasticity and low stiffness).

Similar to the post-processing evaluation experiment (section 3.3.1), a comparison between the data extracted from the US and the ideal model was also performed. Globally, the results (Table 3.2) confirmed a moderate accuracy of the different phantom models, presenting errors lower than 3 mm for both chambers. A slightly superior performance of the silicone-based model was found when compared with the PVA-C model, which is explained by the more detailed walls observed (not so smooth as observed in PVA-C models, Figure 3.9) and also its superior accuracy throughout the phantom construction stage. Although higher errors were found in this experiment (Table 3.2) when compared with experiment 1 (CT acquisition versus ideal model, Table 3.1), it can be easily explained by the difficulties to visualize the boundary positions in US images, image artifacts caused by the water tank walls, the difficulties to detect limits of the generated orifices and the low field of view of the TEE probe (which hamper the identification of the phantom's extreme positions) (Haak *et al.*, 2015; Housden *et al.*, 2013b; Noble and Boukerroui, 2006). In addition and as discussed in other studies (Huang and Zeng, 2017; Noble and Boukerroui, 2006), manual segmentation of US images is more prone to errors and harder to be performed than in CT, justifying again the higher errors found in Table 3.2.

To increase the realism of the current ultrasound image, graphite particles or glycerin should be combined with the flexible material, as suggested in previous studies (Heyde *et al.*, 2012). Such particles will generate speckle noise in the resulting ultrasound image, making the

cardiac wall heterogeneous (*i.e.* multiple intensity values in the ultrasound image) and thus obtaining more realistic, non-saturated walls. Furthermore, although PVA-C is typically described as one of the most realistic materials for ultrasound-based phantom model construction (Ceh *et al.*, 2015), superior performance was not visually found in this study. Thus, further analysis will be required to assess the real performance of each material.

Regarding the mechanical properties, both materials presented a Young modulus higher (720 kPa for the silicone and 110 kPa for the PVA-C) than the expected for the real tissue. Previous studies reported that the Young modulus of the entire atrial wall varies between 20–70 kPa, being not uniform along the entire wall (Howard *et al.*, 2015; Hunter *et al.*, 2012). Specifically for the thin wall region, a value around of 30 kPa is expected (Howard *et al.*, 2015). In this sense, the developed phantom models are stiffer than in reality and assume a homogeneous elasticity throughout the entire model, consequently presenting a sub-optimal performance to mimic the real deformations of the atrial walls. In other words, when puncturing the atrial wall, a higher force (when compared with the real situation) would need to be applied on the needle to create an access route between the two cavities. Nevertheless, similar limitations can be found for previous phantom models (Cygan *et al.*, 2014; Lesniak-Plewinska *et al.*, 2010; Rettmann *et al.*, 2014; Stevanella *et al.*, 2011), due to difficulties to correctly replicate the complex and heterogeneous structure of the cardiac muscle.

Overall, the current phantom models proved their added-value for simulation of inter-atrial interventions. They overcome the previously described rigid or ultrasound non-compatible models, allowing the simulation of all procedural stages. Interestingly, since a clear visualization of both atrial chambers was obtained with CT and US images, the current dual-chamber model also showed potential for its application as a development or validation scenario of novel image fusion strategies. Inspired by a similar goal, Laing *et al.* (2017) presented a flexible phantom model for transseptal puncture simulation. The model also uses realistic atrial models extracted from a CT, showing a high production accuracy when comparing a post-production CT acquisition with the real model. A correct representation of the fossa ovalis (optimal location of the transseptal puncture) is ensured through a post-processing of the obtained atrial surfaces. Nevertheless, a detailed description of the phantom construction strategy is missing. Furthermore, other limitations include: correct modeling of the mid thin atrial walls (except the fossa ovalis region) is not described and not validated; constant outer atrial walls are used; phantom model evaluation through intra-procedural data (*i.e.* ultrasound) is not presented. Finally, their production technique is more time consuming than the current one, taking more than 2 weeks (Laing *et al.*, 2017) against the 3 days required by the proposed

silicone-based phantom (1 week for the PVA-C model), which shows the attractiveness of the proposed method for a routine clinical practice use (Laing *et al.*, 2017). As a final remark, it should be noticed that the construction time of the proposed phantom can be notably reduced through the application of an automatic segmentation strategy focused on both atrial models and its mid-walls (see Chapter 5).

As future work, an exhaustive study about the optimal phantom material will be performed, identifying the compound that correctly mimics the real atrial tissue (*i.e.* similar mechanical properties, similar acoustic properties, among others). Furthermore, we intend to construct the proposed dynamic phantom model (Appendix 3.7.C) and apply it for the simulation of specific inter-atrial interventions. By applying it in a real scenario, we expect to receive a correct and realistic clinical feedback of the proposed model, ultimately validating the proposed phantom for accurate simulation of such interventions.

## 3.6. Conclusions

The proposed production technique showed high accuracy for the generation of patient-specific atrial phantom models with flexible and realistic walls. The current method overcomes some limitations of the state-of-the-art models (*i.e.* the majority are rigid and not personalized to the patient anatomy), allowing its use for intervention planning and training. Phantom production with silicone proved to be more accurate due to its simple manipulation, high viscosity, and a simple construction technique.

Both phantom models proved to be suitable for interventional planning and training based on ultrasound guidance, being both chambers and inter-atrial wall easily identified. Moreover, a realistic anatomy of the entire atrial region was obtained in these two cases.

Overall, due to the simple manipulation and superior accuracy during model construction, the silicone-based phantom appears to be more feasible for the construction of complex anatomies such as the atrial region.

## 3.7. Appendixes

### Appendix A – Mold construction: step-by-step

This appendix describes, in detail, the proposed phantom construction strategy (step-by-step). The description is divided into multiple sub-sections (as explained in section 3.2), namely: 1) Manual Delineation; 2) Virtual Modeling of the Phantom model and 3) Construction of the phantom model using a 3D printer.

**Manual delineation**

1 – Open the DICOM file in MITK software (version 2016.3.0), using "DICOM" menu.

2 – Initialize the segmentation menu clicking on "Segmentation".

2.1. – Initialize a specific label (e.g. LA for left atrium) using the button "New".

2.2 – Delineate multiple 2D slices of the target anatomy using the option "Add". A particular attention with the atrial wall is required.

2.3 – Reconstruct the 3D surface using the "Interpolation" option in "Segmentation" menu.

2.4 – Check the final surface and perform extra 2D delineations if needed.

2.5 – Save the final 3D surface in a .stl (StereoLithography) file using "Save" menu.

3 – Repeat stage 2 for the other chamber (*i.e.* RA) and also for the different access points (PV, VC, MV and TV).

4 – In order to delineate the external atrial wall, the user should select the following steps:

4.1. – Generate a binary mask of the LA and RA surfaces using the option "Surface to Image" ("Segmentation Utilities" Menu).

4.2. – Perform the union between both regions (from stage 4.1) using "Boolean Operations" from "Segmentation Utilities" (select the option "Union").

4.3 – Dilate the resulting mask from step 4.2 with a ball (diameter of 3 mm) using the "Morphological Operations" from "Segmentation Utilities".

4.4 – Refine the mask obtained in step 4.3 using the "Segmentation Menu". Both options "Add", "Subtract" and "Corrections" will be required.

4.5 – Reconstruct the 3D and perform extra modifications if needed.

4.6 – Save the final 3D surface in a .stl file.

**Virtual modeling of the phantom mold – Stage 1**

6 – Open each .stl file in GeoMagic 2012 (e.g. LA). Each .stl file with the 3D surface of the anatomy is converted independently.

6.1 – Transform the imported file in a solid clicking on "Exact Surfaces", "Exact Surfacing" and then "AutoSurface". Organic configuration should be selected as "Geometry Type".

6.2 – Save each file in .step-AP203 format.

7 – Repeat stage 6 for each surface (*i.e.* LA, RA, PV, MV, TV, VC).

**Virtual modeling of the phantom mold – Stage 2**

8 – Generate the virtual cylinders for the PV, MV, TV and VC, opening each model in SolidWorks 2014 as independent parts (simply drag the .step file inside the SolidWorks).

8.1 – For each part, define a plane oriented with the target anatomy. The plane normal should be aligned with the major axis of the target structure.

8.2 – Apply the "Boss Extrude" function, in order to generate a 3D cylinder that represents the entire segmented region.

8.3 – Adapt the cylinder size following Appendix 3.7B.

9 – Repeat step 8 for each access point.

10 – Generate the external mold.

10.1 – Design a sketch of a rectangle.

10.2 – Apply the "Extrude" function to generate a 3D model. The current 3D box should bigger than the target anatomy (see Appendix 3.7B).

11 - Start the "Assembly" environment in SolidWorks, and introduce all the generated solids.

12 – Intersect the negative of the LA and RA solids with the external atrial wall solid, creating the cardiac wall solid (see Figure 3.3). Apply the "Cavity" function (you can find this option in "Insert" menu and then "Features"), setting the external atrial wall component as the main part.

13– Include the multiple cylinders in the cardiac wall solid. Similarly to step 12, intersect the cardiac wall anatomy with the negative of the multiple cylinders using the "Cavity" option.

14 – Intersect the negative of the cardiac wall solid (obtained in 13) with the external mold. Again, apply the "Cavity" function, setting the external mold solid as the main part. As a result, three solids are obtained, represented as the gray mold seen in Figure 3.3. Moreover, the inner molds (yellow and green mold in Figure 3.3) are also obtained.

15 - Adapt the external mold to reduce its dimension, using "Cut Extrude" functions.

16 – Save the multiple molds (three external parts and two internal parts) in independent .stl files. Click on "File", "Save As" and "select" .stl as output type.

**Construction of the phantom model using a 3D printer – Stage 1**

17 – Drag the .stl file inside the Cura software version 2.4.0 (e.g. LA inner mold). Note that, each mold parts is converted independently.

17.1 – Select "High quality" profile.

17.2 – Put the model in the middle of the Ultimaker table, using the "Move" option.

17.3 – Select the "Rotate" option, and align the flat region of the model with the top of the Ultimaker table.

17.4 – Save the file in .gcode using the option "Save to File".

18 – Repeat step 17 for each mold obtained in step 14.

**Construction of the phantom model using a 3D-printer – Stage 2**

19 – Introduce the gcode file in the memory card of the 3D printer (e.g. LA inner mold). Each mold (inner and outer molds) is printed independently.

19.1 – Select the target file using the printer menu and click in "Print".

19.2 – Select "Tune" option (visible in the printer), and performing the following setting:

- Speed: 60%;
- Nozzle temperature: 225 °C;
- Build-plate temperature: 60 °C;
- Material flow: 100 %;
- Fan speed: 50%.

20 – Repeat step 19 for each independent mold (*i.e.* two inner and three external molds).

**Appendix B – Schematic of the proposed phantom**

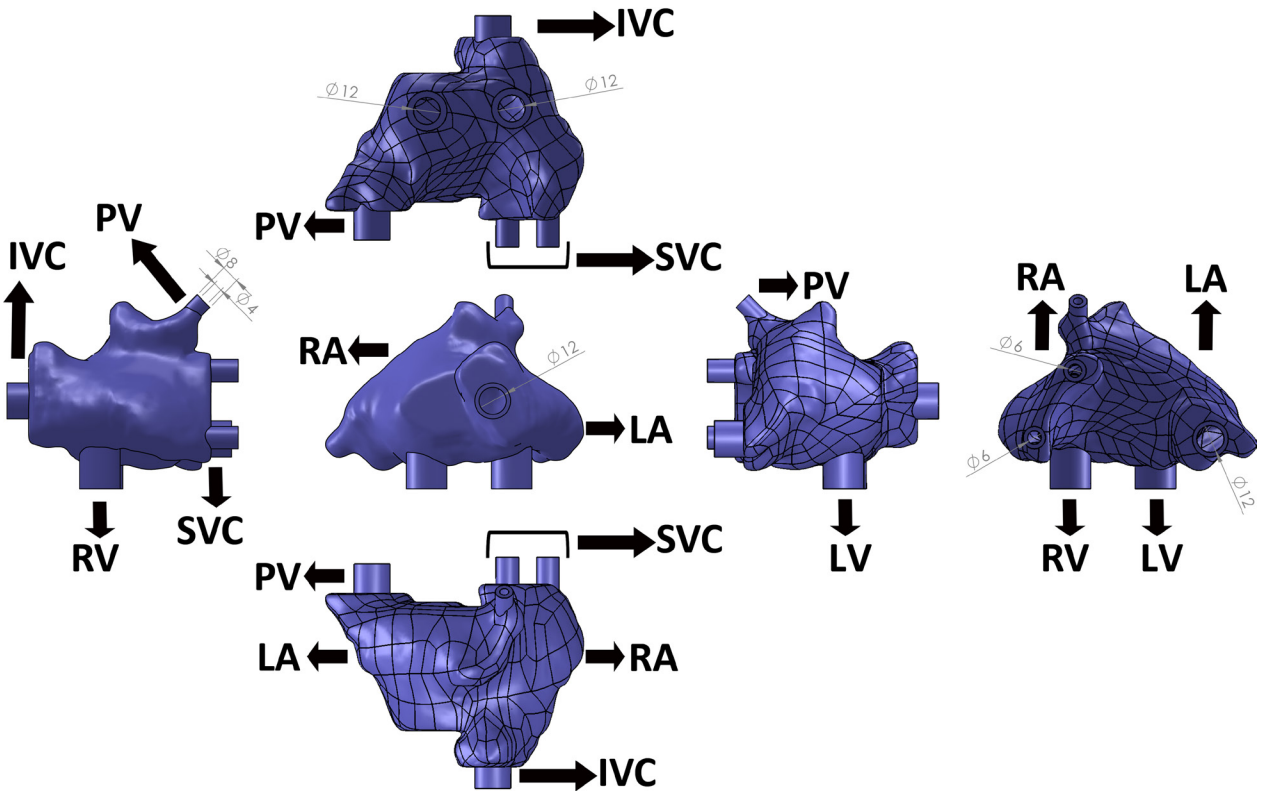


**Figure 3.B.1 – Schematic of the proposed phantom model (dimensions in mm).**

## Appendix C – Dynamic atrial phantom model

In the current appendix, we propose a setup to develop a dynamic version of the proposed phantom model. Inspired by the previous work from Cygan *et al.* (2014), where a hydraulic setup was described to mimic the beating of the left ventricle, we suggest a hydraulic scheme to simulate the beating of both atria. Since the LA and RA volume curves are quasi-synchronous (*i.e.* increase their volume until the end of the T-wave, and then reduce until the end of the ventricular diastole), a continuous water pump can be used to control the volume in each atrium. The pump continuously ejects water into the circuit (outflow in Figure 3.C.1), which circulates through the phantom until a reservoir. Since a closed pump circuit is used, a connection between the inflow (see Figure 3.C.1) of the pump and the reservoir is used. A solenoid valve is used to mimic the atrial valve function and it state is controlled by a virtual electrocardiogram (ECG). The ECG is defined through a graphic user interface, and multiple trigger functions are applied to open or close the circuit. An on/off digital controller (+5/0V) is used to modify the valve position. Specifically,

1) before the T-wave, the valve is closed. As such, the pump will eject water into the setup, increasing the pressure inside the phantom and consequently the atrial volume
2) after the T-wave and until the end of the ventricular diastole, the valve is open. In this sense, there is not pressure (or volume) increase within the phantom model, and the water only circulates through the phantom until the reservoir.

Please note that since the phantom model was segmented (section 3.2.2) at the ventricular end-diastolic phase (*i.e.* minimal atrial volume), the end-systolic phase (*i.e.* maximum atrial volume) can be simulated (as expected physiologically) through the continuous

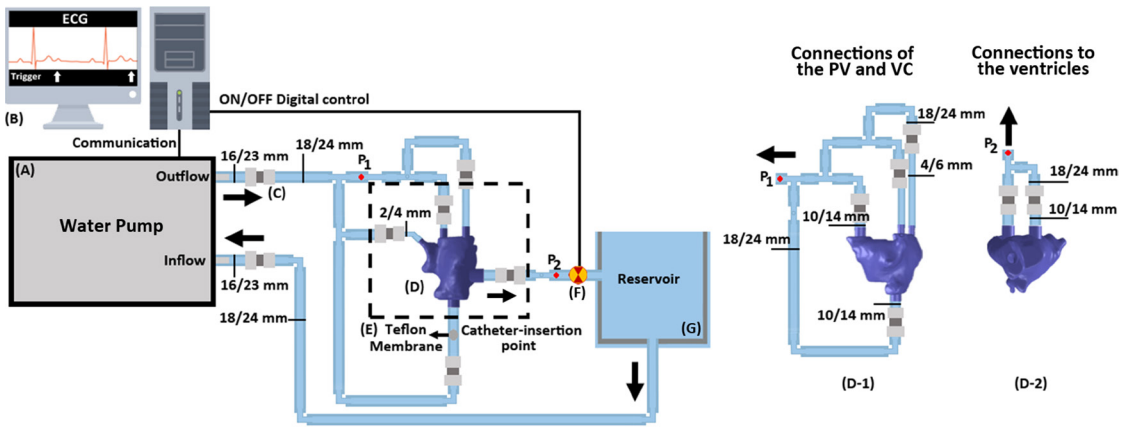


**Figure 3.C.1 - Schematic of the dynamic phantom model.**
(A) – Hydraulic pump; (B) Computer station; (C) Adapter between tubes; (D) Phantom mock model; (E) Teflon membrane to allow catheter insertion for minimally invasive atrial interventions training; (F) – Solenoid valve; (G) – Water reservoir. (D-1) and (D-2) are different views of the connections near the phantom (D). Note that $P_1$ and $P_2$ represent the same positions in both schemes. Furthermore, for each tube, the inner and outer diameter is represented (as inner/outer). PV – Pulmonary veins; VC – Vena Cava.

input of water inside the phantom with the solenoid valve closed (stage 1). In opposition, since the solenoid valve is open in stage 2, the pressure inside the cavity will reduce and the phantom will returns to its initial stage (reducing the volume), mimicking the ventricular end-diastole.

An overview of the setup can be found in Figure 3.C.1. For this specific scheme, we selected a CardioFlow 5000 pump (Shelley Medical Imaging Technologies, Canada), which includes an external controller with an ECG simulation function and multiple triggers embedded. Furthermore, a 3/4'' solenoid valve (Emerson, United State of America) is used.

# Chapter 4

## A novel interventional guidance framework for transseptal puncture in left atrial interventions

This chapter has been published in an international conference: **Pedro Morais**, João L. Vilaça, Sandro Queirós, Pedro L. Rodrigues, João Manuel R. S. Tavares, Jan D'hooge, "A novel interventional guidance framework for transeptal puncture in left atrial interventions", *in MICCAI 2018 Workshop on Bio-Imaging and Visualization for Patient-Customized Simulations*. *Lecture Notes in Computer Sciences (LNCS), Springer.* Minor changes to the original publication have been performed, including further details on the implemented methods, experimental setup and obtained results. The figures and sections numbers were updated with the chapter title and all references were combined in a common final section.

**Keywords:** Image-guided cardiac interventions; Transseptal puncture; Image fusion; Echocardiography; Integrated interventional guidance framework.

**Contents**

## Abstract

Access to the left atrium is required for several percutaneous cardiac interventions. In these procedure, the inter-atrial septal wall is punctured using a catheter inserted in the right atrium under image guidance. Although this approach (termed transseptal puncture - TSP) is performed daily, complications are common. In this work, we present a novel concept for the development of an integrated interventional framework for TSP. The pre-procedural planning stage is fused with 3D intra-procedural images (echocardiography) using manually defined landmarks, transferring the relevant anatomical landmarks to the interventional space and enhancing the echocardiographic images. In addition, electromagnetic sensors are attached to the surgical instruments, tracking and including their spatial position in the enhanced intra-procedural world. Two atrial phantom models were used to evaluate this framework. To assess its accuracy, a metallic landmark was positioned in the punctured location and compared with the ideal one. The intervention was possible in both models, but in one case positioning of the landmark failed. An error of approximately of 6 mm was registered for the successful case. Technical characteristics of the framework showed an acceptable performance, with a frame rate ~5 frames/sec. This study presented a proof-of-concept for an interventional guidance framework for TSP. However, a more automated solution and further studies are required.

## 4.1. Introduction

Access to the left atrium (LA) is mandatory in multiple minimally invasive cardiac interventions, such as left atrial appendage closure, atrial fibrillation ablation, mitral valve replacement, among others (Hsu *et al.*, 2013; Morais *et al.*, 2017b). Since no direct percutaneous access route to LA is available, a transseptal via is typically used. For that, a medical technique termed transseptal puncture (TSP) is applied, where a catheter is inserted via the femoral vein until the right atrium (RA), through which a needle is moved forward to puncture the inter-atrial septal (IAS) wall (using its thinnest region, designated as fossa ovalis) and consequently gain access to the LA body (Hsu *et al.*, 2013). The entire procedure is guided using medical images, namely fluoroscopy and echocardiography (mainly transesophageal echocardiography - TEE) (Morais *et al.*, 2017b). Nevertheless, the success of the intervention is still highly dependent on the operator's expertise, which is sub-optimal, mainly in abnormal anatomical situations (Capulzini *et al.*, 2010). Indeed, when puncturing the IAS wall, not only the fossa ovalis region needs to be identified, but also the target location at the left heart and

the catheter dexterity at this region must be taken into consideration, hampering the identification of the optimal puncture location (Morais *et al.*, 2017b).

To improve the TSP, different innovations were presented during the last years. Three major development fields can be considered, namely: surgical tools, pre-procedural planning techniques and guidance approaches (Chapter 2). A high number of researchers focused on the former, presenting novel radio-frequency/electrocautery needles (instead of the traditional mechanical ones), which proved their clear advantages for abnormal situations (Capulzini *et al.*, 2010; Hsu *et al.*, 2013). Regarding the planning techniques, a small number of studies were presented, focusing on biomechanical simulation of the intervention (Jayender *et al.*, 2011) or identification of relevant landmarks (e.g. fossa ovalis, (Verma *et al.*, 2011)), making the planning stage faster and more reproducible. Regarding the intraoperative guidance, several researchers explored the potential use of novel imaging modalities (beyond the traditional ones, magnetic resonance imaging – MRI, and intracardiac echocardiography) for TSP (Elagha *et al.*, 2008; Ruisi *et al.*, 2013). Moreover, electroanatomical mapping solutions or even electromagnetic guidance solutions were also described (Chapter 2). More recently, some researchers presented image-fusion strategies (Afzal *et al.*, 2017; Biaggi *et al.*, 2015; Bourier *et al.*, 2016), where the bidimensional and low contrast fluoroscopic image is fused with 3D anatomical detailed models (extracted from echocardiography or computed tomography - CT), showing clear advantages for TSP with inferior procedural time and higher success rate in difficult cases. Nevertheless, although such image fusion solutions showed high potential to ease the intervention (Afzal *et al.*, 2017; Biaggi *et al.*, 2015; Bourier *et al.*, 2016), most of them fuse intra-procedural images only (not allowing the inclusion of pre-procedural planning information) or were not validated for TSP.

In this study, we present a novel concept for the development of an integrated interventional guidance framework to assist the physician in successfully performing TSP.

The study is structured as follows. In section 4.2, a description of the interventional guidance framework is presented. Sections 4.3 and 4.4 describes the experimental scenario and associated results, respectively. Section 4.5 evaluates and discusses the performance of the proposed automated method. Finally, the conclusions are presented in Section 4.6.

## 4.2. Methods

### 4.2.1. General concept

The proposed interventional framework is divided into (Figure 4.1): 1) the pre-procedural and 2) the intra-procedural stages. During the first stage, a patient-specific planning

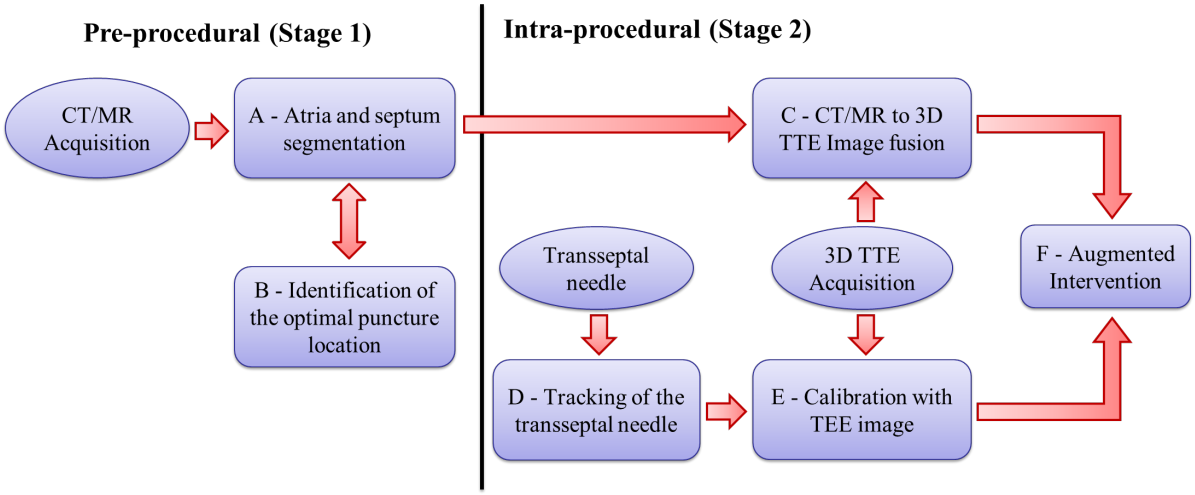


**Figure 4.1 - Blocks diagram of the proposed concept.**

of the TSP intervention is made. For that, identification or delineation (step A) of relevant cardiac chambers (*i.e.* LA and RA) in a highly-detailed image (CT or MR) is performed. Then, based on the estimated contours, the full extent of the fossa ovalis is estimated by evaluating the IAS wall (*i.e.* intermediate positions between both contours), and the optimal puncture location is defined by the expert taking into consideration the target site at the left heart (step B). The entire planning information is then transferred to the intra-procedural world (step C; already in the second stage), by fusing intra- and pre-procedural data (e.g. images, contours or landmarks). Note that intra-procedural data is extracted from echocardiographic images only (in this initial setup, transthoracic echocardiography – TTE – was used). Finally, to also include the surgical instruments into this augmented environment, a tracking strategy is applied using external electromagnetic sensors (step D). Note that an initial calibration between the TTE image world and the electromagnetic sensors is required (step E). By combining all these elements (step F), a radiation-free interventional framework with enhanced anatomical information (from the planning stage) is achieved.

### 4.2.2. Interventional framework

The interventional framework was implemented in C++ and it exploits the potentialities of the VTK (Visualization Toolkit) library (Schroeder *et al.*, 2004) for the visualization of images/surfaces and even 3D rendering (using OpenGL). The framework has 4 independent views (see Figure 4.2), allowing the visualization of the pre- and intra-procedural data through 2D views or 3D renderings. The current version implements the intra-procedural guidance stage only, presenting import functions to include the pre-procedural planning data (*i.e.* high-detailed image, LA and RA contours and relevant landmarks). Moreover, specific libraries to receive,

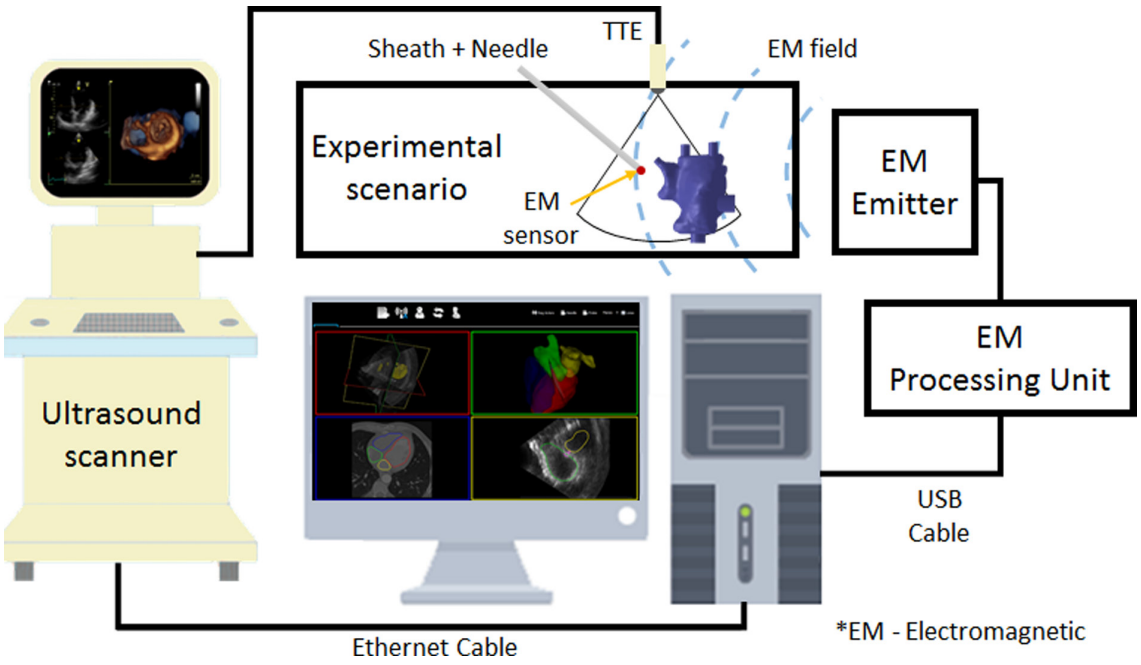


**Figure 4.2 – Overview of the developed interventional setup.**
(1) – Ultrasound scanner, (2) transthoracic transducer, (3) experimental scenario, (4) proposed interventional framework, (5) electromagnetic (EM) emitter) and (6) EM processing Unit.

in real-time, 3D TTE images (from a commercially available ultrasound – US - machine) and the 3D position of the different instruments were used.

As such, the different steps of the described concept were implemented as (Figure 4.2):

Step A: A manual delineation of the LA and RA was performed using the Medical Imaging Interaction Toolkit (MITK) software (Wolf *et al.*, 2005). In detail, multiple 2D slices were delineated and then interpolated into a 3D surface. Manual corrections were later performed to improve the result. Each surface was independently delineated (using different labels) and saved in stl (stereolitrography) format.

Step B: Based on the 3D contours from (A), the fossa ovalis region was manually identified. For that, we start by evaluating the wall thickness and detecting the thinnest region. The full extent of the fossa ovalis was generated by manually delineating multiple 2D slices and later interpolating it into 3D. Then, the optimal puncture location (*i.e.* one position inside the fossa ovalis defined by one observer) was marked and saved in stl format.

Step C: Both pre-procedural (3D CT) and intra-procedural (3D TTE) images were uploaded and streamed in the described framework (Figure 4.2), respectively. The CT image is inserted in the environment of the proposed framework using the DICOM (Digital Imaging and Communications in Medicine) read function currently available in VTK. In opposition, the TTE images were acquired in real-time with a Vivid E95 (GE Vingmed, Horten, Norway) scanner,

equipped with a 4V-D transducer (GE Vingmed) and streamed using a proprietary software. The communication between the scanner and the framework is performed through an Ethernet cable using a TCP/IP protocol. The streamed data is transferred as 3D textures, *i.e.* a volume of 3D texels (Luna, 2012) (stored in the GPU – graphics processing unit - memory), and converted to Cartesian voxels (*i.e.* CPU – central processing unit - memory) into the proposed framework. For that, we start mapping the 3D texture in a pre-defined grid, estimating the value of each voxel through an interpolation strategy. It might be noted that by transferring the data through a set of 3D textures, the size of the streamed data is reduced, allowing a fast communication between the scanner and external devices. Regarding the image-fusion between CT and TTE worlds, the following strategy was applied. By visualizing both images in parallel, a set of landmarks (at least three landmarks) were manually defined in both images (representing the same anatomical position in both images), being later used to fuse both image coordinate space. The optimal transformation between 3D CT-TTE worlds was computed through a least-squares strategy. After estimating the optimal transformation, the surfaces generated throughout steps A and B (which are described in the CT world) are imported (using stl read function available in VTK) and automatically superimposed on the intra-procedural image (*i.e.* TTE images), enhancing the relevant cardiac chambers and the target puncture location.

Step D: A small electromagnetic sensor (Figure 4.2) with 6 degrees of freedom (DOF), Aurora 6DOF Flex Tube, Type 2 (Aurora, Northern Digital, Waterloo, Ontario), was attached to the tip of the transseptal sheath (the Brockenbrough needle - BRK, St. Jude Medical, Minneapolis, MN - is later inserted through the working channel of the sheath).

Step E – A fixed calibration was made to combine the electromagnetic and US worlds. In this sense, a set of positions were identified in the TTE image. Then, the same spatial positions were physically achieved by the electromagnetic sensor. Again, more than three positions (representing the same spatial position) were used, and the final optimal transformation was obtained by applying a least-squares fitting between all positions. By applying this spatial transformation, a unique scenario combining the enhanced intra-procedural image with the needle position was obtained, allowing the correct guidance of the surgical tool until the optimal puncture location. Inside the interventional guidance framework, the needle position was represented as a red dot (Figure 4.2). Regarding the TTE image, it was kept fixed throughout this study, not requiring an extra calibration process between the probe position and the TTE image world.

## 4.3. Experiments

### 4.3.1. Validation scenario

In this preliminary version, two patient-specific mock models of the atria were used (Figure 4.3). Both models were constructed using the strategy described in Chapter 3. In short, based on a CT acquisition, the atria and its wall were manually delineated and then constructed using a mold-cast approach. Two independent materials were used to construct the phantom walls, namely silicone and polyvinyl alcohol crystals (PVA-C). Both phantom models were constructed using the same anatomy. Moreover, no dynamic setup was used. Finally, to permit the simulation of atrial interventions, multiple entry points were defined (*i.e.* mitral valve, tricuspid valve and vena cava positions). The reader is kindly directed to Chapter 3 for further details on the construction of patient-specific atrial phantom models.

### 4.3.2. Implementation details

Since mock models were used, the US probe was kept fixed throughout this intervention. For that, before executing the calibration steps (step C and E), one operator selected the optimal field of the view (FOV) of the model by moving the US probe. Regarding the identification of relevant landmarks (required in step C and E), Figure 4.4 presents an overview of the target

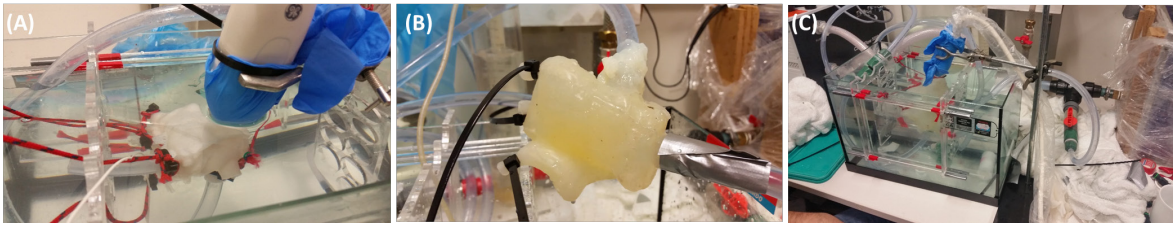


**Figure 4.3 - Experimental validation scenario.**
(A) PVA-C and (B) silicone-based phantom models. (C) General view of the entire setup.

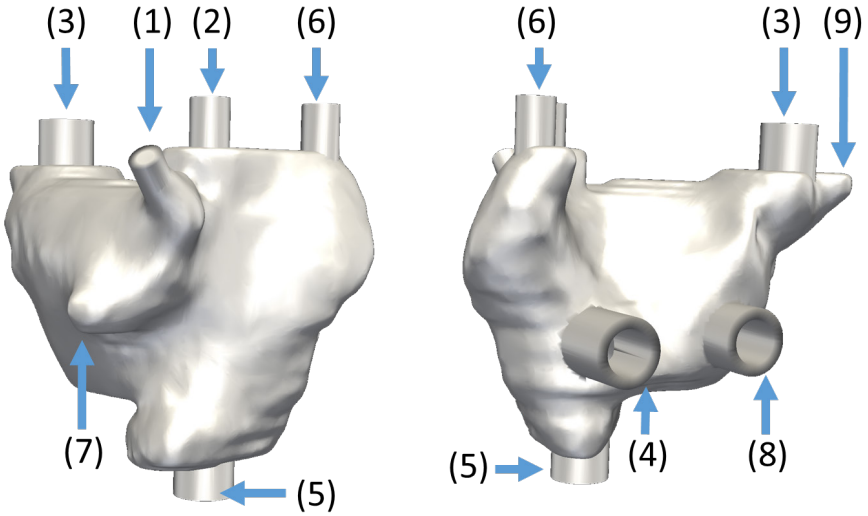


**Figure 4.4 – Relevant landmark positions for alignment of CT, TTE and electromagnetic worlds.**

positions. It should be noted that based on the selected FOV, specific landmarks which could not be observed were removed from the process.

### 4.3.3. Evaluation

One operator applied the described pipeline in each phantom model. Then, using the enhanced visualization, a TSP was performed. To evaluate the error between the selected target location and the exact puncture position, a metallic landmark was later inserted to mark the positioned punctured by the TSP needle. Later, a CT acquisition of the model plus the metallic landmark was performed (Figure 4.5). This post-interventional CT was segmented (*i.e.* LA and RA) and the obtained surfaces were aligned with the planning surfaces using an iterative closest point algorithm, transferring the selected optimal puncture location to the post-procedural space and allowing the computation of the error between the needle position and the selected position.

Finally, the frame rate achieved by this framework for the streaming of US data was also evaluated. All results were computed using a personal laptop with Intel (R) i7 CPU at 2.8 GHz and 16 GB of RAM. An integrated graphics card Nvidia Quadro K2100 was used.

## 4.4. Results

The TSP was possible in both cases. Overall, guidance with the proposed setup was considered challenging, due to limited information about the TSP needle position (only one point was used) and the low flexibility of the entry point of the phantom. Moreover, identification of an optimal 2D view with both needle and target location positions was not straightforward. In the silicone-based model, an error of ~6 mm was found between the selected target position and the metallic landmark. For the PVA-C-based model, it was not possible to insert the metallic landmark, preventing the evaluation of the puncture accuracy.

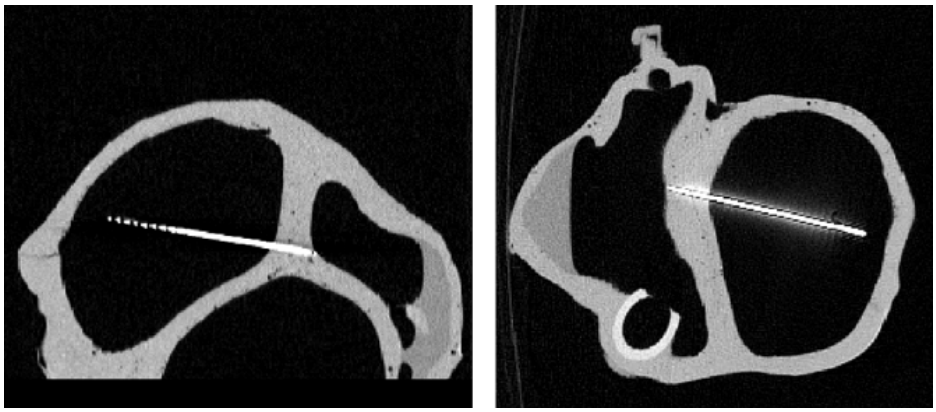

**Figure 4.5 - Post-procedural CT.**
A metallic landmark (brighter structure) is used to mark the punctured location.

Regarding the technical characteristics, the proposed framework obtained a frame rate of approximately 5 frames/second (*i.e.*, 3D US streaming and image enhancement). The technical calibration (step C and E from section 4.2.2) took more than 60 minutes. The planning stage (step A and B from section 4.2.2) required approximately 30 minutes.

## 4.5. Discussion

In this study, a novel interventional framework for TSP is described. It uses the potentialities of the intra-procedural volumetric US image to create an integrated interventional scenario where both pre-planning, intra-procedural data, and surgical instrument position are fused. Thus, the not well contrasted and noisy TTE image is enhanced by superimposing virtual anatomical surfaces. Moreover, the optimal puncture location can also be visualized, potentially increasing the safety and the level of confidence of the physician, thus reducing the interventional time. In opposition to previous studies (Cleary and Peters, 2010), the current concept allows the inclusion of pre-procedural planning information in the interventional world. Indeed, recent solutions, such as the EchoNavigator (Philips Inc., Netherlands), proved its added-value for TSP intervention (Faletra *et al.*, 2017), by adding anatomical information (echocardiographic images) to the traditional fluoroscopic view. Nevertheless, although this solution allows the inclusion of specific landmarks in the interventional image (and then, transferring it to the fluoroscopy world), one is not able to embed pre-procedural planning information (Faletra *et al.*, 2017). In a different way, CT-fluoroscopy image fusion approaches were also described and validated for TSP (Bourier *et al.*, 2016), therefore the usage of pre-procedural data into the interventional scenario. However, since the ultrasound image is not integrated, relevant online anatomical details (e.g. identification of abnormal situations) are lost or ultimately require an independent ultrasound scanner throughout the intervention. As a final remark, some preliminary studies fusing CT-echocardiography-fluoroscopy were also technically described (Housden *et al.*, 2013a), but not validated for the current intervention.

The described framework has as a key novelty the direct usage of 3D US data (by streaming it from the US machine) to fuse intra-procedural data with pre-procedural one. In fact, previous works focused on similar methodologies for different scenarios. Nevertheless, 2D US data was mainly streamed, requiring complex calibration/configuration scenarios to perform 2D-3D alignment/reconstruction (Cleary and Peters, 2010; Lang *et al.*, 2012). Although such approaches have shown interesting results in nearly static structures/organs (Cleary and Peters, 2010), its application in cardiac interventions is limited and not straightforward. In this sense, by capturing the entire 3D volume, 2D-3D

alignment/reconstruction steps are removed from the pipeline, potentially improving the performance and accuracy of image-fusion algorithms (*i.e.* the combination of intra-procedural and pre-procedural worlds), making it suitable to the particularities of the heart. However, the authors would like to emphasize that the described pipeline is only an initial proof-of-concept and it still presents some drawbacks, namely manual interaction is mandatory in all stages, making the configuration of the entire setup extremely time-consuming. In this sense, novel strategies to automatically segment the atrial region and to detect the fossa ovalis extent in CT images (as later described in Chapter 5 and Chapter 6), as well as to segment the atrial chambers in echocardiographic images (currently available in the research team, (Almeida *et al.*, 2016)) are expected to be developed and integrated into the current framework. As a result, the entire planning can be performed quickly and in a totally automatic way, and also intra-procedural and pre-procedural data can be fused by aligning the segmented anatomical models. Regarding the tracking of the different surgical tools, fixed calibration setups (configured before the intervention) can be used (Cleary and Peters, 2010), not altering the normal clinical routine. Nevertheless, in order to improve the guidance of the surgical tools and the identification of the optimal puncture route, two modifications should be performed to the current setup: i) multiple sensors should be embedded along the instrument extension (and not only at the instrument's tip), providing a virtual representation of the entire instrument's shape inside the body (similar to the fluoroscopic view), and ii) an enhanced representation of the optimal puncture route (e.g. by reformatting the ultrasound view using the transseptal needle position as reference) can potentiate the guidance stage and facilitate the identification of the puncture location. Finally, regarding the frame rate, an acceptable performance (5 frames/second) was achieved by this framework, even on a personal laptop.

The obtained results showed that accurate evaluation of the proposed framework was not possible. First, a small number of phantom models were used, limiting the exhaustive validation of the framework and even preventing comparative studies. Second, the strategy applied to mark the punctured location proved to be sub-optimal. Due to the small entry points of the atrial phantom model, visual identification of the small IAS hole created by the TSP was challenging, hampering the insertion of the metallic landmark. Indeed, in one case, such approach was not feasible. Third, quantification of the framework's accuracy through the described approach (*i.e.* aligning post-interventional data with pre-interventional one) is sensitive to small alignment errors. In this sense and in order to improve the described experiments, a novel experimental scenario is required with the following features: 1) a large

number of phantom models with different anatomies are required; 2) inclusion of radiopaque materials at the phantom construction stage to mark the optimal puncture location or even to easily allow an accurate alignment between the pre- and pos- interventional surfaces could be a potential solution to improve the error quantification stage; and 3) instead of using metallic landmarks, the transseptal needle should be kept at the punctured location, accurately marking it. Finally, since the traditional intervention is widely dependent of the fluoroscopy view (due to the simple identification of the surgical instruments), further studies to evaluate the feasibility of this potential radiation-free TSP framework and even to evaluate the required learning curve with this new approach are mandatory to validate it.

Regarding the study limitations, we would like to emphasize that: 1) static phantom models were used, which do not mimic the cardiac intervention; 2) instead of a TEE probe (normally used in this intervention), a TTE one was used; and 3) the ultrasound probe was kept fixed throughout the intervention, again not simulating the real scenario. In fact, in order to overcome these limitations, dynamic phantom setups (by introducing water pumps), as described in Chapter 3 (Appendix 3.7C), should be used, and an electromagnetic sensor should be attached to the ultrasound probe, spatially relating the ultrasound FOV with the probe position, as described by Lang *et al.* (2012), and allowing therefore its free manipulation throughout the intervention. Finally, although the current study was performed with a TTE transducer (since it was simple to be fixated), the TEE probe can also be used without any modification of the current setup.

## 4.6. Conclusions

The described concept for the development of an interventional guidance framework showed its initial potential usefulness for the identification of the optimal puncture location and to guide the TSP intervention. Nevertheless, the current version requires manual interaction in all stages, making the configuration setup extremely time-consuming and difficult to be performed. Moreover, automatic solutions to fuse intra-procedural and pre-procedural data based on real-time image content (and not based on a fixed initial configuration) are missing. Finally, further studies and a different experimental setup are required to accurately validate the proposed framework, and therefore to confirm its added-value for normal clinical practice.

# Chapter 5

## A competitive strategy for atrial and aortic tract segmentation based on deformable models

This chapter has been published in *Medical Image Analysis*: **Pedro Morais**, João L. Vilaça, Sandro Queirós, Felix Bourier, Isabel Deisenhofer, João Manuel R. S. Tavares, Jan D'hooge, "A competitive strategy for atrial and aortic tract segmentation based on deformable models", *Medical Image Analysis*, vol. 42, pp. 102-116, 2017. Only minor changes to the original publication have been performed. The figures and sections numbers were updated with the chapter title and all references were combined in a common final section.

**Keywords:** Image segmentation; Competitive contours; Atrial and aortic tract segmentation; B-spline explicit active surfaces.

**Contents**

## Abstract

Multiple strategies have previously been described for atrial region (*i.e.* atrial bodies and aortic tract) segmentation. Although these techniques have proven their accuracy, inadequate results in the mid atrial walls are common, restricting their application for specific cardiac interventions. In this work, we introduce a novel competitive strategy to perform atrial region segmentation with correct delineation of the thin mid walls, and integrated it into the B-spline Explicit Active Surfaces framework. A double-stage segmentation process is used, which starts with a fast contour growing followed by a refinement stage with local descriptors. Independent functions are used to define each region, being afterward combined to compete for the optimal boundary. The competition locally constrains the surface evolution, prevents overlaps and allows refinement to the walls. Three different scenarios were used to demonstrate the advantages of the proposed approach, through the evaluation of its segmentation accuracy, and its performance for heterogeneous mid walls. Both computed tomography and magnetic resonance imaging datasets were used, presenting results similar to the state-of-the-art methods for both atria and aorta. The competitive strategy showed its superior performance with statistically significant differences against the traditional free-evolution approach in cases with bad image quality or missed atrial/aortic walls. Moreover, only the competitive approach was able to accurately segment the atrial/aortic wall. Overall, the proposed strategy showed to be suitable for atrial region segmentation with a correct segmentation of the mid thin walls, demonstrating its added-value with respect to the traditional techniques.

## 5.1. Introduction

Anatomical assessment of the atrial region (*i.e.* atrial bodies and aortic tract - Ao) through medical imaging has gained particular interest during the last decade. Several researchers extracted/isolated multiple contours of the atrial anatomies using different segmentation strategies (Tobon-Gomez *et al.*, 2015), proving the clinical relevance of a correct anatomical and functional assessment of each atrial region for global cardiac function quantification and even for risk stratification (Hoit, 2014; Melenovsky *et al.*, 2014). Moreover, enhanced minimally invasive cardiac interventions were proposed, using electroanatomic mapping techniques (Rolf *et al.*, 2014) or even superimposing pre-operative anatomical atrial surfaces (Bourier *et al.*, 2016), extracted from highly detailed datasets, into intra-operative imaging (e.g. fluoroscopy). In fact, the fusion of pre- and intra-operative data is an emergent research topic, where the limitations commonly associated with the intra-operative data (e.g.

difficult to detect the cardiac boundaries, or the small field of view) are reduced, facilitating the entire procedure and making it safer even in inexperienced hands.

Automatic and semi-automatic atrial region segmentation solutions have been explored and presented for multiple imaging modalities, such as computed tomography (CT) (Ecabert *et al.*, 2011; Kirişli *et al.*, 2010; Zheng *et al.*, 2008) and magnetic resonance imaging (MRI) (Zuluaga *et al.*, 2013). Since the manual approach is tedious, time-consuming and has a high intra- and inter-observer variability, automated segmentation processes have been widely explored and increasingly accepted in normal clinical practice. The majority of the applied methods are based on deformable models (Ecabert *et al.*, 2011), atlas-based techniques (Kirişli *et al.*, 2010; Zuluaga *et al.*, 2013) and machine learning (Zheng *et al.*, 2008), proving its high accuracy in a high number of cases with different pathologies. Some studies focused only on the left atrium (LA) due to its importance for atrial fibrillation, using a simple initialization strategy through a multi-atlas to obtain a rough contour alignment (Sandoval *et al.*, 2013) or a probabilistic atlas (Stender *et al.*, 2013), followed by a region growing and multiple 2D individual segmentations with circular shape descriptors (Ammar *et al.*, 2013). Moreover, (Zuluaga *et al.*, 2013) presented an atlas-based technique with global and deformable alignment for LA segmentation only. Nevertheless, the current solutions show inaccurate results in thin septal walls (Zhuang *et al.*, 2010) or present a total merge/overlap between atrial contours (Kirişli *et al.*, 2010; Zuluaga *et al.*, 2013). Specifically, the atlas-based technique with a final majority voting per chamber approach presented by Kirişli *et al.* (2010) was unable to prevent overlap between contours. Contrarily, the atlas-based approach from Zuluaga *et al.* (2013) and the deformable model proposed by Ecabert *et al.* (2011) prevented overlapping regions by simply merging these regions. Thus, accurate assessment of the thin walls is currently not possible, missing their use for specific diagnostic purposes and interventional planning related with the thin atrial walls, e.g. transseptal puncture (Chapter 2).

Multiple strategies have been proposed to segment multiple structures, using different formulations to identify the target regions and prevent overlap and gap regions between contours (Jimenez-del-Toro *et al.*, 2016). Initially, several researchers extended their individual structure methods to multi-structures. Some examples are the atlas-based (Okada *et al.*, 2015; Wolz *et al.*, 2013; Xu *et al.*, 2015), and statistical-based approaches (Yan *et al.*, 2005; Yang *et al.*, 2004). Despite the high versatility obtained, overlapping and merged regions were typically found, requiring post-processing techniques through mathematical morphology operations or refinement methodologies (Iglesias and Sabuncu, 2015).

Cooperative strategies (e.g., coupled level sets) were also presented and showed their robustness for multiple structure situations (Yezzi *et al.*, 2002), such as endo- and epicardial left ventricular wall segmentation (Alessandrini *et al.*, 2009; Pedrosa *et al.*, 2017; Queirós *et al.*, 2014). These strategies use multiple functions (one per target region) and combine them during the optimization. Each individual curve is affected by the remaining ones, consequently cooperating to maximize/minimize the functional energy. As such, these strategies are less sensitive to local minima and to the initialization when compared with multiple independent segmentation approaches (Chen *et al.*, 2008; Yezzi *et al.*, 2002). However, these models do not have an intrinsic restriction to prevent overlapping regions (Faisal *et al.*, 2015), consequently requiring several and complex penalty terms (Barbosa *et al.*, 2010) to obtain mutual exclusiveness and boundary share between the different contours (Faisal *et al.*, 2015).

On the contrary, competitive contours use a different multi-structure segmentation paradigm, where the multiple curves that define the target structures interact between them at the contour boundaries to avoid overlapping regions (Brox and Weickert, 2006; Lankton and Tannenbaum, 2008). This interaction is usually performed through act-react strategies (Brox and Weickert, 2006; Lankton and Tannenbaum, 2008), where the contour with stronger force controls the update of the remaining ones. Nevertheless, at regions of no competition, external terms (Brox and Weickert, 2006) are required to prevent empty regions. Initially, these methods were applied for the entire image domain, failing to segment small regions of the image or at least requiring an extra function that represents the background (Gao *et al.*, 2012b). As such, these strategies were sub-optimal for medical imaging problems, where only a few number of organs are typically assessed. In this sense, Gao *et al.* (2012b) presented a local robust statistic driven active contour that uses act-react forces to perform interactive segmentation in small portions of the image. Since full union between contours was not required, this solution proved its added-value for the segmentation of regions with thin walls. Nevertheless, this generic framework presented some limitations to perform accurate segmentation of thin walls with low contrast, generating small bridges/connections between contours.

In this work, we present a novel competitive approach for segmentation of multiple structures. The novel method is applied for atrial region segmentation with correct delineation of the thin mid atrial walls, even in low contrast scenarios. Multiple independent functions are used to control each contour (*i.e.* LA, Ao and right atrium – RA), being afterwards combined to compete for the optimal boundary transition. Indeed, the competition is only applied when two or more contours are near each other, penalizing the surface evolution based on the local distance between contours. As such, fast contour growing is prevented, and a refinement to the

thin wall is achieved. Although this competitive methodology is generic and suitable to be applied in several frameworks, we decided to prove its advantages using the B-spline Explicit Active Surfaces (BEAS) framework (Barbosa *et al.*, 2012), which proved to be suitable for individual cardiac chamber segmentation, such as the left ventricle (Queirós *et al.*, 2014) and the aorta (Queirós *et al.*, 2017; Queirós *et al.*, 2016). It should be noticed that, although coupled BEAS strategies have been proposed for myocardial segmentation using concentric contours (Pedrosa *et al.*, 2017; Queirós *et al.*, 2014), generic competitive approaches that allow segmentation of multiple structures without shape restrictions are still missing.

Hereupon, the current work introduces three novelties, namely: 1) a new competitive strategy that allows accurate segmentation of multi- structures with thin and heterogeneous mid walls; 2) a novel methodology to segment the atrial region in multiple imaging modalities based on the proposed competitive strategy; and 3) exhaustive validation of the novel competitive method for atrial region segmentation.

This work is structured as follows. In section 5.2, a technical description of the proposed strategy for atrial region segmentation is presented, followed by an explanation of the proposed competitive technique. In section 5.3, the validation experiments and their results are presented. Section 5.4 evaluates and discusses the performance of the proposed competitive method against state-of-the-art techniques and free-evolution approaches. Finally, the conclusions of this work are presented in section 5.5.

## 5.2. Methods

In this section, we present the strategy used to segment the LA, RA and Ao. The proposed semi-automatic method relies on three consecutive stages (Figure 5.1): 1) manual identification of the different regions through one click in each chamber and three clicks in the aortic tract; 2) fast growing of the contours using a BEAS-threshold strategy; and 3) contour refinement using BEAS-segmentation with localized energies.

The clicked positions are used to initialize two ideal spheres (for LA and RA) and one cylinder (for Ao), which are afterwards adapted to the anatomy. Each individual click defines the center position of a sphere with a radius of approximately 15 mm and the three clicks in the Ao define the centerline of a cylinder with a radius of approximately 5 mm. Furthermore, in order to identify the mitral and tricuspid valve region, both left and right ventricles (LV and RV) are also initialized (two ideal spheres with radius of 15 mm) with one click in each blood pool. The spatial location of both ventricles is used to locally constrain the atrial surfaces, preventing their evolution inside the ventricle regions (further details in section 5.2.2).

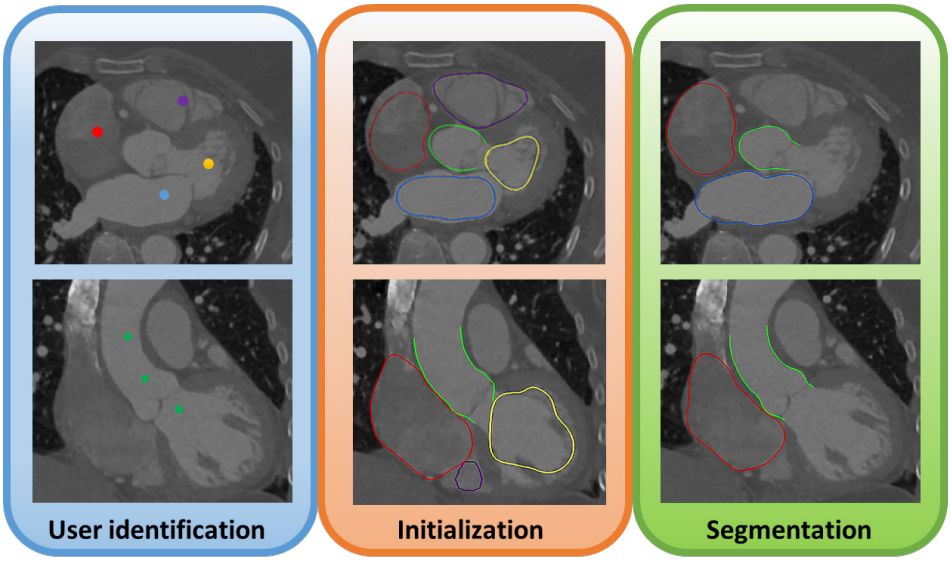


**Figure 5.1 – Overview of the proposed competitive strategy for atrial region segmentation.**

The BEAS-threshold is first used to grow the initialized contour (*i.e.* the cylinder and spheres) using global descriptors, minimizing the influence of the initialization on the segmentation result. The segmentation is then applied to refine the surfaces and to accurately delineate the atrial and aortic walls. In order to increase the robustness of the technique, edge-based and simple shape regularization terms are used during the process. The edge-based terms reduce the influence of the initialization and guide the segmentation in heterogeneous and vacuum regions, while the regularization term uses the curvature information of each contour to regularize the contour and to reduce the degrees of freedom of the segmentation. Moreover, the regularization term controls the contour evolution in vacuum regions (e.g., tricuspid valve).

Two independent implementations are presented, one where each structure evolves independently (henceforward mentioned as free-evolution BEAS, section 5.2.1), and a second where a novel competitive approach is presented, allowing interaction between the contours while guaranteeing the integrity of the thin mid atrial walls (competitive BEAS, section 5.2.2).

It should be noticed that both ventricles (LV and RA) are only evolved in the threshold-based stage (Figure 5.1), allowing their local competition with the atrial chambers and consequently defining the valve plane.

### 5.2.1. Free evolution B-spline Explicit Active Surfaces (BEAS)

#### A. B-spline Explicit Active Surfaces

The BEAS framework was initially proposed by Barbosa *et al.* (2012), having as key novelty the representation of the interface as an explicit function described using B-spline coefficients ($c[\boldsymbol{k}]$). This implies that one of the coordinates of the points of the interface, $\boldsymbol{x} =$

$\{x_1, x_2, \dots, x_N\}$ in a $N$-dimensional space, is expressed as a function of the remaining coordinates (*i.e.* $\boldsymbol{x}^* = \{x_2, \dots, x_N\}$) consequently reducing the dimensionality of the segmentation problem and intrinsically including shape limitations with clear advantages for non-complex shapes.

The explicit function $\psi$ is therefore defined as (Almeida *et al.*, 2016):

$$x_1 = \psi(\boldsymbol{x}^*) = \sum_{k \in \mathbb{Z}^{N-1}} c[\boldsymbol{k}] \beta^d \left( \frac{\boldsymbol{x}^* - \boldsymbol{k} h_r}{h_s} \right), \tag{5.1}$$

where $\beta^d(\cdot)$ is the uniform symmetric $(N-1)$-dimensional B-spline of degree $d$. The knots of the B-splines are located on a regular grid defined on a specific space (e.g., polar or cylindrical space). $h_s$ and $h_r$ are smoothness parameters that control the scaling and spacing of the B-spline kernel, respectively. Specifically for atrial region segmentation, both atria are described through a spherical model, while the aorta tract is represented by a cylindrical one.

Regarding the contour evolution, multiple energies are used to control the optimization process of each contour $i$. Two strategies can be used to optimize the multiple energy terms. The first approach minimizes each energy individually, therefore allowing that one energy converges before the second one. Contrarily, the second approach combines both terms and the iterative process is only stopped when both contours converge. Due to the simplicity of the method, we decided to prove the advantage of our competitive technique using the second strategy. Nonetheless, note that the independent optimization approach could also be implemented. In this sense, the BEAS energy ($E$) for multiple contours is computed through:

$$\begin{aligned} E &= \sum_i E_i. \\ E_i &= \int_\Omega \delta_{\phi_i}(\boldsymbol{x}) \int_\Omega B(\boldsymbol{x}, \boldsymbol{y}). F_i(\boldsymbol{y}) d\boldsymbol{y} d\boldsymbol{x} \end{aligned} \tag{5.2}$$

where $\phi_i(\boldsymbol{x}) = \Gamma_i(\boldsymbol{x}^*) - x_1, i \in \{1, \dots, n\}$ with $n$ representing the total number of contours, $\boldsymbol{x}, \boldsymbol{y}$ are independent spatial locations in the image domain $\Omega$, $\phi_i(\boldsymbol{x})$ is a level-set like function representing the region inside the interface $\Gamma_i$, $\delta_{\phi_i}$ is the dirac function and $F_i$ an image criteria, e.g. localized Chan-Vese energy (Lankton and Tannenbaum, 2008). $B(\boldsymbol{x}, \boldsymbol{y})$ corresponds to a mask function in which the regional parameters that locally drive the contour evolutions are computed and it is defined as the set of points belonging to the normal direction of $\boldsymbol{x}$ and whose distance is lower than $\rho$. Furthermore, the energy is minimized through the computation of the energy derivatives with respect to each B-spline coefficient for each contour $i$, through (Barbosa *et al.*, 2012):

$$\frac{\partial E_i}{\partial c_i[\boldsymbol{k}]} = \int_{\Gamma_i} \bar{g}_i(\boldsymbol{x}^*)\beta_i^d\left(\frac{\boldsymbol{x}^* - \boldsymbol{k}h_{r_i}}{h_{s_i}}\right)d\boldsymbol{x}^*, \tag{5.3}$$

with $\bar{g}_i(\boldsymbol{x}^*)$ representing the feature map (e.g. first derivative of the local Chan-Vese energy, (Lankton and Tannenbaum, 2008)) of each contour $i$. The traditional formulation from BEAS used regional intensity-based terms directly extracted from the image ($\bar{g}^{IM}$), mathematically described as image criteria $F^R$ and feature $\bar{g}^R$. Thus, equations (5.2) and (5.3) are updated to:

$$F_i(\boldsymbol{y}) = F^R(\boldsymbol{y}), \tag{5.4}$$

$$\bar{g}_i(\boldsymbol{x}^*) = \bar{g}_i^{IM}(\boldsymbol{x}^*) = \bar{g}^R(\boldsymbol{x}^*), \tag{5.5}$$

The reader is kindly directed to Barbosa *et al.* (2012) for further details on BEAS.

### B. Edge-based energy term

Queirós *et al.* (2014) presented and integrated an edge-based term in BEAS to segment 2D+t stacks of cine magnetic resonance imaging (MRI) datasets. Inspired by this work, we present a pure 3D edge term, which is computed through the following strategy (Figure 5.2): 1) estimation of the image edges ($S$) through a Canny edge detector (Canny, 1986), and 2) computation of the edge energy term ($\Upsilon$) as an unsigned distance function between each volume point and the identified edges. The representation of $\Upsilon$ as a distance function, improves the robustness of the edge detection strategy, filling small gaps due to missing edges in the map. Specifically, equations (5.4) and (5.5) are now described as:

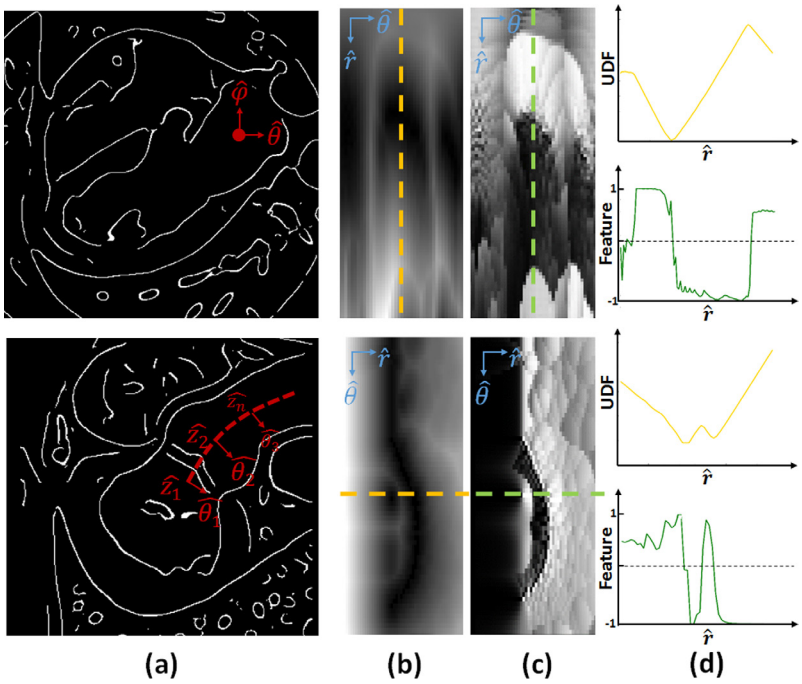


**Figure 5.2 – Overview of the edge term used.**
(a) Canny edge result; (b) unsigned distance function (UDF) in the spherical (top) and cylindrical space (bottom); (c) the respective feature; (d) profile of the energy and the feature used during the segmentation.

$$F_i(\mathbf{y}) = \lambda_i^R . F^R(\mathbf{y}) + \Upsilon(\mathbf{y}), \tag{5.6}$$

$$\bar{g}_i(\boldsymbol{x}^*) = \bar{g}_i^{IM}(\boldsymbol{x}^*) = \lambda_i^R . \bar{g}^R(\boldsymbol{x}^*) + \nabla_r \overline{\Upsilon}(\boldsymbol{x}^*), \tag{5.7}$$

with $\Upsilon(\mathbf{y}) = \min_j(\|\boldsymbol{x} - S_j\|)$, $j$ representing each edge of the map $S$ and $\nabla_r \overline{\Upsilon}(\boldsymbol{x}^*)$ the edge energy map gradient along the radial direction, which is computed through centered finite differences. $\lambda_i^R$ is a positive hyper-parameter that balances the regional and edge-based terms.

**C. Regularization term**

In order to reduce the model's degrees of freedom and to prevent incorrect segmentation due to image artifacts, regularization terms are typically used. In the current work, we apply a curvature-based shape prior regularization to prevent concave shapes. As such, local regions with negative concavities are penalized, consequently pushing the surface outward. Specifically, a binary curvature-based switch is used:

$$\bar{g}^C(\boldsymbol{x}^*) = -\mathcal{K}(\boldsymbol{x}^*) . H\big(-\mathcal{K}(\boldsymbol{x}^*)\big), \tag{5.8}$$

updating equation (5.7) to:

$$\bar{g}_i(\boldsymbol{x}^*) = \bar{g}_i^{IM}(\boldsymbol{x}^*) = \lambda_i^R . \bar{g}^R(\boldsymbol{x}^*) + \nabla_r \overline{\Upsilon}(\boldsymbol{x}^*) + \lambda_i^C . \bar{g}^C(\boldsymbol{x}^*). \tag{5.9}$$

where $\lambda_i^R$ represents positive hyper-parameters that balance the multiple terms used. $\mathcal{K}$ is the local curvature of the contour. Note that, $H(-\mathcal{K}(\boldsymbol{x}^*))$ term guarantees that only concave regions are regularized.

**D. BEAS-threshold**

BEAS-threshold was previously presented in Queirós *et al.* (2014) and Queirós *et al.* (2016) for initialization of a myocardial wall or aortic wall segmentation technique. The method uses *a priori* defined rules to locally expand or shrink the contour. The contour is updated by directly using the B-spline coefficients ($c_i[\boldsymbol{k}]$) as described in equations (5.3) and (5.9), allowing a fast evolution process with intrinsic control of the smoothness degree for each contour. The original BEAS-threshold method is purely based on intensities, using a fixed threshold (e.g. mean intensity of the target region) to generate a feature map to update the contours. Specifically, the fixed threshold is compared with the image intensity in each control point of the surface, and these points are then updated accordingly with the pre-defined rule (*i.e.* expand or shrink). No energy is used to control the contour evolution, being the process finished by simple factors, such as the number of iterations or the area. In this sense, equations (5.3) and (5.9) are used to evolve the multiple contours, *i.e.* $i \in \{LA, RA, AO, LV, RV\}$, with:

$$\bar{g}^R(\boldsymbol{x}^*) = \begin{cases} 1, \ if \ \bar{I}(\boldsymbol{x}^*) \geq th \\ -1, \ otherwise \end{cases}, \tag{5.10}$$

where $\bar{I}(\boldsymbol{x}^*)$ is the image value at position $\boldsymbol{x} = \{x_1 = \psi(\boldsymbol{x}^*), x_2, \dots, x_z\}$, and $th$ is the fixed threshold used. Both intensity and edge-based terms are now used to guide the initialization and make the strategy more suitable for heterogeneous regions.

**E. Contour refinement**

The contours refinement step directly minimizes the energy function in equation (5.2), using its derivative, equations (5.3) and (5.9). The strategy is used to refine the atrial region, assuming three independent contours, *i.e.* $i \in \{LA, RA, AO\}$. In opposition to the BEAS-threshold, the segmentation uses smaller steps computed using small portions of the image, consequently refining the contour to the real anatomy. The regional term ($F^R$) is described using the localized signed Yezzi energy (Queirós *et al.*, 2014):

$$F^R(\boldsymbol{y}) = u_x - v_x \tag{5.11}$$

and its derivative $\bar{g}^R$:

$$\bar{g}^R(\boldsymbol{x}^*) = (\bar{I}(\boldsymbol{x}^*) - u_x) + (\bar{I}(\boldsymbol{x}^*) - v_x), \tag{5.12}$$

where $u_x$ and $v_x$ are the mean intensities inside and outside of the evolving interface at point $\boldsymbol{x}$, calculated using $B$. This energy searches for the optimal position as the maximum contrast point between regions. Since all chambers are brighter than the cardiac wall, a signed version of this energy is used. As such, a specific representation of the target transition (bright to dark) is explicitly embedded into the functional energy, making it less sensitive to artifacts.

### 5.2.2. Competitive B-spline Explicit Active Surfaces

The aforementioned free-evolution strategy allows segmenting multiple structures, but does not prevent overlapping regions, being therefore sub-optimal for several medical applications (e.g. evaluation of mid thin walls). In this section, we expand the previous methodology introducing a novel competitive strategy. This competitive strategy locally constrains the evolution of each contour when they are too near, preventing overlapping regions. Moreover, the novel competitive strategy is expanded to prevent merging between contours, allowing an accurate segmentation of mid thin walls as found in the atrial region. For the sake of clarity, we start by explaining how this competition can be performed between two contours, being subsequently expanded for $n$ contours and specifically for the atrial region problem. The authors would like to emphasize that no restrictions about the models' shapes are made. Moreover, the current methodology can be used for either 2D or 3D problems.

**A. Two contours**

Assuming a hypothetic segmentation scenario with two regions (e.g. LA and RA only), two independent functions and their corresponding evolution energies, $E_1$ and $E_2$, are required. The energy combination is performed using equation (5.2) and the energy minimized using equation (5.3). In order to include a competition strategy between the different contours, a novel term should be included in equation (5.9):

$$\bar{g}_1(\boldsymbol{x}^*) = \bar{g}_1^{IM}(\boldsymbol{x}^*) + \alpha_{1\to2}.\,\bar{g}_{1\to2}^{CPT}(\boldsymbol{x}^*) \text{ and} \tag{5.13}$$

$$\bar{g}_2(\boldsymbol{x}^*) = \bar{g}_2^{IM}(\boldsymbol{x}^*) + \alpha_{2\to1}.\,\bar{g}_{2\to1}^{CPT}(\boldsymbol{x}^*), \text{ with } \alpha_{2\to1} = 1 - |\alpha_{1\to2}|, \tag{5.14}$$

where $\bar{g}^{IM}$ are the features extracted from the image (*i.e.* signed localized Yezzi, edge based and regularization terms) and $\bar{g}^{CPT}$ represents the competition term. Moreover, $\alpha_{1\to2}, \alpha_{2\to1} \in [-1; 1]$ are confidence terms. Both confidence terms are used to increase the influence of one of the contours throughout the competition process, due to *a priori* knowledge of superior image quality in one of the regions. $\alpha_{1\to2} = 0$ means that no penalization related with competition is applied in contour 1, and the contour evolution is only performed based on the image data. In contrast, total penalization ($\alpha_{2\to1} = 1$) is applied in contour 2 based on the competition process. $\alpha_{1\to2} = 0.5$ represents an equal confidence on both contours. Moreover, it may be noted that $\alpha < 0$ is required for concentric contours (*i.e.* contours with the same expansion/shrinking direction), where the penalization factor should be applied in opposing directions, increasing the wall thickness between them and preventing overlapping regions.

Regarding the competition term ($\bar{g}^{CPT}$), it is described as:

$$\bar{g}_{1\to2}^{CPT}(\boldsymbol{x}^*) = (R_T - \boldsymbol{\psi}^{1\to2}).H(R_T - \boldsymbol{\psi}^{1\to2}), \tag{5.15}$$

$$\bar{g}_{2\to1}^{CPT}(\boldsymbol{x}^*) = (R_T - \boldsymbol{\psi}^{2\to1}).H(R_T - \boldsymbol{\psi}^{2\to1}), \tag{5.16}$$

with $R_T$ representing the estimated minimal thickness parameter, $\boldsymbol{\psi}$ is a signed distance map between each node of the surface 1 against the entire surface 2 (and vice-versa), and $H$ a Heaviside operator. Note that $H$ is only equal to one in nodes with $\boldsymbol{\psi}$ lower than $R_T$, being zero in the remaining nodes. Therefore, the competitive strategy is only applied in the nearest regions of the contours (*i.e.* distance lower than $R_T$). Regarding $\boldsymbol{\psi}$, it is computed as the minimal result of three possibilities: 1) a point-to-point distance between all the vertices of both surfaces; 2) an edge-to-point distance defined as the intersection result between all the edges of surface 2 against the target point in surface 1; and 3) a face-to-point distance, computed as the intersection between the multiple faces/planes of surface 2 against the point in surface 1. It should be noticed

that overlapping contour regions are defined as negative distances. The reader is kindly directed to Baerentzen and Aanaes (2005) for further details on signed distance function computation.

A schematic about the competitive workflow can be found in Figure 5.3. As described above, the distance between two surfaces is used to locally constrain the surfaces' evolution. When the distance between contours is lower than $R_T$, a force with opposite direction to the contour evolution direction is applied to prevent fast steps, consequently allowing small refinements of both contours (without changing force orientation, Figure 5.3b). Although a minimal thickness parameter ($R_T$) is defined *a priori*, the final segmentation result with thinner mid-walls between contours (*i.e.* minimal distance lower than $R_T$) is allowed, increasing the flexibility of the model to abnormal situations. Nevertheless, when the thickness between both contours is too small, high penalization is applied requiring both contours to retreat (Figure 5.3c). Then, the minimization continues and correct refinement to the middle wall is possible.

**B. Expansion to *n*-contours**

For $n$ contours (and specifically for atrial region segmentation, *i.e.* LA, RA, Ao), a total of $n$ energies ($n = 3$ for the atrial region) are now required to control each contour as described in section 5.2.1. Contrary to section 5.2.2, multiple competitions between the $n$ contours are now considered requiring a generalization of equations (5.13) and (5.14) to:

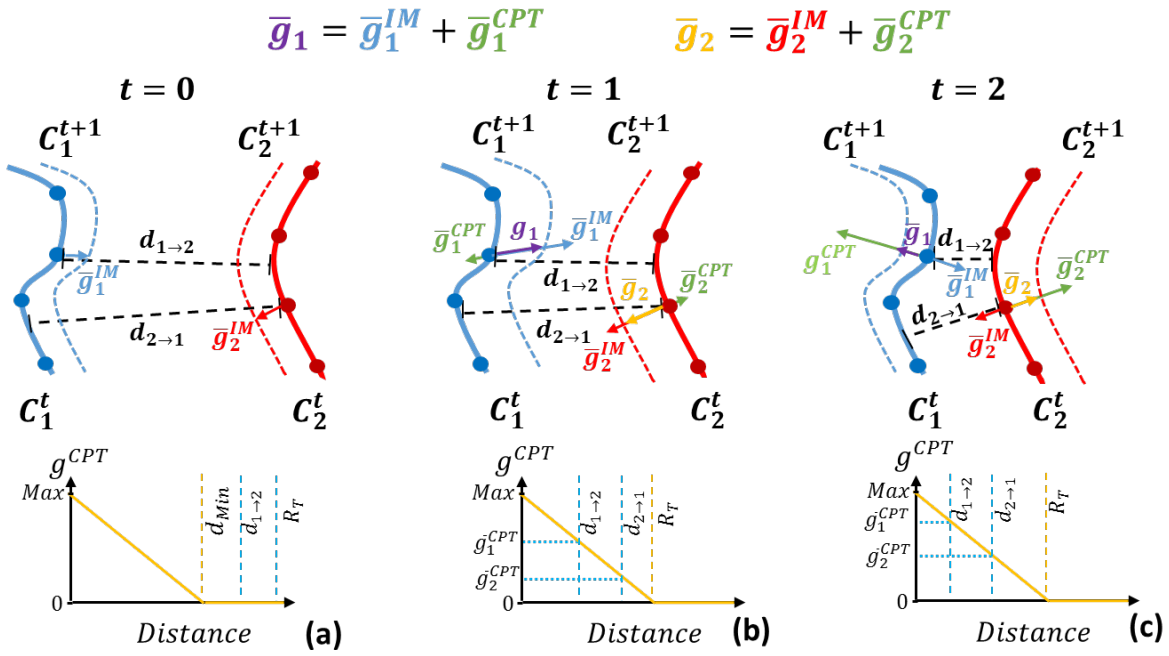


**Figure 5.3 – Schematic diagram of the competitive strategy used.**
(a) No competition is used since the contours are too far; (b) competition is applied but the contour is still moving in the same direction; (c) contours changed their evolution direction due to the small distance between them. Solid and dashed lines represent the contours at time t and t+1, respectively.

$$\bar{g}_i(\boldsymbol{x}^*) = \bar{g}_i^{IM}(\boldsymbol{x}^*) + \sum_{m=1,m\neq i}^{n} \alpha_{i\to m} \cdot \bar{g}_{i\to m}^{CPT}(\boldsymbol{x}^*), \qquad \alpha_{i\to m,i\neq m} = \left(1 - \left|\alpha_{m\to i,i\neq m}\right|\right), \tag{5.17}$$

with,

$$\bar{g}_{i\to m,i\neq m}^{CPT}(\boldsymbol{x}^*) = \left(R_T - \boldsymbol{\psi}^{i\to m}\right).H\left(R_T - \boldsymbol{\psi}^{i\to m}\right). \tag{5.18}$$

Note that equation (5.17) combines all the $n$ contour pairs. As such, in each iteration, the distance between all pairs is computed and all the thin regions refined through the competition between the nearest contours.

The proposed competitive implementation is integrated on both BEAS-threshold and contour refinement stages. During the BEAS-threshold, the competitive strategy is used to: 1) improve the LA-RA-Ao contours initialization thanks to the spatial interactions between them; and 2) define the valve plane through the competition between atria and ventricles. Contrarily, in the contour refinement stage, the LA-RA-Ao contours compete between them to accurately identify the atrial boundaries. The ventricles are not refined throughout the segmentation due to the RV anatomy and the difficulty in describing it using an explicit function.

In Appendix 5.6.A, the mathematical formalism required to expand the proposed competitive strategy for a traditional level-set model is presented.

## 5.3. Experiments and results

Three experimental scenarios are used to prove the advantages of the proposed competitive BEAS for atrial segmentation, namely atrial region evaluation in CT (section 5.3.1), LA benchmark in CT (section 5.3.2) and atrial region evaluation in MR (section 5.3.3).

Two major comparisons are addressed: 1) differences between the competitive BEAS against the free-evolution strategy, and 2) comparison of the competitive strategy with state-of-the-art methods. For each experiment, one observer was responsible for identifying the points required to initialize the method through one click in each chamber and three clicks in the Ao.

### 5.3.1. Atrial region assessment using CT

#### A. Description

Forty-one datasets retrospectively obtained in the clinical practice from patients with suspicion of pathology in the atrial region were used to validate the proposed competitive approach. Specifically, patients with pacemaker, mitral and aortic prosthetic valves, atrial body enlargement and candidates to pulmonary vein ablation were included. ECG-gated cardiac

multi-slice CT images were acquired with multi-detector Siemens CT scanner, Table 5.1. Both end-diastolic and end-systolic phases were included.

**B. Ground truth generation**

The LA and RA segmentation was performed by one expert using the semi-automatic CARTO3 segmentation tool (Biosense Webster, Diamond Bar, CA, USA), followed by manual corrections. More details about the segmentation can be obtained in Bourier *et al.* (2016). In order to identify the atrial body and similarly to the proposed by Tobon-Gomez *et al.* (2015), multiple bounding boxes were generated around the pulmonary veins, vena cava and left and right atrial appendage (LAA and RAA). All bounding boxes were drawn around the ostia of each structure. ParaView (Kitware, Inc.) (Squillacote and Ahrens, 2007) was used to visualize the surface generated by the expert, and to identify the multiple bounding boxes. Mitral valve and tricuspid valve planes were obtained through the following steps: 1) manual delineation of the valve region in several rotated slices, and 2) plane fitting using all scattered points. Furthermore, aortic tract manual delineation was performed through an *in-house* framework (Queirós *et al.*, 2016). Initially, three points along the aortic tract were manually defined to generate a centerline. Then, several planes (25-30 planes) perpendicular to the centerline were used to perform multiple manual 2D delineations. Finally, all scattered points were transformed into a 3D surface. Of note, all bounding boxes and planes were only used to evaluate the segmentation performance, not interfering in the segmentation pipeline.

**C. Implementation details**

The Canny edge detector was computed using a sigma of 1.5 mm, and a lower and upper threshold of 0.7 and 0.9, respectively. $\lambda_i^R$ was set to 0.5 during the initialization, and $\lambda_i^R = 20$ in segmentation. Regularization through curvature analysis ($\lambda_i^C = 20$) was only applied in the RA, RV and LV. Regarding the competition, Table 5.2 presents the parameters used and a $R_T$

**Table 5.1 – Acquisition parameters of the CT scanners**

| Parameter | Brilliance CT and Brilliance iCT | SOMATOM Force |
|---|---|---|
| Manufacturer | Philips | Siemens |
| No. of patients | 30 | 41 |
| Detector rows | 16-,40-,64- and 256-slices | 64, 128 slices |
| Contrast injection | 40-100 ml | 40-100 |
| Image resolution ($mm^2$) | 0.30x0.30 to 0.78x0.78 | 0.69×0.69 |
| Slice thickness | 0.33 to 1.00 mm | 0.8 |
| Matrix size | 512×512 | 512×512 |
| Nº of phases | 1 | 1 |

of 2 mm was employed (Beinart *et al.*, 2011). It may be noted that, during the initialization, the left heart controls the right heart evolution, due to the superior contrast and reduced number of artifacts usually found in the left heart. In other words, during the BEAS-threshold, the left side contours evolve freely pushing the right heart contours. Then, during the segmentation, competitive contours with equal weights ($\alpha = 0.5$) were used. The fixed threshold ($th$) was computed as the average value between the mean intensity on the selected region (window of size equal to $3 \times 3 \times 3$ mm$^3$) and the expected intensity of the atrial/aortic walls (50 HU, (Ecabert *et al.*, 2008)). The stop criteria of the BEAS-threshold method relies on the difference between mesh positions in two consecutive iterations and it finishes when small differences are found. Regarding the BEAS parameters, a total of $40 \times 40$ points were used to represent each contour. Local profiles with 10 mm inward and outward of the contour were used, and $h_{r_i} = h_{s_i} = 1$ for $i \in \{LA, RA, LV, RV\}$ and $h_{r_i} = h_{s_i} = 2$ for $i \in \{AO\}$ were applied.

**D. Statistical analysis**

The absolute point-to-surface (P2S) distance, Dice coefficient (DC) and 95$^{th}$ percentile of Hausdorff distance were computed for each chamber (LA, RA and Ao) to compare the methodology with and without competition. The influence of the virtually generated bounding boxes and mitral/tricuspid valve planes was also assessed. A paired *t*-test ($p<0.05$) between the strategy with or without competition was used to check for statistically significant differences on the results. Furthermore, a small region of interest (ROI) was created around each thin wall (aortic and atrial wall) in order to assess the segmentation accuracy in these regions. The region was defined as the largest connected component with a thickness inferior to 5 mm (computed as LA vs RA, LA versus Ao, RA versus Ao). The errors obtained with and without competition were assessed through P2S, 95$^{th}$ percentile of Hausdorff distance and a Wilcoxon matched-pair test to check for statistically significant differences ($p<0.05$). The influence of the estimated thickness parameter $R_T$ on the final result was also assessed and compared through a paired t-

**Table 5.2 – Parameters used to define the competition between surfaces $\alpha_{S1 \to S2}$**

| | | **S2** | | | | | | | |
|---|---|---|---|---|---|---|---|---|---|
| | Chambers | Initialization | | | | | Segmentation | | |
| | | LA | RA | AO | LV | RV | LA | RA | AO |
| **S1** | LA | - | 0 | 0.5 | 0.5 | 0 | - | 0.5 | 0.5 |
| | RA | 1 | - | 1 | 1 | 0.5 | 0.5 | - | 0.5 |
| | AO | 0.5 | 0 | - | 0.5 | 0 | 0.5 | 0.5 | - |
| | LV | 0.5 | 0 | 0.5 | - | 0 | - | - | - |
| | RV | 1 | 0.5 | 1 | 1 | - | - | - | - |

LA – Left atrium; RA – Right atrium; AO – Aorta; LV – Left ventricle; RV – Right Ventricle;

test ($p<0.05$) to check for statistically significant differences. Finally, the computational time of both approaches (with and without competition) was registered. All results were computed using MATLAB code (no parallelization) on an Intel (R) i7 CPU at 2.8 GHz and 16 GB of RAM. A C++ implementation of the competitive strategy was wrapped in the MATLAB Code.

**E. Results**

Table 5.3 presents the results obtained for both methodologies in terms of P2S, DC and 95$^{th}$ percentile Hausdorff distance. The RA presented the highest P2S error with 1.68 ± 0.47 mm and the Ao the lowest with an error of 0.65 ± 0.12 mm. Moreover, when comparing the competitive strategy and its free-evolution version, a superior performance was always achieved by the competitive version for all the assessed regions (Figure 5.4). Figure 5.5 presents the errors obtained when a small ROI around the aortic/atrial walls is assessed, where a clear advantage of the proposed competitive technique is observed. Globally, the strategy with competition showed a statistically significant superior accuracy when compared with the free-evolution version. The former strategy is however more computationally demanding, requiring 73.4 ± 6.9 seconds per dataset, against the 35.8 ± 3.7 seconds recorded for the free-evolution approach. Representative segmentation cases corresponding to the 10$^{th}$, 30$^{th}$, 50$^{th}$, 70$^{th}$, and 90$^{th}$ percentiles according to the average P2S error are shown in Figure 5.6. Moreover, results in patients with anatomical pathologies are presented in Figure 5.7. Finally, the influence of the $R_T$ parameter throughout the competitive strategy is shown in Figure 5.8a. No significant

**Table 5.3 – Point-to-surface (P2S) error, Dice coefficient and 95$^{th}$ percentile of Hausdorff distance obtained between the semi-automatic method (with and without competition) against the manual delineation in CT**

| Competitive | | P2S (mm) | | Dice | | 95$^{th}$ perc. Hausdorff (mm) | |
|---|---|---|---|---|---|---|---|
| | | With | Without | With | Without | With | Without |
| Left Atrium | Entire | 1.54 ± 0.32* | 1.57 ± 0.33 | 0.91 ± 0.01 | 0.92 ± 0.01 | 6.52 ± 2.41* | 6.67 ± 2.42 |
| | MV | 1.36 ± 0.27* | 1.39 ± 0.28 | 0.93 ± 0.01 | 0.93 ± 0.01 | 5.46 ± 1.87* | 5.55 ± 1.86 |
| | PV | 1.20 ± 0.20 | 1.25 ± 0.23 | 0.94 ± 0.01 | 0.94 ± 0.01 | 4.47 ± 1.63 | 4.85 ± 1.75 |
| | LAA | 1.07 ± 0.17 | 1.14 ± 0.21 | 0.95 ± 0.01 | 0.95 ± 0.01 | 3.36 ± 0.98 | 3.62 ± 1.10 |
| Right Atrium | Entire | 2.13 ± 0.51* | 2.37 ± 0.66 | 0.87 ± 0.03* | 0.85 ± 0.05 | 8.13 ± 2.18* | 8.90 ± 2.47 |
| | TV | 2.01 ± 0.46* | 2.26 ± 0.68 | 0.88 ± 0.03* | 0.87 ± 0.05 | 7.81 ± 1.97* | 8.54 ± 2.48 |
| | VC | 1.87 ± 0.47* | 2.13 ± 0.67 | 0.90 ± 0.02* | 0.89 ± 0.05 | 7.20 ± 2.03* | 8.14 ± 2.63 |
| | RAA | 1.68 ± 0.47* | 1.98 ± 0.72 | 0.91 ± 0.02* | 0.90 ± 0.05 | 6.03 ± 2.04* | 7.52 ± 3.57 |
| Aortic tract | Entire | 0.65 ± 0.12* | 0.68 ± 0.13 | 0.94 ± 0.02 | 0.94 ± 0.02 | 1.61 ± 0.33 | 1.67 ± 0.36 |

* paired t-test between With and Without competitive results ($p<0.05$). MV – Mitral Valve; PV – Pulmonary Veins; LAA – Left Atrial Appendage; TV – Tricuspid valve; VC – Vena Cava; RAA – Right Atrial Appendage.

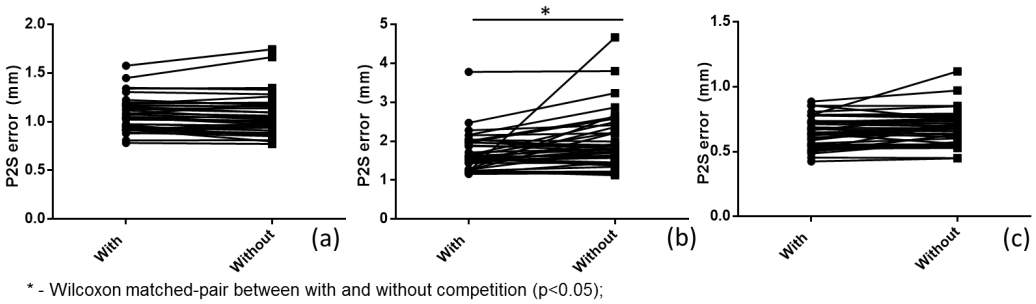


**Figure 5.4 – Error obtained with and without competition for the (a) LA, (b) RA and (c) Ao in CT.**

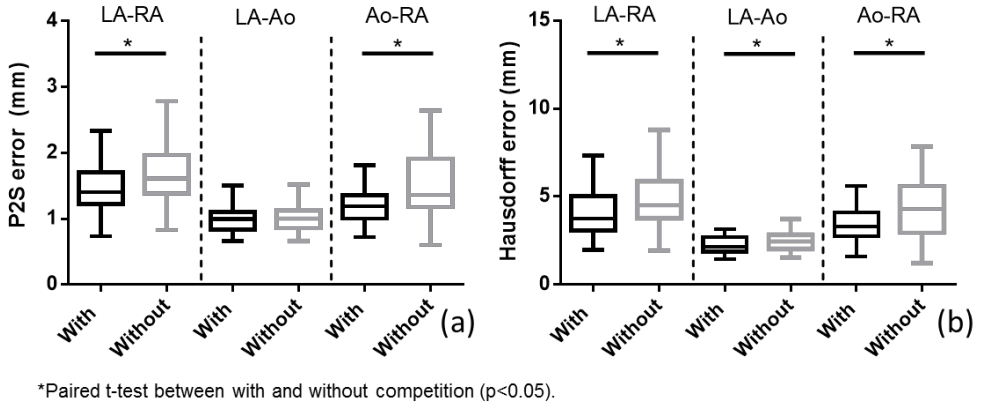


**Figure 5.5 – Point-to-surface (P2S) end 95th percentile of Hausdorff error obtained for each thin wall in CT using the proposed strategy with and without competition.**
LA – Left atrium; RA – Right Atrium; Ao – Aortic tract;

differences were observed between the selected value (*i.e.* 2 mm) and its neighbors, but in contrast, statistically significant differences were found when too high values were used.

### 5.3.2. Left atrium assessment using CT

#### A. Description

Recently, a benchmark (STACOM 2013) was published to assess the accuracy of left atrium segmentation techniques. The public database has thirty datasets, 10 datasets for training and 20 datasets for testing. Only LA segmentation methods are allowed to be evaluated with the current benchmark. Further details about acquisition and ground truth generation are indicated in Table 5.1 and in Tobon-Gomez *et al.* (2015).

#### B. Statistical analysis

The segmentation accuracy was assessed using two metrics described in the original manuscript: P2S and DC. Furthermore, the obtained result with the proposed methodology (with and without competition) was compared with the 5 best works assessed in the current benchmark (total of 9), namely a region growing formulation with rough contour initialization using an atlas-based approach (LTSI-VRG) (Sandoval *et al.*, 2013), a probabilistic atlas approach (LUB-SRG) proposed by (Stender *et al.*, 2013), a marginal space learning strategy

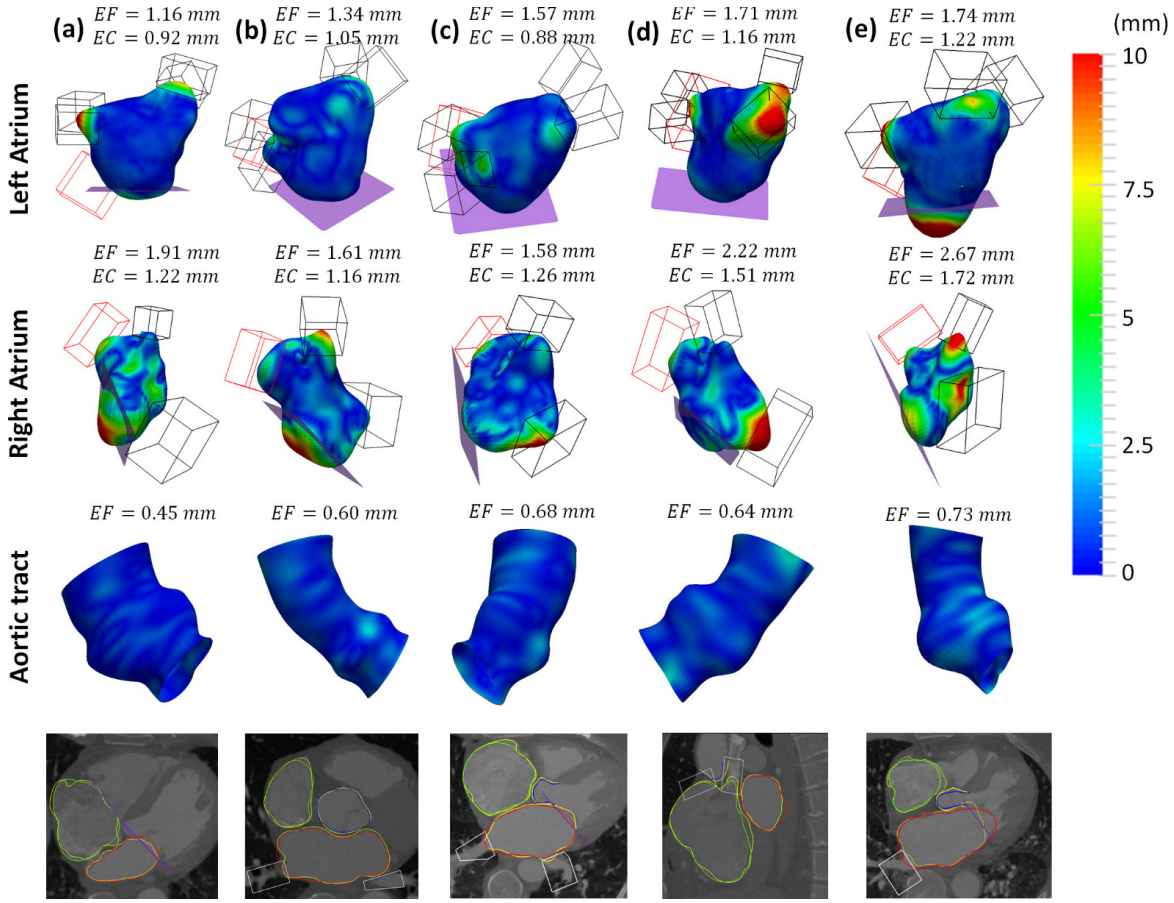


**Figure 5.6 – Segmentation results and error map (EF – entire surface, EC – cropped version) obtained with competitive BEAS technique for the cases corresponding to the 10th (a), 30th (b), 50th (c), 70th (d) and 90th (e) percentiles, according to the average P2S error.**
The bounding boxes (black boxes for pulmonary vein and vena cava, and red box for LAA and RAA) and valve planes (pink plane) are also presented. The bottom panel shows 2D slices with the semi-automatic results (red - LA, green – RA, blue - aortic root and white - bounding boxes) and the ground truth (yellow).

with (SIE-MRG) (Tobon-Gomez *et al.*, 2015) or without refinement (SIE-PMB) (Zheng *et al.*, 2008) through graph-cuts, and a multi-atlas approach with global and local transforms for LA segmentation only (UCL-1C) (Zuluaga *et al.*, 2013). Inter-observer variability is also available. Furthermore, the added-value of the proposed approach was explored, through a comparison of the result obtained with and without competition using an unpaired t-test ($p<0.05$).

### C. Results

Figure 5.9 shows a comparison between the proposed methodology (competitive BEAS) and the state-of-the-art techniques for LA body segmentation. The proposed strategy obtained a P2S error of 0.89 ± 1.03 mm (with competition), proving its robustness and accuracy with results similar to the remaining techniques. Regarding the competitive strategy, statistically significant differences ($p = 0.02$) were found against the free-evolution technique in terms of P2S error.

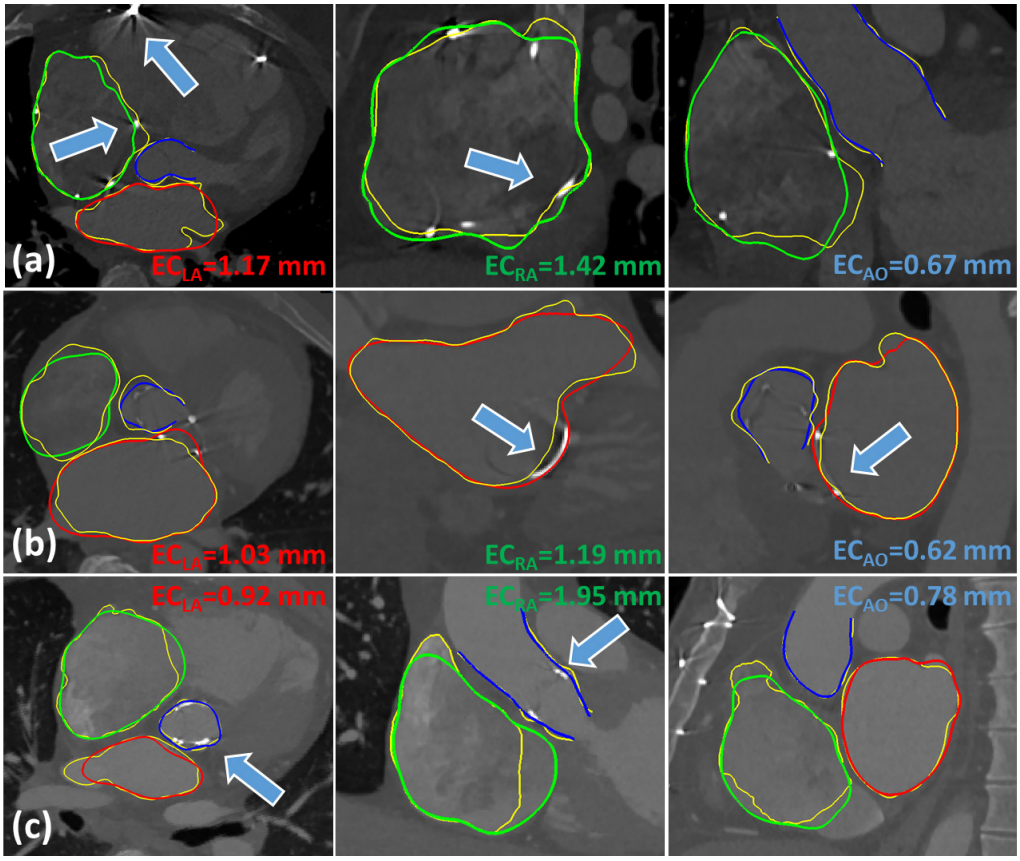


**Figure 5.7 - Segmentation result example in pathological patients.**
(a) Patient with pacemaker; (b) prosthetic mitral valve and (c) prosthetic aortic valve. The left atrium (LA) is represented as red, the right atrium (RA) as green and blue (Ao) is used for the aortic tract. Yellow contours represent manual delineations and the arrows the pathology. The error ($E_C$) is presented using a cropped surface (removing bounding boxes and valve plane).

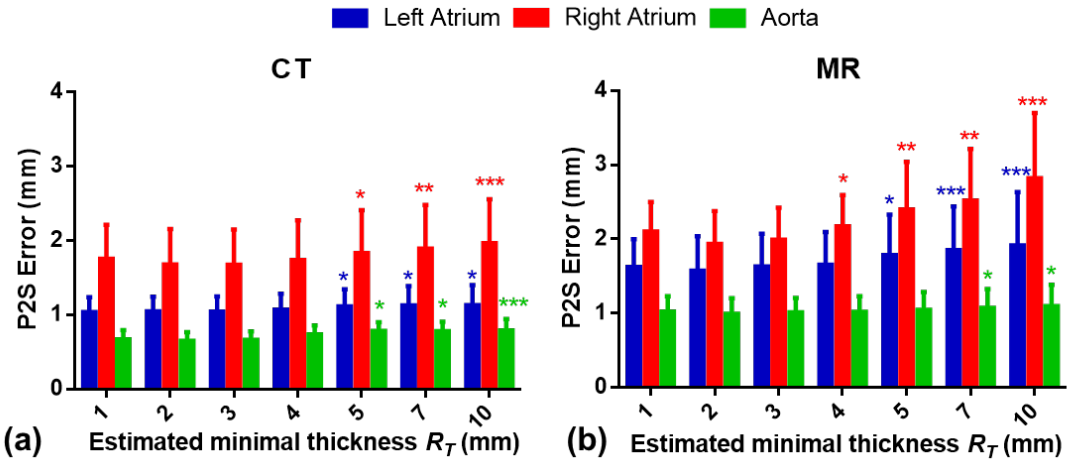


**Figure 5.8 - Influence of $R_T$ parameter in the final segmentation result in (a) CT and (b) MR images.**
* $p < 0.05$ in paired t-test between each result and the selected one (*i.e.* 2 mm).

### 5.3.3. Atrial region assessment using MRI

#### A. Description

Similarly to section 5.3.2, the current data was obtained from an available benchmark (Tobon-Gomez *et al.*, 2015). Again, 30 datasets were acquired, 10 datasets are used as training,

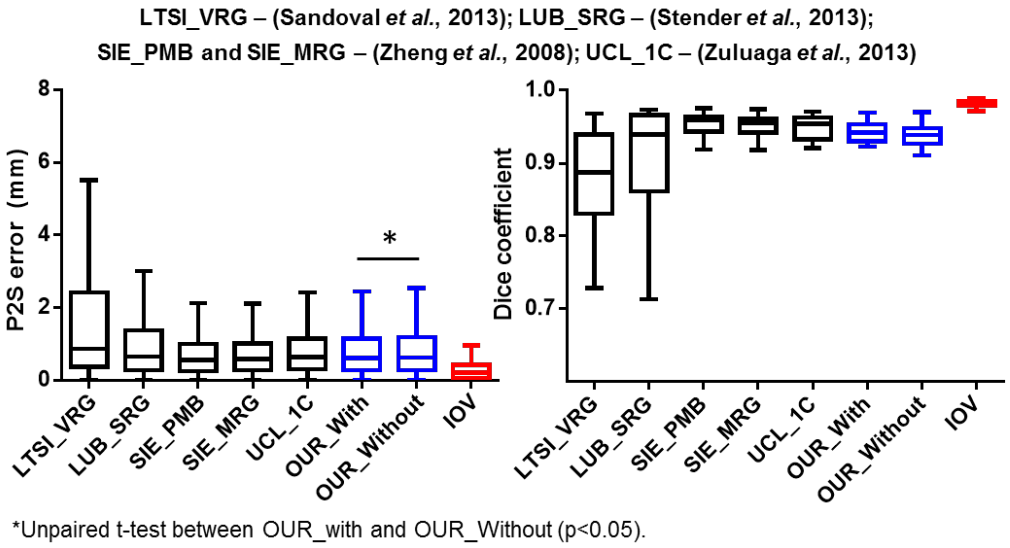


**Figure 5.9 - Assessment of the proposed methodologies (termed OUR, with and without competition) for LA segmentation in CT and comparison against the best results available in the LA benchmark.**
The team's name were defined based on Tobon-Gomez *et al.* (2015). IOV is the inter-observer variability.

while the remaining 20 cases are used for the algorithm evaluation. The reader is kindly directed to Tobon-Gomez *et al.* (2015) for further details about the image acquisition protocol.

**B. Ground truth generation**

The LA was segmented using the strategy described by Tobon-Gomez *et al.* (2015). Contrarily to the CT data, no limitations were imposed on these datasets, allowing their application for further studies. Thus, and in order to assess the accuracy of the competitive strategy in a different imaging modality, a manual contouring of the RA and the aortic tract was additionally performed. The RA was segmented using the MITK software (Medical Imaging Interaction Toolkit) (Wolf *et al.*, 2005), where multiple 2D slices were delineated and then interpolated to a 3D surface. Moreover, bounding boxes and valve plane were generated as explained in section 5.3.1. Regarding the aortic tract, it was segmented as described in 5.3.1B.

**C. Implementation details**

Due to the particularities of the MRI datasets (*i.e.* noisy images, with superior pixel spacing when compared with a CT acquisition), small modifications were required in specific parameters of the segmentation methodology, namely: 1) $\lambda_i^R$ was set to 1 during the threshold stage; 2) each contour was discretized by 32 × 32 points; and 3) $h_{r_i} = 1, h_{s_i} = 2$ for $i \in \{LA, RA\}$. The optimal parameters were estimated using the training datasets only.

**D. Statistical analysis**

The LA body segmentation was assessed in terms of P2S error and DC using the software released with the benchmark. Moreover, the result obtained with the proposed

methodologies was compared with the 5 best strategies described by Tobon-Gomez *et al.* (2015) (a total of 8 were presented). In detail, the multi-atlas approach described by Zuluaga *et al.* (2013) with an atlas database encompassing all cardiac cavities (UCL4C) or LA only (UCL1C) and the 2D segmentation strategy with threshold-based techniques and circularity shape descriptors (TLEMCEN) (Ammar *et al.*, 2013) were included. Furthermore, two versions of the strategy proposed by Sandoval *et al.* (2013) were also considered, one with label fusion through majority voting (LTSI-VRG) and another using the STAPLE (LTSI-VSRG) algorithm. Inter-observer variability is also available. The RA and Ao were assessed in terms of P2S, DC and 95$^{th}$ percentile of Hausdorff distance. A paired *t*-test ($p<0.05$) was computed to check for statistically significant differences between the technique with and without competition. Similarly to section 5.3.1D, the errors found at aortic/atrial wall were assessed using the P2S error, the 95$^{th}$ percentile of Hausdorff and Wilcoxon matched-pair ranked test ($p<0.05$). Furthermore, the influence of the $R_T$ parameter on the atrial segmentation in MRI was also evaluated. Finally, the computational time required by each methodology was recorded.

**E. Results**

Figure 5.10 presents the results obtained by the proposed technique for LA segmentation using the benchmark. The proposed strategy obtained a mean error of 1.57 mm, proving to be similar against the remaining strategies available in literature. A similar performance was obtained by the proposed method when compared with the inter-observer variability. Figure

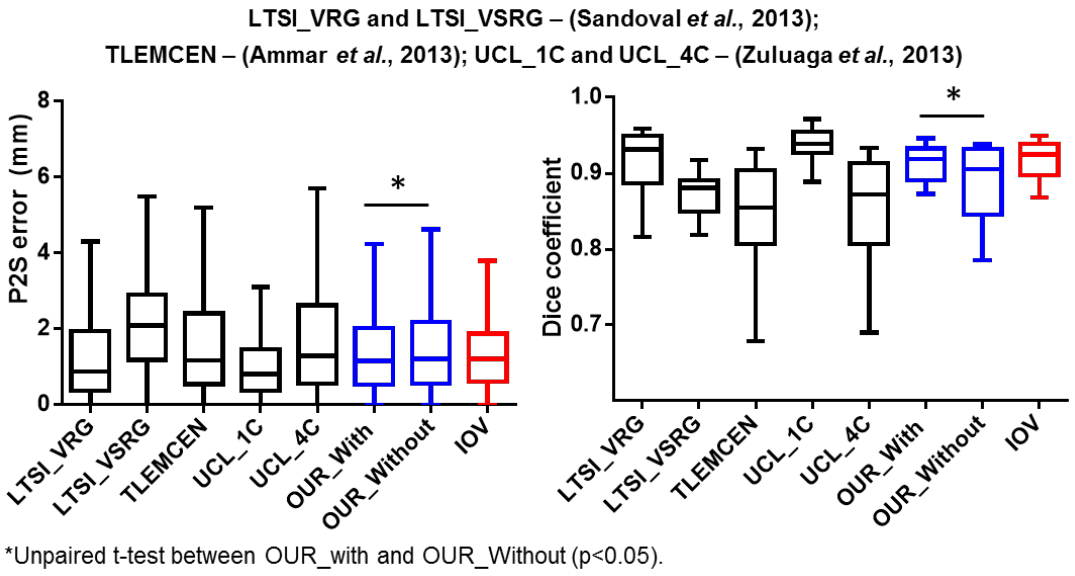


**Figure 5.10 - Assessment of the proposed methodologies (termed OUR, with and without competition) for LA segmentation in MRI and comparison against the best results available in the LA benchmark.**
The team's name were defined based on Tobon-Gomez *et al.* (2015). IOV is the inter-observer variability.

5.11 presents the results in each individual dataset, proving the clear advantages of the competitive strategy (with statistically significant differences, p=0.04) against the traditional BEAS formulation. Regarding the remaining chambers, Table 5.4 indicates the accuracy of each semi-automatic contouring against the manual one. The influence of each region (RAA, vena cava, valve plane) in the final contour was also assessed, showing a correct and accurate definition of the RA body and aortic tract. Again, the competitive strategy proved to be more robust than the free evolution technique, with statistically significant differences. Specifically, the RA proved to benefit most from the proposed competition formulation. Looking for the wall region analysis, a correct definition of these smooth and thin regions was only achieved by the competitive BEAS (Figure 5.12). Furthermore, the sensitivity of the segmentation result for different $R_T$ thickness parameters was evaluated (see Figure 5.8b), presenting a similar trend to the one obtained for CT datasets. Regarding the computational time, the competitive BEAS required 28.9 ± 6.2 seconds, while the traditional BEAS only needed 16.0 ± 1.4 seconds. Representative example results are presented in Figure 5.13.

**Table 5.4 - Point-to-surface (P2S) error, Dice coefficient and 95th percentile of Hausdorff distance obtained between the semi-automatic methods against the manual delineation in MR**

| Competitive | | P2S (mm) | | DICE | | 95th perc. Hausdorff (mm) | |
|---|---|---|---|---|---|---|---|
| | | With | Without | With | Without | With | Without |
| Right Atrium | Entire | 2.74 ± 0.63* | 2.98 ± 0.61 | 0.83 ± 0.04* | 0.80 ± 0.05 | 10.76 ± 2.80 | 11.39 ± 2.56 |
| | TV | 2.66 ± 0.65* | 2.91 ± 0.64 | 0.84 ± 0.04* | 0.83 ± 0.05 | 10.38 ± 2.90 | 10.96 ± 2.55 |
| | VC | 2.26 ± 0.49* | 2.49 ± 0.51 | 0.88 ± 0.03* | 0.87 ± 0.04 | 8.64 ± 2.48* | 9.42 ± 2.19 |
| | RAA | 1.94 ± 0.44* | 2.20 ± 0.51 | 0.90 ± 0.03* | 0.88 ± 0.04 | 6.54 ± 1.97* | 7.71 ± 2.11 |
| Aortic tract | Entire | 0.99 ± 0.21* | 1.21 ± 0.58 | 0.88 ± 0.04* | 0.86 ± 0.07 | 2.52 ± 0.66* | 3.11 ± 2.12 |

* paired t-test against zero (p<0.05). TV – Tricuspid Valve; VC – Vena Cava; RAA – Right Atrial Appendage.

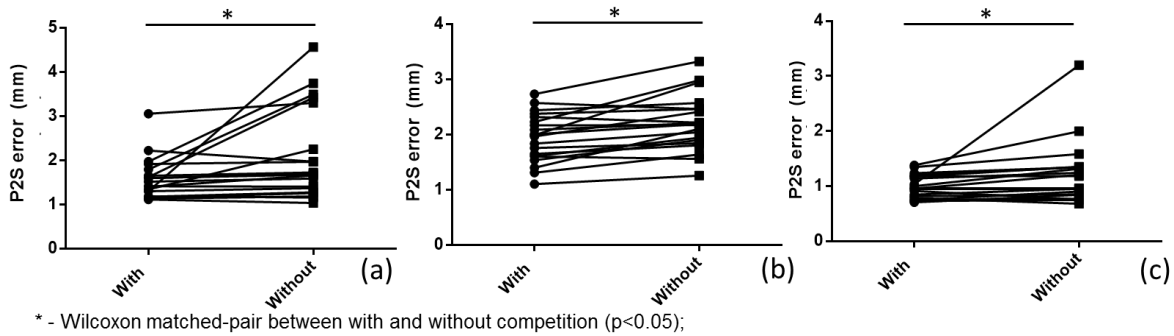


**Figure 5.11 - Point-to-surface error obtained with and without competition for the LA (a), RA (b) and Ao (c) in MRI.**

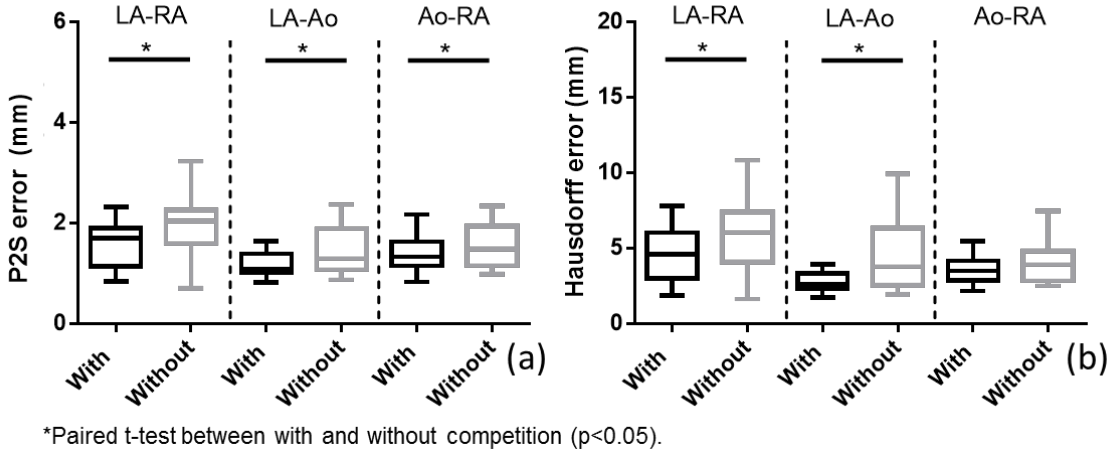


**Figure 5.12 - Point-to-surface (P2S) error and 95th percentile of Hausdorff error obtained for each thin wall in MRI using the proposed strategy with and without competition.**
LA – Left Atrium, RA – Right atrium, Ao – Aortic tract.

## 5.4. Discussion

In this study, we present a novel technique to accurately segment multiple structures. In opposition to the majority of the state-of-the-art techniques, constraints to allow thin walls between multiple structures are embedded. Furthermore, when compared with previous works addressing the same issue (Gao *et al.*, 2012b), the proposed formulation appears to present a superior performance for the delineation of heterogeneous and noisy walls, keeping a minimal wall thickness for all the different scenarios. This technique was integrated into an efficient 3D segmentation framework and the advantages of the novel competitive methodology was proven for atrial body segmentation. Note that evaluation of the mid thin walls is relevant in several clinical evaluations, such as optimal inter-atrial puncture location for transseptal puncture (Morais *et al.*, 2017b) and for the evaluation of the aortic wall thickness (Malayeri *et al.*, 2008). To the author's best knowledge, no previous work was presented for accurate segmentation of the atrial region with intact mid-thin walls, being a clear novelty of this work. Previous works as Ecabert *et al.* (2011) and Zuluaga *et al.* (2013) simply merge the different contours (if overlap happens) or prevented gap/vacuum regions, being sub-optimal strategies for clinical evaluation of these thin regions. Although no significant differences are expected between the merged contour strategies and our approach in terms of segmentation evaluation metrics (e.g. P2S or Dice), the merged contour approaches are not suitable for novel image-guided minimally invasive interventions focused on atrial wall as presented by Bourier *et al.* (2016). A first evaluation of the proposed competitive approach was performed on atrial region segmentation in CT images. The obtained results proved the high accuracy of the method, with errors similar

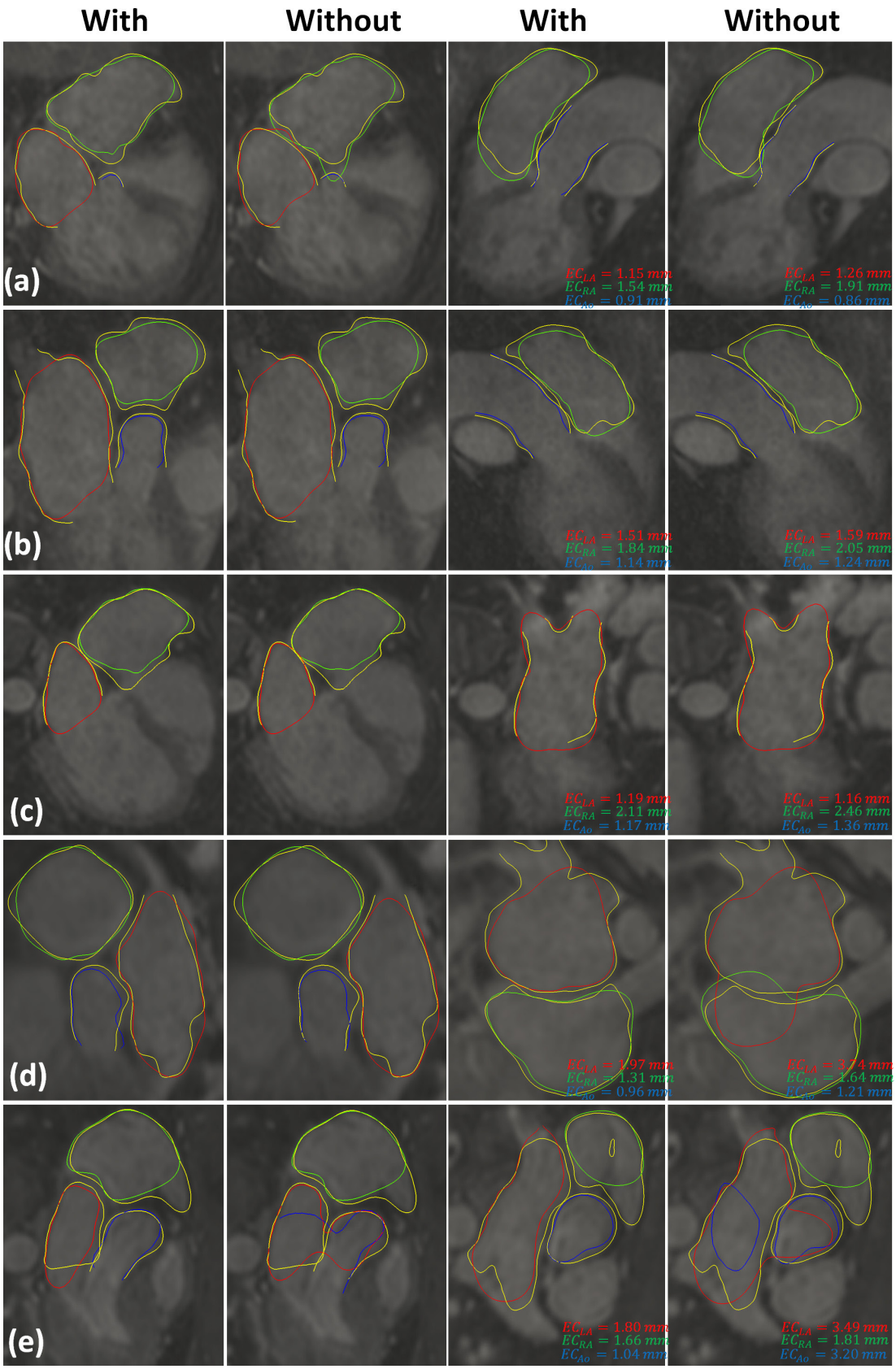


**Figure 5.13 - Segmentation results obtained with/without competitive technique for the cases corresponding to the 10th (a), 30th (b), 50th (c), 70th (d), and 90th (e) percentiles, according to the average P2S error.** Semi-automatic left atrium is represented as red, the right atrium as green and blue is used for the aortic tract. Yellow contours represent manual delineations. The error is presented using a cropped surface (removing bounding boxes and regions below the valve plane).

to the ones found in other studies in literature (Ecabert *et al.*, 2011; Kirişli *et al.*, 2010; Zheng *et al.*, 2008), particularly for LA (Figure 5.9) and aortic tract (Table 5.3). Indeed, the proposed double-stage segmentation approach (*i.e.* BEAS-threshold and BEAS-segmentation) showed its added-value and robustness for atrial segmentation. While the threshold-based stage uses a fast contour growing approach to obtain a rough estimation of the target anatomy, the segmentation stage applies a localized/regional approach to accurately refine the contour to the real anatomic boundaries. Both stages are boosted by the edge-based and regularization terms, which always pushes the contour to the nearest edge (*i.e.* potential optimal transition) and prevents incorrect shapes caused by vacuum regions or noise (e.g. RA), respectively. It should be noted that pure segmentation without an initialization stage is not feasible, since the current initialization (*i.e.* sphere in the middle of the cavity) is too far from the real boundaries being therefore sensitive to local minima or even noisy regions inside the blood pool. Moreover, the proposed method showed its high and superior performance for segmentation of mid thin walls due to the novel proposed competitive strategy (Figure 5.5). Since the current experiment was only focused on the atrial body and the effectiveness of the competitive approach for atrial region segmentation, 3D bounding boxes were virtually generated by one experienced observer to separate the atrial body from the great vessels. Similar strategies to compute the segmentation errors have been presented in literature (Ecabert *et al.*, 2011; Zheng *et al.*, 2008). Furthermore, we would like to emphasize that the current BEAS formulation, based on explicit functions, intrinsically imposes shape limitations on the model, preventing segmentation of the atrial body plus great vessels. For that, a combination of different explicit functions (one function to the body and another to each vessel) would be required. As expected, the errors significantly reduce from the entire mesh situation until the totally cropped version. The biggest differences were found when the appendage's bounding box was considered, which is explained by the variable and complex anatomy found (Tobon-Gomez *et al.*, 2015) (Table 5.3). Nevertheless, previous segmentation strategies showed similar limitations to capture the appendage region (Ecabert *et al.*, 2011; Tobon-Gomez *et al.*, 2015; Zheng *et al.*, 2008). Moreover, the crop through the valve plane showed a small reduction on the final error result, proving the robustness of the initialization technique, *i.e.* the use of the ventricular region during BEAS-threshold to compete with the atria and consequently define the valve planes.

An inferior performance was found for the RA body (Table 5.3 and Figure 5.6). Several issues are typically described in RA segmentation (Ecabert *et al.*, 2011; Zheng *et al.*, 2008), namely: 1) difficulties to distinguish between vena cava region and atrial body, 2) noisy blood pool due to the contrast in certain regions, and 3) cumbersome tricuspid valve identification.

Nevertheless, the proposed initialization strategy proved to be able to deal with these issues, where the well-defined and well-contrasted left heart works as a barrier for the right heart. The competitive approach intrinsically includes spatial constraints between contours, easing and improving the segmentation of noisy regions as typically found in the RA. As such, while the left heart is allowed to freely evolve due to the high signal-to-noise ratio found in the LA body and the clear edge map obtained, the right heart contour is always controlled by the left heart during the BEAS-threshold. Thus, contours' overlap is prevented, by having the right heart surfaces pushed when initialized inside the left heart region.

Figure 5.4 evidenced the importance of this competitive initialization for RA segmentation, with significant differences between the strategy with and without competition. In fact, a competitive strategy with confidence terms was never presented before. Furthermore, our competitive methodology is able to deal with all BEAS shapes (*i.e.* cylindrical, spherical, among others), being a clear advantage and an added-value for this generic framework. We would also like to emphasize that the required minimal thickness parameter ($R_T$) does not have a high influence in the final segmentation result (Figure 5.8a). Since $R_T$ is only used as a threshold value to initialize the competition process, and since walls thinner than $R_T$ are still allowed in the current implementation, optimal selection of the $R_T$ parameter is not required. However, for extreme values, differences are observed due to a high penalization. Regarding the computational time, although the competitive approach is significantly slower than the normal free-evolution BEAS, it is still attractive and notably faster than previously presented multi-structure segmentation techniques with competitive contours (Faisal *et al.*, 2015).

Similar observations were obtained for MRI datasets (Table 5.4). However, larger errors were obtained when compared with the CT results. A similar trend (*i.e.* higher errors in MR data) was found for the remaining state-of-the-methods that segment both CT/MR images and even in terms of inter-observer variability. MR segmentation is more challenging than CT due to the larger pixel size (approximately four times larger than in CT) and inter-slice spacing and the noisy blood pools found in MR (Figure 5.13), as clearly stated in Tobon-Gomez *et al.* (2015). Furthermore, the performance of the edge map is sub-optimal when compared to the CT one due to the multiple transitions found in the atrial bodies, and the holes found in the thin walls. In this sense, and in opposition to the observed in CT, significant differences were found in the entire atrial region between the free-evolution and the competitive BEAS approaches (Figure 5.11). In order to increase the accuracy of the atrial segmentation, we believe that a better initialization (anatomic initialization instead of a point in the middle of the atrial body) and even a complete segmentation of the atrial anatomy (body plus vessels) would be required.

Regarding the LA benchmark for MR (Figure 5.10) (Tobon-Gomez *et al.*, 2015), the proposed methodology proved to be competitive against the best strategies, and similar to the inter-observer variability. It should be noticed that only a few methods were able to accurately segment the LA in both CT and MR, all being computationally demanding strategies, such as atlas-based techniques (Tobon-Gomez *et al.*, 2015; Zuluaga *et al.*, 2013), and requiring reference/atlas cases during the segmentation stage, which constraints the versatility and robustness of the method to the shape variability found in the reference cases. Nevertheless, the proposed methodology is computationally more attractive and no strong assumption (*i.e.* no training dataset) is required, with the relative position between the different cavities of the atrial region being sufficient to achieve successful results. Similarly to the CT evaluation, we also assessed the influence of the estimated $R_T$ parameter in the final MR result (Figure 5.8b), and no significant differences were found between the selected parameter (*i.e.* 2 mm) and the neighboring options. This result proved that exhaustive tuning of this parameter is not mandatory, proving the robustness of this strategy. Indeed and although different $R_T$ values could be selected for the inter-atrial and aortic wall problems, this result also justifies why we applied the same wall thickness for both scenarios.

Overall, the added-value of the proposed competitive approach was easily observed for the segmentation of atrial region and its heterogeneous thin mid walls (Figure 5.5, Figure 5.12 and Figure 5.13). Merged contours were always prevented by the proposed approach, which was not obtained by the traditional approach. Moreover, the need for competitive approaches was more pronounced in noisy situations (e.g., inter-atrial septal wall in MRI, Figure 5.13). In these situations (*i.e.* missing walls), total overlap between contours is obtained with the free evolution strategy (Figure 5.13e), since no boundaries/transitions are found during the segmentation process. Nevertheless, it should be noted that correct segmentation of the mid-thin walls is not only caused by the competitive formulation, depending on the remaining segmentation terms too. The competitive approach only locally constrains the contour evolution when they are too near, reducing the step size used throughout the contour evolution and allowing a correct refinement of the contours to the real anatomy.

Finally, we would like to mention that the implementation of this technique in a different framework (such as the traditional level sets) is also a viable option, allowing the application of the competitive method for segmentation of more complex shape scenarios (see Appendix 5.6.A). Moreover, although the proposed method was proven to be accurate for atrial region segmentation in MR and CT, the competitive approach is generic and it also shows potential for a multitude of applications in multiple imaging modalities, such as: segmentation of left

ventricular myocardial wall ((Queirós *et al.*, 2014), see Appendix 5.6.B), segmentation of both "true" and "false" lumen in aortic dissection ((Chen *et al.*, 2013), see Appendix 5.6.C), carotid artery bifurcation wall (Arias-Lorza *et al.*, 2016), pelvic cavity (Ma *et al.*, 2012), among others.

## 5.5. Conclusion

The proposed competitive approach proved to be suitable for atrial region segmentation problems with results similar to other state-of-the-art methods. No merging/overlap of the multiple contours was obtained, which was not possible with the free-evolution version. Moreover and in opposition to the remaining methods described in the literature, the proposed framework showed its clear added-value for the segmentation of mid thin walls. Finally, segmentation of heterogeneous/noisy regions, bad image quality and missed walls cases were significantly improved with the proposed competitive approach.

## 5.6. Appendixes

### Appendix A - Generalization for a standard level-set framework

In a standard level-set framework as described by Lankton and Tannenbaum (2008), the general expression of its energy is formulated as:

$$E = \int_{\Omega} \delta_{\phi}(\boldsymbol{x}) \int_{\Omega} B(\boldsymbol{x},\boldsymbol{y}).F(\boldsymbol{y})d\boldsymbol{y}d\boldsymbol{x}, \tag{5.A.1}$$

with,

$$F(\boldsymbol{y}) = f_{in}(\boldsymbol{y}).H_{\phi}(\boldsymbol{y}) + f_{out}(\boldsymbol{y}).(1 - H_{\phi}(\boldsymbol{y})), \tag{5.A.2}$$

where, $f_{in}$ and $f_{out}$ define the energy criteria for the interior and exterior of the interface $\Gamma$. $H_{\phi}$ is the Heaviside operator applied to the level-set like function $\phi$. Its expansion for multi-structure segmentation problems is straightforward, as described in equation (5.2). Multiple energies (*i.e.* one per contour $i$) are used ($n$ energies), which are posteriorly combined during the optimization (equation (5.2)).

The curve evolution is computed as the first derivative of each energy with respect to $\phi_i$, as exhaustively described by Lankton and Tannenbaum (2008):

$$\frac{\partial \phi_i}{\partial t}(\boldsymbol{x}) = \delta_{\phi_i}(\boldsymbol{x}) \int_{\Omega} B(\boldsymbol{x},\boldsymbol{y}).\nabla_{\phi_i(\boldsymbol{y})}F_i(\boldsymbol{y})d\boldsymbol{y}, \tag{5.A.3}$$

where $\nabla_{\phi(\boldsymbol{y})}F(\boldsymbol{y})$ is the first derivative of $F_i$ with respect to $\phi_i$.

Similarly to equation (5.17), the competition strategy between $n$ contours can be embedded in this standard framework through:

$$\nabla_{\phi_i(\boldsymbol{y})} F_i(\boldsymbol{y}) = \delta_{\phi_i(\boldsymbol{y})} \cdot \left( \bar{g}_i^{IM}(\boldsymbol{y}) + \sum_{m=1, m\neq i}^{n} \alpha_{i\to m} \cdot \bar{g}_{i\to m}^{CPT}(\boldsymbol{y}) \right), \qquad (5.A.4)$$

$$\alpha_{i\to m, i\neq m} = \left(1 - \alpha_{m\to i, i\neq m}\right),$$

with $\bar{g}_i^{IM}$ representing the image-based terms (e.g. localized Chan-Vese, among others) and $\bar{g}_{i\to m}^{CPT}$ the competition term. $\bar{g}_{i\to m}^{CPT}$ is defined as presented in equation (5.18).

**Appendix B – Application for LV segmentation in CT images**

Data Description: Five CTs selected from the database described in section 5.3.1.

Experiment and results: Both LV myocardial walls (*i.e.* endo and epicardium) were segmented with the competitive framework. The two walls were described by independent surfaces with a spherical representation. A manual initialization was required with one click in the center of the LV cavity. The same position was used to initialize the endo- and epicardial surface. The double-stage segmentation was applied as described in section 5.2 with $\lambda_i^C = 20$, $\lambda_i^R = 0.5$ (BEAS-threshold), $\lambda_i^R = 20$ (BEAS-segmentation), $R_T = 7mm$ and $\alpha_{endo\to epi} = 0$ (BEAS-threshold), $\alpha_{endo\to epi} = 0.5$ (BEAS-segmentation) and $i \in \{endo; epi\}$.

Each dataset was manually delineated, and used to assess the added-value of the competitive method for LV (Figure 5.B.1). The mean P2S error between the manual and semi-

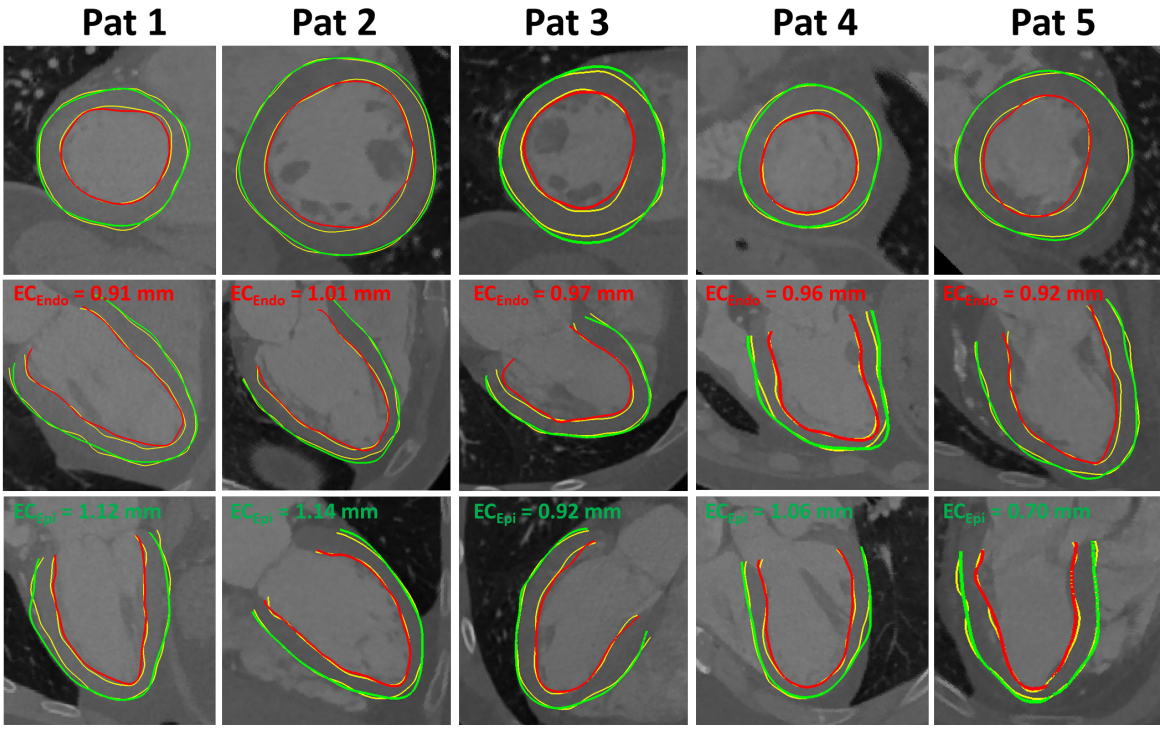


**Figure 5.B.1 – Segmentation of the left ventricular wall with the proposed competitive framework.** The automatic results was compared with manual delineations (yellow) using point-to-surface error (EC). For error assessment, both contours were clipped by a plane (defined at the left ventricular outflow tract plane) selected by the user. Red – Endocadium, Green – epicardium.

automatic result was 0.96 ± 0.04|0.99 ± 0.18 mm (endo|epicardium). The DC was 93.99 ± 0.50|95.39 ± 0.59 (endo|epicardium) and the 95$^{th}$ percentile of the Hausdorff distance was 2.76 ± 0.24 and 3.03 ± 0.45 mm for the endo and epicardium, respectively.

## Appendix C – Application for aortic dissection situation in CT images

Data description: An abdominal CT dataset (Figure 5.C.1) from one patient with aortic dissection was used. The acquisition was performed with an Aquilion ONE (Toshiba, Japan), with a slice thickness of 3 mm, image resolution of 0.78x0.78 mm$^2$ and a matrix size of 512x512. Contrast was applied and the image reconstructed at an end-diastolic phase.

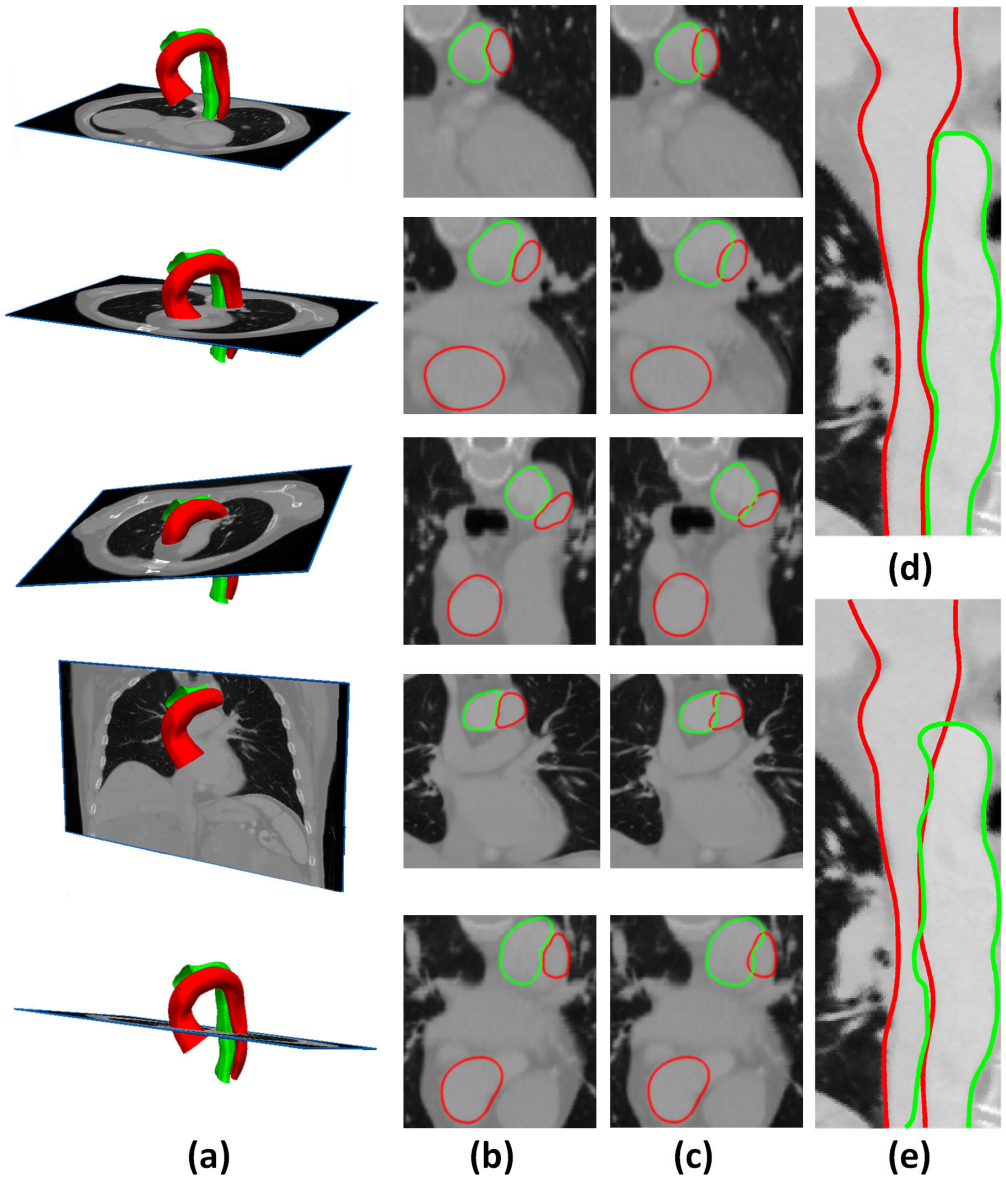


**Figure 5.C.1 - Segmentation of the aortic route (red) and the false lumen (green) through the proposed semi-automatic strategy (with and without competition).**
(a) shows the 3D segmentation result obtained with the proposed technique; (b) and (c) present multiple slices and the respective contour obtained with and without competition, respectively. (d) and (e) shows a multi-planar reconstruction of the image for each approach. It should be noticed that the final portion of the "false lumen" was not correctly segmented due to the pure cylindrical model used.

Experiment and results: In order to segment both lumens (aortic route - $L_1$ and "false lumen" - $L_2$) with the proposed framework, two independent cylindrical models were used. Similar to the atrial region case, a manual identification of some landmarks (5 points along the route for each lumen) was performed, defining the centerline of the models. Both competitive BEAS-threshold and BEAS-segmentation were used. Specifically, $\lambda_i^C = 0$, $\lambda_i^R = 0.5$ (BEAS-threshold), $\lambda_i^R = 20$ (BEAS-segmentation), $R_T = 3\ mm$ and $\alpha_{L_1 \to L_2} = 0.5$ were used.

The differences between the free-evolution and competitive BEAS approaches are presented in Figure 5.C.1. Both results were compared with a manual delineation, presenting a point-to-surface error of 1.13|0.89 mm ($L_1|L_2$) and 1.42|1.37 mm for the competitive and free-evolution BEAS, respectively. The 95$^{th}$ percentile of the Hausdorff distance was 2.56|1.99 mm (competitive) and 3.90|4.01 mm, with the Dice being 0.92|0.94 and 0.89|0.92, for the competitive and free-evolution versions, respectively.

# Chapter 6

## Automated segmentation of the atrial region and fossa ovalis towards computer-aided planning of inter-atrial septal wall interventions

This chapter has been published in *Computer Methods and Programs in Biomedicine*: **Pedro Morais**, João L. Vilaça, Sandro Queirós, Alberto Marchi, Felix Bourier, Isabel Deisenhofer, Jan D'hooge, João Manuel R. S. Tavares, "Automated segmentation of the atrial region and fossa ovalis towards computer-aided planning of inter-atrial interventions", *Computer Methods and Programs in Biomedicine*, vol. 161, pp. 73-84, 2018. Only minor changes to the original publication have been performed. The figures and sections numbers were updated with the chapter title and all references were combined in a common final section.

**Keywords:** Image segmentation; Cardiac intervention planning; Inter-atrial wall interventions; Competitive segmentation strategy; Atlas-based initialization.

**Contents**

## Abstract

Image-fusion strategies have been applied to improve inter-atrial septal (IAS) wall minimally invasive interventions. Hereto, several landmarks are initially identified on richly detailed datasets throughout the planning stage and then combined with intra-operative images, enhancing the relevant structures and easing the procedure. Nevertheless, such planning is still performed manually, which is time-consuming and not necessarily reproducible, hampering its regular application. In this article, we present a novel automatic strategy to segment the atrial region (left/right atrium and aortic tract) and the fossa ovalis (FO). The method starts by initializing multiple 3D contours based on an atlas-based approach with global transforms only and refining them to the desired anatomy using a competitive segmentation strategy. The obtained contours are then applied to estimate the FO by evaluating both IAS wall thickness and the expected FO spatial location. The proposed method was evaluated in 41 computed tomography datasets, by comparing the atrial region segmentation and FO estimation results against manually delineated contours. The automatic segmentation method presented a performance similar to the state-of-the-art techniques and a high feasibility, failing only in the segmentation of one aortic tract and of one right atrium. The FO estimation method presented an acceptable result in all the patients with a performance comparable to the inter-observer variability. Moreover, it was faster and fully user-interaction free. Hence, the proposed method proved to be feasible to automatically segment the anatomical models for the planning of IAS wall interventions, making it exceptionally attractive for use in the clinical practice.

## 6.1. Introduction

Anatomically, the atria are complex cardiac chambers with high variability between subjects (Anderson *et al.*, 2004; Tobon-Gomez *et al.*, 2015). Although their body is typically described as simple concave shapes in normal cases (Hauser *et al.*, 2008), atrial enlargement of one chamber is common, negatively affecting the other chamber and changing their anatomies (Abhayaratna *et al.*, 2006). Moreover, high spatial and shape variations are frequently found in their connected structures (*i.e.* pulmonary veins - PV, vena cava - VC and appendages) and even in specific anatomical regions (e.g. fossa ovalis - FO) (Anderson *et al.*, 2004; Hauser *et al.*, 2008; Morais *et al.*, 2017b; Tobon-Gomez *et al.*, 2015). Due to all these reasons, minimally invasive atrial interventions are difficult, requiring multiple imaging modalities for planning (mainly computed tomography - CT) and guidance (e.g. ultrasound) (Babaliaros *et al.*, 2008; Cleary and Peters, 2010). Firstly, during the planning stage, the clinician visually evaluates the richly detailed images, searching for anatomical variations. Next, throughout the intervention,

real-time images are used to guide the different instruments inside the human body until the target positions (Cleary and Peters, 2010).

Traditionally, both planning and interventional data are independently evaluated in a manual manner, being subsequently mentally combined by the expert throughout the intervention (Cleary and Peters, 2010). Nevertheless, such approach requires high experience, is time-consuming, and frequently results in procedural failures/complications (Cleary and Peters, 2010; Yao *et al.*, 2013). Thus, automated image-fusion strategies were proposed (Bourier *et al.*, 2016; Liao *et al.*, 2013). Usually, these strategies start with a segmentation of the target structures, being subsequently fused with the intra-procedural data (Bourier *et al.*, 2016). As a result, the high-detail of the pre-operative stage is transferred to the intervention, enhancing intra-procedural images (Bourier *et al.*, 2016; Cleary and Peters, 2010).

The success of the aforementioned image-fusion strategies is directly related to the accuracy of the image alignment approach (Cleary and Peters, 2010). While some researchers focused on strategies to align the pre- and intra-procedural data using 2D/3D alignment approaches (Liao *et al.*, 2013), landmark identification (Thaden *et al.*, 2016) and/or image registration (Huang *et al.*, 2009), other researchers optimized the planning stages suggesting automated solutions (Queiros *et al.*, 2016; Tobon-Gomez *et al.*, 2015). These solutions showed a performance comparable to the manual analysis (Ecabert *et al.*, 2011; Tobon-Gomez *et al.*, 2015; Zheng *et al.*, 2008), requiring none or little user input, removing or minimizing the variability between observers and reducing the time spent during the planning (Tobon-Gomez *et al.*, 2015). Specifically for cardiac applications, atlas-based (Kirişli *et al.*, 2010; Zuluaga *et al.*, 2013), deformable models (Ecabert *et al.*, 2011; Morais *et al.*, 2017c) and machine learning strategies (Zheng *et al.*, 2008) were proposed to segment the different cardiac chambers. Particularly, the methodologies described by Ecabert *et al.* (2011) and Zheng *et al.* (2008) successfully segmented the four cardiac chambers plus the attached great vessels, and the atlas-based methodology from Kirişli *et al.* (2010) proved its added-value for cardiac chamber segmentation in large databases of contrast-enhanced (Kirişli *et al.*, 2010) and non-contrast-enhanced CT images (Shahzad *et al.*, 2017). However, these solutions still present inaccurate results in the thin mid-walls, showing overlapping regions (Kirişli *et al.*, 2010) or merging of different contours (Ecabert *et al.*, 2011). As such, we recently proposed a competitive deformable model strategy to segment the atrial region (*i.e.* atrial bodies and aortic tract - Ao) with a correct delineation of the mid atrial walls (Chapter 5). Such formulation allowed correct evaluation of the inter-atrial septal (IAS) wall, allowing its application for IAS interventions (e.g. transseptal puncture) and even improving the planning of multiple minimally invasive

atrial interventions (e.g. atrial fibrillation, atrial appendage closure) (Morais *et al.*, 2017b; Wang *et al.*, 2010). However, a semi-automatic version was described in Chapter 5, requiring an initialization of each chamber. Moreover, specific landmarks/regions inside the inter-atrial wall, such as FO, were not detected.

The FO is the thinnest region of the IAS wall, presenting an oval or circular shape and usually located posteriorly, at the junction of the mid and lower third of the right atrium (RA) (Babaliaros *et al.*, 2008). It is described as a depression, composed by a thin flap (floor of the FO) and its surrounding margins designated as FO limbus (Faletra *et al.*, 2017). Since direct physical access to the left atrium (LA) is not possible, the FO is used as an access point between the RA and LA (Babaliaros *et al.*, 2008). This technique is termed transseptal puncture, which consists of a needle that is inserted percutaneously until the RA, puncturing the FO and accessing the LA. The correct identification of the FO is crucial to identify the optimal access route between both atria (Thaden *et al.*, 2016), preventing complications, or multiple puncture attempts (Morais *et al.*, 2017b). Moreover, the FO identification is also relevant in other LA interventions, namely for device selection and optimal route identification for catheter ablation, mitral valve (MV) replacement and left atrial appendage (LAA) occlusion (Faletra *et al.*, 2017; Morais *et al.*, 2017b; Wang *et al.*, 2010). Some researchers have investigated the added-value of the FO identification in a pre-interventional stage, proving that it eases the real intervention, especially for challenging anatomies (Bourier *et al.*, 2016; Jayender *et al.*, 2011; Verma *et al.*, 2011). Nonetheless, its identification is still performed manually (Bourier *et al.*, 2016; Verma *et al.*, 2011), hampering its application in the clinical practice.

To overcome the aforementioned difficulties, a fully automatic segmentation strategy is proposed in this article to generate the atrial region models and the FO in CT datasets. Both models can improve the current IAS interventional planning, making it faster, more reproducible and simpler. The method starts by segmenting the relevant cardiac chambers (*i.e.* atrial region) around the IAS wall, allowing an accurate evaluation of wall thickness and shape. The proposed segmentation method is an extension of Chapter 5, with a robust initialization through an atlas-based technique. Then, since a correct representation of the IAS wall is used, the FO region is identified by assessing the intermediate mid wall positions of all contour pairs and spatial location information.

Overall, this work introduces three novelties: 1) extension of our previously presented atrial segmentation method with a fully automatic one; 2) a novel methodology to accurately segment the FO; 3) a clinical validation of the proposed method.

This study is structured as follows. In section 6.2, a technical description of the proposed fully automatic atrial segmentation method is presented. In section 6.3, the validation experiments and their results are presented. Section 6.4 discusses the performance of the proposed method against the state-of-the-art and expected inter-/intra-observer variability. Finally, the conclusions of this study are presented in section 6.5.

## 6.2. Methods

The proposed fully automatic method comprises three sequential conceptual blocks (Figure 6.1): 1) automatic and rough identification of the cardiac chambers through an atlas-based technique with global transformation models; 2) refinement of the target region boundaries using a competitive segmentation methodology that guarantees the integrity of the mid thin walls; and 3) identification of the FO region through the combination of the patient-specific wall thickness information (extracted from the anatomical models obtained in (2)) and a set of known anatomical references that provides the spatial location.

### 6.2.1. Atlas based contours' initialization

Due to the high feasibility previously demonstrated by atlas-based techniques (Kirişli *et al.*, 2010), a similar methodology was selected to initialize our method. The traditional formulation finds the optimal transformation that aligns the target image with a labelled dataset

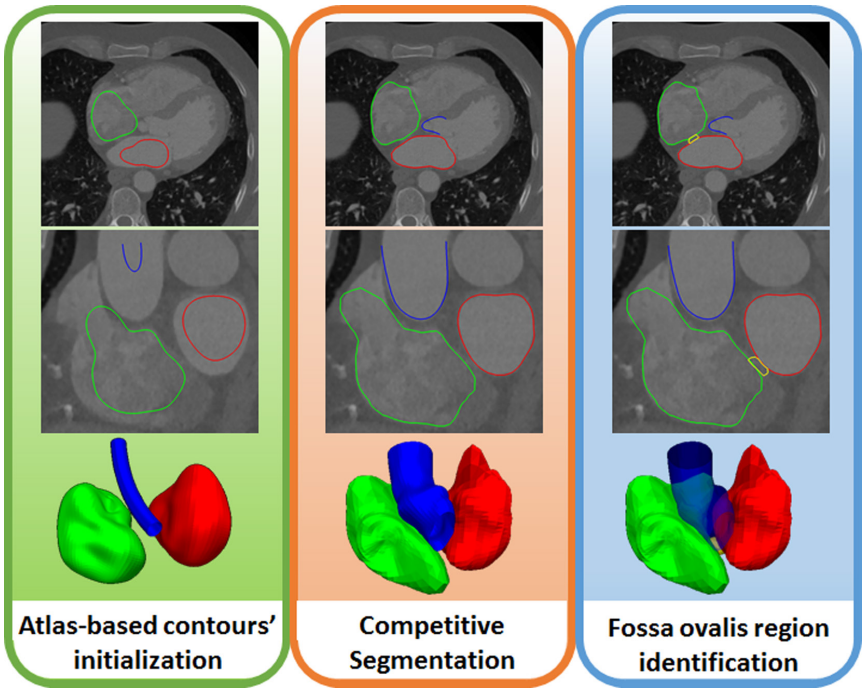


**Figure 6.1 - Overview of the proposed fully automatic method for atrial region segmentation.**
Left atrium (red), right atrium (green), aortic tract (blue) and fossa ovalis (yellow).

(designated as atlas), subsequently applying it to the labels and transferring the relevant anatomies to the target image. Different transformation models have been used, for example, global transforms (rigid or affine) are used to roughly align the different cardiac cavities and local transforms (deformable registration) are then applied to adapt the results toward the anatomy (Kirişli *et al.*, 2010; Zuluaga *et al.*, 2013). Since anatomical variations are expected, multiple atlases are usually used and all the results are combined through a label fusion process. However, the current strategies still present disadvantages: they are very time-consuming, the resulting shape variability is dependent of the atlases used, the target and atlas image should present a similar field of view (FOV) and should be in the same cardiac phase (Kirişli *et al.*, 2010; Tobon-Gomez *et al.*, 2015; Zuluaga *et al.*, 2013).

Taken into consideration all the aforementioned drawbacks, we modified the traditional atlas-based approach (Kirişli *et al.*, 2010) through:

1 - A pre-processing strategy that defines a FOV around the heart region (Figure 6.2A). The method defines a bounding box using the lung positions, which are binarized through the Hounsfield units (HU). The inferior limit of the bounding box is defined by the inferior tip of the lungs and its central position is defined by the centroid of both binarized lungs. Of note, the lungs were selected, due to its particular HU value.

2 – Instead of global and local registrations, the current strategy only applies affine transforms, allowing a fast initialization of the cardiac anatomy. Moreover, a two-stage sequential process is used: i) a full image and ii) a regional (left or right heart) alignment. The full image approach aligns the entire image (target image and atlas), initializing all chambers simultaneously (Figure 6.2B). The resulting contours are then applied to mask the left (Figure 6.2C) and right heart (Figure 6.2D) in the target image. In order to prevent overlaps between the left and right alignment stages and to compensate sub-optimal global alignments, each

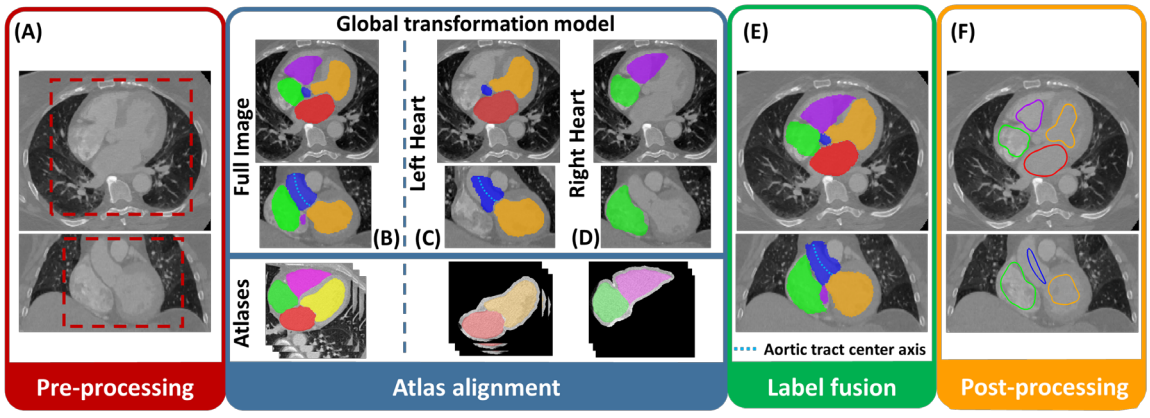


**Figure 6.2 - Atrial region initialization through an atlas-based strategy.**
(A) Cropping of the heart region; Global alignment using the (B) full cropped image and the (C) left and (D) right heart. (E) Label fusion using a majority voting and final post-processing of each label (F).

masked region is dilated (in our experiments, by 10 mm). Finally, both regions are independently aligned with masked left and right atlases, respectively.

3 – The Ao center axis (defined as 5 points) is also transferred to the target image (dashed line in Figure 6.2) using the optimal transformation. The axis is later referred to in section 6.2.2A.

4 – The final label fusion is performed for all organs at once using a majority voting (Iglesias and Sabuncu, 2015) (Figure 6.2E). Next, a post-processing based on Otsu threshold is applied (Otsu, 1975) (Figure 6.2F), improving the robustness of the method for sub-optimal results. In detail, the preliminary result of each chamber is used to mask the image, and each masked region is then divided into two groups based on its image intensities. The group with the largest number of voxels is selected as the final result. Specifically for the Ao, we fit a spline to all possible points obtained previously.

5 – Two atlas database are used: i) a public database (Kirişli *et al.*, 2010) with 8 atlas at end-diastole (ED), and ii) an *in-house* database with 4 atlas at end-systole (ES). The phase of the target image should be selected or extracted from the acquisition parameters.

### 6.2.2. Competitive Segmentation

The proposed segmentation method relies on our previously developed atrial region segmentation strategy (Chapter 5). A set of independent functions are used to control the evolution of each 3D contour (*i.e.* LA, RA, Ao, left ventricle - LV, right ventricle - RV), and a set of image descriptors are used to identify the optimal boundaries. The segmentation problem is an iterative process guided by intensity-based (signed local Yezzi – SLY) (Queirós *et al.*, 2014) and edge-based energies (unsigned distance function to the nearest edge). The edge map is generated using a Canny edge filter. In order to prevent overlapping regions, a competitive approach is applied between all the contours pairs. In detail, when the distance between two contours is lower than a pre-defined value ($R_T$), a force with opposite direction to the propagation direction is applied to each contour, locally preventing fast steps or even changing the contour evolution direction. The magnitude of the competitive force is computed based on the distance between contours, assuming a small value when the distance between contours is near $R_T$ (allowing refinement to mid walls) and applying a high penalization (preventing overlapping) when the distance is almost zero.

In order to make the method computationally attractive, the B-spline Explicit Active Surfaces (BEAS) framework is used (Barbosa *et al.*, 2012). As such, each contour uses an analytic representation described as a linear combination of B-splines. Furthermore, explicit

functions (cylindrical model for the Ao and spherical representation for the remaining contours), and independent smoothing terms are applied to each contour, reducing the dimensionality of the segmentation problem and allowing independent control of the smoothing degree of each contour, respectively.

The segmentation pipeline relies on Chapter 5, namely: 1) fast growing of the initialized contours using a competitive BEAS (CBEAS) threshold with global descriptors (Figure 6.3A); 2) Ao axis correction (Figure 6.3B); 3) contour refinement using the CBEAS segmentation with local descriptors (Figure 6.3C). Note that that the LV and RV contours are only evolved throughout the first stage (*i.e.* fast growing with CBEAS threshold) to define the valve planes. Moreover, contrary to Chapter 5, an axis correction stage is now included to compensate for sub-optimal Ao axis results throughout the 6.2.1.

As the output of this step, a set of meshes $S_i$ with $i \in \{LA, RA, Ao\}$ are obtained. Each mesh is represented by multiple vertices $\boldsymbol{x} = [x, y, z]$ and a connectivity matrix $\boldsymbol{c}$.

### A. Aortic Axis Correction

The atlas-based technique allows a coarse identification of the Ao axis, presenting a sub-optimal performance in the left ventricular outflow tract (LVOT) region, due to the lack of walls. Inspired by Queiros *et al.* (2016), we propose an Ao axis correction technique. The method starts by estimating the leaflets positions through a Canny edge filter (Figure 6.3B-2) applied on a region of interest (ROI). The ROI is defined based on the Ao contour computed at the BEAS-threshold stage (Figure 6.3B-2). Then, the obtained edge map is represented in the

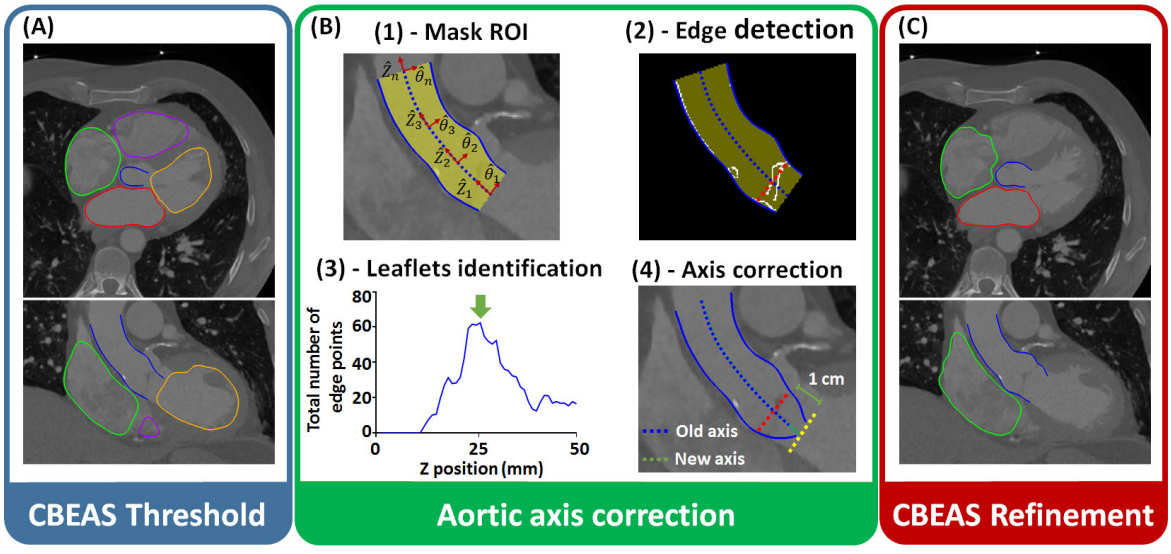


**Figure 6.3 - Pipeline of the segmentation strategy.**
(A) Fast contour growing using threshold-based competitive BEAS (CBEAS); (B) Aortic axis correction; and C) Contours refinement using local CBEAS. $\hat{\boldsymbol{\theta}}$ and $\hat{\boldsymbol{z}}$ represents the coordinates of the cylindrical space.

cylindrical space. For each $\hat{z}$ level, the number of $\hat{\theta}$ coordinates with an edge point is counted, and the level with the maximum number of edges is used to define the leaflets regions (Figure 6.3B-3). Finally, we generate a novel axis assuming a fixed spacing (in our results this spacing was defined equal to 10 mm) between the leaflets and the LVOT plane (Figure 6.3B-4), and reinitialize the Ao contour.

### 6.2.3. Fossa ovalis identification

The FO is identified by the evaluation of two different parameters (Figure 6.4): i) IAS wall thickness, computed using the boundary of the atrial contours; and ii) spatial location of the expected FO region, aligning the obtained anatomical atrial surfaces with manual delineated references that contain the FO region. While the first parameter provides accurate anatomical information, the second one computes a smooth voting map that represents the FO spatial variation. Thus, by combining both parameters, local minima caused by incorrect segmented regions or incorrect spatial locations are penalized, enhancing the real FO region.

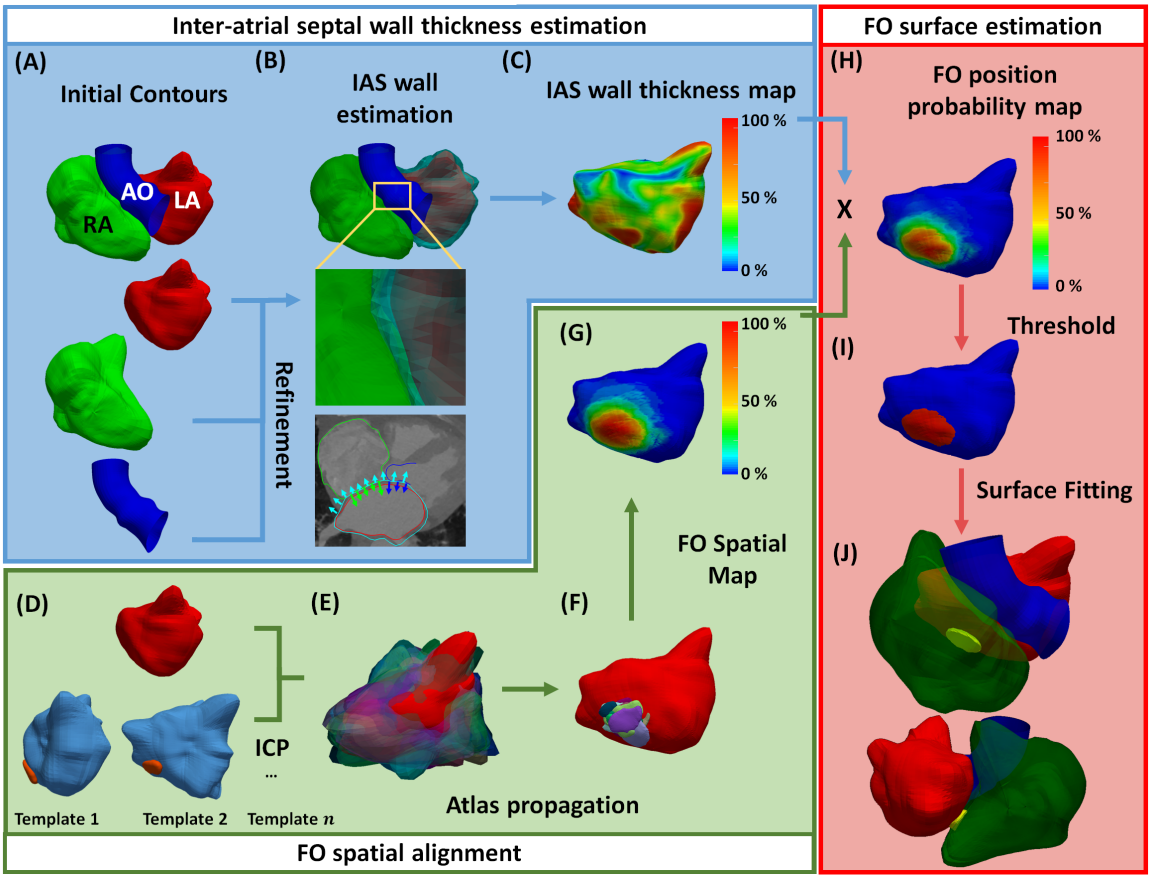


**Figure 6.4 - Strategy to automatically identify the FO.**
The method starts by (B) estimating a wall surface (cyan contour) based on the original contours (A) and (C) computing the distance between the IAS and the LA (red contour) contours to define the $\boldsymbol{IAS_{Thick}}$ map. (D) The LA contour is also aligned with a set of templates with known FO region through an iterative-closest-point (ICP) strategy. (E-F) All the template results are combined into one generating the $\boldsymbol{FO_{Spatial}}$ map (G). (H) Both maps are finally merged and a threshold is used to binarize the optimal region (I). A surface fitting (yellow surface) is applied to reconstruct the FO (J).

To simplify the searching of the FO region, the proposed method is applied to the LA surface only. In this sense, the FO at the left heart is initially located, and then interpolated towards a 3D volume using the spatial relation between chambers. The LA is used due to its superior image quality and higher segmentation accuracy (Morais *et al.*, 2017c).

**A. Inter-atrial septal wall thickness estimation**

In order to estimate the IAS wall thickness, an extra segmentation process is applied focused on the mid walls. Although this information could be extracted from atrial contours, its result is dependent on the segmented regions in all chambers. Since the FO region is located near the intersection between the inferior vena cava (IVC) and the RA body, its accurate detection is hampered due to a sub-optimal RA segmentation result in the IVC. In this sense, a new contour focused on the particularities of the IAS wall shape is initialized and evolved (Figure 6.4B). This contour is defined based on the LA position and its evolution is controlled by the previously obtained atrial models (Figure 6.4A). Thus, the wall details found between the atrial contours are directly integrated on the final IAS surface, and also applied to accurately estimate the wall thickness in regions with sub-optimal segmentation result.

Starting from the LA contour, an extra BEAS surface representing the wall thickness is initialized (Figure 6.4B). Both surfaces are combined using a coupled strategy (Figure 6.4C), meaning that the wall surface is represented based on the LA contour position ($\psi^{Pos}$) plus the wall thickness ($\psi^{Thick}$). The reader is kindly directed to Appendix 6.6.A and to Pedrosa *et al.* (2017) for further details on coupled methodologies in the BEAS framework.

The original LA contour is not updated throughout this stage, working only as an anchor for the segmentation of the mid-walls and keeping the $\psi^{Pos}$ unaltered. As such, a novel optimization process targeting the identification of the optimal thickness map $\psi^{Thick}$ is started. Specifically, the evolution of the IAS contour is guided by a SLY energy (targeting black to white transitions) with no edge terms. Negative thicknesses are not allowed, preventing overlaps between both LA and IAS contours (Queirós *et al.*, 2014).

In order to ease the wall boundaries identification, a competitive strategy is also applied between the IAS contour and the RA and Ao contours. Again, the RA and Ao are not optimized during this stage, working as a barrier. Since no empty spaces are physically expected between the IAS wall and the Ao|RA, the $R_T$ was set to 0 mm, penalizing overlapping regions only.

The wall thickness map $IAS_{Thick}$ is defined at the vertices $\boldsymbol{x}$ of the LA and computed as the distance between $S_{LA}$ and the IAS wall contours (Figure 6.4C). Finally, relative distances are computed by normalizing the value in each vertex by the maximum value in the map.

**B. Fossa ovalis spatial alignment**

The FO spatial location is estimated based on a surface alignment technique applied between the automatic and a set of templates with the desired anatomy. The references correspond to datasets manually evaluated by one expert, which includes both LA and FO surfaces (Figure 6.4D). In detail, the target LA is aligned with a set of LA references using an iterative closest point (ICP) strategy (Figure 6.4E). We start by rigidly aligning both surfaces and then compensating the scaling differences using a similarity transform. The final transform for each case is independently applied to the FO label, propagating it to the target LA (Figure 6.4F). Then, the distance between each point of the transformed FO surface and the vertices $\boldsymbol{x}$ of the automatic LA is computed, and the nearest LA vertices considered as valid FO points.

Finally, a voting map $FO_{Spatial}(\boldsymbol{x})$ is constructed, by counting the different number of FO templates in each vertex $\boldsymbol{x}$ and normalizing it with the maximum value (Figure 6.4G).

**C. Fossa ovalis surface estimation**

*FO probability map estimation and binarization:* The final probability map is obtained by combining both $IAS_{Thick}$ and $FO_{Spatial}$ maps in each vertex $\boldsymbol{x}$ through (Figure 6.4H):

$$FO_{Position}(\boldsymbol{x}) = (1 - IAS_{Thick}(\boldsymbol{x})) \times FO_{Spatial}(\boldsymbol{x}). \quad (6.1)$$

Both $IAS_{Thick}$ and $FO_{Spatial}$ are normalized between [0-1], with 1 representing the maximal thickness position and the optimal anatomical location of FO, respectively. By inverting the $IAS_{Thick}$ map and multiplying it with the $FO_{Spatial}$, the FO region is enhanced.

Finally, the optimal position of the FO is extracted from the $FO_{Position}$ map, by applying a relative threshold value (Figure 6.4I). All the positions $\boldsymbol{x}$ with a value higher than this threshold are considered as valid FO points.

*FO surface fitting:* Starting from the valid FO points, a 3D FO surface is reconstructed based on the spatial relations between the chambers. As such, we compute the distance between each FO point and the remaining surfaces (*i.e.* RA and Ao). In detail, for each selected point, the nearest position is selected as a valid FO boundary, generating a point cloud representing the FO anatomy. Finally, a structured surface is estimated by deforming an ideal spherical mesh with the point-cloud through (Amberg *et al.*, 2007) (Figure 6.4J).

## 6.3. Experiments and results

The fully automatic framework (henceforward referred as FA) was evaluated based on: 1) the differences found between the FA atrial region segmentation strategy relatively to the

previous semi-automatic technique (termed SA) and manual contours; and 2) the analysis of the FO estimated by the proposed strategy and the corresponding one manually delineated.

### 6.3.1. Data Description

Forty-one datasets retrospectively obtained in clinical practice from patients with suspicion of pathology in the atria were used. In detail, patients with normal anatomy, pacemaker, prosthetic valves, atrial body enlargement and candidates to pulmonary vein ablation were included. ECG-gated cardiac multi-slice CT images were acquired with a multi-detector SOMATOM Force (Siemens, Germany) CT scanner, with the number of rows varying between 64-128 slices. An image resolution of 0.69 x 0.69 $mm^2$, slice thickness of 0.8 mm, and a matrix size of 512 x 512 was used. The X-ray tube current varied between 1844-2597 mA and the peak voltage varied between 70-110 kV. A contrast injection (Imeron 350, Bracco-Byk Gulden, Konstanz, Germany) of 40-100 ml was applied and a unique phase was acquired (both end-diastolic and end-systolic phases were included). Each dataset was reconstructed using the convolution kernel Bv36d. All the described acquisition parameters were defined based on the normal clinical practice at the German Heart Centre Hospital. An overview of the clinical dataset cases can be found in Appendix 6.6.B.

### 6.3.2. Fully automatic atrial region segmentation

#### A. Ground truth generation

Both LA and RA contours were manually delineated by one expert using the semi-automatic CARTO3 segmentation tool (Biosense Webster, Diamond Bar, CA, USA), followed by manual corrections (Bourier *et al.*, 2016). The Ao was manually delineated using an *in-house* software through the following steps: 1) Ao centerline definition, by providing multiple clicks along the Ao tract; 2) delineation of multiple planes (25-30 planes) perpendicular to the centerline and, 3) surface reconstruction. Moreover, similarly to our initial work (Chapter 5), multiple bounding boxes were manually generated using a 3D visualization software (Paraview Kitware Inc.) (Squillacote and Ahrens, 2007), limiting the influence of the connecting structures of the atrial body, *i.e.*, PV, VC and left/right atrial appendages (LAA/RAA), in the final result of the proposed method. Note that each bounding box was generated around the ostia of each structure. Moreover, two planes representing the mitral and tricuspid valve (TV) were built and used to evaluate the accuracy of the proposed segmentation method. In detail, each plane was defined using the following strategy: 1) manual delineation of the valve's ring in several rotated planes (centered on the valve center position); and 2) plane fitting to these points.

### B. Implementation details

The regular bounding box used to define the FOV in CT images (section 6.2.1) had a size of 20 x 20 cm along the axial direction, and its height was computed as the distance between the lung's centroid and the lung's tip. Regarding the segmentation parameters (section 6.2.2), all were kept from the original work (Chapter 5). The reader is kindly directed to Chapter 5 for further details on them.

### C. Statistical analysis

The FA contours were compared against the corresponding manual and SA results (available in Chapter 5) in terms of absolute point-to-surface (P2S) distance, Dice coefficient (DC) and 95$^{th}$ percentile of the Hausdorff distance. Moreover, the influence of the generated bounding boxes and valve planes to separate the atrial body from its connected structures was also evaluated. Regarding the FA results, independent databases were used to initialize the method through the atlas-based strategy (section 6.2.1). Note that, in contrast to our previous study (Chapter 5), where the same Ao axis was used for the manual and the SA method, the new method automatically estimates the Ao axis. Thus, the Ao result was evaluated using the entire surface and the common region only (*i.e.* clipping both automatic and manual surfaces with the surface's limits). A paired *t*-test ($p<0.05$) between the SA and FA errors when compared with manual contours was used to check for statistically significant differences in the results. Moreover, the error obtained for each stage of the FA error was also evaluated and compared with a paired t-test ($p<0.05$). Finally, the computational time of the FA approach was registered. All results were computed using MATLAB code on an Intel (R) i7 CPU at 2.8 GHz and 16 GB of RAM. A C++ implementation of the competitive strategy and of the registration algorithm (Klein *et al.*, 2010) was used.

### D. Results

Table 6.1 shows the differences between the results obtained by the FA and the manual approaches. Of note, the FA was not feasible in two cases, namely: in one case the Ao axis was wrongly initialized (entering inside the superior vena cava), and, in another one, the TV valve was wrongly estimated. Moreover, the SA results were also presented against the ones obtained by the FA version, showing a similar performance for the LA and RA segmentations. Again, the maximal accuracy was obtained for the LA chamber with an error of $1.05 \pm 0.19$ mm (FA version). A notable improvement was observed for the Ao (SA vs FA), achieving not-statistically significant differences only for the clipped version.

**Table 6.1 - Point-to-surface (P2S) error, Dice coefficient and 95th percentile of Hausdorff distance obtained between the proposed method (semi-automatic – SA and fully automatic – FA) against manual contours for atrial region segmentation**

| Segmentation | | P2S (mm) | | Dice | | 95th perc. Hausdorff (mm) | |
|---|---|---|---|---|---|---|---|
| | | SA | FA | SA | FA | SA | FA |
| LA | Entire | 1.54 ± 0.32 | 1.52 ± 0.33 | 0.91 ± 0.01 | 0.91 ± 0.01 | 6.52 ± 2.41 | 6.64 ± 1.75 |
| | Cropped | 1.07 ± 0.17 | 1.05 ± 0.19 | 0.95 ± 0.01 | 0.95 ± 0.01 | 3.36 ± 0.98 | 3.38 ± 0.80 |
| RA | Entire | 2.13 ± 0.51 | 2.17 ± 0.54 | 0.87 ± 0.03 | 0.86 ± 0.04 | 8.13 ± 2.18 | 8.10 ± 1.98 |
| | Cropped | 1.68 ± 0.47 | 1.69 ± 0.35 | 0.91 ± 0.02 | 0.92 ± 0.02 | 6.03 ± 2.04 | 6.11 ± 1.34 |
| AO | Entire | 0.65 ± 0.12* | 0.83 ± 0.44* | 0.94 ± 0.02* | 0.91 ± 0.05* | 1.61 ± 0.33* | 2.28 ± 1.71* |
| | Clipped | - | 0.71 ± 0.38 | - | 0.94 ± 0.04 | - | 1.87 ± 1.46 |

* paired t-test between the FA and SA result ($p<0.05$).

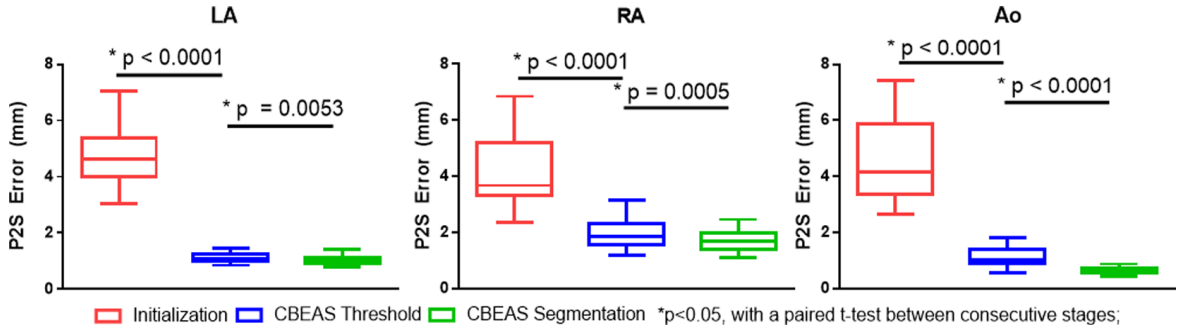


**Figure 6.5 - Point-to-surface (P2S) error obtained throughout the different stages of the fully automatic segmentation method.**
Specifically: i) initialization of the contours (red); ii) fast contour growing (blue) and iii) refinement (green).

Figure 6.5 presents the FA segmentation error in each stage of the proposed method, showing a significant reduction of the error between all steps. Finally, representative FA segmentation results are shown in Figure 6.6. For clarity sake, we also presented the IAS wall contour (cyan contour) which is applied to estimate the FO region. Regarding the computational time, the contours initialization through an atlas-based technique took 61.4 ± 5.1 seconds, while the competitive segmentation required 42.1 ± 6.0 seconds. The manual analysis made by the expert took approximately 10 minutes per patient.

### 6.3.3. Fully automatic identification of the fossa ovalis region

#### A. Ground truth generation

Two experts (Obs1 and Obs2) identified the FO region in all the 41 datasets. Moreover, one expert repeated the analysis for 10 cases two weeks later. In detail, multiple 2D slices of the FO were delineated and then interpolated into a 3D surface. Manual corrections were finally performed to improve the result. The manual delineation strategy was performed using the MITK (Medical Imaging Interaction Toolkit) (Wolf *et al.*, 2005).

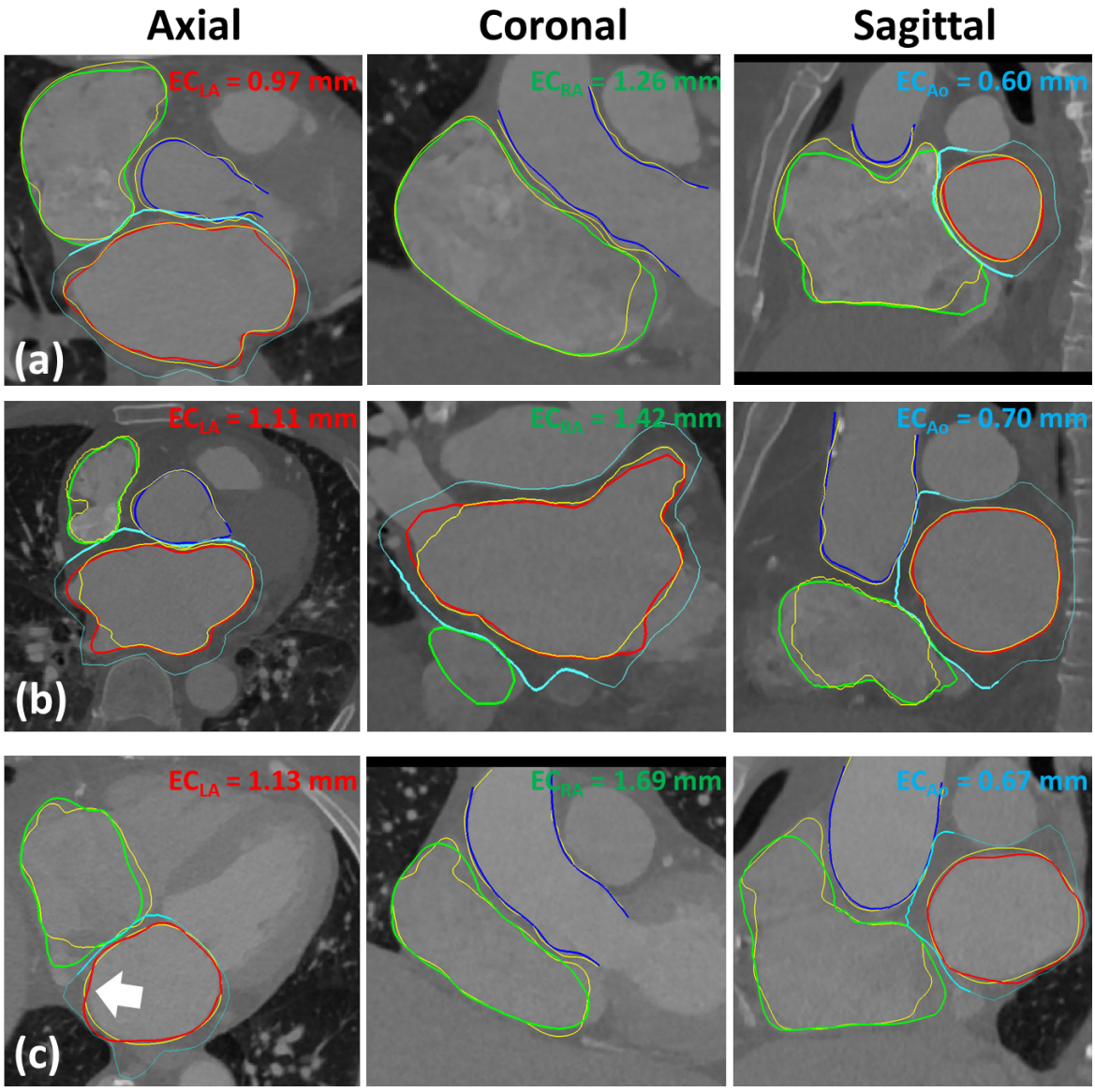


**Figure 6.6 - Automatic segmentation results for the cases corresponding to the (a) 25th, (b) 50th and (c) 75th percentile according to the point-to-surface (P2S) distance.**
LA – red; RA – green; Ao – blue; Inter-atrial wall – Cyan; Ground truth – yellow. EC represents the P2S error obtained with a cropped contour.

### B. Implementation details

Here, the IAS contour (section 6.2.3A) was defined using a spherical representation with a total of 40 × 40 points and the regional intensity-based energies were defined using image profiles with 3 mm inward and outward of the contour. The $FO_{Spatial}$ map was estimated using all manually evaluated CTs as templates using a leave-one-out strategy (*i.e.* the target case was removed from the database). The influence of the number of templates used is addressed in Appendix 6.6.C. Regarding the relative threshold (section 6.2.3C), the 90th quartile of the probabilistic map was used. It should be noted that the threshold was defined without the

positions with probability equal to 0. For further details about parameter tuning, the reader is kindly directed to the Appendix 6.6.C.

### C. Statistical analysis

The FA results were compared with the corresponding manual contours in terms of P2S, Dice and centroid position error, *i.e.* computed as the distance between the centroid of both surfaces (CPE). The intra- and inter-observer variability was computed using the difference between the manual analysis, and compared with the FA results using an unpaired and paired t-test ($p<0.05$), respectively. Finally, the computational time was registered and compared with the manual practice.

### D. Results

The FA method was able to estimate successfully the FO in all the 41 cases. Overlaps between FA and manual surfaces were always obtained and the optimal FO position (maximum value of $FO_{Position}$) was always found inside the manual contours. Figure 6.7 shows the intra- and inter-observer variability and also the evaluation results of the FA method against the manual analysis in terms of P2S, Dice and CPE. A similar performance was found between the FA method and inter-observer variability for the P2S (intra-observer: 1.39 ± 0.35 mm, inter-observer: 1.74 ± 0.68 mm, FA-Obs1: 1.77 ± 0.66 mm and FA-Obs2: 1.88 ± 0.58 mm) and Dice (intra-observer: 70.66 ± 4.74%, inter-observer: 65.40 ± 9.08%, FA-Obs1: 60.92 ± 11.92% and FA-Obs2: 61.33 ± 9.06%). Statistically significant differences were found between the FA evaluation and the inter-observer variability for the CPE measure (intra-observer: 2.50 ± 1.37 mm, inter-observer: 2.43 ± 1.20 mm, FA-Obs1: 2.90 ± 1.28 mm and FA-Obs2: 2.90 ± 1.17 mm). Figure 6.8 allows the assessment of these differences by showing the spatial distribution

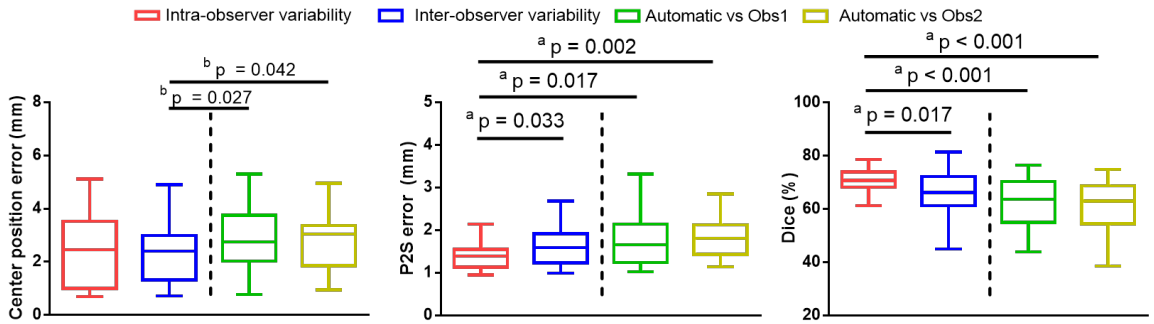


[a]p < 0.05, unpaired t-test with Welch's correction between intra-observer variability and Auto-Obs1/Auto-Obs2;
[b]p < 0.05, paired t-test between inter-observer variability and Auto-Obs1/Auto-Obs2;
[c]p < 0.05, paired t-test between Auto-Obs1 and Auto-Obs2;

**Figure 6.7 - Evaluation of the accuracy of proposed fossa ovalis estimation method.**
The centroid position error, point-to-surface error (P2S) and Dice were applied to evaluate the FA method against two manual observers (Obs1, Obs2). The intra- and inter-observer variability is also presented.

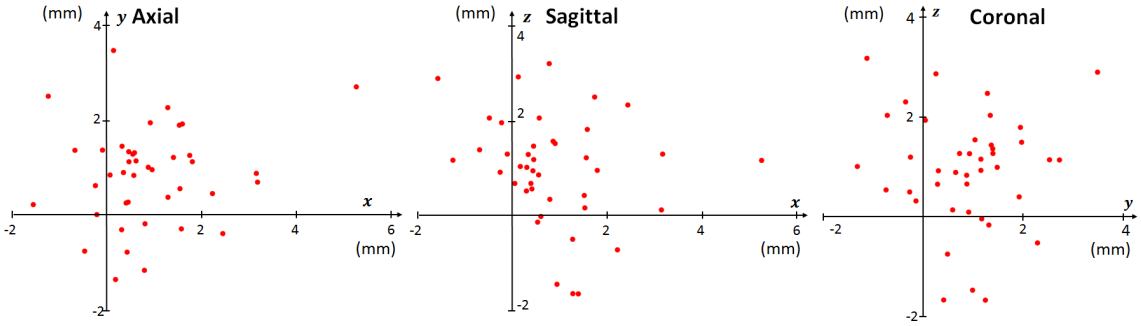


**Figure 6.8 - Distribution of the spatial centroid position errors (axial, coronal and sagittal directions) between the mean manual results and the automatic ones.**

of the CPE. In detail, the error between the manual (mean of both observers) and the automatic centroid in each spatial direction (*i.e.* axial, sagittal and coronal) was computed. A clear tendency to generate the FO contour superiorly was found with the manual method when compared with the FA one. Figure 6.9 shows representative FO results. Finally, the FA required 15.0 ± 1.6, 21.3 ± 1.9 seconds for the spatial location map and 0.7 seconds for the algorithm's steps from sections 6.2.3A, 6.2.3B, and 6.2.3C, respectively. The manual delineation took approximately 4 minutes per patient.

## 6.4. Discussion

In the article, we present a novel fully automatic strategy to segment both atrial region models and the fossa ovalis. The proposed method is divided into three sequential stages with a robust initialization through the use of an atlas, atrial chambers segmentation and mid-walls using a competitive approach and anatomical landmark identification by combining wall thickness information and spatial landmark location. Globally, the proposed framework showed a high feasibility and accuracy, corroborating its added-value for IAS intervention planning. Although in two independent cases the segmentation was considerable not feasible, possibly requiring a small user input correction, acceptable results were achieved for all the FO surfaces. Note that, no user-input was allowed and all results were obtained without any user interaction. Indeed, since an accurate delineation of the atrial and aortic walls was still achieved in these two cases, correct identification of the FO was possible.

The importance of a correct IAS intervention planning through identification of relevant landmarks was previously described (Bourier *et al.*, 2016; Jayender *et al.*, 2011; Knecht *et al.*, 2008c; Verma *et al.*, 2011; Wagdi and Alkadhi, 2012). In addition to be crucial in abnormal anatomical situations, correct planning also improves the physician's confidence, reduces the number of procedural failures, eases the entire intervention, and improves the intervention result

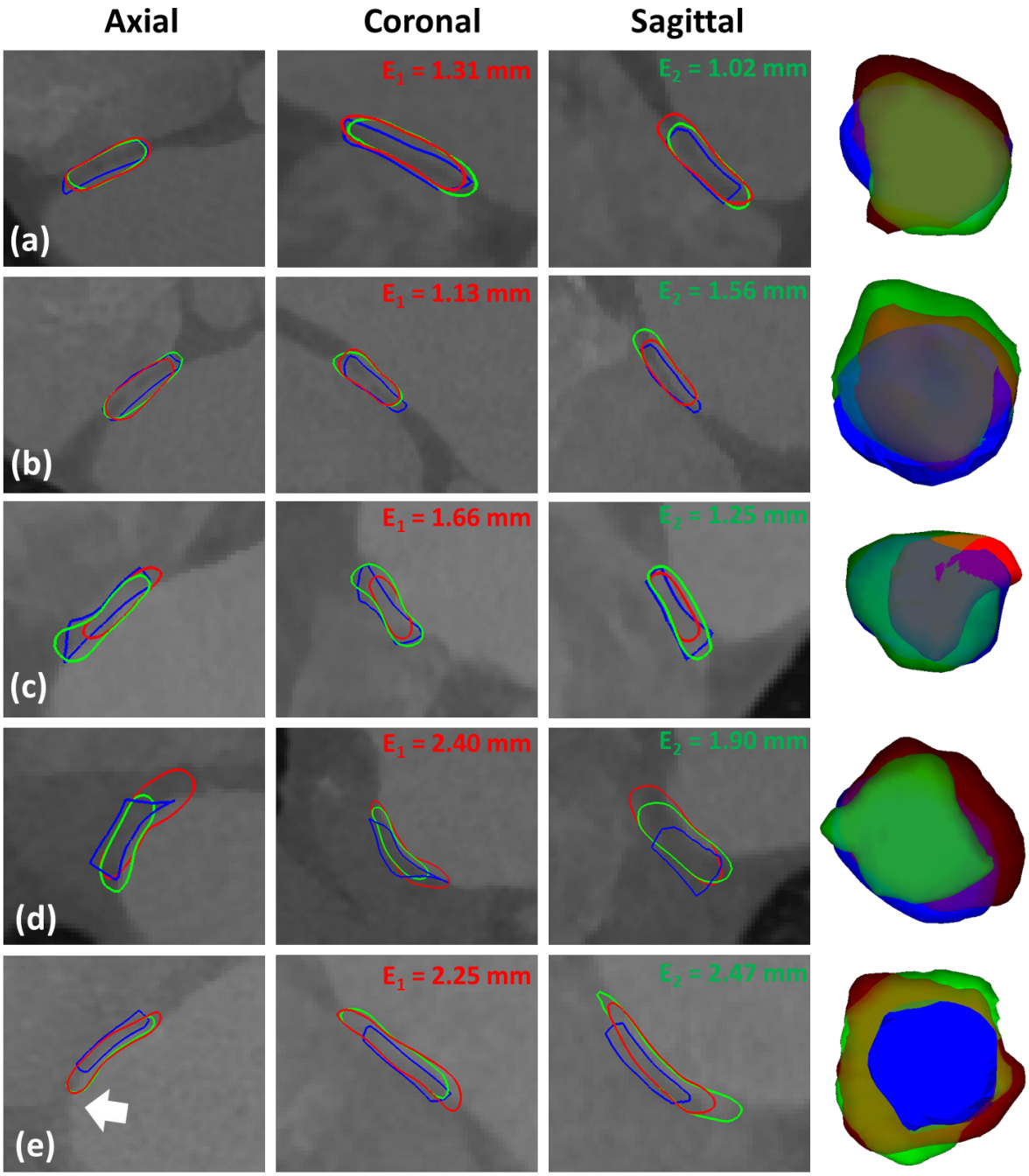


**Figure 6.9 - Estimation of the fossa ovalis region (in blue) by the automatic method (FA).**
The presented cases correspond to the (a) 10th, (b) 30th, (c) 50th, (d) 70th and (e) 90th percentile according to the point-to-distance (P2S) error. The difference between FA and each manual observer (red: Obs1 and green: Obs2) is also presented ($\boldsymbol{E_1}$ – FA/Obs1, $\boldsymbol{E_2}$ – FA/Obs2).

(Bourier *et al.*, 2016; Morais *et al.*, 2017b; Wagdi and Alkadhi, 2012). Nevertheless, the planning stage is usually performed manually (Bourier *et al.*, 2016; Verma *et al.*, 2011), which is extremely time-consuming (taking more than 14 minutes per patient) and presents high intra-/inter-observer variability, hampering its application during clinical routine. In this sense, the proposed FA strategy appears as a potential and promising solution, showing high robustness, accuracy and low computational burden (full planning requires 2-3 minutes). Regarding its

computational cost and taking into consideration the expected high variability of the FOV used in clinical CT acquisitions (*i.e.* cardiac region only, full thorax, full body, among others), different strategies were implemented to reduce the influence of the number of samples used (*i.e.* image size) in the computational burden of the proposed method, namely: 1) pre-processing of the entire image to detect a target FOV throughout the atlas alignment stage; 2) competitive segmentation using regional-based energies defined based on the contour's position; and 3) FO identification based on 3D surfaces only. To the author's best knowledge, no previous work focusing on the automatic planning of IAS interventions was presented, being a clear novelty of this work. Currently, few software tools are available to evaluate all cardiac chambers and even great vessels (Ecabert *et al.*, 2011; Zheng *et al.*, 2008). However, evaluation of the atrial walls is not possible (Ecabert *et al.*, 2011; Zuluaga *et al.*, 2013). Finally, and in a different way, some researchers are now exploring the potentialities of novel augmented reality setups, fusing multiple imaging modalities, to ease the visual identification of the FO (Faletra *et al.*, 2017).

Starting to evaluate the proposed segmentation method, the combination of both global atlas alignment with a refinement through a competitive strategy showed its high accuracy and feasibility (Table 6.1), with a performance comparable to other automatic methods (Ecabert *et al.*, 2011; Kirişli *et al.*, 2010; Zheng *et al.*, 2008). Additionally to the described clinical database, the method's accuracy was also corroborated in one recent benchmark (STACOM 2013, Appendix 6.6.D) (Tobon-Gomez *et al.*, 2015), allowing a direct comparison between the errors obtained by the FA method and the variability between manual observers, which was not possible by the clinical database used. Similarly to our previous study (Chapter 5), the RA showed the highest errors (approximately 1.7 mm for the FA and SA), which is explained by the noisy regions found, the difficulty in distinguishing between VC and atrial body, and even low contrast or missing walls at the TV valve plane. No differences were achieved between the SA and FA methods for the LA and RA results. A similar performance between FA and SA methods was observed for the entire and cropped contours situation (Table 6.1 and Figure 6.6). In contrast, significant differences were found between the SA and FA for the entire AO contour, due to the initialization used in the new method (Table 6.1). While both SA and manual contouring were performed using the same centerline, the FA estimates the Ao axis totally based on the image content (coronal view of Figure 6.6A). As such and as previously observed in other studies (Queirós *et al.*, 2017; Queirós *et al.*, 2016), small differences between central axis will result in high P2S errors. When evaluating the common Ao region, *i.e.* clipped version, no statistically significant differences were found, proving that the lower performance found for the FA is related to the initialization strategy applied. Regarding the computational time,

and similar to the previous observed in Chapter 5, the segmentation through a competitive based BEAS approach corroborated its low computational time (less than 1 minute to segment the LA, RA and Ao) and attractiveness for the normal clinical practice.

Similarly to the multi-atlas segmentation strategies (Kirişli *et al.*, 2010; Zuluaga *et al.*, 2013), the high feasibility of the proposed method is related with the atlas-based technique applied and its atlas database. Only a rough estimation of each chamber (by identifying its central region) is required by our methodology, being posteriorly refined to the real anatomy based on the spatial location of the multiple contours (Figure 6.5). As such, the result of the proposed method is theoretically not so sensitive to the atrial anatomical shape variability available in the atlas database, as observed for the totally-based multi-atlas case. In fact, our methodology appears to be more versatile for atrial region segmentation when compared with pure atlas-based techniques, particularly in abnormal cases. Note that the clinical database was constructed by retrospectively and sequentially selecting datasets from the hospital database. Therefore, a high shape variability and even different image properties are found between the different subjects, including normal and multiple pathological cases (see Appendix 6.6.B). Regarding the computational time, the proposed method is much faster (~2 minutes in a personal computer laptop) than traditional atlas approaches, making it more attractive for clinical practice. However, the authors would like to mention that the multi-atlas strategies are generic formulations with a large application in different scenarios (not only the heart) (Iglesias and Sabuncu, 2015) and without any model description limitation (Kirişli *et al.*, 2010; Zuluaga *et al.*, 2013). Moreover, although we considered our method to be fast, optimized tools that segment all chambers in a few seconds are available (Ecabert *et al.*, 2011; Zheng *et al.*, 2008).

In a second stage, we presented a novel strategy to extract relevant landmarks from the aforementioned atrial models. Since the automatic FO detection stage is totally dependent of the initial contours, the current FO strategy is not feasible without an accurate segmentation process. Contrary to previous studies where the FO is visually detected (Knecht *et al.*, 2008b; Knecht *et al.*, 2008c), either by manually marking on one specific image position (Graham *et al.*, 2007), or by identifying the thinnest position of the atrial wall in two/three orthogonal planes (Verma *et al.*, 2011), we automatically extract an entire 3D surface showing the extent of the FO region. This realistic surface can be used to facilitate and improve the detection of the optimal access routes for transseptal puncture by identifying the optimal position that guarantees maximum catheter dexterity at the left side (Bourier *et al.*, 2016; Jayender *et al.*, 2011; Knecht *et al.*, 2008b; Tomlinson *et al.*, 2008), as a relevant landmark region for IAS defect closure (Faletra *et al.*, 2014b) and for optimal device selection for other LA procedures

(Babaliaros *et al.*, 2008; Faletra *et al.*, 2017; Wang *et al.*, 2010). In order to identify the FO, we combined both patient-specific information, measured as the IAS wall thickness, and spatial maps representing the expected FO position. The IAS wall thickness is defined based on the initial atrial contours, being used as fixed references. Although the FO contour is defined along the LA surface, only the points at the interaction positions (and its neighbors, dark cyan line in Figure 6.6) between the different contours are relevant for the identification of the FO. In order to obtain a high detail on IAS wall, low smoothing terms were applied, making it correctly defined for the IAS region but a little jaggy for the remaining regions.

Regarding the FO spatial map strategy, it aligns the unknown case with a set of different anatomies, transferring the labeled FO for the novel patient. Although such strategy makes the results dependent on the anatomies available in the template database, it only generates a global map describing the anatomical regions where the FO can be found. Indeed, the influence of the number of cases used on the template database was also evaluated, obtaining a similar performance when using half or the entire database, corroborating therefore the method's robustness (Appendix 6.6.C). It might be noted that the computational cost of this step is directly related to the number of templates used. Nevertheless, since we only need to estimate a global map of the FO location, a high number of templates is not required, thus keeping the method computationally attractive. Then, and in order to adapt the result to the particularities of each patient, the global map is refined using the patient-specific anatomy extracted from the wall thickness map. In fact, accurate detection of the FO region using only the spatial or thickness map is not feasible (Appendix 6.6.C). Therefore, the combination of both IAS wall thickness and the spatial maps is required to compensate for possible segmentation errors, generating a probabilistic map that represents the optimal FO positions. Moreover, the application of one spatial map is also crucial to make the current strategy less sensitive to the image acquisition parameters (e.g. differences in terms of contrast). As a final remark, although the obtained probabilistic map could be directly used as a relevant reference for interventional planning, we decided to apply a fixed threshold to binarize the most probable region. Of note, no over-tuning of this parameter was applied and a different value could be also used without losing performance. Different threshold strategies with extra terms (such as area, maximum length, adaptive approach) could be an interesting solution to improve the method's performance. Nevertheless, we would like to emphasize that the maximum probability's position was included inside the manual FO surfaces (by both observers), corroborating the method's accuracy.

Figure 6.7 allows one to conclude that the FA method presented a performance similar to the inter-observer variability for the FO identification, validating the potential of the proposed method. Statistically significant differences were found between the intra-observer variability and the remaining cases, which can be explained by the small number of cases used and even by different manual delineation strategies applied. While one of the observers tended to segment the inner portion of the central depression of the FO only, the second one included both FO and the initial transition of the FO limbus, obtaining a larger contour. Interestingly, our automatic strategy typically generates a contour at the intermediate position of both manual contours (Figure 6.9). The CPE results corroborated the high accuracy of the proposed automatic method, particularly, considering the mean size – 17 ± 2.7 mm - of the FO in the test database, but with statistically significant differences against the inter-observer variability, which indicates a misalignment between manual and FA surfaces. These differences can be explained by the sub-optimal segmentation result at the top of the atrial roof, due to its high curvature and its irregular shape (white arrow on Figure 6.6C and Figure 6.9E). These last observations are corroborated by Figure 6.8, where it is depicted that the manual centroid positions are typically located superiorly (at the coronal and sagittal directions) than the centroid of the automatic result.

The authors would like to emphasize that although the proposed methodology, focused on anatomical alignment and contour refinement, proved its high accuracy and robustness for the segmentation of the atrial region (mainly at the thin mid atrial walls) and fossa ovalis, different solutions based on machine learning approaches (mainly deep learning techniques) are also potentially interesting. Indeed, such solutions are expected to be developed during the next years, both for the segmentation of the cardiac chambers and even for the fossa ovalis region. Nevertheless, when comparing end-to-end deep learning approaches with the proposed technique, there are several challenges that need to be addressed in the near future: 1) to the author's best knowledge, large training databases or even benchmarks with strong manual references delineated by multiple observers are not available for this problem; 2) due to its low thickness (in some situations could be one pixel or even not visible), correct modelling of the inter-atrial is not straightforward with the pure machine learning approach, requiring further research; and 3) method's sensitivity to image artifacts (e.g. pacemakers) or abnormal anatomies (possibly not represented in the training database) needs to be studied.

As a future work, we intend to apply the proposed framework for real planning of inter-atrial intervention (Bourier *et al.*, 2016; Verma *et al.*, 2011). Not only the physician will use the automatically estimated surfaces to identify the optimal path, as also the obtained models will

be included in the real intervention (combining fluoroscopy and CT data through) (Bourier *et al.*, 2016), improving the interventional data and easing the identification of relevant anatomical regions. The FO will be represented as an accurate 3D surface, representing its entire shape and not only one specific point (Graham *et al.*, 2007), easing the selection of the optimal route and preventing procedural complications/failures (Babaliaros *et al.*, 2008; Morais *et al.*, 2017b). Furthermore, we also believe that our method could also be applied to improve IAS intervention simulation tools (Jayender *et al.*, 2011), by applying realistic and accurate models of the atrial region and the FO, instead of mean atrial region models or entire IAS wall surfaces. Finally, the proposed fully automatic atrial region segmentation strategy can be efficiently applied in clinical practice for accurate evaluation of the relevant global indicators (e.g., volume, dimension) of the LA, RA and Ao. Moreover, although it was not within the scope of the current study, the current fully automatic methodology can be extended, keeping its high accuracy and robustness, for other cardiac chambers (e.g. LV) or even different imaging modalities (e.g. 3D magnetic resonance imaging), thereby increasing the potential of the proposed framework for the clinical environment. Nevertheless, and as explained in our previous study (Chapter 5), segmentation of the RV with the current atlas-based approach followed by competitive BEAS is not feasible. Since BEAS relies on explicit functions, intrinsic shape limitations are imposed (e.g. spherical or cylindrical space), being therefore – in its present form - not suitable to describe complex anatomies as the RV.

The current study has some limitations, namely: 1) accurate identification of FO is unfeasible on non-contrasted CT or datasets with larger pixel spacing due to the low contrast and resolution of the thin IAS wall (as a consequence, a non-refined $IAS_{wall}$ map is obtained), respectively; 2) extreme abnormal atrial anatomies can present a sub-optimal result when performing the atlas alignment or when estimating the $FO_{Spatial}$ map due to the limited shape representation on the reference templates; 3) a sub-optimal FO result can be obtained in patients with patent foramen ovale; and 4) a larger and multi-center database with manual references from several experts are required to exhaustive validate the proposed pipeline.

## 6.5. Conclusion

The proposed fully automatic framework showed its added-value for IAS interventional planning, making it more accurate, simpler, without observer variability and faster. The new atrial region segmentation approach obtained results comparable to the remaining state-of-the-art methods, but providing superior results for the mid atrial walls. No differences were found between the new and our previous segmentation approaches; however, it should be noted that

with the new approach, the segmentation is free of user interaction. Regarding the fossa ovalis segmentation, the proposed method obtained results similar to the ones manually delineated by experts, allowing a correct and fast identification of the optimal route for transseptal puncture or optimal device selection for LA interventions.

## 6.6. Appendixes

### Appendix A – Coupling formulation

B–spline Explicit Active Surface (BEAS): The BEAS framework represents the different contours as explicit functions, which means that one of the coordinates of the points of the interface, $\boldsymbol{x} = \{x_1, x_2, \dots, x_N\}$ in a $N$-dimensional space, is expressed as a function of the remaining coordinates (*i.e.* $\boldsymbol{x}^* = \{x_2, \dots, x_N\}$) reducing therefore, the dimensionality of the segmentation problem. Consequently, each explicit function $\psi_i$ ($i \in \{LA, RA, Ao\}$) is defined as (Almeida *et al.*, 2016):

$$\psi_i(\boldsymbol{x}^*) = \sum_{k \in \mathbb{Z}^{N-1}} c_i[\boldsymbol{k}] \beta_i^d \left( \frac{\boldsymbol{x}^* - \boldsymbol{k} h_{r_i}}{h_{s_i}} \right), \tag{6.A.1}$$

where $\beta_i^d(\cdot)$ is the uniform symmetric $(N-1)$-dimensional B-spline of degree $d$ of each contour $i$. The knots of the B-splines are located on a regular grid defined on a specific space; $h_s$ and $h_r$ are smoothness parameters that control the scaling and spacing of the B-spline kernel, respectively; $c_i[\boldsymbol{k}]$ are the B-spline coefficients of contour $i$.

As previously described in our initial work (Chapter 5), the evolution of each contour $i$ is independently controlled, and finally combined through:

$$\begin{aligned} E &= \sum_i E_i, \\ E_i &= \int_\Omega \delta_{\phi_i}(\boldsymbol{x}) \int_\Omega B(\boldsymbol{x}, \boldsymbol{y}) . F_i(\boldsymbol{y}) d\boldsymbol{y} d\boldsymbol{x}, \end{aligned} \tag{6.A.2}$$

where $\phi_i(\boldsymbol{x}) = \Gamma_i(\boldsymbol{x}^*) - x_1, i \in \{LA, RA, Ao\}$ with $n$ representing the total number of contours, $\boldsymbol{x}, \boldsymbol{y}$ are independent spatial locations in the image domain $\Omega$, $\phi_i(\boldsymbol{x})$ is a level-set like function representing the region inside the interface $\Gamma_i$ and $\delta_{\phi_i}$ is the Dirac function and $F_i$ an image criteria (e.g. localized Chan-Vese energy) (Lankton and Tannenbaum, 2008). $B(\boldsymbol{x}, \boldsymbol{y})$ corresponds to a mask function in which the regional parameters that locally drive the contour evolutions are computed. In order to identify the optimal contour positions, energy $E$ is minimized through the computation of the energy derivatives with respect to each $c_i[\boldsymbol{k}]$, as described by Barbosa *et al.* (2012):

$$\frac{\partial E_i}{\partial c_i[\boldsymbol{k}]} = \int_{\Gamma_i} \bar{g}_i(\boldsymbol{x}^*)\beta_i^d\left(\frac{\boldsymbol{x}^* - \boldsymbol{k}h_{r_i}}{h_{s_i}}\right)d\boldsymbol{x}^*, \tag{6.A.3}$$

with $\bar{g}_i(\boldsymbol{x}^*)$ representing the feature map (e.g. first derivative of the local Chan-Vese energy) (Lankton and Tannenbaum, 2008) of each contour $i$.

Coupling strategy: Starting from the obtained LA contour (section 6.2.2), an extra BEAS surface representing the wall thickness is initialized (henceforward referred as IAS wall contour), meaning that $i \in \{LA, RA, Ao, IAS\}$.

The IAS contour is defined based on the LA contour (*i.e.* same centroid) plus a constant thickness (here of 5 mm, Figure 6.A.1a). Instead of the free evolution of the IAS contour, we decided to combine it with the LA surface. Therefore, the IAS contour is modeled as a combination of two explicit functions representing the LA position ($\psi^{Pos}$) and IAS wall thickness ($\psi^{Thick}$), respectively (Figure 6.A.1). In detail, the IAS contour ($S_{IAS}$) is now described as (Pedrosa *et al.* 2017):

$$S_{IAS}(\boldsymbol{x}^*) = \Gamma_{IAS}(\boldsymbol{x}^*) = \psi^{Pos}(\boldsymbol{x}^*) + \psi^{Thick}(\boldsymbol{x}^*), \tag{6.A.4}$$

and the energy derivatives as:

$$\begin{aligned}\frac{\partial E_{IAS}}{\partial c_{IAS}[\boldsymbol{k}]} = &\int_{\Gamma_{IAS}} \bar{g}_{IAS}^{Pos}(\boldsymbol{x}^*)\beta_{IAS}^d\left(\frac{\boldsymbol{x}^* - \boldsymbol{k}h_{r_{IAS}}}{h_{s_{IAS}}}\right)d\boldsymbol{x}^* \\ &+ \int_{\Gamma_{IAS}} \bar{g}_{IAS}^{Thick}(\boldsymbol{x}^*)\beta_{IAS}^d\left(\frac{\boldsymbol{x}^* - \boldsymbol{k}h_{r_{IAS}}}{h_{s_{IAS}}}\right)d\boldsymbol{x}^*,\end{aligned} \tag{6.A.5}$$

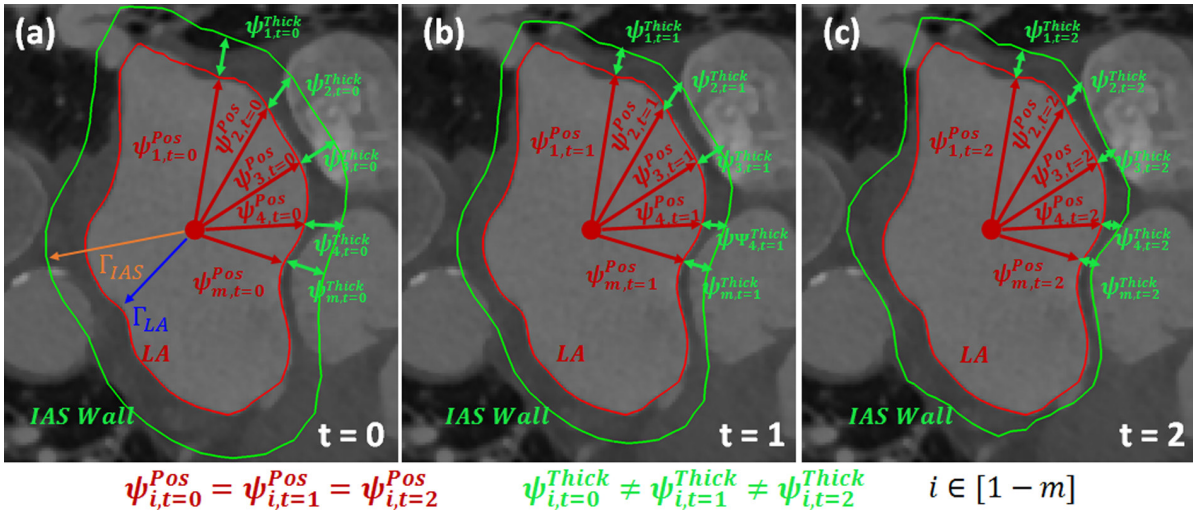


**Figure 6.A.1 – Illustration of the coupling strategy.**
The IAS wall contour is described based on the LA position ($\boldsymbol{\psi^{Pos}}$) plus the wall thickness ($\boldsymbol{\psi^{Thick}}$); Algorithm's result at temporal moment (a) 0; (b) 1 and (c) 2. Please note that the LA contour (red) is not modified.

where $\bar{g}_{IAS}^{Pos}$ and $\bar{g}_{IAS}^{Th}$ represent the feature map of the wall surface position and wall thickness, respectively. Moreover, it should be noted that LA contour is equal to $\psi^{Pos}$.

Since the LA contour is only used as an anchor, keeping its original position throughout this algorithm step, $\psi^{Pos}$ is kept unaltered (Figure 6.A.1). Therefore, equation (6.A.5) can be described as:

$$\frac{\partial E_{IAS}}{\partial c_{IAS}[\boldsymbol{k}]} = \int_{\Gamma_{IAS}} \bar{g}_{IAS}^{Thick}(\boldsymbol{x}^*)\beta_{IAS}^{d}\left(\frac{\boldsymbol{x}^* - \boldsymbol{k}h_{r_{IAS}}}{h_{s_{IAS}}}\right)d\boldsymbol{x}^*. \tag{6.A.6}$$

It should be noted that the IAS wall contour is only estimated based on wall thickness parameter and not directly on the final wall position (Figure 6.A.1). Such strategy prevents irregular regions caused by low contrast and even missing walls.

Finally, since the IAS wall segmentation is only applied after the atrial region segmentation, being the atrial region contour not altered at this step, the evolution energy is only represented as:

$$E = E_{IAS}. \tag{6.A.7}$$

**Appendix B – Representative cases of the clinical database**

Representative image cases of the applied clinical database are available in Figure 6.B.1.

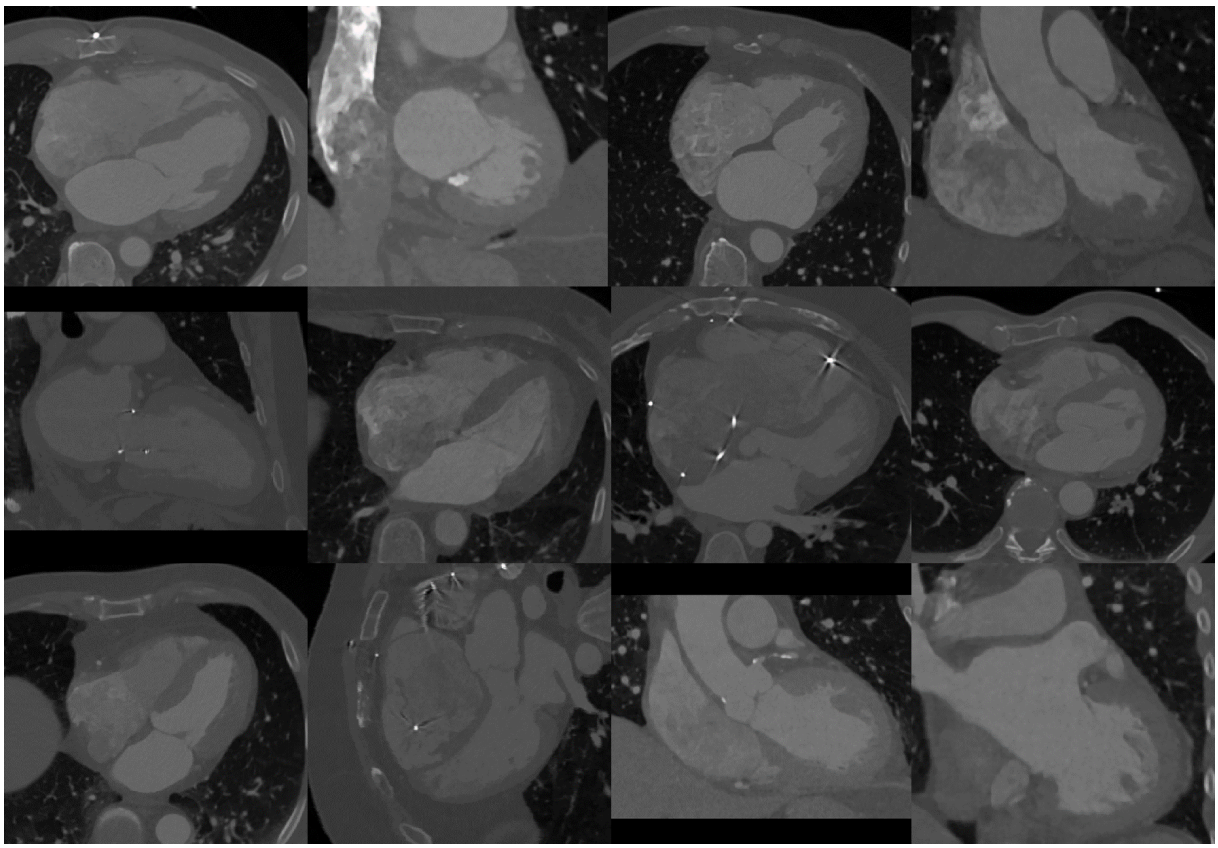

**Figure 6.B.1 - Representative cases of the clinical database.**

**Appendix C – Influence of the model's parameters**

Data Description: The 41 clinical datasets described section 6.3.1 were used.

Experiments and Results: A parameter tuning analysis of the proposed fully automatic method to identify the FO is presented. First, the influence of the multiple maps (*i.e.* thickness and spatial information maps generated throughout sections 6.2.3A and 6.2.3B, respectively) was assessed. Next, the influence of the transformation model (*i.e.*, rigid, affine or similarity) applied on the ICP algorithm (section 6.2.3B) and also the threshold used to binarize the FO region was evaluated. All the parameter pairs were compared through a paired t-test ($p<0.05$). Finally, the influence of the number of templates used to estimate the spatial map ($FO_{Spatial}$) was also investigated.

Figure 6.C.1a shows the influence of the different steps of the new identification algorithm, proving that a superior performance is obtained when both maps (*i.e.* thickness and spatial location) are combined. In one hand, the results proved that the thickness map is sensitive to local minima found throughout the entire left atrial surface. On the other hand, the spatial map is able to roughly detect the FO region, failing to refine the result to the target anatomy, which is achieved by combining the spatial and thickness maps. Figure 6.C.1b evaluates the different transformation models applied in the surface alignment through ICP. Globally, the results proved that a double alignment strategy, where both surfaces are initially rigidly aligned and then its sizing differences compensated through a similarity or affine model, achieved the best performance with statistically significant differences when compared with the other possibilities. Finally, the influence of the threshold (described in section 6.2.3C) is presented in Figure 6.C.1c. The results proved that a different value (varying between the percentile $70^{th}$ and $90^{th}$) could be applied without statistically significant differences.

Figure 6.C.2 shows the P2S error evolution with the variation of the total number of templates (required on section 6.2.3B for the $FO_{Spatial}$ map estimation). It should be noted that for all the possibilities, the reference database was always constructed without the target case. An increase of the P2S errors was observed when a small number of templates are used (~less than 10 cases), which is explained by the voting strategy applied on the $FO_{Spatial}$ map estimation step and the limited shape variability. Indeed, due to the limited number of samples, a sparse $FO_{Spatial}$ map was obtained (caused by sub-optimal alignment results), preventing a correct estimation of the FO region. In opposition, a similar performance with high accuracy was obtained for cases with a high number of templates (20-40 samples, with 40 representing

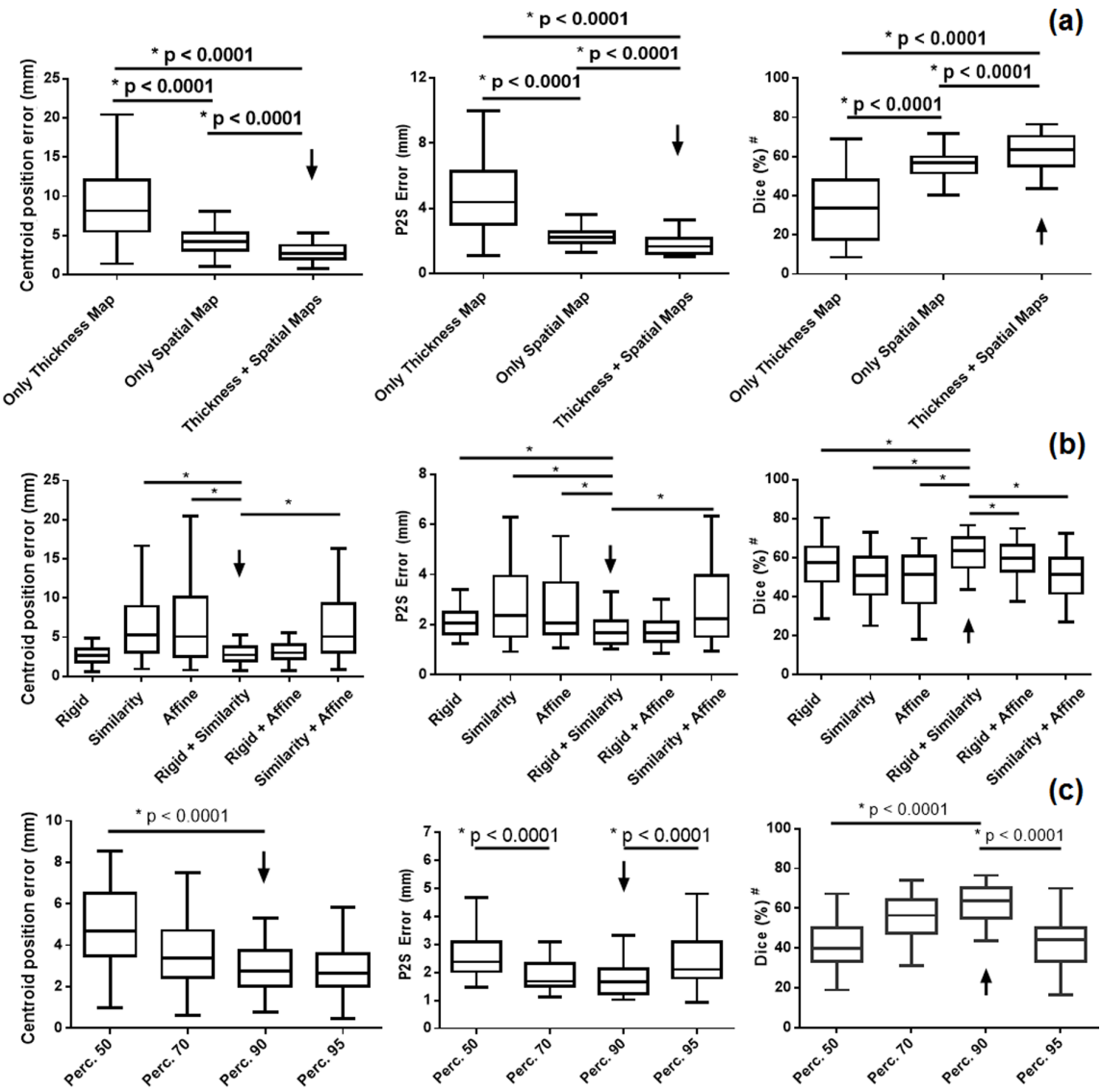


**Figure 6.C.1 – Sensitivity analysis of the different parameters and algorithm's step described in the fossa ovalis identification strategy.**
a) evaluates the influence of the thickness and spatial location maps; b) assesses the method's accuracy with different transformation applied in the surface alignment step; and c) shows the influence of the selected threshold to binarize the FO position. The centroid position error (first column), point-to-surface (P2S, second column) error and Dice (third column) were used as evaluation metrics. The arrow identifies the selected parameter; * p<0.05 with a paired t-test between all the parameters' pairs; # - Cases without surface's overlap were excluded.

the entire template database). This result reinforces the advantages of the proposed method, showing that $FO_{Spatial}$ map is only required to estimate the most probable spatial location of the FO region being posteriorly refined using patient-specific information extracted from the $IAS_{Map}$. When using a high number of templates (more than 20, *i.e.* half of the entire reference database), the influence of sub-optimal results is minimized and the most common region is therefore, enhanced (*i.e.* region where a high number of templates will vote as optimal position). Nevertheless, a notable improvement of the method's accuracy is not predictable with the

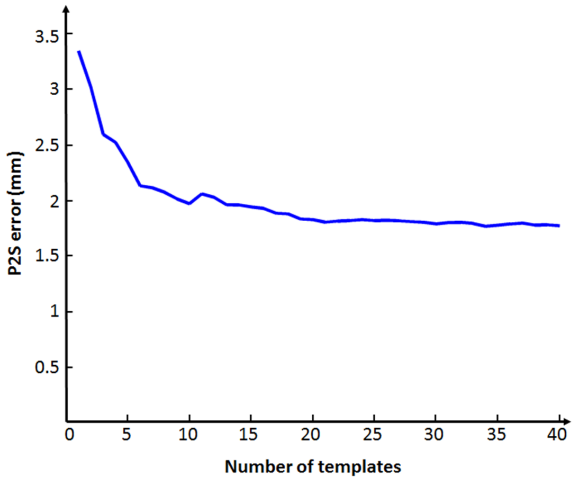


**Figure 6.C.2 – Influence of the total number of templates used throughout the $FO_{Spatial}$ map estimation in the final accuracy of the proposed method.**

increase of the total database (*i.e.* more than 40). In fact, it is only expected a slight enhancement of the optimal FO region.

### Appendix D – LA segmentation benchmark

Data Description: The accuracy of the proposed fully automatic segmentation method was evaluated using a public available benchmark database (STACOM 2013). The public database has thirty datasets, 10 datasets for training and 20 datasets for testing. Only LA contours are allowed to be evaluated with the current benchmark. The reader is kindly directed to the original work (Tobon-Gomez *et al.*, 2015) for further details on imaging acquisition and ground truth generation.

Experiments and Results: The FA method was applied successfully to segment the LA in all the datasets. Its results were compared with the ones of other state-of-the-art techniques in terms of P2S and Dice coefficient. Although a total of 9 works was initially evaluated in this challenge, only the 5 best results are presented and compared with the FA method. Moreover, the SA version of the proposed competitive strategy (Chapter 5) is also presented and directly compared with the FA method through an unpaired t-test ($p<0.05$).

The proposed FA method obtained a P2S error of 0.85 ± 1.02 mm, proving its robustness and accuracy with a performance similar to the remaining state-of-the-art methods; namely, machine learning, atlas-based and deformable models based methods, Figure 6.D.1. Moreover, no statistically significant differences were found between the FA and SA methods, corroborating the method's accuracy. Finally, since the proposed method is totally automatic (no user interaction) and fast (less than 2 minutes in a common personal laptop computer), it proved its added-value for normal clinical practice.

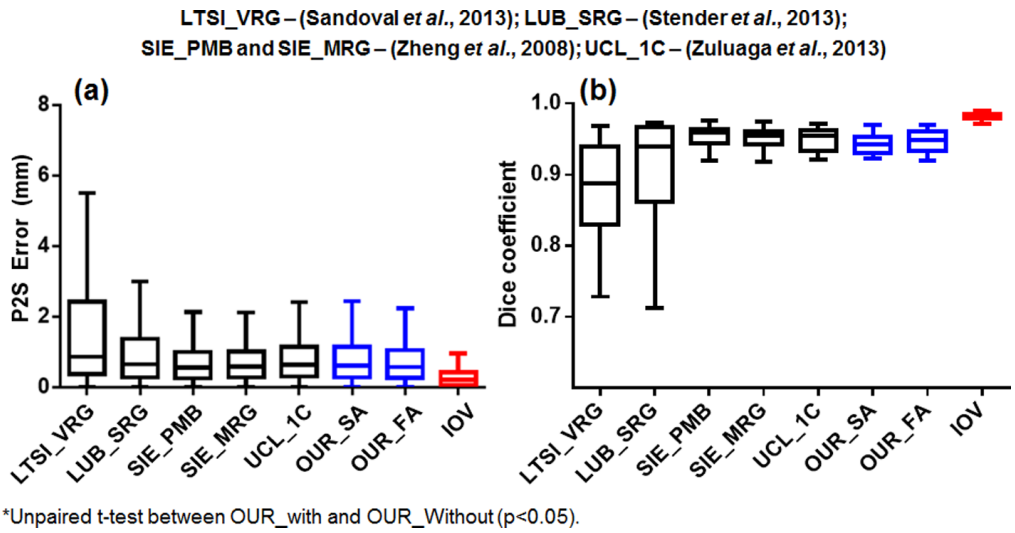


**Figure 6.D.1 - Assessment of the proposed fully automatic method for left atrium segmentation in CT data and comparison against the best results available in this public available benchmark.**
Moreover, the performance of our previous developed semi-automatic method is also presented. Each team's name was defined based on Tobon-Gomez *et al.* (2015); IOV represents the inter-observer variability.

# Part II

## Left atrial appendage occlusion

This part focuses on the development and validation of novel image-based planning solutions for left atrial appendage occlusion. Initially, a strategy to semi-automatically segment the left atrial appendage in 3D transesophageal images is described. Then, an automated solution to estimate the relevant clinical indicators to identify the optimal occluding device is presented.

**Contents**

# Chapter 7

## Fast segmentation of the Left Atrial Appendage in 3D Transesophageal Echocardiographic Images

This chapter has been submitted for publication in an international journal and is currently under review: **Pedro Morais**, Sandro Queirós, Pieter De Meester, Werner Budts, João L. Vilaça, João Manuel R. S. Tavares, Jan D'hooge, "Fast Segmentation of the Left Atrial Appendage in 3D Transesophageal Echocardiographic images" (2018).

**Keywords:** 3D image segmentation; Left atrial appendage; Curvilinear blind-ended model; B-spline Explicit Active Surface.

**Contents**

## Abstract

Left atrial appendage (LAA) has been generally described as "our most lethal attachment", being considered the major source of thromboembolism in patients with non-valvular atrial fibrillation (NVAF). Currently, LAA occlusion can be offered as a treatment for NVAF patients, obstructing the LAA through a percutaneously delivered device. Nevertheless, correct device sizing is not straightforward, requiring the manual analysis of peri-procedural images. This approach is sub-optimal, time demanding and highly variable between experts, which can result in lengthy procedures and excessive manipulations. In this article, a novel semi-automatic LAA segmentation technique for 3D transesophageal echocardiography (TEE) images is presented. Specifically, the proposed technique relies on a novel segmentation pipeline where a curvilinear blind-ended model is optimized through a double stage strategy: 1) fast contour evolution using global terms and 2) contour refinement based on regional energies. To reduce its computational cost, and thus make it more attractive to real interventions, the B-spline Explicit Active Surface framework was used. This novel method was evaluated in a clinical database of 20 patients. Manual analysis performed by two observers was used as ground truth. The 3D segmentation results corroborated the accuracy, robustness to the variation of the parameters and computationally attractiveness of the proposed method, taking approximately 14 seconds to segment the LAA with an average accuracy of ~0.9 mm. Moreover, a segmentation performance comparable to the inter-observer variability was found. Finally, the advantages of the segmented 3D model were evaluated while semi-automatically extracting the clinical measurements for device selection, showing a similar accuracy but with a higher reproducibility when compared to the current practice. Overall, the proposed segmentation method shows potential for an improved planning of LAA occlusion intervention, indicating added-value for normal clinical practice.


## 7.1. Introduction

Left atrial appendage (LAA) is the remnant of the embryonic left atrium (LA) and it is commonly described as a long tubular, trabeculated blind-ended structure attached to the LA body (Figure 7.1) (Meier *et al.*, 2014; Park *et al.*, 2011; Wunderlich *et al.*, 2015). High variability in LAA shape and morphology is expected between subjects and different size and complex multi-lobular structures are common. Although doubts remain about its real function (Beutler *et al.*, 2014), some recent studies proved that the LAA is the source of thromboembolism in approximately 90% of patients with non-valvular atrial fibrillation (NVAF) (Meier *et al.*, 2014; Wunderlich *et al.*, 2015). Anticoagulation therapy is clinically

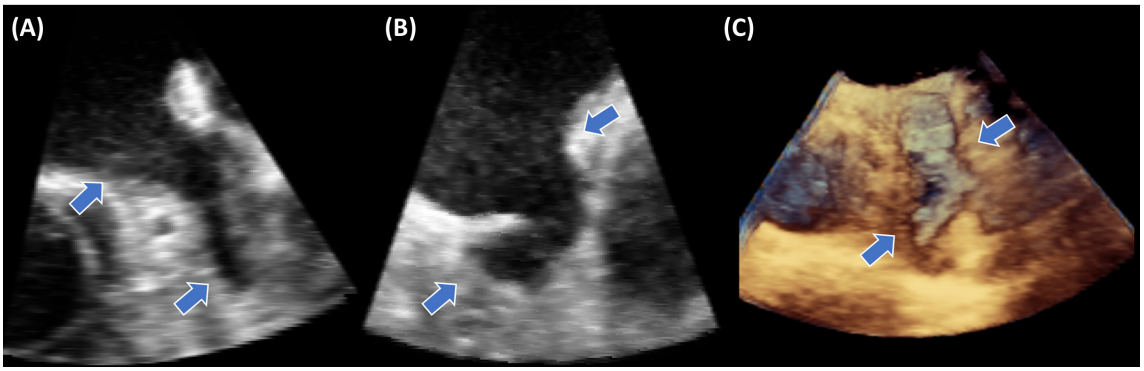


**Figure 7.1 – Left atrial appendage.**
(A-B) Orthogonal 2D views and (C) 3D representation of the LAA.

accepted as the main embolism prevention treatment for patients with atrial fibrillation, but with a poor long-term compliance and potential bleeding complications (Murarka *et al.*, 2017; Park *et al.*, 2011). In this sense, percutaneous LAA occlusion appeared as a recommended treatment for NVAF patients that present high stroke risk and contraindications for oral anticoagulation treatment (Reddy *et al.*, 2017; Wunderlich *et al.*, 2015).

The LAA occlusion is a minimally invasive cardiac intervention, where a specific foldable implant/device is percutaneously delivered, via a transseptal route (Morais *et al.*, 2017b), at the LAA ostium obstructing the orifice and reducing the risk of a thromboembolism (Meier *et al.*, 2014). The entire procedure is guided through fluoroscopy and 2D/3D transesophageal echocardiography (TEE) imaging, requiring a pre-procedural planning with a TEE examination to rule out LAA thrombus and to evaluate the LAA morphology. Moreover, recently, researchers (Christiaens *et al.*, 2010; Di Biase *et al.*, 2012; Pellegrino *et al.*, 2016; Song *et al.*, 2016; Wang *et al.*, 2016a) have proven the added-value of computed tomography (CT) acquisition for accurate identification of the LAA shape.

Due to the high shape variability between subjects, different manufacturers produce occluding devices with different sizes and shapes (Meier *et al.*, 2014). As a result, clinical measurements, which vary between manufacturers, must be taken to identify the optimal model, increasing the difficulty of the intervention. Indeed, recent studies suggest that the device selection stage is one of the most critical stages during LAA occlusion (Goitein *et al.*, 2017; Wang *et al.*, 2016a). Although some experts prefer to identify the device size based on detailed pre-procedural data (*i.e.*, CT images) (López-Mínguez *et al.*, 2014; Rajwani *et al.*, 2016; Wang *et al.*, 2016a), the majority of the interventionists still performs this stage using peri-procedural imaging. Indeed, since the CT data is acquired before the intervention (24h-48h), anatomical variations can occur, which may influence the selected device (Nucifora *et al.*, 2011). For this reason, during the real intervention, the experts perform multiple image acquisitions (both

fluoroscopy and ultrasound) and visually assess the resulting images to identify the optimal device (Bai *et al.*, 2017). However, such approach still presents several disadvantages, namely: 1) it is time-consuming, requiring several minutes to correctly identify the optimal device; 2) the correct identification of the 3D LAA shape through peri-procedural data is not straightforward; and 3) the clinical analysis is totally manual, lacking intra- and inter-observer reproducibility (Song *et al.*, 2016).

Recently, a few studies focusing on novel planning techniques for LAA occlusion were presented (Liu *et al.*, 2016; Pellegrino *et al.*, 2016; Song *et al.*, 2016). The majority of them rely on 3D-printed models. More specifically, the LAA anatomy is extracted from 3D CT (Pellegrino *et al.*, 2016) or TEE images (Liu *et al.*, 2016), being subsequently edited and physically generated through 3D-printers. The accurate model is then provided to the physician prior to the intervention, allowing a correct interpretation of the 3D LAA shape and identification of the optimal occluding device. Although this approach has gained, recently, particular attention, it is complex, time demanding (several hours to print the 3D model) and not automated, requiring user-interaction at multiple stages. Other researchers developed image processing techniques to segment the target anatomy, particularly for CT datasets, using simple image-based techniques (Song *et al.*, 2016), deformable models (Grasland-Mongrain *et al.*, 2010) or machine learning strategies (Jin *et al.*, 2018; Wang *et al.*, 2016b). Interestingly, the image-based technique from Song *et al.* (2016) was also applied in TEE images, extracting realistic LAA shapes but being extremely time-demanding due to the high number of manual corrections required. Indeed, taking into consideration the state-of-the-art, efficient and automated strategies to segment the LAA in TEE images were, to the authors' best knowledge, not described, particularly due to: 1) the complex curvilinear and tubular anatomical shape of the LAA; 2) the high anatomical variability of this structure; and 3) the low image quality.

In this article, a novel strategy is proposed to accurately and quickly segment the LAA anatomy in 3D TEE images, which can ease the interpretation of peri-procedural ultrasound data and ultimately has the potential to simplify LAA occlusion planning. The novel strategy captures all the particularities of the LAA by applying a double stage segmentation process focused on the evolution of a curvilinear blind-ended model. In detail, a standard model is initially generated by manually defining its centerline, being then refined to the patient anatomy through a fast contour evolution approach with global descriptors followed by a refined image segmentation step with regional terms. The segmentation method was implemented based on the B-spline Explicit Active Surface framework (BEAS), extending its current formulation by presenting a novel curvilinear blind-ended BEAS model.

Hereupon, this work introduces two novelties: 1) a novel LAA segmentation technique for 3D TEE images based on the evolution of a curvilinear blind-ended BEAS model; and 2) a clinical validation of this method, by comparing its performance against the traditional manual practice in terms of segmentation accuracy and reliability of the extracted measurements.

This work is structured as follows. In section 7.2, a technical description of the segmentation pipeline is presented. An initial explanation of the curvilinear blind-ended BEAS model is provided, being afterward described the different steps of the proposed LAA segmentation pipeline. In Section 7.3 and Section 7.4, the validation experiments and the results are presented, respectively. Section 7.5 evaluates and discusses the performance of the proposed method. Finally, the conclusions of the work are presented in Section 7.6.

## 7.2. Methods

In this section, a description of the LAA segmentation pipeline is presented. We start by explaining the basic concepts of the BEAS framework (section 7.2.1), later expanding its formulation to a curvilinear blind-ended model (section 7.2.2), making it suitable to capture the particularities of the LAA. Finally, a detailed description of the novel double-stage LAA segmentation framework applied to optimize the curvilinear surface is presented (section 7.2.3).

### 7.2.1. B-spline Explicit Active Surfaces

The key concept of the BEAS framework is to represent an object interface as an explicit function described as a linear combination of B-spline basis functions. Thanks to this explicit description, a reduction of the dimensionality $n$ of the segmentation problem is possible, being one of the coordinates of the interface points, $\boldsymbol{x} = \{x_1, x_2, \dots, x_n\}$, described as a function of the remaining ones, $x_1 = \psi(\boldsymbol{x}^*) = \psi(x_2, \dots, x_n)$. As such, the explicit function $\psi$ is defined as:

$$x_1 = \psi(x_2, \dots, x_n) = \psi(\boldsymbol{x}^*) = \sum_{\boldsymbol{k} \in \mathbb{Z}^{n-1}} c[\boldsymbol{k}] \beta^d \left( \frac{\boldsymbol{x}^*}{h} - \boldsymbol{k} \right), \tag{7.1}$$

where $\beta^d(.)$ is the uniform symmetric $(n-1)$-dimensional B-spline of degree $d$. The knots of the B-splines are located on a grid defined on a specific coordinate system, with a spacing represented by $h$. $c[\boldsymbol{k}]$ represents the B-spline coefficients.

The evolution model is controlled by a regional-based energy ($E$), defined as:

$$E = \int_{\Omega} \delta_{\phi}(\boldsymbol{x}) \int_{\Omega} B(\boldsymbol{x}, \boldsymbol{y}) . F(\boldsymbol{y}) d\boldsymbol{y} d\boldsymbol{x}, \tag{7.2}$$

where $\boldsymbol{x}, \boldsymbol{y}$ represents independent spatial locations in the image domain $\Omega$. $\delta_{\phi}$ is the Dirac and $F(\boldsymbol{y})$ is an image criteria (e.g., local Chan-Vese (Lankton and Tannenbaum, 2008)). $B(\boldsymbol{x}, \boldsymbol{y})$ is

a local mask function where the regional parameters that drive the contour evolution are estimated and it is defined as a set of points ($\boldsymbol{y}$) along the normal direction ($\hat{\boldsymbol{r}}$) of $\boldsymbol{x}$ whose distance is lower than $\rho$ (Lankton and Tannenbaum, 2008):

$$B(\boldsymbol{x},\boldsymbol{y}) = \begin{cases} 1, if\ \boldsymbol{y} = \boldsymbol{x} + m \times \hat{\boldsymbol{r}}, m \in [-\rho,\rho] \\ 0, \quad otherwise \end{cases}. \tag{7.3}$$

The energy minimization is performed using a gradient descent approach through the computation of the energy derivatives with respect to each B-spline coefficient $c[\boldsymbol{k}]$:

$$\frac{\partial E}{\partial c[\boldsymbol{k}]} = \int_{\Gamma} \bar{g}(\boldsymbol{x}^*)\, \beta^d \left(\frac{\boldsymbol{x}^*}{h} - \boldsymbol{k}\right) d\boldsymbol{x}^*, \tag{7.4}$$

$$\bar{g}(\boldsymbol{x}^*) = \bar{g}^{IM}(\boldsymbol{x}^*) + \alpha.\, \bar{g}^{Reg}(\boldsymbol{x}^*), \tag{7.5}$$

$\phi(\boldsymbol{x})$ is a level-set like function representing the region inside the interface Γ (*i.e.* $\phi(\boldsymbol{x}) = \Gamma(\boldsymbol{x}^*) - x_1$) and $\bar{g}^{IM}(\boldsymbol{x}^*)$ is the first derivative of $F(\boldsymbol{y})$ (e.g. first derivative of the local Chan-Vese (Lankton and Tannenbaum, 2008)). To reduce the sensibility of the model to local minima, a shape-based regularization term $\bar{g}^{Reg}(\boldsymbol{x}^*)$ (e.g. curvature-based regularization) is included in the final feature map. $\alpha$ is a positive hyperparameter that balances the image-based and regularization terms. It must be specifically defined based on the selected terms (e.g. regularization strategy used). For further details on the BEAS mathematical formalism, the reader is kindly directed to the original work (Barbosa *et al.*, 2012).

### 7.2.2. Curvilinear blind-ended model

#### A. Description

In order to capture the particularities of the LAA shape, a novel BEAS model is proposed. Hereto, a description of the tubular blind-ended LAA shape is presented as a combination of both cylindrical and spherical spaces. Moreover, in order to take into account the LAA anatomical variability (allowing straight and non-straight shapes), a cylindrical system defined along a pre-defined curved axis is used (Morais *et al.*, 2017c; Queirós *et al.*, 2016).

Figure 7.2A presents an illustrative schematic of the proposed model. Each coordinate $\boldsymbol{x}$ of the 3D surface is described in terms of its longitudinal ($p_L$) and circumferential coordinates ($p_C$) plus its respective orthogonal distance ($r$) to the curved centerline axis, *i.e.*, $\boldsymbol{x} = \{r, p_L, p_C\}$. Two independent spaces are used to describe the target model: 1) the tubular body of the LAA is defined based on a cylindrical space with a curved axis (*i.e.* $p_L$ and $p_C$ described as distance along axis - $s$ - and azimuth - $\theta$, respectively) and 2) the LAA tip through a spherical coordinate system (*i.e.*, $p_L$ and $p_C$ described as elevation - $\varphi$ - and azimuth - $\theta$, respectively). Considering a long-axis view as presented in Figure 7.2A, a set of $p_L$ coordinates with different positions

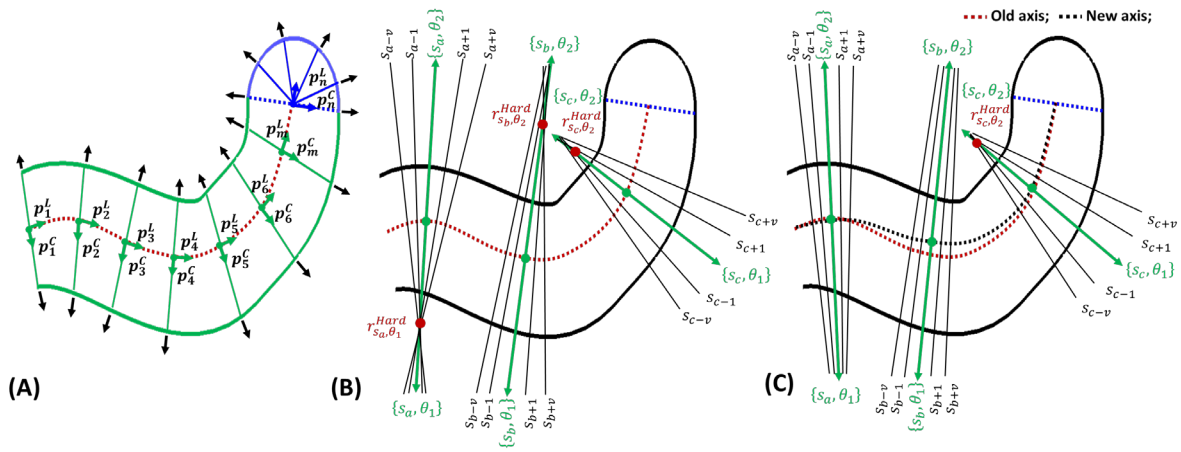


**Figure 7.2 – Blind-ended BEAS model.**
(A) Schematic of the curvilinear blind-ended model; (B) Hard Regularization strategy; (C) Axis recenter approach.

and orientations, which were defined based on the model centerline and the tangent to each position, is used to generate the curvilinear tubular surface (green line in Figure 7.2A). Then, at the final portion of the cylindrical model (*i.e.*, LAA tip), and taking into account its position and orientation, a half sphere is positioned by defining the respective $p_L$ coordinate according to a spherical space (blue line in Figure 7.2), ultimately generating the blind-ended LAA model. In order to describe this model with the BEAS framework, Equation (7.1) is now rewritten as:

$$r = \psi(p_L, p_C) = \psi(\boldsymbol{x}^*), \tag{7.6}$$

with,

$$p_L = \begin{cases} s, if\ s < s_{Max} \\ \varphi_{s_{Max}},\ if\ s = s_{Max} \end{cases} \quad \text{and} \tag{7.7}$$

$$p_C = \theta, \tag{7.8}$$

where $s_{Max}$ defines the $s$ level interface between the cylindrical and spherical components. Additionally, $\theta \in [0; 2\pi[$, $s \in [0; s_{Max}[$ and $\varphi_{s_{Max}} \in \left[\frac{\pi}{2}; \pi\right[$.

Finally, the current 3D model is evolved using a discretized surface grid with size $(n_s + n_\varphi) \times n_{p_C}$. $n_s$ and $n_\varphi$ express the size of the cylindrical and spherical grid component at the longitudinal direction, respectively. $n_\theta$ represents the size of the grid at the circumferential direction. Therefore, each point of the abovementioned grid is described as $\boldsymbol{x}(i,m) = [r_{i,m}, p_{L_i}, p_{C_m}]$, with $i \in [0; n_s + n_\varphi[$, $m \in [0; n_{p_C}[$. It might be noted that the original grid $\boldsymbol{x}$ can be independently separated into the cylindrical and spherical components as $\boldsymbol{x}_{Cyl}(i,m)$ (with $i \in [0; n_s[$) and $\boldsymbol{x}_{Sph}(i,m)$ (with $i \in [n_s; n_s + n_\varphi[$), respectively.

### B. Hard regularization

Due to the curvilinear nature of the proposed model, a strategy to prevent folding of surface regions is required. Indeed, at these position, points in the 3D Cartesian space can be

described by multiple coordinates $\boldsymbol{x}_{Cyl}(i,m)$ in the cylindrical space, which could result in intersections or folding portions along the final surface. Therefore, a hard regularization term is applied to preserve the surface shape (Figure 7.2B). This term relies on a map, $\boldsymbol{r}^{Hard}$ (defined in the cylindrical space only), representing the nearest possible intersection or folding radii position (described as $r_{i,m}^{Hard}, i \in [0; n_s[$) for each specific coordinate pair $(s_i, \theta_m)$. In detail, for each $(s_i, \theta_m)$ (each green arrow in Figure 7.2A), the hard limit is computed by intersecting a line (denoted as a set of points $\{(r^L, s_i, \theta_m), \forall\, r^L \in \mathbb{R}^+\}$) with a set of planes representing the remaining discrete $s$ levels of the cylindrical model (exemplified as dark lines in Figure 7.2B, and expressed as $\left\{[r^P, s_{j,j\neq i}, \theta^P], \forall\, \{r^P \in \mathbb{R}^+, \theta^P \in [0; 2\pi[\}\right\},\ j \in \{[i-v; i+v] \cap [0; n_s]\}$). Please note that, by intersecting a specific line with a particular $s$ level, one obtains a local estimation of the maximum radii value where no folding regions are found. Moreover, since multiple intersection positions can occur along a specific line (particularly, if considered the intersection between the line and all the remaining $s$ levels), the final hard boundary position $[r_{i,m}^{Hard}, s_i, \theta_m]$ is defined as the intersection position with minimal radii (red dot in Figure 7.2B). Finally, to limit the influence of too far planes on a particular position, which would drastically restrict the model and make the method computationally demanding, only the nearest $v$ planes are considered for each line (Figure 7.2B). Additionally, in order to reduce the search region and assuming a given maximum size for the target object, a maximum radii $\beta$ was considered.

To regularize the surface throughout the evolution, the following feature was included:

$$\bar{g}^{Reg}(\boldsymbol{x}^*) = -H(\boldsymbol{x}^* - \boldsymbol{r}^{Hard}), \tag{7.9}$$

with $H$ representing a Heaviside operator. As such, at possible folding positions (*i.e.,* $\boldsymbol{x}^* - \boldsymbol{r}^{Hard} > 0$), high penalization is locally applied at the surface, preventing therefore its growth and ultimately avoiding surface folding. In the opposite case (*i.e.,* $\boldsymbol{x}^* - \boldsymbol{r}^{Hard} < 0$), no regularization is applied. Since this regularization term is only locally applied during a few iterations to keep the LAA shape coherent (presenting a value of zero in the remaining situations and not influencing the model's optimization), no specific tuning of the hyperparameter $\alpha$ was performed. Therefore, $\alpha = 1$ was used in our experiments.

**C. Axis recenter**

Since the proposed model is optimized based on an initial fixed axis, a highly curved or complex surface not representing the particularities of the patient's anatomy is expected after a few iterations, requiring therefore multiple hard boundaries to prevent folding regions. Thus, in order to minimize the influence of the hard regularization term throughout the optimization, a

strategy to correct a highly curved axis is applied. By correcting these points of the axis (Figure 7.2C), not only the influence of the hard boundaries on the final result is reduced, but also increase the potentialities of the model to capture more particularities of the anatomy. Specifically, for each iteration, points on the curved axis with high curvature are identified as regions with a hard boundary radii lower than the pre-defined maximum value $\beta$. Then, a novel axis (Figure 7.2C) is estimated by fitting a spline to all other points of the original axis. Note that the extreme positions of the centerline are always kept during this process, working as anchor positions and allowing a reconstruction of a novel axis centered on the target anatomy. Finally, taking into consideration the novel axis, the entire surface is resampled accordingly.

### 7.2.3. Framework overview

Taking into account the previous description of the curvilinear blind-ended model, a detailed explanation of the LAA segmentation methodology is now presented (Figure 7.3). A constant model is initialized, by manually defining a centerline using three or more sequential clicks along the LAA. The different clicks are provided in the 3D space, by freely navigating through the volume using three orthogonal planes. Two evolution stages are subsequently applied: 1) a fast evolution stage based on a BEAS-threshold approach to capture the global shape of the LAA model; and 2) refinement of the 3D surface to the real patient anatomy by applying a BEAS-segmentation technique with regional/local energies.

#### A. Fast contour growing

Due to the sensitivity of model-based segmentation approaches to the initialization, a strategy to compensate for sub-optimal initializations is presented. This method uses global terms and large evolution steps to quickly evolve the LAA model (e.g., global threshold values), allowing to recover the global and non-refined LAA shape. No energies are used to control this stage, requiring simple decision strategies (namely, the number of iterations) to stop the process.

The global model is evolved using two independent terms: 1) direct image content through a fixed threshold value, and 2) a global edge map estimated using phase-based filters

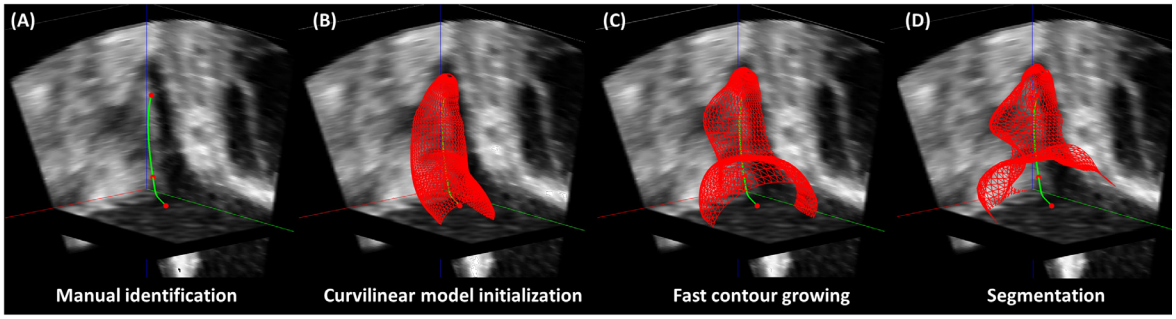


**Figure 7.3 - Overview of the proposed LAA segmentation method.**

(Belaid *et al.*, 2011). Both terms are computed based on a set of image profiles $P$ defined radially with respect to the centerline (yellow arrows in Figure 7.4A). Regarding the first term, the optimal threshold is computed assuming a Gaussian mixture model with 3 independent regions (*i.e.,* lumen, LAA trabeculae and cardiac wall). Then, an Expectation-Maximization algorithm is applied to estimate the location of each Gaussian, and the mean value of the second Gaussian model used as threshold ($th$). In its turn, the edge transitions (for each $P$) are estimated by evaluating the even and odd responses of each image profile by applying Riesz filters (Felsberg and Sommer, 2001) and a band-pass zero-DC filter (which attenuates undesirable frequencies), followed by the searching of asymmetry positions in the image's spectrum (Figure 7.4b). This method was selected due to its theoretical intensity-invariance, making it suitable for the low-contrast and noisy TEE images (Grau *et al.*, 2007; Rajpoot *et al.*, 2009). To increase the method's robustness to image noise (particularly at the lumen), the signed version (focusing on dark-to-bright transitions) recently proposed by Torres (2016) is applied in this study to obtain a rough estimation of the LAA. Moreover, for each $P$, only the position with maximum asymmetry was considered as a valid edge (Figure 7.4C). Please note that, by combining both edge-based and image-based terms, the method robustness is notably increased. Indeed, the edge term constrains the model evolution compensating for sub-optimal threshold values and making the strategy less sensitive to the number of iterations used. Moreover, due to the signed edge strategy, image noise at the lumen is easily surpassed. Finally, the combination of both terms improved the method's performance to distinguish between LAA trabeculae and wall.

This strategy was added into the described pipeline, by modifying Equation (7.5) as:

$$\bar{g}^{IM}(\boldsymbol{x}^*) = \bar{g}^{Th}(\boldsymbol{x}^*) + \bar{g}^{Edge}(\boldsymbol{x}^*), \tag{7.10}$$

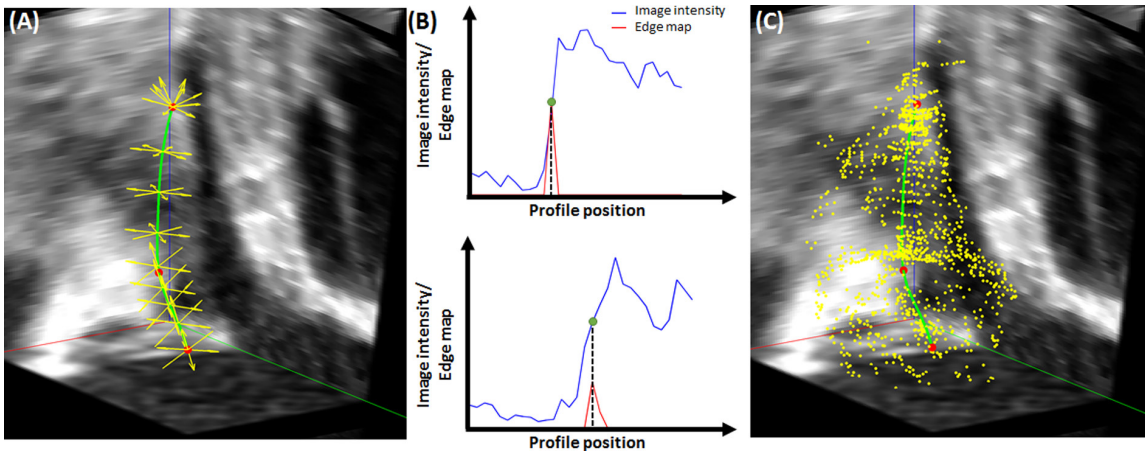


**Figure 7.4 - Fast contour initialization strategy.**
(A) Multiple image profiles (yellow arrows) are used to estimate the optimal edge position and the threshold value; (B) Edge estimation through a phase-based technique and (C) resulting edge positions.

$$\bar{g}^{Th}(\boldsymbol{x}^*) = \begin{cases} 1, & if\ \bar{I}(\boldsymbol{x}^*) \leq th \\ -1, & otherwise \end{cases}, \tag{7.11}$$

$$\bar{g}^{Edge}(\boldsymbol{x}^*) = H(\boldsymbol{r}^{Edge} - \boldsymbol{x}^*) - H(\boldsymbol{x}^* - \boldsymbol{r}^{Edge}), \tag{7.12}$$

with $\boldsymbol{r}^{Edge}$ being a map representing the edge radii ($r_{i,m}^{Edge}$, $i \in [0; n_s + n_\varphi[$) for each image profile $P$ (described as a function of $p_{L_i}$ and $p_{C_m}$). $\bar{I}(\boldsymbol{x}^*)$ is the image value at position $\boldsymbol{x} = \{x_1 = \psi(\boldsymbol{x}^*), x_2, \dots, x_n\}$. Of note, the term $\bar{g}^{Edge}$ is always attracting the contour to the nearest edge, pushing it outward and inward when the contour position is inside (*i.e.* $\boldsymbol{x}^* - \boldsymbol{r}^{Edge} < 0$) or outside of the LAA blood pool (*i.e.* $\boldsymbol{x}^* - \boldsymbol{r}^{Edge} > 0$), respectively. It might be noted that, since both terms use a similar range (*i.e.*, -1 or 1), no weight hyperparameter is required in equation (7.10) to balance the influence of the different feature maps.

**B. Segmentation**

The rough model is refined to the patient anatomy using a segmentation process with regional-based energies. The optimization process is guided by a local Yezzi energy (Queirós *et al.*, 2014), which estimates the optimal contour's position as the maximum contrast point between inner and outer regions. Moreover, since the LAA walls are brighter than the lumen, a signed version of this energy is used, explicitly embedding a specific representation of the target transition (*i.e.* dark-to-bright) into the functional energy, improving therefore its robustness to noise and image artifacts.

The current energy is integrated into the segmentation model by considering the following image criteria in equation (7.2):

$$F(\boldsymbol{y}) = w_{in}.u_x - v_x, \tag{7.13}$$

and using its derivative to identify the local minima, through:

$$\bar{g}^{IM}(\boldsymbol{x}^*) = w_{in}\frac{I(\boldsymbol{x}^*) - u_x}{A_u} + \frac{I(\boldsymbol{x}^*) - v_x}{A_v}, \tag{7.14}$$

where $u_x$ and $v_x$ are the mean intensities inside and outside of the evolving interface at point $\boldsymbol{x}$, calculated using mask $B$. $w_{in}$ is a scalar weight applied to the inner region and $A_u$ and $A_v$ represent the area of the inner and outer region, respectively. It might be noted that due to presence of trabeculae at the LAA body (being darker than the wall and brighter than the lumen), a correct setting of $w_{in}$ is required to intrinsically modify the equilibrium position between both inner and outer regions (Queirós *et al.*, 2014). Moreover, due to the high performance typically found by the signed local Yezzi in ultrasound imaging, and contrary to the previous step described in section 7.2.3A, no edge term is applied during this step.

### 7.2.4. Implementation details

In order to increase the method's robustness to the initialization and to improve its performance at the initial portion of the LAA (*i.e.*, interface between left atrium and LAA), a sequential segmentation scheme (section 7.2.3B) is applied, namely: 1) initial estimation of the optimal contour position using a large region $B$ with large image profiles ($\rho \simeq 6\,mm$); and 2) result refinement using narrowing regions $B$ with more localized image profiles ($\rho \simeq 2\,mm$). It might be noted that, since the walls around the LAA are typically thicker, the application of the current double-stage strategy improves the method's performance to identify the optimal boundary, without drastically increasing the risk of segmenting an outer structure.

A total of $40 \times 48$ points were used to represent the surface grid (*i.e.*, $n_s = 32$, $n_\varphi = 8$ and $n_\theta = 48$), with $h = 2$ (for both coordinates $p_L$ and $p_C$). Moreover, $w_{in}$ was set to 0.7 for all the experiments. The feature map presented in equation (7.5) is post-processed to prevent too large and local evolution steps caused by noisy regions or artifacts during the iterative process and to increase the stability of the segmentation process. Specifically, when the maximum value of the map (in absolute) is higher than 1, the entire map is normalized (keeping it in the range of [-1;1]), dividing it by the maximum value. No post-processing is applied in the opposite situation (*i.e.* maximum value lower than 1). The fast initialization, based on BEAS-threshold and an edge term, was applied throughout 20 iterations and each profile $P$ had a length of approximately $7\,mm$. For the phase-based edge term, a band-pass zero-DC Difference-of-Gaussians filter was used. The two Gaussians were set with a sigma of approximately 2.3 mm and 3.2 mm, respectively. No scales or deviation gain term was used. Finally, regarding the hard regularization term, the maximum search region ($\beta$) was set to 20 mm with a total of 5 neighboring planes ($v$). In section 7.3.3, the influence of the selected terms and parameters is addressed and the influence of their variation explored.

## 7.3. Experiments

Three different experiments were set to evaluate the performance of the method: 1) influence of the parameters on the final method's accuracy; 2) evaluation of the segmentation error against manual analysis; and 3) differences between automated and manual analysis for the estimation of the clinical measurements for the planning of a LAA occlusion intervention.

### 7.3.1. Data description

A total of 20 TEE datasets were retrospectively selected from clinical practice, including patients with suspicion of pathology but with normal anatomy and abnormal cases. Due to the

shape variability typically found at the LAA, one expert classified each case based on *Beigel et al.* (2014), obtaining the following representation: chicken wings – 45% (9 patients); windsock – 20% (4 patients); cauliflower – 20% (4 cases); and cactus – 15% (3 cases).

The acquisitions were performed using a 3D TEE probe with different ultrasound scanners, namely: GE Vivid E95 (GE Vingmed, Horten, Norway), Philips IE33 (Philips Ultrasound, Bothell, USA) and Philips Epiq 7. No modification to the normal clinical routine was required throughout the dataset acquisition. Specifically, an electrocardiogram (ECG)-gated acquisition was performed in mid-esophageal position using zoom mode and acquiring the LAA body, part of the mitral valve, left atrium and pulmonary veins (Beigel *et al.*, 2014). The resulting image presented a resolution and size that varied from 0.20 to 0.45 mm and $126 \times 122 \times 117$ to $357 \times 413 \times 208$ voxels, respectively. The datasets were initially stored in a raw-data form and subsequently exported to a workstation with EchoPac (GE HealthCare, Horten, Norway) or QLab (Philips Ultrasound, Bothell, USA). Then, each case was anonymized, exported into an externally-readable format and converted to an isotropic voxel spacing. The entire dataset was constructed using the resources of the University Hospital Leuven with approval of the Ethics Committee (S59406).

### 7.3.2. Ground truth generation

Two observers manually delineated the 3D surface of the LAA for each patient, allowing the evaluation of the inter-observer variability. The delineation was performed using a custom non-commercial software, Speqle3D (Queirós *et al.*, 2018), using the following strategy: 1) manual definition of the LAA centerline by providing three clicks along the anatomy; 2) 2D delineation of multiple LAA short-axis (SAx) views (30-40), defined perpendicular to the centerline; 3) 2D delineation of multiple LAA long-axis (LAx) views (2-5); and 4) 3D surface reconstruction using the obtained points along the different SAx and LAx views. Moreover, one of the observers repeated the analysis two weeks later, allowing the assessment of the intra-observer variability. In order to assess the influence of the initialization on the final result, each observer performed the analysis using independent LAA centerlines (henceforward referred as "Different axis" situation). Later, one observer repeated the segmentation process using the centerline defined by the other observer (henceforward mentioned as "Same axis" scenario).

Next, each observer manually extracted the relevant clinical measurements (defined as $Obs_1$ and $Obs_2$), namely: diameter of the ostium and landing zone and length of LAA, as described by (Song *et al.*, 2016; Wang *et al.*, 2016a; Wunderlich *et al.*, 2015). Both observers performed this task independently, allowing the measurement of the reproducibility between

them. For that, the user freely navigated along the 3D image using 3 orthogonal planes or resliced the data along the LAA centerline. The ostium and landing zone were defined by selecting the respective optimal image planes, and manually delineating their boundaries. Then, area-derived diameters were extracted for each case based on the 2D contours. The LAA depth was computed as the distance between the LAA tip (selected in a LAx view) and the centroid of the landing zone. In order to assess the inter-observer variability caused by the 2D delineation process only, the second observer repeated the manual delineation at the ostium/landing zone defined by the first observer (henceforward referred as $Obs_2R$). For the LAA depth, the second observer selected the LAA tip using the LAx view defined by the first observer.

### 7.3.3. Parameter tuning

In the current experiment, an evaluation of the method's sensitivity to its parameters is performed. The following parameters were assessed: number of iterations used in the BEAS-threshold stage (section 7.2.3A), the influence of the $w_{in}$ weight, the impact of the scaling term ($h$) and the influence of the threshold value ($th$) in the final result. For each case, the nearest values to the selected one were evaluated. The $th$ term was evaluated by summing/subtracting a fixed value (5%, 10%, 15% and 20% of the intensity range of the full image) to the automatically estimated one. In order to prevent over-tuning, a total of 10 cases were randomly selected from the clinical database. Moreover, the automated method was initialized using the same centerline used throughout the manual segmentation by $Obs_1$.

The influence of each parameter was assessed in terms of the point-to-surface error (P2S error), by comparing the automated segmentation result (for a specific parameter) against the manual result. An analysis of variance (ANOVA) was applied to each parameter to check for statistically significant differences ($p<0.05$). Moreover, a two-tailed paired t-test ($p<0.05$) was applied between each parameter and the optimal one.

### 7.3.4. Segmentation accuracy

The accuracy of the proposed segmentation technique is addressed throughout this experiment. In contrast to section 7.3.3, the entire database (20 cases) is now used.

The difference (referred as $Auto_{3D}$) between automated and manual analysis ($Obs_1$), inter-observer and intra-observer variability were assessed in terms of P2S, Dice value and 95$^{th}$ percentile of the Hausdorff distance (95HS). Similarly to section 7.3.2, the automated method was evaluated in two independent scenarios: 1) considering the influence of the initialization, by initializing the automated method with a LAA centerline different than the one used by the manual analysis; and 2) assuming an equal centerline for the automated method and to the

manual analysis. In order to check for statistically significant differences between each group (*i.e.* automated, inter- and intra-observer), a two-tailed paired t-test between each pair was computed. Furthermore, in order to validate the proposed pipeline, the influence of each stage was assessed in terms of P2S error. Finally, the computational time of the proposed automated method was compared with the time required to perform a manual analysis. All results were computed using MATLAB code (no parallelization) on a common personal laptop with an Intel (R) i7 CPU at 2.8 GHz and 16 GB of RAM.

#### 7.3.5. Clinical measurements

Similar to experiment 7.3.4, the accuracy of the proposed automated method was compared with the manual analysis for the semi-automatic extraction of the relevant clinical measurements. Specifically for the proposed method, the 3D LAA surface was clipped using the manually defined ostium and landing zone planes (independently selected by each observer), and the final clinical value estimated as an area-derived diameter (termed as $Auto_1$ and $Auto_2$ for $Obs_1$ and $Obs_2$ levels, respectively). Regarding the LAA depth, it was computed as a distance between: 1) the centroid of the automated landing zone; and 2) the resulting position from the intersection between a line, which was manually defined by the observer by providing one click at the LAA tip and the centroid of its landing zone and the 3D LAA surface.

The differences in clinical measurements between semi-automated and manual results were evaluated in terms of bias (*i.e.*, mean error of the differences), and limits of agreement (LOA, given as mean ± 1.96 times the standard deviation). The same analysis was performed to compare the difference between observers ($Obs_1$-$Obs_2$) and even to evaluate the 2D delineation reproducibility ($Obs_1$-$Obs_2R$). For each comparison pair, a two-tailed paired t-test and F-test were used to identify statistically significant differences ($p<0.05$) in the obtained biases and LOAs, respectively.

### 7.4. Results

#### 7.4.1. Parameter tuning

Figure 7.5 depicts the influence of the different parameters on the method's accuracy. In fact, the results corroborated the method's robustness, showing no statistically significant differences for the majority of the tested parameters (except for $w_{in}$).

#### 7.4.2. Segmentation accuracy

Table 7.1 indicates the differences between the automated and manual analysis in terms of P2S error, Dice and 95HS error (at the "Same Axis" scenario). Globally, a similar

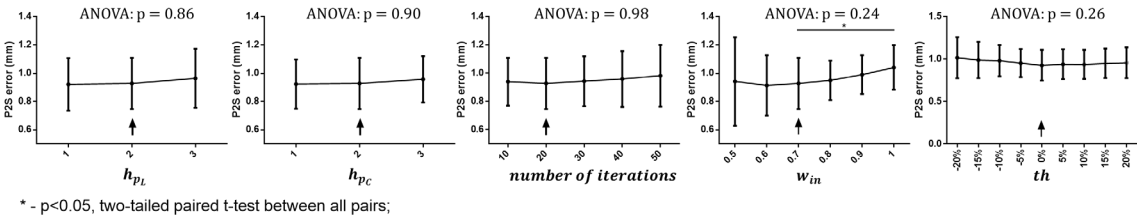


**Figure 7.5 - Influence of the segmentation parameters in the final accuracy of the proposed pipeline.** Specifically, the scale in the longitudinal $\boldsymbol{h_{p_L}}$ and circumferential $\boldsymbol{h_{p_C}}$ direction, the number of iterations throughout the fast refinement stage, the scalar weight $\boldsymbol{w_{in}}$ and the threshold $\boldsymbol{th}$ value.

performance was found when comparing the $Auto_{3D}$ error against the inter-observer variability, with statistically significant differences against the intra-observer variability (for both cases). In terms of P2S error, a mean error lower than 1 mm was obtained for all the scenarios. The influence of the centerline axis was addressed, showing no statistically significant differences when modifying it (Figure 7.6a). Figure 7.6b also evaluates the method's performance at each step of the pipeline, showing a reduction (with statistically significant differences) between consecutive steps. Representative segmentation results are shown in Figure 7.7. The proposed method required $14.0 \pm 4.8$ seconds (excluding initial centerline definition, which took ~45 seconds per case), while the manual 3D segmentation took ~40 minutes per case.

**Table 7.1 – Segmentation errors of the proposed semi-automated technique.**
(Both manual and automated approaches were initialized using the same LAA centerline).

| | P2S (mm) | Dice (%) | 95th HS (mm) |
|---|---|---|---|
| $Auto_{3D}$ | 0.88±0.20[b] | 82.5±3.6[b] | 2.49±0.73[b] |
| Inter | 0.91±0.18[b] | 84.3±5.2[b] | 2.20±0.64[b] |
| Intra | 0.53±0.15 | 89.4±2.8 | 1.42±0.45 |

P2S – Point-to-surface; HS – Hausdorff; [a] p<0.05, two paired t-test against the inter-observer variability (Inter). [b] p<0.05, two-tailed paired t-test against the intra-observer variability (Intra).

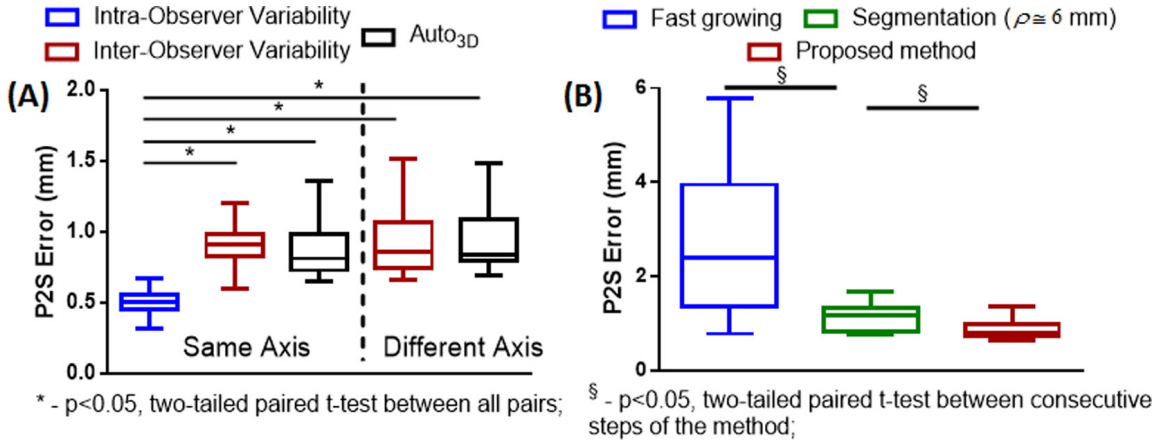


**Figure 7.6 – (A) The accuracy of the proposed segmentation approach using the same and a different centerline; (B) P2S error throughout the different stages of the proposed method.**

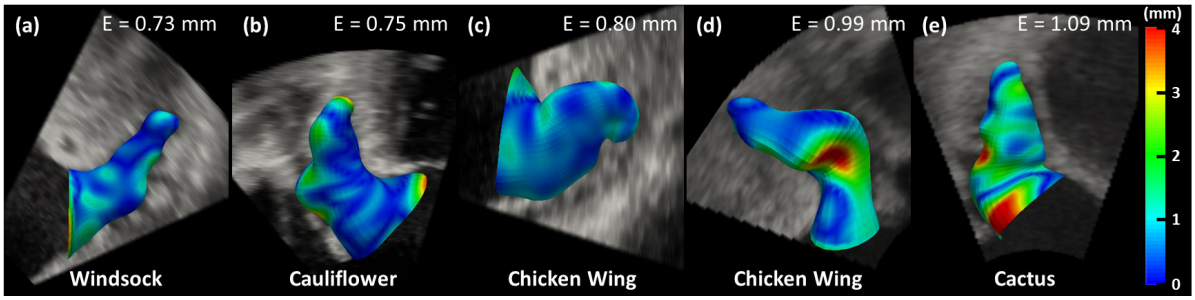


**Figure 7.7 – Semi-automatic segmentation results.**
These results correspond to the (a) 10th, (b) 30th, (c) 50th, (d) 70th and (e) 90th percentile of the P2S error.

### 7.4.3. Clinical measurements

Table 7.2 indicates the differences between automated and manual analysis for each of the relevant clinical measurements. It might be noted that a centroid error (computed assuming the 2D contours) of 1.55 ± 1.29|1.21 ± 0.70 mm and a difference in terms of plane orientation of 10.15 ± 5.05°|8.04 ± 4.27° were found between both observers for the ostium|landing zone planes, respectively. Globally, a similar performance was found between automated and manual approaches for the ostium, but with statistically significant differences at the landing zone and LAA depth. The worst performance in terms of automated and even inter-observer variability was found for the LAA depth. Low biases were found for the majority of the comparisons, presenting only statistically significant differences on $Auto_1$-$Obs_1$ at the landing zone and for the inter-observer variability for the LAA depth. Interestingly, the automated analysis versus a manual one always obtained narrower LOAs compared to the differences between observers. A second study was conducted where only the influence of the 2D delineation stage was evaluated (Table 7.3). High similarity (in terms of bias and LOAs) was obtained between the automated method and the observer variability for all the measurements. Finally, Figure 7.8 shows manual tracings and automated segmentation results at the ostium and landing zone. All tracings were contoured at the same SAx plane, showing accurate delineations for all the levels. Of note, the manual analysis took ~ 3 minutes (identification of the 3 measurements) per patient.

**Table 7.2 – Agreement for area-derived diameters between manual analysis ($Obs_1$, $Obs_2$) and semi-automatic derived measurements ($Auto_1$, $Auto_2$).**

| | Ostium | | Landing zone | | LAA depth | |
|---|---|---|---|---|---|---|
| | Bias (mm) | LOA (mm) | Bias (mm) | LOA (mm) | Bias (mm) | LOA (mm) |
| $Auto_1$-$Obs_1$ | 0.38 | [-1.31;2.07] | -0.42[a] | [-2.09;1.24][c] | -0.35 | [-2.56;1.85] |
| $Auto_2$-$Obs_2$ | 0.32 | [-1.45;2.08] | -0.05 | [-1.88;1.78] | 0.46[b] | [-1.55;2.47][c] |
| $Obs_1$-$Obs_2$ | 0.02 | [-2.34;2.39] | 0.57 | [-2.13;3.27] | 0.80[a] | [-2.53;4.12] |
| $Auto_1$-$Auto_2$ | 0.08 | [-1.73;1.90] | 0.20 | [-1.38;1.78][c] | 0.01 | [-1.96;2.00][c] |

LOA – Limits of agreement (given as $\mu \pm 1.96\sigma$). [a] $p<0.05$, two-tailed paired t-test against 0; [b] $p<0.05$, two tailed paired t-test against $Obs_1$-$Obs_2$; [c] $p<0.05$, two tailed F-test against $Obs_1$-$Obs_2$.

**Table 7.3 – Agreement between automated and manual analyses when at the same levels.**

| | Ostium | | Landing zone | | LAA depth | |
|---|---|---|---|---|---|---|
| | Bias (mm) | LOA (mm) | Bias (mm) | LOA (mm) | Bias (mm) | LOA (mm) |
| $Auto_1$- $Obs_2R$ | 0.18 | [-1.63;1.98] | 0.52[a] | [-1.22;2.27] | -0.05 | [-2.53;2.42] |
| $Obs_1$-$Obs_2R$ | -0.20 | [-1.80;1.40] | 0.95[a] | [-1.13;3.03] | 0.30 | [-2.11;2.72] |

LOA – Limits of agreement (given as $\mu \pm 1.96\sigma$). [a] $p<0.05$, two-tailed paired t-test against 0; [b] $p<0.05$, two tailed F-test against $Obs_1$-$Obs_2R$; [c] $p<0.05$, two tailed F-test against $Obs_1$-$Obs_2$; [d] $p<0.05$, two tailed F-test against $Auto_1$-$Obs_1$; [e] $p<0.05$, two tailed F-test against $Auto_1$-$Auto_2$.

## 7.5. Discussion

In this article, a novel semi-automatic methodology for LAA segmentation of peri-procedural data is proposed. The proposed method is initialized by a manually defined centerline along the LAA, which is subsequently corrected throughout the segmentation process, minimizing the influence of the observer's input and experience. Then, global and regional-based stages are applied to roughly estimate the LAA boundaries and to refine the contour to the real anatomy, respectively. Globally, the experimental findings corroborated the accuracy and feasibility of the proposed method, showing its potential for normal clinical practice, by generating a realistic 3D anatomical model that eases the interpretation of the TEE images. Moreover, it also simplifies the identification of the LAA shape and can even be used for an accurate planning of LAA occlusion intervention by semi-automatically extracting the relevant measurements for the selection of the optimal device. Finally, due to its low computational time, which is approximately 100 times faster than the manual segmentation, the potential and interest of the proposed methodology is enlarged. Additionally, thanks to the

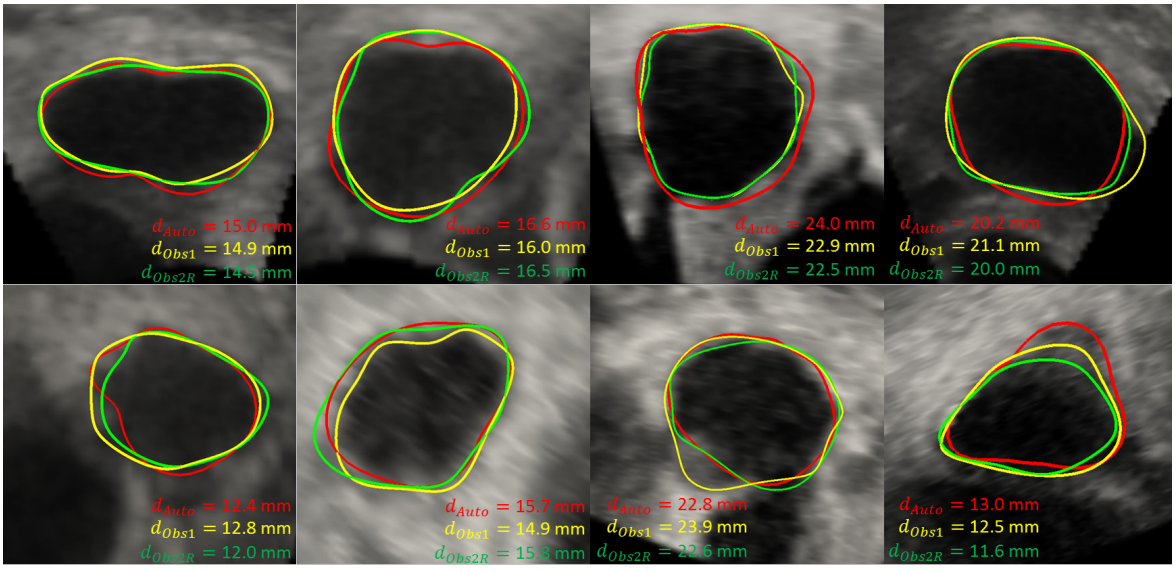


**Figure 7.8 - Manual tracing ($Obs_1$ - yellow, $Obs_2R$ - green) and automated segmentation result (red) at the different clinical levels (1st line - ostium, 2nd line - landing zone).**

current method and its computational cost (less than 20 seconds), 3D evaluation of the LAA anatomy throughout the peri-procedural stage (which typically requires several minutes) is now possible and feasible, adding relevant anatomical information and potentially improving the current interventional practice.

In contrast to other LAA segmentation techniques applied on CT images (Grasland-Mongrain *et al.*, 2010; Wang *et al.*, 2016b), the proposed method, to the best of our knowledge, is the first directly applied on peri-procedural TEE data. Although previous studies compared both CT- and 3D TEE-based planning of LAA occlusion (Bai *et al.*, 2017; Budge *et al.*, 2008; Goitein *et al.*, 2017; Nucifora *et al.*, 2011; Rajwani *et al.*, 2016; Wang *et al.*, 2016a), suggesting a superior performance of the first one (Goitein *et al.*, 2017; López-Mínguez *et al.*, 2014; Rajwani *et al.*, 2016), this is still sub-optimal due to the possible anatomical variations after the pre-operative acquisition and even the radiation exposure required (Nucifora *et al.*, 2011). Since one of the major limitations of the 3D TEE-based planning is the correct interpretation of the images, showing high variability between observers, automated tools to facilitate this task are of special interest (Song *et al.*, 2016). Thus, by applying the proposed solution in 3D TEE data, an exact evaluation of the patient's anatomy is allowed, ultimately improving the current planning scenario. Of note, although the proposed method is described as the first automated approach for segmentation of LAA in 3D TEE, a previous work (Song *et al.*, 2016) applied interactive and time-demanding strategies, *i.e.* threshold selection followed by manual correction, to obtain the 3D surface.

The proposed segmentation strategy is performed based on a curvilinear blind-ended model embedded into the BEAS framework (Figure 7.2 and Figure 7.3). In contrast with previous BEAS techniques applied to different cardiac chambers using individual coordinate systems (Morais *et al.*, 2017c; Queirós *et al.*, 2016), the current complex model was constructed by combining two independent spaces. In order to prevent any type of artifacts at the transition zone between both coordinate systems, both models are simultaneously optimized and combined into a unique grid of B-spline coefficients (Figure 7.2 and Figure 7.7). Moreover, due to the curvilinear nature of the method, a regularization approach was required to control the model shape (preventing folding), which showed high performance in the current database (see Appendix 7.7A). Although the current blind-ended model was proposed and validated to segment the LAA, it also shows potential for other situations, such as the left ventricle (LV) and LA. Indeed, recently, researchers (Zhou *et al.*, 2015) applied a similar concept (*i.e.*, fusion of different coordinate systems) on an anatomical tracking of the LV.

In order to evaluate the proposed method, a comparison between the automated result and the traditional manual delineation strategy was initially performed. The values in Table 7.1 proved the high accuracy (~0.9 mm) of the automated method, obtaining a performance similar to the one seen between observers (see also Appendix 7.7B). This high performance is corroborated by Figure 7.7. The highest errors were found at the opening region (transition between LA body and LAA) and the LAA tip. The first is easily explained by the axis correction strategy. Indeed, small modifications along the longitudinal direction of the initial axis will result in different opening planes, and therefore in large differences between surfaces. Additionally, at this plane, specific portions of the lumen-wall interface can be missed due to the limited field of the TEE acquisition, hampering the evolution of the proximal LAA model. The second is explained by the low contrast found at the LAA tip, as previously reported in Song *et al.* (2016). Statistically significant differences were found when comparing the automated result with the intra-observer variability. This result demonstrated the high robustness of the manual delineation approach when performed by the same observer, showing a significant worst result when considering the inter-observer variability. The automated method clearly improves this scenario, making the method less dependent on the user. Moreover, the automated method is much faster than manual analysis, making it an attractive solution for the clinical usage.

Regarding the influence of the different model parameters (Figure 7.5), the results showed high robustness to their variation, obtaining non-statistically significant differences for the majority of the situations. Only a careful selection of the $w_{in}$ weight is required to compensate the presence of trabeculae between the LAA blood pool and the wall. The influence of the manual initialization was also addressed, by evaluating the method's performance using a second independent axis (Figure 7.6A). A slightly worst result was obtained when compared with the initial study, but with no statistically significant differences. It should be noticed that since the axis is constantly corrected throughout the proposed pipeline, the influence of sub-optimal initializations is minimized throughout the optimization process. The importance of each algorithm's step was also evaluated (Figure 7.6B). A significant improvement of the method's accuracy was always observed between consecutive steps of the proposed pipeline, validating the proposed method. In fact, and as previously demonstrated by other studies (Chapter 5), model initialization using a fast growing approach (section 7.2.3A) shows high feasibility and robustness. Here, it should be highlighted the high robustness of this fast growing strategy to the variation of the $th$, showing a similar performance (statistically not significant) even when modifying it using 20% of the full image intensity range (Figure 7.5). Then, the

rough shape (obtained during the fast growing stage) is locally adapted using a double segmentation stage, where the method starts by globally identifying the optimal boundary (using a large search window) and refining it through a small search window.

In addition to the previous validation, the performance of the proposed method in terms of semi-automatic extraction of the clinical measurements for occluding device selection was evaluated. Table 7.2 proved the high performance of the automated method, obtaining narrow LOA for all the situations, even when compared with the inter-observer variability (with statistically significant differences for the landing zone and LAA depth). The advantages of the automated results are corroborated when considering the mean size of each clinical measurement (ostium – 20.2 ± 5.2 mm, landing zone – 17.1 ± 4.5 mm and LAA depth - 20.5 ± 7.5 mm, further details on Appendix 7.7C). Moreover, when compared to previous studies focused on the LAA occlusion intervention, notably narrower LOAs were obtained (Bai *et al.*, 2017; Goitein *et al.*, 2017; Nucifora *et al.*, 2011). Nevertheless, the majority of them focused on multi-modality validation studies, explaining these large differences. Specifically for the ostium and landing zone, the current results corroborated the advantage of the proposed approach, *i.e.*, estimating the relevant clinical measurements based on a full 3D surface, when compared with the traditional practice, where an expert traces a given 2D plane without guaranteeing a 3D shape consistency. Indeed, this independent approach is prone to errors (due to image artifacts) and highly dependent on the observer. In contrast, by extracting a full 3D surface, a realistic and continuous model with a certain degree of smoothing is obtained, reducing the variability found when measuring the relevant indicator at nearby locations (*i.e.*, different planes selected by different observers). In fact, similar observations were obtained by a previous study focused on a different cardiac structure (Queirós *et al.*, 2016).

Assessing each measurement individually, the lowest errors were found at the level of the ostium while the largest differences were registered for the LAA depth. This tendency is explained by the clear and well-contrasted image usually found at the ostium (first line of Figure 7.8) and the difficulties to correctly visualize the LAA tip due to its anatomical position in relation to the probe tip (Song *et al.*, 2016), respectively. Interestingly, although constant differences in terms of delineation strategy were found between observers, an intermediate result was always obtained by the proposed method. The influence of the 2D measurement extraction at the same plane was also assessed (Table 7.3). A reduction of the inter-observer variability was seen for all measurements, but without statistically significant differences with respect to Table 7.2. Remarkably, and in contrast to the previous observation, a high similarity is now found between the automated result (in both Table 7.2 and Table 7.3) and the inter-

observer variability (Figure 7.8). In fact, the proposed method achieved a similar performance when evaluated in both scenarios (*i.e.*, measurement extracted at different levels defined by different observers - Table 7.2 - and at the exact same level – Table 7.3), corroborating the method's robustness and emphasizing its potential for normal clinical practice. Notwithstanding, statistically significant biases were again found at the landing zone level, again demonstrating the difficult analysis at this level.

Regarding the obtained 3D shapes (Figure 7.7 and Appendix 7.7A), high anatomical variability was found between different patients. It might be noted that the clinical database used presented representative cases of the different LAA types with a similar prevalence to previous studies (Bai *et al.*, 2017; Beigel *et al.*, 2014). By evaluating the obtained 3D shape, correct classification (*i.e.*, as chicken wings, cactus, windsock or cauliflower) is facilitated, since the main properties of each class are captured by the model. Indeed, unilobular and multi-lobular structures were possible to be segmented (Appendix 7.7A), being the cases with higher prevalence (Beigel *et al.*, 2014). Nevertheless, the final result is highly smoothed when compared with the real anatomy, failing to capture specific details (Di Biase *et al.*, 2012). Moreover, in particular situations, small bridges connecting consecutive, nearby and small lobes can occur, slightly modifying the LAA shape and being a drawback of this technique. Nevertheless, these small lobes tend to be less important for the LAA occlusion intervention. Additionally, extreme, totally independent and large multi-lobular structures are not suitable to be processed by the current methodology. Notwithstanding, the authors would like to emphasize that even with the abovementioned slightly modified shapes, correct extraction of the clinical measurements is still possible. Since the relevant measurements (namely, ostium and landing zone) are typically extracted at the proximal portion (Lacomis *et al.*, 2007), which is usually tubular and free of large multi-lobes, the method's applicability in these situations is not limited, reinforcing again the added-value of the proposed technique.

## 7.6. Conclusion

The proposed semi-automatic method proved its potential for LAA segmentation, showing high accuracy, robustness and low computational time. Furthermore, by performing the planning of LAA occlusion intervention through the obtained 3D model, it is expected that accurate and more reproducible measurements will be obtained, corroborating the added-value of the proposed method for daily clinical practice.

## 7.7. Appendixes

### Appendix A – 3D example results

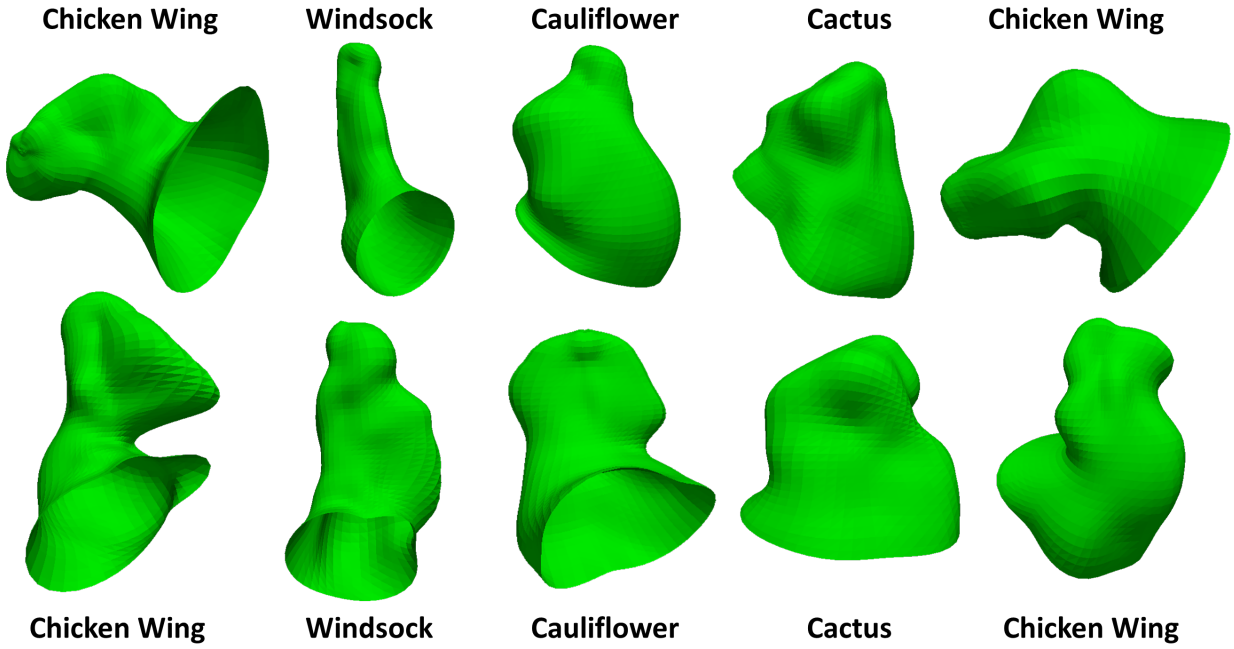


**Figure 7.A.1 – Representative 3D results obtained by the proposed method.**

### Appendix B – 2D Example results

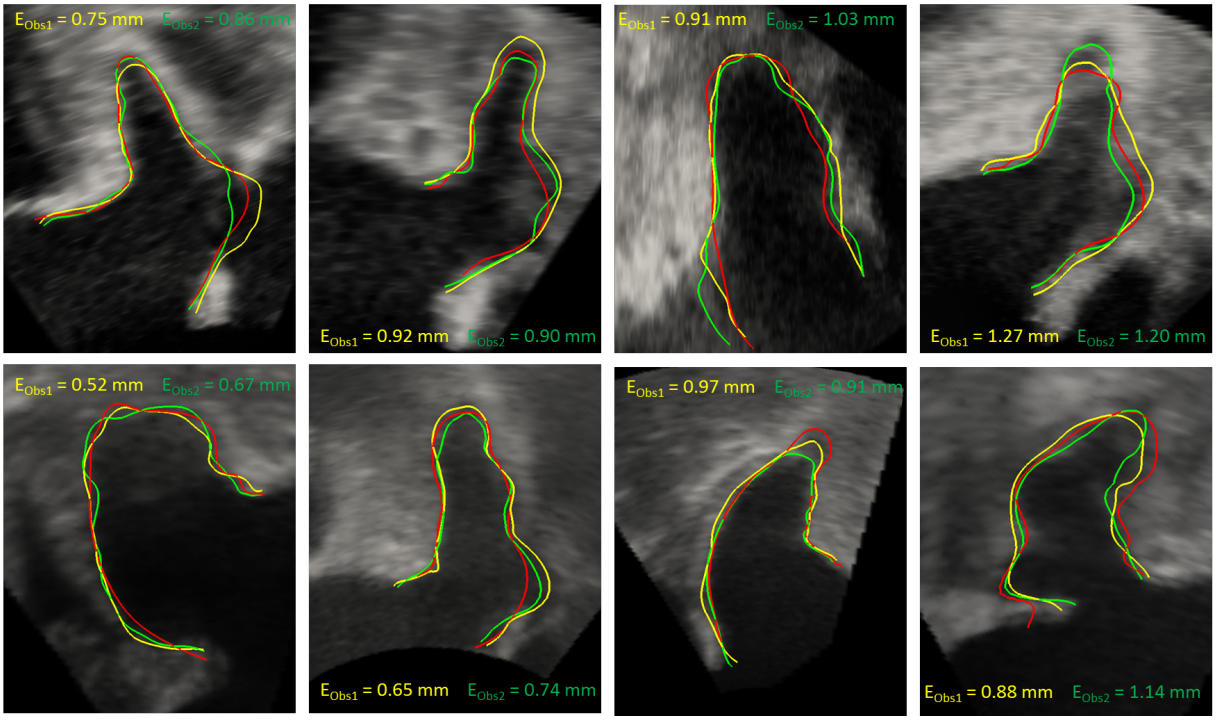


**Figure 7.B.1 – Examples of contour-sliced results obtained by the automatic and the manual approach.**
Red – Automatic, Yellow – Obs1, Green – Obs2.

## Appendix C – Reference values for the clinical measurements

**Table 7.C.1 – Mean (in mm) and standard deviation (in mm) of the clinical measurements obtained by the proposed method ($Auto_1$) and manual analysis ($Obs_1$ and $Obs_2$)**

| | Ostium | Landing zone | LAA depth |
|---|---|---|---|
| $Auto_1$ | 20.3 ± 5.2 | 17.2 ± 4.6 | 20.6 ± 7.7 |
| $Obs_1$ | 19.9 ± 5.1 | 17.0 ± 4.4 | 20.2 ± 7.3 |
| $Obs_2$ | 20.2 ± 5.2 | 17.0 ± 4.5 | 20.7 ± 7.6 |

# Chapter 8

## Semi-automatic image-based planning of Left Atrial Appendage Occlusion in 3D TEE images

This chapter has been submitted for publication in an international journal and is currently under review: **Pedro Morais**, João L. Vilaça, Sandro Queirós, Pieter De Meester, Werner Budts, João Manuel R. S. Tavares, Jan D'hooge, "Semi-automatic image-based planning of Left Atrial Appendage Occlusion in 3D Transesophageal Echocardiographic Images" (2018).

**Keywords:** Left Atrial Appendage Occlusion; Semi-automatic occluding device identification; 3D Image Segmentation; Iterative Closest Point; 3D Transesophageal Echocardiography.

**Contents**

## Abstract

Left atrial appendage (LAA) occlusion is used to reduce the risk of thromboembolism in patients with non-valvular atrial fibrillation, by obstructing the LAA through a percutaneously delivered device. Nonetheless, correct device sizing is complex, requiring the manual estimation of different measurements in pre-/peri-procedural images, which is tedious, time-consuming and with high inter- and intra-observer variability. In this work, a semi-automatic solution to estimate the required relevant clinical measurements is described. This solution starts with the 3D segmentation of the LAA in 3D transesophageal echocardiographic (TEE) images, using a constant blind-ended model initialized through a manually defined spline. Then, the segmented LAA surface is aligned with a set of templates, *i.e.* 3D surfaces plus relevant measurement planes (manually defined by one observer), transferring the latter to the unknown situation. Specifically, the alignment is performed in three consecutive steps, namely: 1) rigid alignment using the LAA clipping plane position, 2) orientation compensation using the circumflex artery location and 3) anatomical refinement through a weighted iterative closest point algorithm. The novel solution was evaluated in a clinical database with 20 volumetric TEE images. Two experiments were set up to assess: 1) the sensitivity of the model's parameters and 2) the accuracy of the proposed solution for the estimation of the clinical measurements. Measurement levels manually identified by two observers were used as ground truth. The proposed solution obtained results comparable to the inter-observer variability, presenting narrower limits of agreement for all measurements. Moreover, this solution proved to be fast, taking nearly 40 seconds (manual analysis took 3 minutes) to estimate the relevant measurements while being robust to the variation of the model's parameters. Overall, the proposed solution showed its potential for fast and robust estimation of the clinical measurements for occluding device selection, proving its added-value for clinical practice.

## 8.1. Introduction

Left atrial appendage (LAA) occlusion is a minimally invasive cardiac intervention, where a foldable device is percutaneously implanted at the proximal portion of the LAA, obstructing this orifice and blocking the communication between the left atrium (LA) and its appendage (Meier *et al.*, 2014). Since 90% of thrombi are found at the LAA for patients with non-valvular atrial fibrillation, LAA occlusion is usually performed to reduce the high thromboembolism and stroke risks of these patients (Meier *et al.*, 2014; Wunderlich *et al.*, 2015). Although different medical treatments are also available, namely anticoagulants and

epicardial LAA exclusion, LAA occlusion shows inferior bleeding complications with long-term compliance (Saw and Lempereur, 2014; Suradi and Hijazi, 2017).

Due to the high anatomical variability of the LAA, multiple occluding devices are produced by different manufacturers (Meier *et al.*, 2014; Saw and Lempereur, 2014). Therefore, during the intervention, multiple clinical measurements are extracted to identify the optimal device for the patient. These measurements are performed on 2D/3D pre-procedural (*e.g.* computed tomography, CT) (Wang *et al.*, 2016a) or peri-procedural images (*e.g.* fluoroscopic or transesophageal echocardiography, TEE, images) (Saw and Lempereur, 2014), by acquiring 2D planes at pre-defined anatomical views and then detecting the optimal level or by reformatting the 3D volume at specific locations followed by manual delineation. Overall, three LAA measurements are typically evaluated: 1) LAA ostial plane, determined by the circumflex artery (CA) to a position 1-2 cm within the Coumadin ridge; 2) LAA landing zone (LZ) plane, defined approximately 10 mm distally from the LAA ostium; and 3) LAA depth, computed as the distance from the LZ level to the distal LAA tip (Saw and Lempereur, 2014; Song *et al.*, 2016; Wang *et al.*, 2016a; Wunderlich *et al.*, 2015). It might be noted that the extracted measurements are specific to each manufacturer, requiring previous training/experience of the operator (Meier *et al.*, 2014; Saw and Lempereur, 2014). Currently, these levels are manually identified, being a very tedious and time-consuming task and with high intra- and inter-observer variability. Alternatively, 3D-printed models of the LAA anatomy were also proposed as a potential solution for identifying the optimal device to be employed (Liu *et al.*, 2016; Pellegrino *et al.*, 2016). In this case, the relevant anatomy is physically constructed and the different devices are tested. However, such approach is extremely time-consuming (requiring several days), manual and expensive (demanding extra devices to test it in the phantom model). Moreover, small anatomical variations between the model and the real anatomy are expected, which might negatively influence the selected device.

To automate the planning of the LAA occlusion, different researchers suggested strategies to segment the LAA lumen in 3D CT and TEE images. Specifically for CT, image-based techniques (Song *et al.*, 2016), deformable models (Grasland-Mongrain *et al.*, 2010) and machine learning (Jin *et al.*, 2018; Wang *et al.*, 2016b) algorithms were proposed. Concerning TEE images, pure image-based approaches followed by multiple manual corrections were mainly described, requiring further validation studies (Song *et al.*, 2016). Recently, a novel strategy based on the evolution of a curvilinear blind-ended B-spline Explicit Active Surface (BEAS) model was proposed to segment the LAA in 3D TEE images (Chapter 7). In this solution, the optimization is performed on two consecutive stages, starting with a fast evolution

with global descriptors to increase the robustness of the method to the initialization, followed by contour refinement with local descriptors to adapt the surface's boundaries to the anatomy (Chapter 7). Although the aforementioned state-of-the-art segmentation solutions proved their added-value for the assessment of the LAA 3D shape, they have never been used for the estimation of the relevant clinical measurements and therefore, for the identification of the optimal device.

Therefore, a novel methodology to semi-automatically estimate the relevant clinical measurements in 3D TEE images is proposed in this article. Its accuracy is computed in a clinical database and is assessed against the traditional workflow, which relies on manual contouring at specific levels.

Hereupon, this article introduces two novelties: 1) a novel method to automatically estimate the relevant clinical levels, *i.e.* ostial and LZ planes and the LAA depth, in 3D TEE images; and 2) a clinical validation of the proposed planning method for LAA occlusion.

This study is structured as follows. In section 8.2, a technical description of the novel methodology for the estimation of the relevant clinical measurements for LAA occlusion is presented. Sections 8.3 and 8.4 present the validation experiments that were performed and associated results, respectively. Section 8.5 discusses the performance of the proposed method. Finally, the conclusions are pointed out in Section 8.6.

## 8.2. Methods

In this section, a description of the proposed method for the planning of LAA occlusion is presented. This method is divided into three sequential conceptual blocks: 1) initialization of the LAA by providing at least three clicks (blue points in Figure 8.1A); 2) segmentation of the LAA lumen (Figure 8.1B, section 8.2.1); and 3) estimation of the relevant clinical

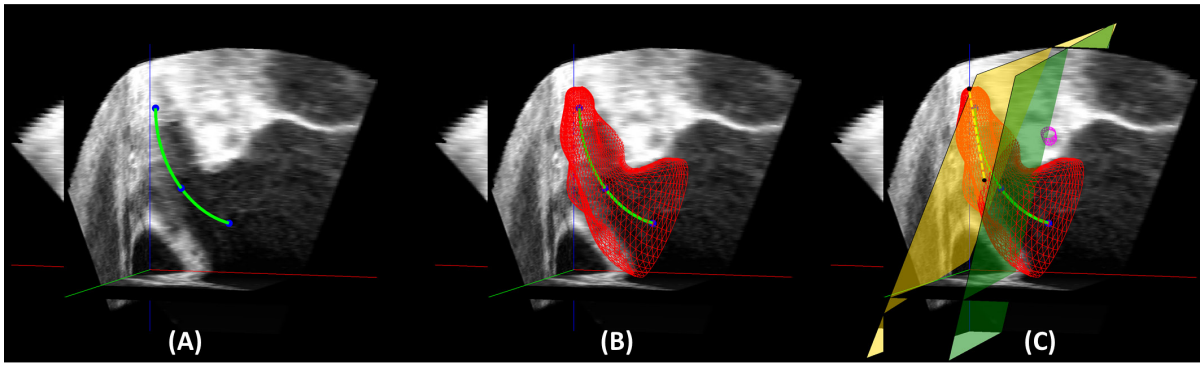


**Figure 8.1 - Overview of the proposed semi-automatic method for the planning of LAA occlusion.**
Green – Ostium, Yellow – Landing Zone, Yellow dashed line – LAA depth.

measurements (Figure 8.1C) through the alignment of the target surface with a set of known references (section 8.2.2).

Regarding the initialization stage (block 1), it consists on a manually definition of a spline representing the LAA centerline. For that, three points (or more) are provided throughout the extent of the LAA; mainly, at least one point at the proximal part of the LAA, one point or more at the central region of the LAA and a final point at the distal part of the LAA.

### 8.2.1. LAA segmentation BEAS

The segmentation of the LAA lumen is performed using our previously described semi-automatic method (Chapter 7). In short, a constant blind-ended BEAS model is initialized using a spline manually defined (Figure 8.1A). The LAA BEAS model is generated using explicit functions described in both cylindrical and spherical spaces. A tube represented in the cylindrical space (described as $s$ levels along the axis and the azimuth $\theta$) and its final closed portion represented as a half-sphere (described as elevation $\varphi$ and azimuth $\theta$) are used, generating the blind-ended model. Then, the model is automatically evolved to the anatomy using a two-step approach, namely: 1) fast contour growing and 2) contour refinement. The former uses global terms defined based on a fixed threshold value (directly estimated from the image) and edge positions computed through a phase-based filter. Moreover, large evolution steps are used at this stage to recover a non-refined LAA shape and to decrease the method's sensitivity to the initialization. The latter stage uses regional energies, specifically the signed local Yezzi (targeting black to white transitions), to locally refine the contour to the anatomy. No edge term is used in the refinement stage. Due to the curved nature of the LAA model, hard shape regularization and LAA axis re-centering strategies are applied to prevent folding regions, keeping its shape anatomically realistic. The former identifies all possible folding regions, generating a map of hard boundaries that constrain the model evolution, *i.e.* define specific limits to the LAA model where its shape is kept realistic. The latter estimates highly curved axis positions, smoothing and correcting these positions. Due to this smooth axis, the number of possible folding regions is minimized, therefore, reducing the number of hard boundaries required in the abovementioned regularization approach.

### 8.2.2. Automated estimation of clinical measurements

The relevant clinical measurements, namely the ostial and LZ levels and the LAA depth, for LAA occlusion are estimated through 3D alignment of the target/unknown LAA surface with a set of references (*i.e.* 3D LAA surface plus manually-defined relevant clinical levels). This alignment is performed in three consecutive steps, namely: (1) a rigid alignment of both

surfaces using the clipping plane position (*i.e.* level that separates the LAA from the LA body); (2) correction of the surface's orientation based on the anatomical position of the CA; and (3) refinement of the alignment result using a weighted ICP algorithm.

Generally, there are two main challenges that need be taken into account to efficiently align LAA surfaces, particularly: 1) the highly variable field of view, in terms of position and orientation, of the ultrasound acquisition; and 2) the anatomical variability, in terms of shape and size, of the LAA shape. Thus, while the two initial steps of the proposed method roughly align both surfaces, minimizing therefore the influence of the misalignment of both surfaces and the variable FOV of ultrasound, the final step (step 3) compensates the anatomical differences between both surfaces.

Regarding the pre-alignment steps (steps 1 and 2), the centroid position and the normal vector of the clipping plane from both target and reference cases are rigidly aligned (Figure 8.2, Step 1), removing the global misalignment, mainly the translation components, between surfaces. Then, the position of the CA (section 8.2.2A) relatively to the LAA is used to anatomically align both surfaces, compensating the high orientation variability of the FOV of the ultrasound acquisition. In more detail, using the parametric space of the target LAA surface, the angular difference, in terms of azimuth, between the target's CA and the reference one is estimated, being then used to correct the orientation between both surfaces (Figure 8.2, step 2).

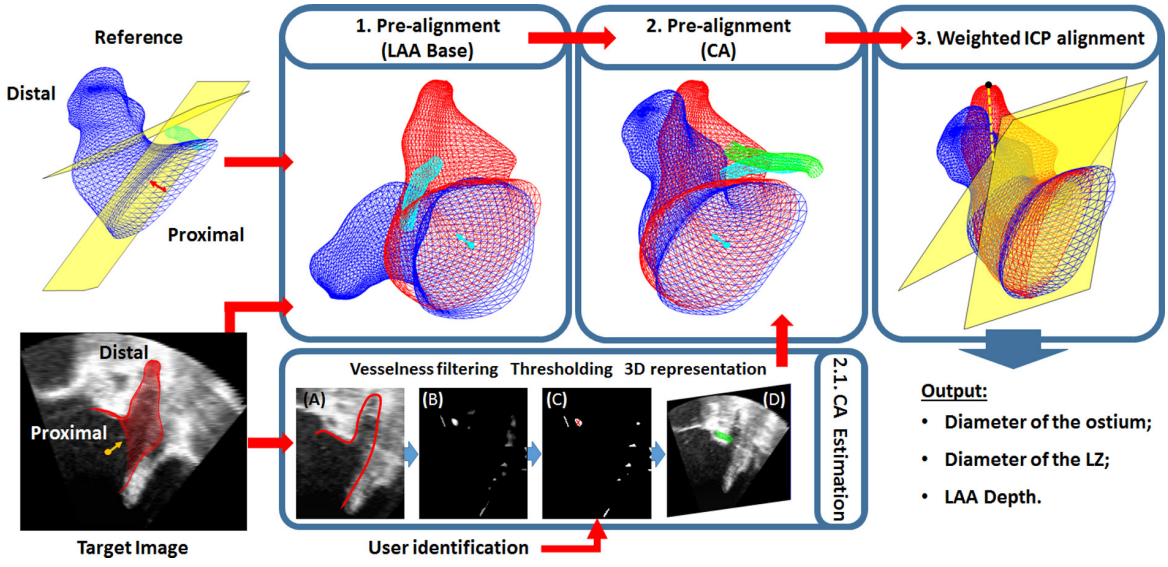


**Figure 8.2 – Automated identification of the relevant clinical measurements.**
The contour of the target image is aligned with a set of references (with pre-defined clinical levels – yellow planes) using the following approach: 1) rigid initialization using the normal of the clipping plane (red and yellow arrow for the reference and target cases, respectively); 2) orientation correction based on the position of the circumflex artery (CA), *i.e.* cyan and green mesh for the reference and target cases, respectively; and 3) refinement of the alignment using a weighted iterative closest point (ICP) approach. By aligning both surfaces, the reference clinical levels can be transferred to the target case. The CA is estimated through a semi-automatic approach, using a vesselness filtering strategy followed by thresholding of the obtained map.

After the pre-alignment based on fixed anatomical references (steps 1 and 2), a weighted ICP strategy with similarity transforms is applied to adapt the reference anatomy to the particularities of the target patient (Figure 8.2, step 3). A similarity transform was selected due to the high variability in terms of shape and size of the LAA (see Appendix 8.7.A for further details). Instead of using all the points of both surfaces with the same level of confidence throughout the optimization process, a specific weight function that varies with the axis position $s$ is used. The weight function is defined using an erf function through:

$$weight(s) = \frac{1}{2}\left(1 - erf\left(\frac{w}{\sqrt{2}}\left(\frac{s}{n_s - 1} - \frac{1}{2}\right) - c\right)\right) \quad (8.1)$$

where $w$ and $c$ are parameters that define the window size and the center position of the $erf$ function, respectively - in our experiments, $w = 6$ and $c = -1$ were used (see Appendix 8.7.A for further details); and $s$ represents the axis position along the cylindrical space and $n_s$ the number of coordinates along the axis. A representation of the weight function is presented in Figure 8.3. Low penalization is applied, a weight equal to one, at the proximal part of the LAA, and the opposite, a weight equal to zero, at the LAA tip. In this sense, by applying this function, it is possible to minimize the influence of certain LAA portions during the ICP alignment, enhancing the performance of the method to highly variable shapes. Indeed, since the proximal part of the LAA, *i.e.* the LAA base, shows a regular tubular shape, presenting high heterogeneity mainly at the distal part (*i.e.* near the LAA tip), the current weighted strategy is required to improve the alignment performance. Note that the relevant clinical levels, particularly the ostial and LZ planes, are extracted at the proximal and tubular region of the LAA, implying their detection is not negatively affected by the proposed weighted ICP technique.

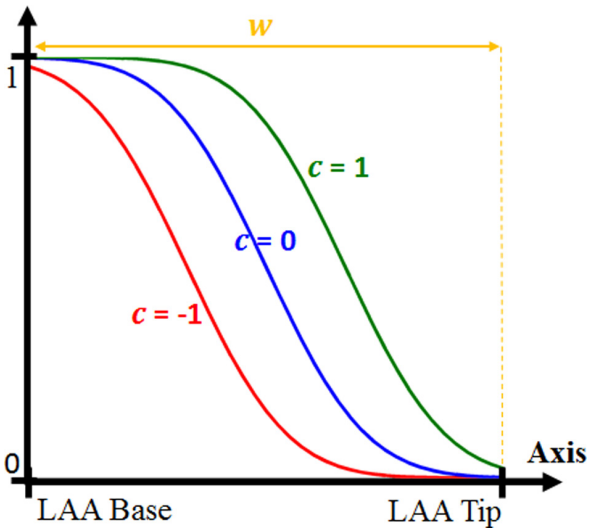


**Figure 8.3 – Representation of the weight function.**

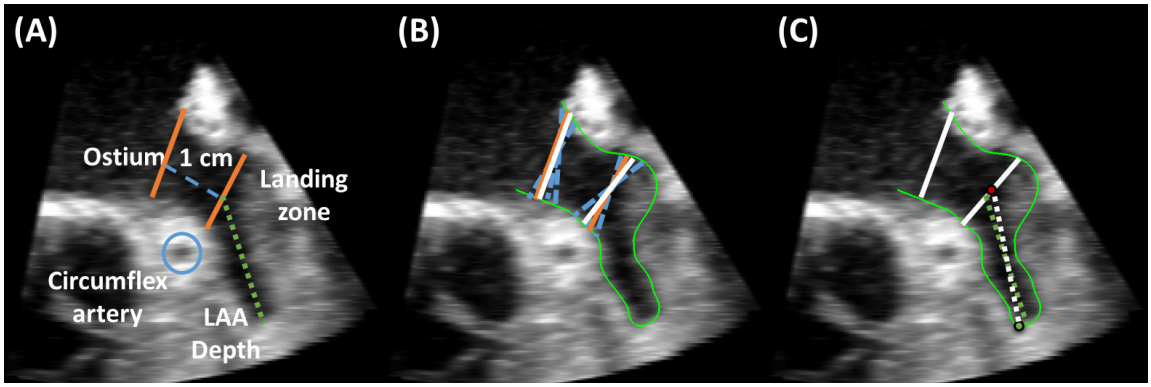


**Figure 8.4 – Identification of the relevant clinical levels for LAA occlusion.**
(A) Manual definition of the clinical measurements (orange planes). (B) Automated estimation of the ostial and landing zone levels (white planes) through the alignment of multiple references with the target case and combining the resulting candidate planes (blue dashed line). (C) Automated estimation of the LAA depth.

Finally, the alignment process is repeated for multiple references, and the final ostial and LZ planes (white plane in Figure 8.4B) computed as the mean result of all candidates (blue dashed line in Figure 8.4B). Later, the LAA depth is defined as the distance (white dashed line in Figure 8.4C) between the centroid of the estimated LZ level, which is defined by clipping the target LAA surface with the LZ plane and computing the centroid (red dot in Figure 8.4C) and the farther distal LAA surface position (green dot in Figure 8.4C).

**A. Segmentation of the circumflex artery**

The semi-automatic segmentation of the CA is performed using the following strategy (Figure 8.2): 1) enhancement of small vessels through a vesselness filter; and 2) thresholding the map created in (1) and selecting the optimal vessel region selection based on a manual click.

The used vesselness filter is described by Frangi *et al.* (1998) and it is focused on the detection of tubular regions with a pre-defined diameter: an expected anatomical diameter of the CA: 2-4 mm (Dodge *et al.*, 1992), through the evaluation of the eigenvectors of the Hessian matrix of the image. To improve the method's performance, the following features were also considered: 1) the appearance of the CA in TEE images, *i.e.* darker than the neighborhood; and 2) the anatomical position of the CA relatively to the LAA, *i.e.* near the LAA base. The former was embedded in the vesselness function, targeting the detection of tubular regions with dark vessels only. The latter was applied by defining a region of interest (ROI) around the pre-segmented LAA, represented as a dilated version - in our experiments by 5 mm - of the LAA surface's mask. Finally, the obtained map is binarized using an Otsu thresholding approach (Otsu, 1975), and the optimal region selected based on a manual click provided by the user (illustrative results can be found in Appendix 8.7.B).

## 8.3. Experiments

Two experiments were performed to evaluate the performance of the proposed method for the estimation/definition of the relevant clinical measurements, namely: 1) influence of the different parameters/steps on the final method's accuracy; and 2) comparison of the proposed method performance against the inter-observer variability.

### 8.3.1. Data description

A total of 20 TEE images were retrospectively selected from clinical practice, including patients with suspicion of pathology but with normal anatomy, as well as abnormal cases. Due to the high shape variability of the LAA, one expert classified the LAA shape in each case based on Beigel *et al.* (2014), obtaining 9 chicken wings (45%), 4 windsocks (20%), 4 cauliflowers (20%), and 3 cactus (15%).

The 3D TEE images were acquired using a GE Vivid E95 (GE Vingmed, Horten, Norway), Philips IE33 (Philips Ultrasound, Bothell, USA) or a Philips Epiq 7 scanner. A total of 9 and 11 exams were acquired with the Philips and GE ultrasound machines, respectively. An electrocardiogram-gated acquisition was performed in mid-esophageal position using zoom mode (Beigel *et al.*, 2014). The acquired image presented a resolution and size that varied from $0.20$ to $0.45$ mm and $126 \times 122 \times 117$ to $357 \times 413 \times 208$ voxels, respectively. The datasets were initially stored in a raw-data format and then exported to a workstation with EchoPac or QLab. Each case was then anonymized, exported into an externally-readable format and converted to an isotropic voxel spacing. All datasets were acquired using the resources of the University Hospital Leuven with the approval of the Ethics Committee (S59406).

### 8.3.2. Ground truth generation

Two observers, henceforward referred as $Obs_1$ and $Obs_2$, manually extracted the relevant clinical levels, specifically diameter of the ostial and LZ planes and distance of the LAA depth, as described by (Saw and Lempereur, 2014; Song *et al.*, 2016; Wang *et al.*, 2016a; Wunderlich *et al.*, 2015). Each was blinded to the other's analyses. The ostial and LZ diameters were computed by manually selecting the optimal image plane, followed by manual delineation of the resulting short-axis view. Then, area-derived diameters were extracted from the 2D contours. The LAA depth was computed as the distance between the LZ centroid, which was computed based on the 2D contour, and one extra point defined along the long-axis view at the LAA tip. Please note that, each observer freely navigated in the 3D TEE image using 3 orthogonal planes or resliced the image along a pre-defined LAA centerline. All analysis were performed using a custom non-commercial software, Speqle3D (Queirós *et al.*, 2018).

### 8.3.3. Evaluation of the algorithm's performance

In this experiment, the sensitivity of the automated method to its parameters was initially explored. Specifically, the parameters of the weight function and the influence of the number of references used were studied. The errors were evaluated in terms of absolute point-to-plane distance (P2PI) and normals' angular difference. Regarding the P2Pl metric, it was computed using the following approach: 1) estimation of the centroid position of the observer's delineated contour; 2) definition of a line using the centroid position estimated in (1) and the normal vector of the short-axis image plane used for manual delineation; and 3) intersection of this line with the automated plane. The distance between the centroid of the manual plane (1) and the intersected position at the automated level (3) defines the P2Pl distance error. Furthermore, to check for statistically significant differences, a two-tailed paired t-test ($p<0.05$) was computed between consecutive values of the studied parameter. Finally, the accuracy of the proposed method throughout the different steps of section 8.2.2 was also explored using the P2Pl distance error and normals' angular difference. A two-tailed paired t-test ($p<0.05$) was used to check for statistically significant differences between consecutive steps.

### 8.3.4. Accuracy of the estimated anatomical levels and resulting measurements

The differences between the proposed approach, henceforward referred as $Auto_{3D}$, and the inter-observer variability in terms of clinical measurements were assessed using the average difference (*i.e.*, bias) and the limits of agreement (LOA, given as 1.96 times the standard deviation). The performance of the previously described semi-automatic (SA) approach (Chapter 7), which involves the clipping of the 3D segmented contour at the manually defined levels, was also evaluated, taking into account $SA_1$ and $SA_2$ for the planes defined by $Obs_1$ and $Obs_2$, respectively. Moreover, the errors between proposed and manual approaches were also studied using the P2Pl distance and the normals' angular difference.

Taking into consideration the traditional clinical practice for the definition of the landing zone, particularly the LZ plane defined based on the ostial plane with a distance between centroids of 10 mm, a comparison between this approach (referred as "Fixed Translation") and the proposed method, which involves the simultaneous identification of both planes by aligning multiple references, was performed. Both P2Pl distance and normals' angular difference were computed. Moreover, the LOA of the obtained clinical measurements were also assessed.

### 8.3.5. Computational time

The computational time of the automated method was recorded. All results were computed using MATLAB code (without parallelization) on an Intel (R) i7 CPU at 2.8 GHz

and 16 GB of RAM. For computational efficiency, a MATLAB-generated C implementation of the ICP algorithm was wrapped in the MATLAB code.

## 8.4. Results

From the original 20 datasets, 2 cases were excluded because the manual identification of the circumflex artery was not feasible due to low image quality, which prevents the application of the proposed solution. Therefore, all the results here presented are regarding the remaining 18 cases. Regarding the reference database used for the ICP alignment, a leave-one-out strategy was used; therefore, the target case was removed from the reference database.

### 8.4.1. Evaluation of the algorithm's performance

Figure 8.5 and Figure 8.6 depict the influence of proposed weight function and the number of references used throughout the alignment step (section 8.2.2), respectively. The former proved that a superior performance was achieved, with statistically significant

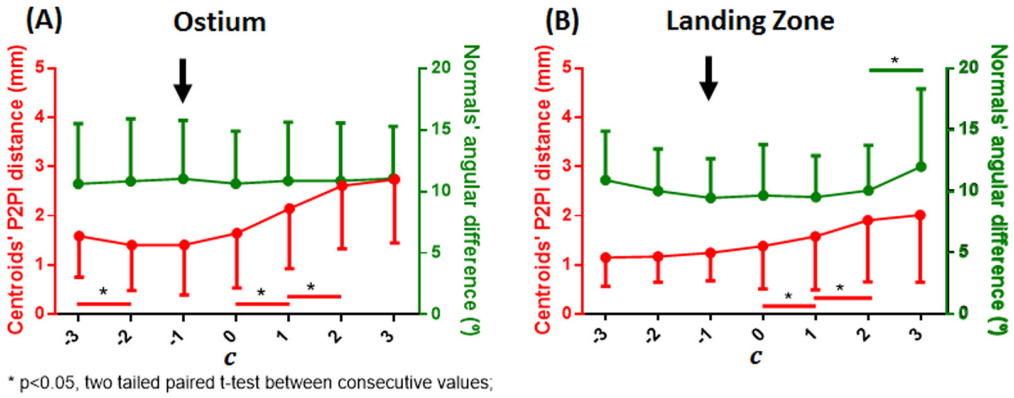


**Figure 8.5 - Influence of the *c* parameter of the weight function in the method's performance for the (A) ostial and (B) LZ levels.**

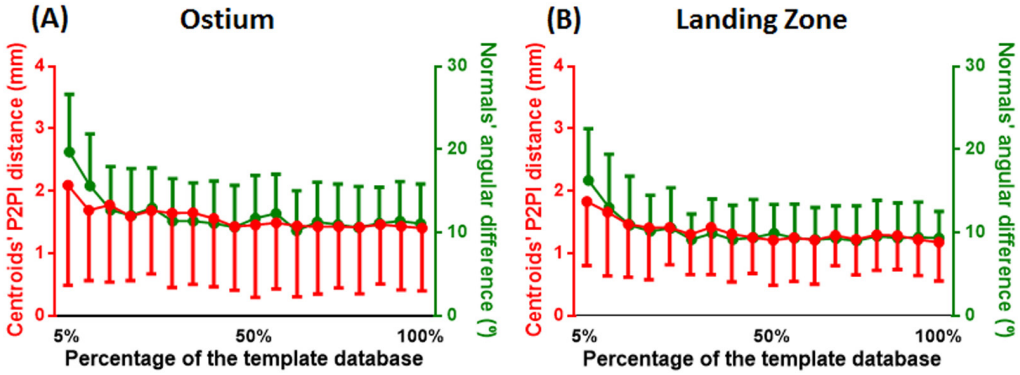


**Figure 8.6 – Influence of the total number of references used in the method's performance for the (A) ostial and (B) LZ levels.**

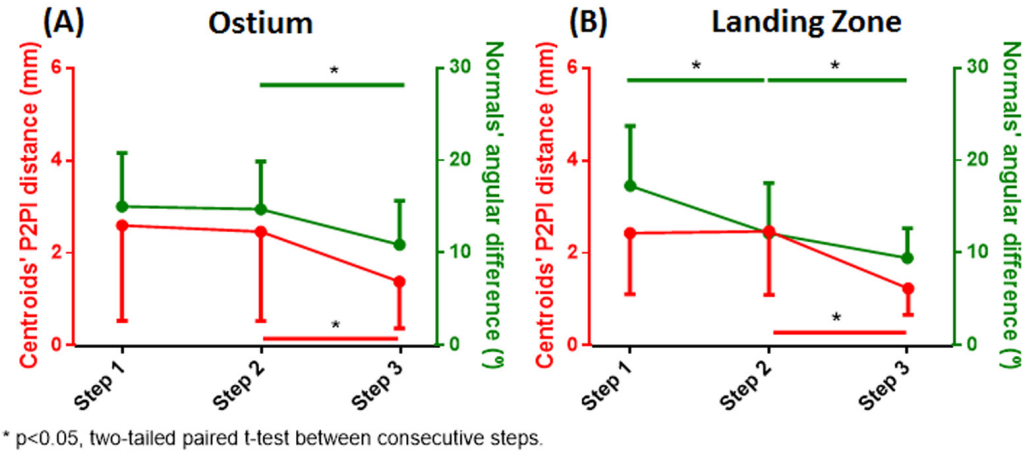


**Figure 8.7 - Error evolution throughout the different steps of section 8.2.2.**
Step 1 - Rigid alignment using the LAA clipping plane; Step 2 - Orientation correction based on the anatomical position of the circumflex artery; Step 3 - Weighted ICP approach.

differences, by reducing the influence of the LAA tip in the weighted ICP. The latter corroborated the method's high accuracy when a large number of references is used. In contrast, unsatisfactory results are achieved when a small number of templates are considered (less than ~60% of the original database). Interestingly, using 60% of the reference database led to a performance similar to one obtained when the entire reference database was used.

Figure 8.7 shows the error evolution throughout the different steps of section 8.2.2.A significant reduction of the error in terms of orientation was found between all the steps, corroborating the entire methodology. Moreover, a significant reduction in terms of centroids' errors was found when applying the final alignment based on ICP.

### 8.4.2. Accuracy of estimated clinical levels and resulting measurements

Table 8.1 presents the differences between proposed and manual approaches for the relevant clinical measurements. Moreover, Figure 8.8 shows Bland-Altman plots of the $Auto_{3D}$

**Table 8.1 - Accuracy of the proposed method ($Auto_{3D}$) against the SA version and manual one (Obs)**

| | # | Ostium | | Landing zone | | LAA depth | |
|---|---|---|---|---|---|---|---|
| | | Bias | LOA (mm) | Bias | LOA (mm) | Bias | LOA (mm) |
| $Auto_{3D}$-$Obs_1$ | 18 | -0.53 | [-2.72; 1.65] | $-0.40^{b}$ | [-2.21;1.42] | $-0.36^{b,f}$ | [-2.87;2.14] |
| $Auto_{3D}$-$Obs_2$ | 18 | $-0.92^{a,b}$ | [-2.94; 1.08] | $-0.97^{a,b,f}$ | [-2.83;0.88] | 0.27 | [-2.34;2.88] |
| $Obs_1$-$Obs_2$ | 18 | -0.01 | [-2.48;2.46] | 0.53 | [-2.25;3.30] | 0.68 | [-2.61;3.96] |
| $SA_1$-$Obs_1$ | 18 | 0.39 | [-1.31;2.09] | $-0.41^{b}$ | [-2.16;1.35] | -0.28 | [-2.49;1.93] |
| $SA_2$-$Obs_2$ | 18 | 0.26 | [-1.48;2.01] | $-0.12^{b}$ | $[-1.81;1.58]^{c}$ | 0.48 | [-1.64;2.60] |

LOA – Limits of agreement (given as Bias [mm] $\pm 1.96\sigma$ [mm]). [a] $p<0.05$, two-tailed t-test against 0; [b] $p<0.05$, two tailed paired t-test against $Obs_1$-$Obs_2$; [c] $p<0.05$, two tailed F-test against $Obs_1$-$Obs_2$; [d] $p<0.05$, two tailed paired t-test against $SA_1$-$Obs_1$; [e] $p<0.05$, two tailed F-test against $SA_1$-$Obs_1$; [f] $p<0.05$, two tailed paired t-test against $SA_2$-$Obs_2$; [g] $p<0.05$, two tailed F-test against $SA_2$-$Obs_2$.

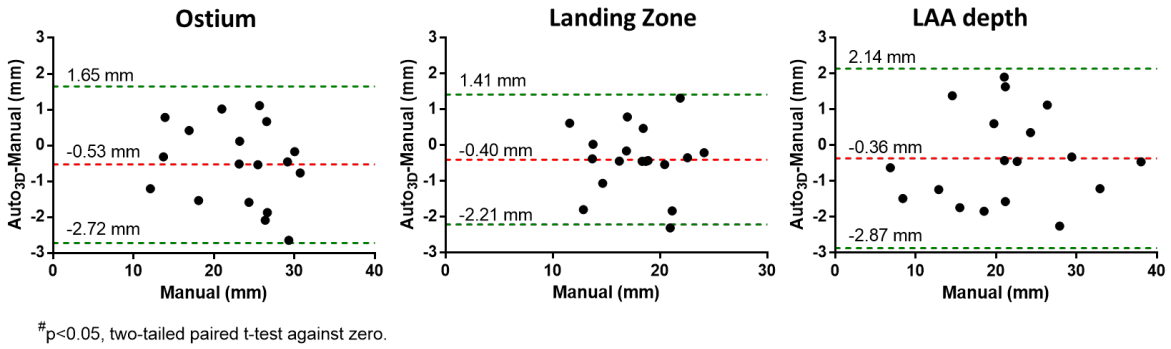


**Figure 8.8 - Bland-Altman plot of the errors obtained with the proposed method for the estimation of the relevant measurements.**

performance. Overall, the results proved the high performance of the proposed solution, with narrower limits of agreement when compared with the manual ones. A slightly worst performance, which is not statistically significant, was obtained by the proposed solution when compared with the previous (SA) methodology (Chapter 7). Assessing the differences in terms of plane definition, an absolute P2Pl error of 1.40 ± 1.01|1.24 ± 0.57 mm (ostial|LZ plane) and normals' angular difference of 11.01 ± 4.77°|9.42 ± 3.20° (ostial|LZ plane) was achieved by the proposed method against the manual one. As a reference, an absolute P2Pl error of 1.57 ± 1.36|1.22±0.71 mm (ostial|LZ plane) and normals' angular difference of 9.30 ± 4.13°|7.96 ± 4.42° (ostial|LZ plane) was found between observers. Regarding the relative P2Pl distance, an error of 0.88 ± 1.67 mm at the ostial level and 0.19 ± 1.57 mm at the landing zone was registered by the proposed approach, indicating a tendency to define the ostial plane deeper inside the LAA when compared to normal practice. Nevertheless, this tendency (*i.e.* bias) was not statistically significant. Representative cases of the proposed solution's performance are depicted in Figure 8.9.

Finally, the difference between the proposed solution and the "Fixed Translation" strategy for the LZ plane was assessed, revealing a performance in terms of P2Pl error, but with statistically significant differences when assessing the normals' angular difference, Figure 8.10.

### 8.4.3. Computational time

The proposed method required 14.0 ± 4.8 and 4.1 ± 1.9 seconds, for the 3D segmentation of the LAA and the CA, respectively. It should be noticed that, the time required to manually define the initial spline and to detect the CA was not included (only processing time is presented). The estimation of the clinical levels (3 measurements) by the proposed solution took 7.0 ± 1.3 seconds. As a reference, the manual delineation of the LAA and the manual estimation of the clinical levels took approximately 40 and 3 minutes (for all the 3 levels), respectively.

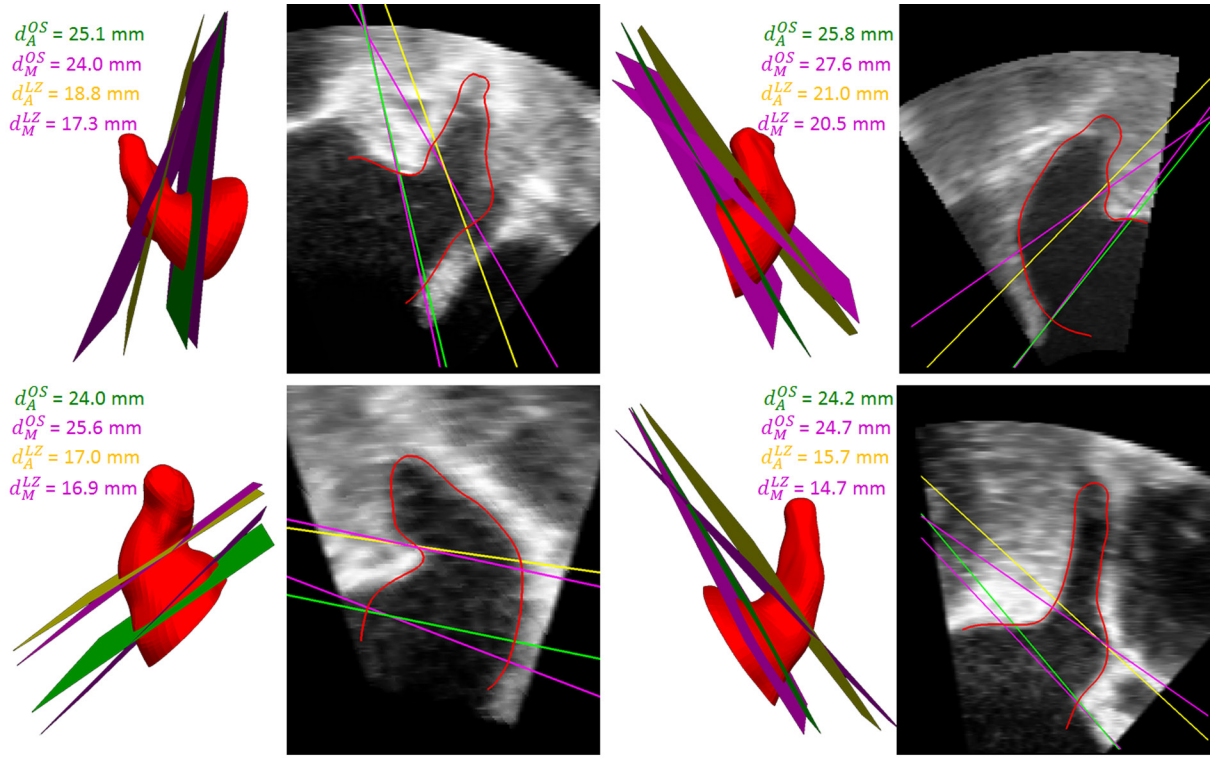


**Figure 8.9 - Representative examples of the clinical levels estimated by the proposed method.**
Green – Estimated Ostium; Yellow - Estimated LZ; Magenta - Manual.

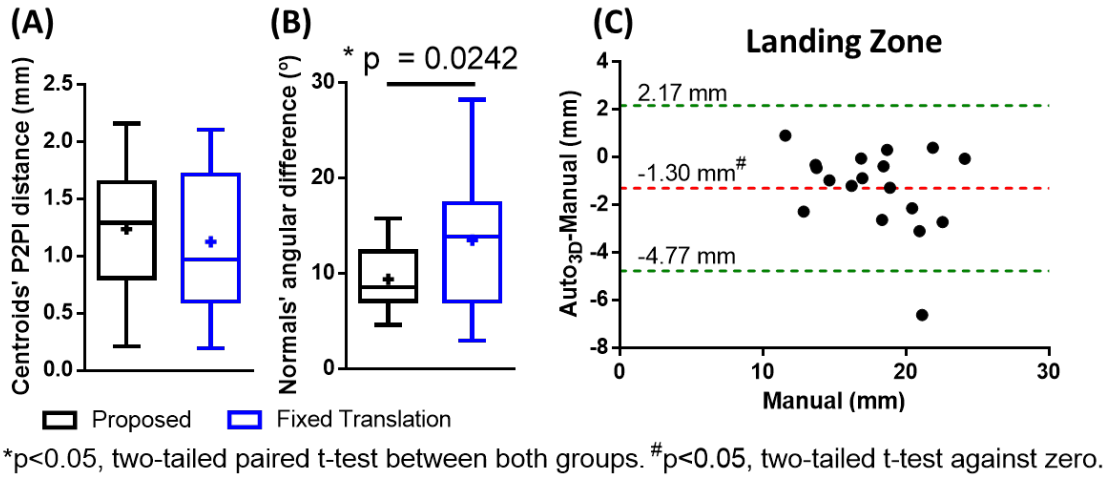


**Figure 8.10 - Difference between the proposed and fixed translation approaches for the definition of the LZ.**
The errors were evaluated using the (A) P2Pl distance, (B) normals' angular difference. (C) The Bland-Altman plot of the errors obtained by the "Fixed Translation" approach against the manual practice for the estimation of the LZ diameter is also explored.

## 8.5. Discussion

In this study, a novel solution for the semi-automatic planning of LAA occlusion is proposed. This applies a fast 3D segmentation approach on volumetric TEE images, obtaining realistic and accurate anatomical models of the LAA. Then, based on the extracted surfaces, an alignment process with multiple manually evaluated references (*i.e.* 3D surface plus the relevant

anatomical levels) is applied, transferring the relevant levels to the target anatomy and allowing the estimation of the final measurements. As such, not only the inter- and intra-observer variability is notably minimized, but also a faster estimation of the measurements is achieved - the proposed solution required ~40 seconds to estimate all clinical levels while the manual approach took ~3 minutes - with clear advantages for both patients and the medical team.

To the authors' best knowledge, this is the first study describing a semi-automatic solution for the estimation of the relevant clinical measurements for the identification of the optimal device for LAA occlusion. Regarding the current method's feasibility, acceptable results were obtained in all the cases (see Figure 8.9), proving its high robustness. Two patients were removed from the study due to bad image quality that hamper the identification of the circumflex artery, and therefore the application of the proposed method. Although in these cases manual identification of the relevant planes was possible, by evaluating the global LAA anatomy, a high disagreement was found between observers due to missing relevant anatomical landmarks. The proposed alignment method (section 8.2.2) uses a reference database to identify the relevant planes in the target case. For that, due to the highly variable FOV, in terms of position and orientation, of the TEE acquisition, a strong initialization using the LAA clipping plane position and the CA orientation is applied, later refining the result to the anatomy using a weighted ICP approach. As clearly seen in Figure 8.7, the method's performance is sensitive to all steps (*i.e.* initialization and refinement), which validated the proposed workflow. Obviously, a notable and statistically significant improvement is observed when applying the weighted ICP, due to the anatomical alignment. Nevertheless, the success of the ICP result is totally dependent on the initialization, being unfeasible without the initial steps. Specifically, considering the initial tubular shape of the LAA, accurate identification of the correct orientation was not possible without external anatomical landmarks, here the CA. As a final remark, it might be noted that by comparing the proposed alignment method with pure image-based approaches, e.g., the identification of relevant landmarks through threshold-based techniques, a superior robustness to image artifacts or to the limited FOV of the ultrasound acquisition is expected. Moreover, although the proposed solution was tested on TEE images only, its application in a different imaging modality, particularly in CT, is also viable and expected to be explored soon, increasing the applicability of the method.

Due to the proposed weighted formulation of the ICP, which applies different weights based on the cylindrical axis position, highly variable shapes, as expected for the LAA, were possible to be efficiently processed by the described method. One can note that, as described in section 8.3.1, different LAA shapes were found and its prevalence is in accordance with

previous studies (Bai *et al.*, 2017; Beigel *et al.*, 2014). The weighted ICP intrinsically reduces the influence of certain patches of the LAA surface throughout the optimization process. Although direct clipping of the LAA surface (by keeping its tubular surface only) could also be a potential solution, a correct separation between the tubular (*i.e.* the region of interest) and the heterogonous LAA parts is not straightforward. In this sense, by studying and adapting the influence of this weight function (Figure 8.5), it is possible to enhance, without defining a fixed clipping level, the proximal LAA portion relatively to the distal part. Moreover, although the distal portion of the LAA shape is quite heterogeneous, some specific information, e.g. curvature and orientation of this region, are also relevant to improve the success of the ICP. By evaluating the model's parameters (Figure 8.5 and Figure 8.6), only a small number of them need to be set, namely the center position ($c$) and the window size ($w$) of the weight function. Importantly, the center position $c$ defines the level that separates the tubular and the heterogeneous parts of the LAA. Worse results were obtained when increasing the influence of the distal portion of the LAA, mainly LAA tip, in the optimization process ($c > 0$), showing similar results, but not statistically significant, for the remaining cases (Figure 8.5). Regarding the size of the weight function, the method showed high robustness to the variation of this parameter, showing similar results for narrow and large windows (see Appendix 8.7.A). Finally, since the proposed method requires a reference database, the influence of the number of references used was also evaluated (Figure 8.6). Globally, low performance was found when using a small number of references, due to the limited anatomical variability, presenting similar results when a high number of cases were used; similar performance was registered when more than 10 reference cases. Although identification of the most similar references, e.g. evaluating the accuracy of the alignment stage or based on the LAA shape, could be an interesting approach to improve the solution's accuracy, a larger database would be required.

When evaluating the performance of the proposed solution using the metrics presented in Table 8.1, similar results were achieved between the $\text{Auto}_{3D}$, SA version and the inter-/intra-observer variability. As observed in Chapter 7, both versions ($\text{Auto}_{3D}$ and SA) showed narrower LOA when compared to the manual approach (Table 8.1 and Figure 8.8). Interestingly, the LOA achieved by $\text{Auto}_{3D}$ and SA methods were similar to the difference between consecutive occluding devices (2 mm). The superior performance of both approaches relative to the manual one can be explained, as previously found in Chapter 7, by the continuous 3D contour used and the respective strategy to estimate the final measurement, particularly by clipping the 3D contour at the selected level. Indeed, due to the smoothing applied to the 3D contour across all directions, small differences while defining the relevant clinical level will result in a small

variation of the final clinical measurement. In contrast, the manual approach relies on the 2D delineation of the identified levels (by reformatting the 3D volume), being therefore, totally dependent of the in-plane information, making it sensitive to artifacts or low image quality (Chapter 7) (Wunderlich *et al.*, 2015). In contrast, when comparing both $Auto_{3D}$ and SA results, a slightly superior performance in terms of LOA was achieved by the SA. This difference can be easily explained by the strategy applied to define the relevant levels, *i.e.* the SA uses the level defined by the observer while the Auto3D estimates (through an alignment strategy) the level. Notwithstanding, no significant differences were found between them, demonstrating the accuracy of the proposed solution.

Taking into account each measurement independently (Table 8.1), similar observations were found between $Auto_{3D}$ and SA versions, namely: 1) the LAA depth showed the highest disagreement, due to the difficulty in detecting the LAA tip; and 2) both ostial and LZ levels showed high reproducibility with narrower LOA, notably inferior when compared with previous studies. Here, one can note that, the majority of these studies focused on inter-modality comparison studies (Bai *et al.*, 2017; Nucifora *et al.*, 2011). In contrast to the finding in Chapter 7, narrower LOA were obtained at the LZ level for the $Auto_{3D}$ method, instead of the ostium, as found in the SA version. Moreover, a negative bias was obtained at the ostial level, while the SA version reported a positive one. Indeed, the inferior performance at the ostial level of the Auto3D method is explained by the proposed alignment step. A tendency, although not statistically significant, to define this plane more distally - proved by the relative P2Pl distance of 0.88 ± 1.67 mm registered at this level - was observed, underestimating therefore, the ostial value. It can be noted that a constant reduction of the LAA diameter is observed throughout its tubular portion, being its diameter larger at the opening region. Nevertheless, these differences are not significant. Interestingly, an opposite conclusion was observed for the LZ plane, where high similarity, in terms of bias and LOA, was found between $Auto_{3D}$ and SA versions, with a reduced relative P2Pl distance of 0.19 ± 1.57 mm. In fact, the current result potentiates the application of this framework in the clinical environment, since the LZ measurement is the main clinical measurement for the identification of specific devices (for example, Amulet, St. Jude Medical, Minnesota, USA) (Meier *et al.*, 2014). Additionally, the current result also corroborates the advantage of using the proposed alignment strategy (with ICP) for the definition of the LZ, instead of the "Fixed Translation" approach (Figure 8.10). Although the LZ centroid could be estimated based on the ostial level, a correct and accurate definition of the LZ plane orientation is not straightforward in a 3D space. In this sense, by using an alignment strategy, which includes both relevant planes, a robust estimation of the centroid and the plane

orientation is obtained. As can been seen from Figure 8.10a, a similar performance in terms of centroid was found between proposed and fixed translation approaches, proving that a correct separation between clinical planes was achieved by the proposed alignment approach. In contrast, statistically significant differences were found when comparing the normals' angular difference between both methods (Figure 8.10b), reinforcing the advantage of the proposed solution. Looking for the Bland-Altman plot of the fixed translation approach (Figure 8.10c), wider LOA and higher bias, which was found to be statistically significant, were found when compared with the proposed method.

The method's accuracy was also evaluated using manual analysis performed by different observers (Table 8.1). For both cases, the proposed method showed similar LOA, but with a notably higher bias value against the second observer. This difference is directly related to the reference database used. Indeed, the current reference database was generated using the manual analysis performed by $Obs_1$ (for all the situations). Therefore, the proposed alignment method estimates the clinical levels by "mimicking" the strategy adopted by the $Obs_1$, obviously generating a small bias when compared with a different observer. Since the LOA were kept constant between observers, a reduced reproducibility of the proposed method with a different observer is not expected. Notwithstanding, to improve the method's performance, a specific database generated by each observer could be gathered, possibly removing the registered bias.

Finally, in regards to the study limitations the authors would like to emphasize that: 1) extreme or abnormal LAA shapes can present a sub-optimal segmentation and alignment result due to the shape limitations of the blind-ended model and the limited anatomical representation in the reference database, respectively; 2) a large multi-center clinical database with manual delineation of the LAA and definition of the clinical levels is required to exhaustively validate the proposed method; and 3) a comparison of the estimated clinical values and the implanted device is required to evaluate the real accuracy of the semi-automatic TEE measurements.

## 8.6. Conclusion

The proposed solution proved its potential for the semi-automatic estimation of the relevant clinical measurements for the LAA occlusion, showing high accuracy, robustness and low computational cost. By comparing it with the traditional manual practice, more reproducible results and a fast decision on the optimal device was achieved by the novel solution, corroborating its added-value for normal clinical practice.

## 8.7. Appendixes

### Appendix A – Influence of the remaining parameters

Data Description: The abovementioned 18 clinical datasets were used.

Experiments and Results: The influence of the parameter *w* of the weight function (its size) and the transformation model used in the ICP algorithm were evaluated. For both cases, a two-tailed paired t-test ($p<0.05$) was performed to check for statistically significant differences between different parameter values.

The results for both parameters are presented in Figure 8.A.1, proving that: 1) the proposed method showed high robustness to the variation of the window size; and 2) both similarity and affine transformation models are suitable for the alignment of LAA surfaces. Note that due to the high shape/dimension variability of the LAA, rigid models (*i.e.* only rotation and translation, without scaling parameters) are not suitable for this problem.

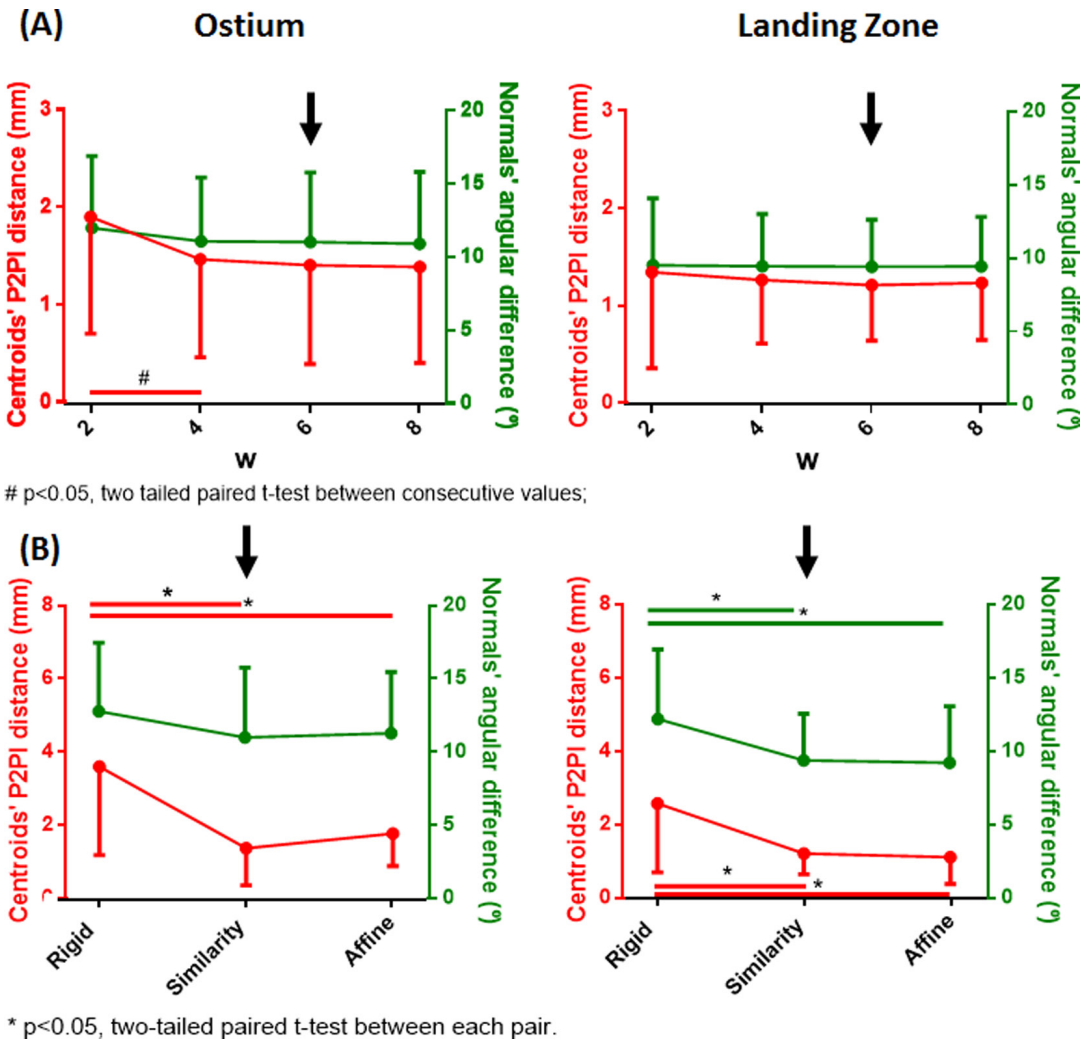


**Figure 8.A.1 - (A) Influence of the window size (*w*) of the erf function and (B) the transformation model of the ICP algorithm in the final method's accuracy.**
The arrow represents the selected value.

## Appendix B – Segmentation of the circumflex artery

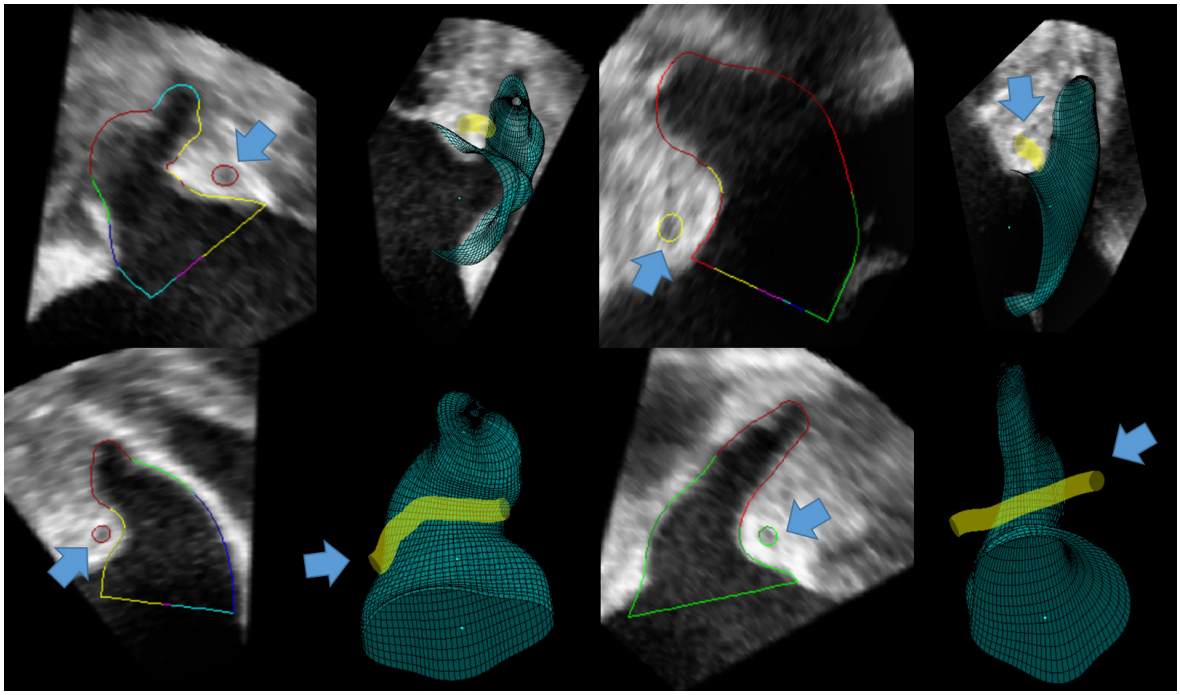

**Figure 8.B.1 - Illustrative examples of the LAA and circumflex artery segmentation results.**
The blue arrow indicates the circumflex artery contour position.

# Chapter 9

## Final remarks and future perspectives

This final chapter presents the main conclusions of this thesis. Furthermore, future perspectives of novel planning strategies for left atrial interventions are presented and discussed.

**Contents**

## 9.1. Concluding remarks

The current thesis focused on the planning stage of left atrial (LA) interventions, presenting novel automated solutions to accurately extract anatomical models and identify relevant clinical landmarks for two specific interventions, namely: Part I – Transseptal puncture (TSP) and Part II – Left atrial Appendage (LAA) occlusion. Overall, the proposed solutions are of interest to the clinical practice, since they reduce the analysis time, increase the reproducibility between observers and ultimately may facilitate/potentiate the medical processes. Moreover, due to their reduced computational cost, an online interactive analysis can be performed, increasing the potential of the proposed tools. As clearly observed in the literature, only few studies focusing on planning solutions for the described interventions were presented, missing clinical validations (in specific cases) and being little widespread around the world. In this sense, the current practice in most of the centers relies on manual or standard semi-automatic solutions/practices (*i.e.* threshold-based approaches), showing high dependence on the operator expertise and being therefore sub-optimal approaches.

Regarding Part I, a patient-specific atrial phantom for inter-atrial interventions was initially developed (Chapter 3). Two requirements were pursued while constructing this model, namely: 1) a realistic anatomy and flexible walls were required; and 2) the current model must be compatible with intra-procedural imaging modalities, particularly ultrasound. By comparing the current phantom with the state-of-the-art, the proposed model proved its interest thanks to the correct modeling of the inter-atrial septal (IAS) wall and the faster construction process. Furthermore, in opposition to previous studies, the high accuracy of the manufacturing process was assessed and proved. In this sense, its usage for both intervention planning/simulation and improved medical training are possible clinical applications. With the current model, the expert can test all procedural stages and even use it to detect the optimal puncture location or measure the catheter dexterity at the target location, ultimately improving the planning stage.

The current model was later used in an experimental scenario to initially validate a novel interventional framework, where high-detailed pre-procedural models were fused with volumetric ultrasound imaging to guide TSP (Chapter 4). Although the current version of the framework required user interaction in all stages, only implementing an initial and global concept, its complete development can probably reduce TSP procedural time, the radiation dose exposure, the number of complications and failures. To automate the planning stage of this framework, a novel strategy to segment the relevant cardiac chambers was developed. Although multiple researchers have developed robust and accurate methods to segment all cardiac chambers (and great vessels) in images with large field of view (FOV), namely computed

tomography (CT) and magnetic resonance imaging (MRI), no focus at the mid thin inter-atrial wall was given, simply merging or post-processing the different contours, hampering their application for IAS wall interventional scenarios. The proposed method uses a competitive deformable model approach to define the thin wall borders by combining spatial location between multiple contours with edge and localized image-based energies (Chapter 5). Although the method was validated in atrial region segmentation problems, the current formulation is generic and may be applied in a high variety of situations. Additionally, in this work, important methodological contributions to the B-spline Explicit Active Surface (BEAS) framework were also presented, mainly by expanding it towards a multiple contour formulation with a coherent spatial relationship between them.

Nevertheless, the initial atrial region segmentation work was semi-automatic and does not extract relevant anatomical landmarks, requiring manual interaction at different stages and limiting, therefore, the clinical applicability of this tool. As such, a novel module was added to the previous segmentation chain, by automatically initializing the different contours through an atlas-based technique (Chapter 6). The atlas-based initialization was selected due to its previously demonstrated high robustness. However, instead of refined alignments (which are extremely time-consuming), global ones were used. Thus, only a rough estimation of the different cardiac chambers is obtained, being later refined to the patient anatomy using the described competitive segmentation approach. When compared to the traditional full atlas-based strategies (which have previously shown high accuracy and robustness), the described method is also accurate and robust, but computationally more attractive, requiring only a few minutes instead of several hours, as reported by pure atlas-based techniques, being therefore a more appealing solution to the clinical routine. Finally, an automatic strategy to obtain relevant anatomical landmarks (namely the fossa ovalis, FO) from the obtained three-dimensional (3D) atrial contours was also explored (Chapter 6). The evaluation of the full extent of the FO region is crucial to define the optimal puncture position and route, to select the different surgical tools and even to detect possible anatomical variations, which can hamper the procedure. Moreover, as previously discussed in the literature, the inclusion of such anatomical landmark in the real intervention may reduce the procedural time and increase its feasibility. The automatic FO region segmentation approach can also potentiate the development of novel and more efficient planning and guidance tools, including simulation tools to compute/measure the optimal puncture location or an improved interventional framework to facilitate TSP.

As a final remark, despite not addressed in this thesis, some of the developed methodologies (e.g. segmentation of atrial region and fossa region) are suitable to be

immediately integrated in the proposed interventional framework (as plug-ins), automating the different processes and reducing the time required to configure the setup. Nevertheless, further studies to evaluate its feasibility, accuracy and the learning curve are required.

Regarding Part II, it focused on the development of segmentation solutions to peri-procedural data, namely transesophageal echocardiographic (TEE) images, for LAA occlusion intervention. In contrast to pre-operative images (e.g. CT), the peri-procedural images allow an accurate and more realistic evaluation of the patient anatomy (not neglecting anatomical variations that occur during the intervention), possibly improving the current planning stage, namely the identification of the optimal occluding device. Nevertheless, correct processing of ultrasound-based images is challenging, due to its small FOV, sub-optimal image quality and high noise/artifacts present in the image. With this in mind, and taking into consideration its previous application with high robustness and accuracy in other ultrasound-based segmentation problems, the BEAS framework was selected. However, since only relatively simple shapes are suitable to be modeled by the traditional BEAS formulation, due to its limited degrees of freedom in terms of shape representation, its application for the LAA anatomy is not straightforward. To solve this issue, a novel BEAS model (termed blind-ended model) was proposed (Chapter 7), by combining different topologies. In fact, such approach (*i.e.* combination of different topologies in the BEAS framework) is an important technical contribution of the current thesis, which may allow the future expansion of this framework towards the segmentation of complex shapes (e.g. atrial models plus veins or right ventricle). By evaluating the performance of the proposed blind-ended segmentation model, its high accuracy was corroborated when compared to manual contouring. Furthermore, direct application of this solution in the real intervention proved to be feasible, due to its low computational time (a few seconds, while manual contouring took more than 30 minutes). Indeed, the current software opens new research opportunities by allowing 3D anatomical evaluation of the LAA shape throughout the intervention, which will ease the interpretation of the peri-procedural data and even provide extra relevant anatomical information. Furthermore, the initial results proved that the estimation of relevant clinical indicators using the proposed method showed higher reproducibility than the traditional approach (*i.e.* manual evaluation). Later, the current solution was expanded, allowing the estimation of the relevant measurements directly from the segmented surface (Chapter 8). As such, the time demanded to identify the optimal device can be notably reduced, being advantageous both to the patient (by reducing the procedural time and avoiding or reducing the radiation dose) and the medical team/services (by reducing costs). Finally, by automating the measurements estimation stage, the inter- and intra-

observer variability is minimized and the intervention performance in less experienced centers is potentiated.

In short, the developed planning solutions proved their technical and clinical contributions for specific LA interventions, corroborating their potential and added-value to improve the daily clinical practice. It is expected that their regular application in the clinical routine can improve medical processes, making it more reproducible and faster, ultimately reducing the number of complications and failures, and may reduce the high costs related to minimally invasive interventions.

## 9.2. Future work

Despite the described contributions of the current PhD thesis, further developments to improve the different stages of the LA interventions may be envisioned.

Starting with the TSP intervention, the development of novel integrated interventional guidance framework (as described in Chapter 4) is expected. While the different planning stages can be performed using the methodologies described in this thesis, further methods to fuse intra-procedural and pre-procedural data must be explored. Although some possible strategies were described in the literature, mainly through rigid approaches, dynamic alignment strategies by combining a fast atrial segmentation approach, applied in intra-procedural images, with pre-operative anatomical models are expected to be further developed. In this sense, pre-operative anatomical models can be superimposed on the intra-procedural images, enhancing the relevant anatomies and landmarks. These models are then adapted throughout the cardiac cycle by directly applying the motion information extracted from ultrasound images (by applying consecutive segmentations on these images or tracking the relevant anatomies using feature tracking strategies). Later, large experimental scenarios are required to assess the accuracy of the framework and its advantages to standard clinical practice. At this point, the added-value of the accurate pre-operative planning strategy (atrial contours plus fossa ovalis) developed during this thesis is projected to be validated in real interventional cases.

To improve the planning and training of TSP interventions, novel atrial phantom models are anticipated to be presented. For that, instead of realistic inter-atrial septal wall representation only, correct modeling of the atrial valves and even inclusion of the ventricular region must be also considered. Interestingly, modeling of the ventricular region using a similar manufacturing process was already demonstrated to be feasible by Gomes-Fonseca et al. (2018). At this stage, automatic segmentation strategies (as described in this PhD thesis) will be applied to speed-up the model construction process. Additionally, the dynamic version of the proposed phantom

may also be constructed and validated. As a potential solution to increase the degrees of freedom for the anatomy construction stage or even to accelerate the construction process, direct 3D printing of the heart anatomy (instead of the described mold-cast approach) using ultrasound compatible material must be investigated. As a final step, exhaustive clinical validation (using multiple normal and abnormal anatomies) of the proposed model is mandatory.

Taking into consideration the proposed competitive segmentation method, its application for full heart segmentation (*i.e.* all chambers plus aorta), or even different applications (e.g. carotid artery bifurcation wall, aortic dissection) using a different deformable model formulation will be pursued. Additionally, clinical validation of the global clinical indicators (e.g. atrial volume) obtained with the current segmentation approach must be performed in a large multi-center clinical database. Finally, evaluation of both atrial region and fossa ovalis segmentation methods in a more exhaustive clinical database (with novel abnormal anatomy situations) must also be studied, assessing the robustness of both strategies.

Regarding the LAA occlusion, application of the described blind-ended segmentation strategy in high detailed images (*i.e.* CT and MRI) must be considered, allowing the evaluation of the LAA anatomy in different imaging modalities, which may improve the planning of LAA occlusion intervention. Additionally, a novel strategy to fully automatically initialize the blind-ended LAA model, by detecting the LAA centerline, must be developed. A clinical validation of the proposed methodology in multiple imaging modalities acquired at different centers (*i.e.* a multi-center and multi-modality validation) must be performed, ultimately assessing the method's accuracy, robustness and possible limitations. Then, an exhaustive validation of the proposed approach to estimate relevant clinical measurements against the real implanted devices must also be performed, confirming its potential and accuracy to detect the optimal occluding device. Moreover, clinical application of the developed planning method in a real-intervention scenario will also be explored (*i.e.* selection, throughout the intervention, of the occluding device based on the described framework), validating the added-value of the described method in a real scenario situation.

Novel strategies to generate patient-specific LAA models for both intervention planning and even improved medical training must be explored. To reduce the manufacturing time, automatic modeling of the LAA anatomy using the abovementioned segmentation method may be applied, increasing its interest in the clinical routine. Moreover, construction of patient-specific occluding devices (instead of the standard devices currently available) based on the extracted LAA anatomy must be further investigated. In fact, such strategy can probably reduce the risk of sub-optimal implantation and residual leaks. However, exhaustive validations and

studies to define optimal construction materials (which must be biocompatible, among other properties), to evaluate the long-term performance of the novel device and even to evaluate its applicability in human anatomies are mandatory.

The development of strategies to evaluate the LAA function (four-dimensional, 4D, assessment) by combining the 3D segmentation tool plus feature tracking strategies must be explored, allowing a fast, reproducible and accurate evaluation of both LAA anatomy and function. As such, not only the planning of LAA occlusion can be performed with the developed tool, but also patient risk stratification for thromboembolism can be routinely evaluated.

Finally, the extension of the developed methods for other LA interventions or medical procedures is expected. In detail, the atrial region models and FO model can also be relevant anatomical information for other interventions such as catheter ablation for atrial fibrillation, atrial septal defect closure and percutaneous mitral valve replacement, requiring further studies. Additionally, these anatomical models can be used in clinical practice to evaluate the cardiac anatomy and to detect possible abnormal cases. The development of novel solutions to improve the catheter manipulation step throughout the LAA occlusion by combining both developed methods (*i.e.* one strategy to detect FO position and other to segment the LAA) is also expected. Specifically, taking into consideration the target region in the LAA and the FO position, the optimal puncture position (*i.e.* the location that guarantees maximum catheter dexterity at the LAA) can be estimated/simulated, improving therefore the traditional intervention.

## Bibliography

Abed, H.S., Alasady, M., Lau, D.H., Lim, H.S., Sanders, P., 2012. Approach to the difficult transseptal: diathermy facilitated left atrial access. Heart, Lung and Circulation 21, 108-112.

Abhayaratna, W.P., Seward, J.B., Appleton, C.P., Douglas, P.S., Oh, J.K., Tajik, A.J., Tsang, T.S., 2006. Left atrial size: physiologic determinants and clinical applications. Journal of the American College of Cardiology 47, 2357-2363.

Achenbach, S., Anders, K., Kalender, W.A., 2008. Dual-source cardiac computed tomography: image quality and dose considerations. European radiology 18, 1188-1198.

Afzal, S., Veulemans, V., Balzer, J., Rassaf, T., Hellhammer, K., Polzin, A., Kelm, M., Zeus, T., 2017. Safety and efficacy of transseptal puncture guided by real-time fusion of echocardiography and fluoroscopy. Netherlands Heart Journal 25, 131-136.

Akagi, T., 2015. Current concept of transcatheter closure of atrial septal defect in adults. Journal of cardiology 65, 17-25.

Aksu, T., Guler, T.E., Yalin, K., Golcuk, S.E., Ozcan, K.S., Guler, N., 2017. A novel deep inspiration maneuver for difficult transseptal puncture. American Journal of Cardiology 119, 428-433.

Al-Saady, N., Obel, O., Camm, A., 1999. Left atrial appendage: structure, function, and role in thromboembolism. Heart 82, 547-554.

Alessandrini, M., Friboulet, D., Basset, O., D'hooge, J., Bernard, O., 2009. Level-set segmentation of myocardium and epicardium in ultrasound images using localized bhattacharyya distance, in IEEE International Ultrasonics Symposium, Roma, Italy, pp. 2468-2471.

Alkhouli, M., Rihal, C.S., Holmes Jr, D.R., 2016. Transseptal techniques for emerging structural heart interventions. JACC: Cardiovascular Interventions 9, 2465-2480.

Almeida, N., Friboulet, D., Sarvari, S.I., Bernard, O., Barbosa, D., Samset, E., D'hooge, J., 2016. Left-Atrial Segmentation From 3-D Ultrasound Using B-Spline Explicit Active Surfaces With Scale Uncoupling. IEEE Transactions on Ultrasonics, Ferroelectrics, and Frequency Control 63, 212-221.

Amberg, B., Romdhani, S., Vetter, T., 2007. Optimal step nonrigid ICP algorithms for surface registration, in IEEE Conference on Computer Vision and Pattern Recognition, 2007. CVPR'07., pp. 1-8.

Ammar, M., Mahmoudi, S., Chikh, M.A., Abbou, A., 2013. Toward an automatic left atrium localization based on shape descriptors and prior knowledge, International Workshop on Statistical Atlases and Computational Models of the Heart. Springer, pp. 42-48.

Anderson, R.H., Razavi, R., Taylor, A.M., 2004. Cardiac anatomy revisited. Journal of Anatomy 205, 159-177.

Anderson, R.H., Webb, S., Brown, N.A., 1999. Clinical anatomy of the atrial septum with reference to its developmental components. Clinical Anatomy 12, 362-374.

Arias-Lorza, A.M., Petersen, J., van Engelen, A., Selwaness, M., van der Lugt, A., Niessen, W.J., de Bruijne, M., 2016. Carotid artery wall segmentation in multispectral MRI by coupled optimal surface graph cuts. IEEE Transactions on Medical Imaging 35, 901-911.

Arkles, J., Zado, E., Supple, G., Frankel, D.S., Callans, D., Marchlinski, F., Dixit, S., 2015. Feasibility of transseptal access in patients with previously scarred or repaired interatrial septum. Journal of cardiovascular electrophysiology 26, 963-968.

Babaliaros, V.C., Green, J.T., Lerakis, S., Lloyd, M., Block, P.C., 2008. Emerging Applications for Transseptal Left Heart Catheterization Old Techniques for New Procedures. Journal of the American College of Cardiology 51, 2116-2122.

Baerentzen, J.A., Aanaes, H., 2005. Signed distance computation using the angle weighted pseudonormal. IEEE Transactions on Visualization and Computer Graphics 11, 243-253.

Bai, W., Chen, Z., Tang, H., Wang, H., Cheng, W., Rao, L., 2017. Assessment of the left atrial appendage structure and morphology: comparison of real-time three-dimensional transesophageal echocardiography and computed tomography. The international journal of cardiovascular imaging 33, 623-633.

Baldus, S., Schillinger, W., Franzen, O., Bekeredjian, R., Sievert, H., Schofer, J., Kuck, K.H., Konorza, T., Möllmann, H., Hehrlein, C., 2012. MitraClip therapy in daily clinical practice: initial results from the German transcatheter mitral valve interventions (TRAMI) registry. European journal of heart failure 14, 1050-1055.

Ballesteros, G., Ramos Ardanaz, P., Neglia, R., Palacio Solis, M., Diaz Fernandez, C., Lopez Gonzalez, G., Janiashvili, E., García-bolao, I., 2017. Mediguide-Assisted Transseptal Puncture without Echocardiographic Guidance. Pacing and Clinical Electrophysiology 40, 545-550.

Barbosa, D., Bernard, O., Savu, O., Dietenbeck, T., Heyde, B., Claus, P., Friboulet, D., D'hooge, J., 2010. Coupled B-spline active geometric functions for myocardial segmentation: A localized region-based approach, in IEEE International Ultrasonics Symposium, pp. 1648-1651.

Barbosa, D., Dietenbeck, T., Schaerer, J., D'hooge, J., Friboulet, D., Bernard, O., 2012. B-spline explicit active surfaces: An efficient framework for real-time 3-D region-based segmentation. IEEE Transactions on Image Processing 21, 241-251.

Basman, C., Parmar, Y.J., Kliger, C., Jelnin, V., Pasala, T.K., Ruiz, C.E., Kronzon, I., 2017. Fusion Imaging for Structural Heart Disease Interventions. Current Cardiovascular Imaging Reports 10, 41.

Bayrak, F., Chierchia, G.-B., Namdar, M., Yazaki, Y., Sarkozy, A., de Asmundis, C., Muller-Burri, S.A., Rao, J., Ricciardi, D., Sorgente, A., 2012. Added value of transoesophageal echocardiography during transseptal puncture performed by inexperienced operators. Europace 14, 661-665.

Beigel, R., Wunderlich, N.C., Ho, S.Y., Arsanjani, R., Siegel, R.J., 2014. The left atrial appendage: anatomy, function, and noninvasive evaluation. JACC: Cardiovascular imaging 7, 1251-1265.

Beinart, R., Abbara, S., Blum, A., Ferencik, M., Heist, K., Ruskin, J., Mansour, M., 2011. Left atrial wall thickness variability measured by CT scans in patients undergoing pulmonary vein isolation. Journal of cardiovascular electrophysiology 22, 1232-1236.

Belaid, A., Boukerroui, D., Maingourd, Y., Lerallut, J.-F., 2011. Phase-based level set segmentation of ultrasound images. IEEE Transactions on Information Technology in Biomedicine 15, 138-147.

Bertrand, P.B., Grieten, L., De Meester, P., Verbrugge, F.H., Mullens, W., Verhaert, D., Rivero-Ayerza, M., Budts, W., Vandervoort, P.M., 2014. Etiology and relevance of the figure-of-eight artifact on echocardiography after percutaneous left atrial appendage closure with the Amplatzer Cardiac Plug. Journal of the American Society of Echocardiography 27, 323-328. e321.

Besl, P.J., McKay, N.D., 1992. Method for registration of 3-D shapes, Robotics-DL tentative 1992. in International Society for Optics and Photonics., pp. 586-606.

Beutler, D.S., Gerkin, R.D., Loli, A.I., 2014. The morphology of left atrial appendage lobes: a novel characteristic naming scheme derived through three-dimensional cardiac computed tomography. World Journal of Cardiovascular Surgery 4, 17.

Biaggi, P., Fernandez-Golfín, C., Hahn, R., Corti, R., 2015. Hybrid imaging during transcatheter structural heart interventions. Current cardiovascular imaging reports 8, 33.

Biermann, J., Bode, C., Asbach, S., 2012. Intracardiac echocardiography during catheter-based ablation of atrial fibrillation. Cardiology research and practice 2012.

Boron, W.F., Boulpaep, E.L., 2008. Medical Physiology. Elsevier Health Sciences.

Bourier, F., Reents, T., Ammar-Busch, S., Buiatti, A., Grebmer, C., Telishevska, M., Brkic, A., Semmler, V., Lennerz, C., Kaess, B., 2015. Sensor-Based Electromagnetic Navigation (Mediguide®): How Accurate Is It? A Phantom Model Study. Journal of cardiovascular electrophysiology 26, 1140-1145.

Bourier, F., Reents, T., Ammar-Busch, S., Semmler, V., Telishevska, M., Kottmaier, M., Lennerz, C., Grebmer, C., Kolb, C., Deisenhofer, I., 2016. Transseptal puncture guided by CT-derived 3D-augmented fluoroscopy. Journal of cardiovascular electrophysiology 27, 369-372.

Brost, A., Wimmer, A., Liao, R., Hornegger, J., Strobel, N., 2010. Catheter tracking: Filter-based vs. learning-based, Pattern Recognition. Springer, pp. 293-302.

Brox, T., Weickert, J., 2006. Level set segmentation with multiple regions. IEEE Transactions on Image Processing 15, 3213-3218.

Budge, L.P., Shaffer, K.M., Moorman, J.R., Lake, D.E., Ferguson, J.D., Mangrum, J.M., 2008. Analysis of in vivo left atrial appendage morphology in patients with atrial fibrillation: a direct comparison of transesophageal echocardiography, planar cardiac CT, and segmented three-dimensional cardiac CT. Journal of interventional cardiac electrophysiology 23, 87-93.

Camm, A.J., Colombo, A., Corbucci, G., Padeletti, L., 2014. Left atrial appendage closure: a new technique for clinical practice. Heart Rhythm 11, 514-521.

Canny, J., 1986. A computational approach to edge detection. IEEE Transactions on Pattern Analysis and Machine Intelligence, 679-698.

Capulzini, L., Paparella, G., Sorgente, A., de Asmundis, C., Chierchia, G.B., Sarkozy, A., Muller-Burri, A., Yazaki, Y., Roos, M., Brugada, P., 2010. Feasibility, safety, and outcome of a challenging transseptal puncture facilitated by radiofrequency energy delivery: a prospective single-centre study. Europace 12, 662-667.

Carton, A.-K., Bakic, P., Ullberg, C., Derand, H., Maidment, A.D., 2011. Development of a physical 3D anthropomorphic breast phantom. Medical physics 38, 891-896.

Ceh, D., Peters, T.M., Chen, E.C., 2015. Acoustic characterization of polyvinyl chloride and self-healing silicone as phantom materials, in SPIE Medical Imaging 2015: Physics of Medical Imaging. International Society for Optics and Photonics, p. 94123G.

Chen, D., Müller-Eschner, M., von Tengg-Kobligk, H., Barber, D., Böckler, D., Hose, R., Ventikos, Y., 2013. A patient-specific study of type-B aortic dissection: evaluation of true-false lumen blood exchange. Biomedical engineering online 12, 1.

Chen, T., Babb, J., Kellman, P., Axel, L., Kim, D., 2008. Semiautomated segmentation of myocardial contours for fast strain analysis in cine displacement-encoded MRI. IEEE Transactions on Medical Imaging 27, 1084-1094.

Chierchia, G.-B., Casado-Arroyo, R., de Asmundis, C., Rodriguez-Manero, M., Sarkozy, A., Conte, G., Sieira, J., Levinstein, M., Baltogiannis, G., Di Giovanni, G., 2013. Impact of transseptal puncture site on acute and mid-term outcomes during cryoballoon ablation: A comparison between anterior, medial and posterior transatrial access. International journal of cardiology 168, 4098-4102.

Chierchia, G.B., Capulzini, L., de Asmundis, C., Sarkozy, A., Roos, M., Paparella, G., Boussy, T., Van Camp, G., Kerkhove, D., Brugada, P., 2008. First experience with real-time

three-dimensional transoesophageal echocardiography-guided transseptal in patients undergoing atrial fibrillation ablation. Europace 10, 1325-1328.

Christiaens, L., Varroud-Vial, N., Ardilouze, P., Ragot, S., Mergy, J., Bonnet, B., Herpin, D., Allal, J., 2010. Real three-dimensional assessment of left atrial and left atrial appendage volumes by 64-slice spiral computed tomography in individuals with or without cardiovascular disease. International journal of cardiology 140, 189-196.

Clark, B.C., Sumihara, K., Berul, C.I., Moak, J.P., 2017. Off the pedal: Fluoroless transseptal puncture in pediatric supraventricular tachycardia ablation. Pacing and Clinical Electrophysiology 40, 1254-1259.

Clark, J., Bockoven, J., Lane, J., Patel, C., Smith, G., 2008. Use of Three-Dimensional Catheter Guidance and Trans-Esophageal Echocardiography to Eliminate Fluoroscopy in Catheter Ablation of Left-Sided Accessory Pathways. Pacing and Clinical Electrophysiology 31, 283-289.

Cleary, K., Peters, T.M., 2010. Image-guided interventions: technology review and clinical applications. Annual review of biomedical engineering 12, 119-142.

Crystal, M.A., Mirza, M.A., Benson, L.N., 2010. A radiofrequency transseptal needle: initial animal studies. Catheterization and Cardiovascular Interventions 76, 769-773.

Cygan, S., Werys, K., Błaszczyk, Ł., Kubik, T., Kałużyński, K., 2014. Left ventricle phantom and experimental setup for MRI and echocardiography–Preliminary results of data acquisitions. Biocybernetics and Biomedical Engineering 34, 19-24.

Dandel, M., Hetzer, R., 2009. Echocardiographic strain and strain rate imaging—clinical applications. International journal of cardiology 132, 11-24.

Davies, A., Blakeley, A.G.H., Kidd, C., McGeown, J.G., 2001. Human Physiology. Churchill Livingstone.

De Buck, S., Ector, J., La Gerche, A., Maes, F., Heidbuchel, H., 2009. Toward image-based catheter tip tracking for treatment of atrial fibrillation, in CI2BM09-MICCAI Workshop on Cardiovascular Interventional Imaging and Biophysical Modelling, p. 8 pages.

De Ponti, R., Marazzi, R., Picciolo, G., Salerno-Uriarte, J.A., 2010. Use of a novel sharp-tip, J-shaped guidewire to facilitate transseptal catheterization. Europace 12, 668-673.

Di Biase, L., Santangeli, P., Anselmino, M., Mohanty, P., Salvetti, I., Gili, S., Horton, R., Sanchez, J.E., Bai, R., Mohanty, S., 2012. Does the left atrial appendage morphology correlate with the risk of stroke in patients with atrial fibrillation?: results from a multicenter study. Journal of the American College of Cardiology 60, 531-538.

Dodge, J.T., Brown, B.G., Bolson, E.L., Dodge, H.T., 1992. Lumen diameter of normal human coronary arteries. Influence of age, sex, anatomic variation, and left ventricular hypertrophy or dilation. Circulation 86, 232-246.

Dong, J.-Z., Ning, M., Yu, R.-H., Long, D.-Y., Tang, R.-B., Sang, C.-H., Jiang, C.-X., Bai, R., Du, X., Nie, S.-P., 2015. A simple method to localize transseptal puncture site during catheter ablation for atrial fibrillation. European Heart Journal Supplements 17, C59-C64.

Earley, M.J., 2009. How to perform a transseptal puncture. Heart 95, 85-92.

Ecabert, O., Peters, J., Schramm, H., Lorenz, C., von Berg, J., Walker, M.J., Vembar, M., Olszewski, M.E., Subramanyan, K., Lavi, G., 2008. Automatic model-based segmentation of the heart in CT images. IEEE Transactions on Medical Imaging 27, 1189-1201.

Ecabert, O., Peters, J., Walker, M.J., Ivanc, T., Lorenz, C., von Berg, J., Lessick, J., Vembar, M., Weese, J., 2011. Segmentation of the heart and great vessels in CT images using a model-based adaptation framework. Medical image analysis 15, 863-876.

Ehrlinspiel, D.M., Gass, M., Balmer, C., 2017. Transseptal puncture for radiofrequency catheter ablations of left-sided arrhythmias in a paediatric population. Cardiology in the Young 27, 267-272.

Elagha, A.A., Kocaturk, O., Guttman, M.A., Ozturk, C., Kim, A.H., Burton, G.W., Kim, J.H., Raman, V.K., Raval, A.N., Wright, V.J., 2008. Real-Time MR Imaging–guided Laser Atrial Septal Puncture in Swine. Journal of Vascular and Interventional Radiology 19, 1347-1353.

Elayi, C.S., Gurley, J.C., Di Sessa, T.G., Kakavand, B., 2011. Surgical electrocautery facilitated transseptal puncture in children. Pacing and Clinical Electrophysiology 34, 827-831.

Erden, İ., Erden, E.Ç., Golcuk, E., Aksu, T., Yalin, K., Güler, T.E., Özcan, K.S., Turan, B., 2016. Impact of transesophageal echocardiography during transseptal puncture on atrial fibrillation ablation. Journal of arrhythmia 32, 170-175.

Esch, J.J., Triedman, J.K., Cecchin, F., Alexander, M.E., Walsh, E.P., 2013. Radiofrequency-assisted transseptal perforation for electrophysiology procedures in children and adults with repaired congenital heart disease. Pacing and Clinical Electrophysiology 36, 607-611.

Estevez, M.E., Lindgren, K.A., Bergethon, P.R., 2010. A novel three-dimensional tool for teaching human neuroanatomy. Anatomical sciences education 3, 309-317.

Faisal, A., Ng, S.-C., Goh, S.-L., George, J., Supriyanto, E., Lai, K.W., 2015. Multiple LREK Active Contours for Knee Meniscus Ultrasound Image Segmentation. IEEE Transactions on Medical Imaging 34, 2162-2171.

Faletra, F.F., Biasco, L., Pedrazzini, G., Moccetti, M., Pasotti, E., Leo, L.A., Cautilli, G., Moccetti, T., Monaghan, M.J., 2017. Echocardiographic-Fluoroscopic Fusion Imaging in Transseptal Puncture: A New Technology for an Old Procedure. Journal of the American Society of Echocardiography 30, 886-895.

Faletra, F.F., Nucifora, G., Ho, S.Y., 2011. Imaging the atrial septum using real-time three-dimensional transesophageal echocardiography: technical tips, normal anatomy, and its role in transseptal puncture. Journal of the American Society of Echocardiography 24, 593-599.

Faletra, F.F., Pedrazzini, G., Pasotti, E., Muzzarelli, S., Dequarti, M.C., Murzilli, R., Schlossbauer, S.A., Slater, I.P., Moccetti, T., 2014a. 3D TEE during catheter-based interventions. JACC: Cardiovascular Imaging 7, 292-308.

Faletra, F.F., Perk, G., Pandian, N.G., Nesser, H.-J., Kronzon, I., 2014b. Closure of Patent Foramen Ovalis and Atrial Septal Defect. Real-Time 3D Interventional Echocardiography. Springer, pp. 21-41.

Feld, G.K., Tiongson, J., Oshodi, G., 2011. Particle formation and risk of embolization during transseptal catheterization: comparison of standard transseptal needles and a new radiofrequency transseptal needle. Journal of Interventional Cardiac Electrophysiology 30, 31-36.

Feld, G.K., Yao, B., 2014. Evaluation of the safety and effectiveness of the CryoMedix cryoablation catheter system for the treatment of atrial flutter and fibrillation. Journal of Interventional Cardiac Electrophysiology 39, 37-44.

Felsberg, M., Sommer, G., 2001. The monogenic signal. IEEE Transactions on Signal Processing 49, 3136-3144.

Ferguson, J.D., Helms, A., Mangrum, J.M., Mahapatra, S., Mason, P., Bilchick, K., McDaniel, G., Wiggins, D., DiMarco, J.P., 2009. Catheter ablation of atrial fibrillation without fluoroscopy using intracardiac echocardiography and electroanatomic mapping. Circulation: Arrhythmia and Electrophysiology 2, 611-619.

Frangi, A.F., Niessen, W.J., Vincken, K.L., Viergever, M.A., 1998. Multiscale vessel enhancement filtering, in International Conference on Medical Image Computing and Computer-Assisted Intervention. Springer, pp. 130-137.

Fromageau, J., Gennisson, J.-L., Schmitt, C., Maurice, R.L., Mongrain, R., Cloutier, G., 2007. Estimation of polyvinyl alcohol cryogel mechanical properties with four ultrasound elastography methods and comparison with gold standard testings. IEEE Transactions on Ultrasonics, Ferroelectrics, and Frequency Control 54, 498-509.

Fromentin, S., Sarrazin, J.-F., Champagne, J., Nault, I., Philippon, F., Molin, F., Blier, L., O'Hara, G., 2011. Prospective comparison between conventional transseptal puncture and transseptal needle puncture with radiofrequency energy. Journal of Interventional Cardiac Electrophysiology 31, 237-242.

Gafoor, S., Schulz, P., Heuer, L., Matic, P., Franke, J., Bertog, S., Reinartz, M., Vaskelyte, L., Hofmann, I., Sievert, H., 2015. Use of EchoNavigator, a Novel Echocardiography-Fluoroscopy Overlay System, for Transseptal Puncture and Left Atrial Appendage Occlusion. Journal of interventional cardiology 28, 215-217.

Gao, G., Penney, G., Ma, Y., Gogin, N., Cathier, P., Arujuna, A., Morton, G., Caulfield, D., Gill, J., Rinaldi, C.A., 2012a. Registration of 3D trans-esophageal echocardiography to X-ray fluoroscopy using image-based probe tracking. Medical Image Analysis 16, 38-49.

Gao, Y., Kikinis, R., Bouix, S., Shenton, M., Tannenbaum, A., 2012b. A 3D interactive multi-object segmentation tool using local robust statistics driven active contours. Medical Image Analysis 16, 1216-1227.

Gard, J., Swale, M., Asirvatham, S., 2011. Transseptal access for the electrophysiologists: anatomic considerations to enhance safety and efficacy. J Innov Cardiac Rhythm Manage 2, 332-338.

Gerstenmaier, J.F., McCarthy, C.J., Brophy, D.P., Cantwell, C.P., 2013. Evaluation of the Particulate Concentration in a Gelatin-Based Phantom for Sonographically Guided Lesion Biopsy. Journal of Ultrasound in Medicine 32, 1471-1475.

Geva, T., Martins, J.D., Wald, R.M., 2014. Atrial septal defects. The Lancet 383, 1921-1932.

Giudici, M.C., Mickelsen, S.R., Bhave, P.D., Arteaga, R.B., Iqbal, O.J., 2015. A Safe, Simple Technique for Transseptal Catheterization. Pacing and Clinical Electrophysiology 38, 295-296.

Goitein, O., Fink, N., Hay, I., Di Segni, E., Guetta, V., Goitein, D., Brodov, Y., Konen, E., Glikson, M., 2017. Cardiac CT Angiography (CCTA) predicts left atrial appendage occluder device size and procedure outcome. The international journal of cardiovascular imaging 33, 739-747.

Gomes-Fonseca, J., Morais, P., Queirós, S., Veloso, F., Pinho, A.C., Fonseca, J.C., Correia-Pinto, J., Vilaça, J.L., 2018. Personalized dynamic phantom of the right and left ventricles based on patient-specific anatomy for echocardiography studies—Preliminary results, in 2018 IEEE 6th International Conference on Serious Games and Applications for Health (SeGAH).

Gowda, S.T., Qureshi, A.M., Turner, D., Madan, N., Weigand, J., Lorber, R., Singh, H.R., 2017. Transseptal puncture using surgical electrocautery in children and adults with and without complex congenital heart disease. Catheterization and Cardiovascular Interventions 90.

Graham, L.N., Melton, I.C., MacDonald, S., Crozier, I.G., 2007. Value of CT localization of the fossa ovalis prior to transseptal left heart catheterization for left atrial ablation. Europace 9, 417-423.

Grasland-Mongrain, P., Peters, J., Ecabert, O., 2010. Combination of shape-constrained and inflation deformable models with application to the segmentation of the left atrial

appendage, in IEEE International Symposium on Biomedical Imaging: From Nano to Macro, 2010, pp. 428-431.

Grau, V., Becher, H., Noble, J.A., 2007. Registration of multiview real-time 3-D echocardiographic sequences. IEEE Transactions on Medical Imaging 26, 1154-1165.

Greenstein, E., Passman, R., Lin, A.C., Knight, B.P., 2012. Incidence of tissue coring during transseptal catheterization when using electrocautery and a standard transseptal needle. Circulation: Arrhythmia and Electrophysiology 5, 341-344.

Haak, A., Ren, B., Mulder, H.W., Vegas-Sanchez-Ferrero, G., van Burken, G., van der Steen, A.F., van Stralen, M., Pluim, J.P., van Walsum, T., Bosch, J.G., 2015. Improved segmentation of multiple cavities of the heart in wide-view 3-D transesophageal echocardiograms. Ultrasound in Medicine & Biology 41, 1991-2000.

Haegeli, L.M., Calkins, H., 2014. Catheter ablation of atrial fibrillation: an update. European Heart Journal 35, 2454-2459.

Haegeli, L.M., Wolber, T., Ercin, E., Altwegg, L., Krasniqi, N., Novak, P.G., Sterns, L.D., Brunckhorst, C.B., Lüscher, T.F., Leather, R.A., 2010. Double transseptal puncture for catheter ablation of atrial fibrillation: safety of the technique and its use in the outpatient setting. Cardiology research and practice 2010, 295297.

Hall, J.E., 2006. Textbook of medical physiology. Elsevier Saunders.

Hauser, T.H., Peters, D.C., Wylie, J.V., Manning, W.J., 2008. Evaluating the left atrium by magnetic resonance imaging. Europace 10, iii22-iii27.

Heinroth, K.M., Hartkopf, T., Plehn, A., Wilhelm, J., Unverzagt, S., Frantz, S., Schirdewan, A., 2017. Wire-and needle potentials facilitating transseptal puncture. Journal of electrocardiology 50, 358-367.

Heyde, B., Cygan, S., Choi, H.F., Lesniak-Plewinska, B., Barbosa, D., Elen, A., Claus, P., Loeckx, D., Kaluzynski, K., D'hooge, J., 2012. Regional cardiac motion and strain estimation in three-dimensional echocardiography: A validation study in thick-walled univentricular phantoms. IEEE Transactions on Ultrasonics, Ferroelectrics, and Frequency Control 59, 668-682.

Ho, S.Y., McCarthy, K.P., Faletra, F.F., 2011. Anatomy of the left atrium for interventional echocardiography. European Heart Journal-Cardiovascular Imaging 12, i11-i15.

Hoit, B.D., 2014. Left atrial size and function: role in prognosis. Journal of the American College of Cardiology 63, 493-505.

Housden, R.J., Basra, M., Ma, Y., King, A.P., Bullens, R., Child, N., Gill, J., Rinaldi, C.A., Parish, V., Rhode, K.S., 2013a. Three-modality registration for guidance of minimally invasive cardiac interventions, in Functional Imaging and Modeling of the Heart. Springer, pp. 158-165.

Housden, R.J., Ma, Y., Arujuna, A., Nijhof, N., Cathier, P., Gijsbers, G., Bullens, R., Gill, J., Rinaldi, C.A., Parish, V., 2013b. Extended-field-of-view three-dimensional transesophageal echocardiography using image-based x-ray probe tracking. Ultrasound in Medicine & Biology 39, 993-1005.

Houston, J.D., Davis, M., 2001. Fundamentals of fluoroscopy. Gulf Professional Publishing.

Howard, S.A., Quallich, S.G., Benscoter, M.A., Holmgren, B.C., Rolfes, C.D., Iaizzo, P.A., 2015. Tissue Properties of the Fossa Ovalis as They Relate to Transseptal Punctures: A Translational Approach. Journal of interventional cardiology 28, 98-108.

Hsu, J.C., Badhwar, N., Gerstenfeld, E.P., Lee, R.J., Mandyam, M.C., Dewland, T.A., Imburgia, K.E., Hoffmayer, K.S., Vedantham, V., Lee, B.K., 2013. Randomized Trial of Conventional Transseptal Needle Versus Radiofrequency Energy Needle Puncture for Left Atrial Access (the TRAVERSE-LA Study). Journal of the American Heart Association 2, e000428.

Hu, Y.-F., Tai, C.-T., Lin, Y.-J., Chang, S.-L., Lo, L.-W., Wongcharoen, W., Udyavar, A.R., Tuan, T.-C., Chen, S.-A., 2008. The change in the fluoroscopy-guided transseptal puncture site and difficult punctures in catheter ablation of recurrent atrial fibrillation. Europace 10, 276-279.

Huang, Q., Zeng, Z., 2017. A Review on Real-Time 3D Ultrasound Imaging Technology. BioMed research international 2017.

Huang, X., Moore, J., Guiraudon, G., Jones, D.L., Bainbridge, D., Ren, J., Peters, T.M., 2009. Dynamic 2D ultrasound and 3D CT image registration of the beating heart. IEEE Transactions on Medical Imaging 28, 1179-1189.

Hunter, R.J., Liu, Y., Lu, Y., Wang, W., Schilling, R.J., 2012. Left atrial wall stress distribution and its relationship to electrophysiologic remodeling in persistent atrial fibrillation. Circulation: Arrhythmia and Electrophysiology 5, 351-360.

Iglesias, J.E., Sabuncu, M.R., 2015. Multi-atlas segmentation of biomedical images: a survey. Medical Image Analysis 24, 205-219.

Jauvert, G., Grimard, C., Lazarus, A., Alonso, C., 2015. Comparison of a Radiofrequency Powered Flexible Needle with a Classic Rigid Brockenbrough Needle for Transseptal Punctures in Terms of Safety and Efficacy. Heart, Lung and Circulation 24, 173-178.

Jayender, J., Patel, R.V., Michaud, G.F., Hata, N., 2011. Optimal transseptal puncture location for robot-assisted left atrial catheter ablation. The International Journal of Medical Robotics and Computer Assisted Surgery 7, 193-201.

Jeevan, M., Jebaraj, R., Krishnakumar, R., 2014. In-vitro Validation of Image Guided Surgery System with 3D Pre-Operative Visualization for Atrial Transseptal Puncture, in 18th International Conference on Information Visualisation (IV), 2014, pp. 342-345.

Jimenez-del-Toro, O., Müller, H., Krenn, M., Gruenberg, K., Taha, A.A., Winterstein, M., Eggel, I., Foncubierta-Rodríguez, A., Goksel, O., Jakab, A., 2016. Cloud-based evaluation of anatomical structure segmentation and landmark detection algorithms: VISCERAL anatomy benchmarks. IEEE Transactions on Medical Imaging 35, 2459-2475.

Jin, C., Feng, J., Wang, L., Liu, J., Yu, H., Lu, J., Zhou, J., 2018. Left Atrial Appendage Segmentation Using Fully Convolutional Neural Networks and Modified Three-dimensional Conditional Random Fields. IEEE Journal of Biomedical and Health Informatics (in press).

Karagöz, T., Akın, A., Aykan, H.H., 2014. NRG RF powered transseptal needle: a useful technique for transcatheter atrial septostomy and Fontan fenestration: report of three cases. Bosnian Journal of Basic Medical Sciences 14, 259-262.

Kataria, V., Berte, B., Vandekerckhove, Y., Tavernier, R., Duytschaever, M., 2017. Modified Transseptal Puncture Technique in Challenging Septa: A Randomized Comparison to Conventional Technique. BioMed research international 2017.

Katritsis, G.D., Siontis, G.C., Giazitzoglou, E., Fragakis, N., Katritsis, D.G., 2013. Complications of transseptal catheterization for different cardiac procedures. International journal of cardiology 168, 5352-5354.

Kautzner, J., Peichl, P., 2012. The role of imaging to support catheter ablation of atrial fibrillation. Cor et Vasa 54, e375-e385.

Kirchhof, P., Benussi, S., Kotecha, D., Ahlsson, A., Atar, D., Casadei, B., Castella, M., Diener, H.-C., Heidbuchel, H., 2016. 2016 ESC Guidelines for the management of atrial fibrillation developed in collaboration with EACTS. EP Europace 18, 1609-1678.

Kirişli, H., Schaap, M., Klein, S., Papadopoulou, S., Bonardi, M., Chen, C.-H., Weustink, A., Mollet, N., Vonken, E., van der Geest, R., 2010. Evaluation of a multi-atlas based method for segmentation of cardiac CTA data: a large-scale, multicenter, and multivendor study. Medical physics 37, 6279-6291.

Klein, A.L., Murray, R.D., Grimm, R.A., 2001. Role of transesophageal echocardiography-guided cardioversion of patients with atrial fibrillation. Journal of the American College of Cardiology 37, 691-704.

Klein, S., Staring, M., Murphy, K., Viergever, M.A., Pluim, J.P., 2010. Elastix: a toolbox for intensity-based medical image registration. IEEE Transactions on Medical Imaging 29, 196-205.

Knadler, J.J., Anderson, J.B., Chaouki, A.S., Czosek, R.J., Connor, C., Knilans, T.K., Spar, D.S., 2017. Utility and safety of the SafeSept™ transseptal guidewire for electrophysiology studies with catheter ablation in pediatric and congenital heart disease. Journal of Interventional Cardiac Electrophysiology 48, 369-374.

Knecht, S., Jaïs, P., Nault, I., Wright, M., Matsuo, S., Madaffari, A., Lellouche, N., O'Neill, M.D., Derval, N., Deplagne, A., 2008a. Radiofrequency puncture of the fossa ovalis for resistant transseptal access. Circulation: Arrhythmia and Electrophysiology 1, 169-174.

Knecht, S., Nault, I., Wright, M., Matsuo, S., Lellouche, N., Somasundaram, P.E., O'neill, M.D., Lim, K.-T., Sacher, F., Deplagne, A., 2008b. Imaging in catheter ablation for atrial fibrillation: enhancing the clinician's view. Europace 10, iii2-iii7.

Knecht, S., Skali, H., O'neill, M.D., Wright, M., Matsuo, S., Chaudhry, G.M., Haffajee, C.I., Nault, I., Gijsbers, G.H., Sacher, F., 2008c. Computed tomography–fluoroscopy overlay evaluation during catheter ablation of left atrial arrhythmia. Europace 10, 931-938.

Knecht, S., Wright, M., Lellouche, N., Nault, I., Matsuo, S., O'Neill, M.D., Lomas, O., Deplagne, A., Bordachar, P., Sacher, F., 2008d. Impact of a patent foramen ovale on paroxysmal atrial fibrillation ablation. Journal of cardiovascular electrophysiology 19, 1236-1241.

Koektuerk, B., Yorgun, H., Koektuerk, O., Turan, C.H., Gorr, E., Horlitz, M., Turan, R.G., 2016. Rotational Angiography Based Three-Dimensional Left Atrial Reconstruction: A New Approach for Transseptal Puncture. Cardiovascular therapeutics 34, 49-56.

Koermendy, D., Nietlispach, F., Shakir, S., Gloekler, S., Wenaweser, P., Windecker, S., Khattab, A.A., Meier, B., 2014. Amplatzer left atrial appendage occlusion through a patent foramen ovale. Catheterization and Cardiovascular Interventions 84, 1190-1196.

Kozlowski, P., Bandaru, R.S., D'hooge, J., Samset, E., 2017. Real-time catheter localization and visualization using three-dimensional echocardiography, in SPIE Medical Imaging 2017: Image-Guided Procedures, Robotic Interventions, and Modeling. International Society for Optics and Photonics, p. 1013518.

Krijthe, B.P., Kunst, A., Benjamin, E.J., Lip, G.Y., Franco, O.H., Hofman, A., Witteman, J.C., Stricker, B.H., Heeringa, J., 2013. Projections on the number of individuals with atrial fibrillation in the European Union, from 2000 to 2060. European heart journal 34, 2746-2751.

Kumar, V., Abbas, A.K., Fausto, N., Aster, J.C., 2014. Robbins and Cotran pathologic basis of disease, professional edition e-book. Elsevier health sciences.

Kwong, Y., Troupis, J., 2015. Cardiac CT imaging in the context of left atrial appendage occlusion. Journal of cardiovascular computed tomography 9, 13-18.

Lacomis, J.M., Goitein, O., Deible, C., Moran, P.L., Mamone, G., Madan, S., Schwartzman, D., 2007. Dynamic multidimensional imaging of the human left atrial appendage. Europace 9, 1134-1140.

Laing, J., Moore, J., Bainbridge, D., Drangova, M., Peters, T., 2017. Patient-specific atrium models for training and pre-procedure surgical planning, in SPIE Medical Imaging

2017: Image-Guided Procedures, Robotic Interventions, and Modeling. International Society for Optics and Photonics, p. 101351A.

Lakkireddy, D., Rangisetty, U., Prasad, S., Verma, A., Biria, M., Berenbom, L., Pimentel, R., Emert, M., Rosamond, T., Fahmy, T., 2008. Intracardiac Echo-Guided Radiofrequency Catheter Ablation of Atrial Fibrillation in Patients with Atrial Septal Defect or Patent Foramen Ovale Repair: A Feasibility, Safety, and Efficacy Study. Journal of cardiovascular electrophysiology 19, 1137-1142.

Lang, P., Rajchl, M., Li, F., Peters, T.M., 2011. Towards model-enhanced real-time ultrasound guided cardiac interventions, in International Conference on Intelligent Computation and Bio-Medical Instrumentation (ICBMI), pp. 89-92.

Lang, P., Seslija, P., Chu, M.W., Bainbridge, D., Guiraudon, G.M., Jones, D.L., Peters, T.M., 2012. US–fluoroscopy registration for transcatheter aortic valve implantation. IEEE Transactions on Biomedical Engineering 59, 1444-1453.

Lang, R.M., Bierig, M., Devereux, R.B., Flachskampf, F.A., Foster, E., Pellikka, P.A., Picard, M.H., Roman, M.J., Seward, J., Shanewise, J., 2006. Recommendations for chamber quantification. European journal of echocardiography 7, 79-108.

Lankton, S., Tannenbaum, A., 2008. Localizing region-based active contours. IEEE Transactions on Image Processing 17, 2029-2039.

Lehrmann, H., Schneider, J., Jadidi, A.S., Park, C.I., Schiebeling-Romer, J., Allgeier, J., Arentz, T., Weber, R., 2014. Transseptal Access for Left Atrial Ablation: The Catheter-Probing Techniques Are Not Without Risk. Journal of cardiovascular electrophysiology 25, 479-484.

Lesniak-Plewinska, B., Cygan, S., Kaluzynski, K., D'hooge, J., Zmigrodzki, J., Kowalik, E., Kordybach, M., Kowalski, M., 2010. A dual-chamber, thick-walled cardiac phantom for use in cardiac motion and deformation imaging by ultrasound. Ultrasound in Medicine & Biology 36, 1145-1156.

Leśniak-Plewińska, B., Cygan, S., Żmigrodzki, J., Kałużyński, K., A new thick-walled conical model of the Left Ventricle, Computational Vision and Medical Image Processing V: Proceedings of the 5th Eccomas Thematic Conference on Computational Vision and Medical Image Processing (VipIMAGE 2015, Tenerife, Spain, October 19-21, 2015). CRC Press, p. 273.

Liang, K.-W., Fu, Y.-C., Lee, W.-L., Wang, K.-Y., Ting, C.-T., Jan, S.-L., Lin, W.-W., Lin, I.-H., 2010. Comparisons of mechanical versus phase-array intracardiac echocardiography-assisted transseptal puncture in patients with dilated left atrium undergoing percutaneous transvenous mitral commissurotomy. Journal of the Chinese Medical Association 73, 471-476.

Liao, R., Miao, S., Zheng, Y., 2013. Automatic and efficient contrast-based 2-D/3-D fusion for trans-catheter aortic valve implantation (TAVI). Computerized Medical Imaging and Graphics 37, 150-161.

Libby, P., 2008. Cardiovascular magnetic resonance imaging. Springer Science & Business Media.

Lim, H.E., Pak, H.-N., Tse, H.-F., Lau, C.-P., Hwang, C., Kim, Y.-H., 2009. Catheter ablation of atrial fibrillation via superior approach in patients with interruption of the inferior vena cava. Heart Rhythm 6, 174-179.

Linte, C.A., Moore, J., Wedlake, C., Peters, T.M., 2010a. Evaluation of model-enhanced ultrasound-assisted interventional guidance in a cardiac phantom. IEEE Transactions on Biomedical Engineering 57, 2209-2218.

Linte, C.A., White, J., Eagleson, R., Guiraudon, G.M., Peters, T.M., 2010b. Virtual and augmented medical imaging environments: Enabling technology for minimally

invasive cardiac interventional guidance. IEEE Reviews in Biomedical Engineering 3, 25-47.

Liu, P., Liu, R., Zhang, Y., Liu, Y., Tang, X., Cheng, Y., 2016. The value of 3D printing models of left atrial appendage using real-time 3D transesophageal echocardiographic data in left atrial appendage occlusion: applications toward an era of truly personalized medicine. Cardiology 135, 255-261.

López-Mínguez, J.R., González-Fernández, R., Fernández-Vegas, C., Millán-Nuñez, V., Fuentes-Cañamero, M.E., Nogales-Asensio, J.M., Doncel-Vecino, J., Yuste Dominguez, M., Garcia Serrano, L., Sánchez, Q.D., 2014. Comparison of imaging techniques to assess appendage anatomy and measurements for left atrial appendage closure device selection. J Invasive Cardiol 26, 462-467.

Luna, F.D., 2012. Introduction to 3D game programming with DirectX 11. Jones & Bartlett Publishers.

Ma, Z., Jorge, R.N.M., Mascarenhas, T., Tavares, J.M.R., 2012. Segmentation of female pelvic cavity in axial T2-weighted MR images towards the 3D reconstruction. International journal for numerical methods in biomedical engineering 28, 714-726.

Mah, D.Y., Miyake, C.Y., Sherwin, E.D., Walsh, A., Anderson, M.J., Western, K., Abrams, D.J., Alexander, M.E., Cecchin, F., Walsh, E.P., 2014. The use of an integrated electroanatomic mapping system and intracardiac echocardiography to reduce radiation exposure in children and young adults undergoing ablation of supraventricular tachycardia. Europace 16, 277-283.

Mahmoud, H.M., Al-Ghamdi, M.A., Ghabashi, A.E., Anwar, A.M., 2015. A proposed maneuver to guide transseptal puncture using real-time three-dimensional transesophageal echocardiography: pilot study. Cardiology research and practice 2015.

Malayeri, A.A., Natori, S., Bahrami, H., Bertoni, A.G., Kronmal, R., Lima, J.A., Bluemke, D.A., 2008. Relation of aortic wall thickness and distensibility to cardiovascular risk factors (from the Multi-Ethnic Study of Atherosclerosis [MESA]). The American journal of cardiology 102, 491-496.

Mansour, M., Afzal, M.R., Gunda, S., Pillarisetti, J., Heist, K., Acha, M.R., Heard, M., Ruskin, J., Lakkireddy, D., 2015. Feasibility of transseptal puncture using a nonfluoroscopic catheter tracking system. Pacing and Clinical Electrophysiology 38, 791-796.

Martini, F., 2018. Fundamentals of Anatomy & Physiology. 18th. Pearson Education, Inc., New York.

Matoshvili, Z., Bastani, H., Bourke, T., Braunschweig, F., Drca, N., Gudmundsson, K., Insulander, P., Jemtrén, A., Kennebäck, G., Saluveer, O., 2017. Safety of fluoroscopy-guided transseptal approach for ablation of left-sided arrhythmias. EP Europace 19, 2023-2026.

Matsumoto, J.S., Morris, J.M., Foley, T.A., Williamson, E.E., Leng, S., McGee, K.P., Kuhlmann, J.L., Nesberg, L.E., Vrtiska, T.J., 2015. Three-dimensional physical modeling: Applications and experience at mayo clinic. Radiographics 35, 1989-2006.

Matsumoto, T., Kar, S., 2013. Latest advances in transseptal structural heart interventions. Circulation journal: official journal of the Japanese Circulation Society 78, 1782-1790.

Mcwilliams, M.J., Tchou, P., 2009. The use of a standard radiofrequency energy delivery system to facilitate transseptal puncture. Journal of cardiovascular electrophysiology 20, 238-240.

Medi, C., Evered, L., Silbert, B., Teh, A., Halloran, K., Morton, J., Kistler, P., Kalman, J., 2013. Subtle post-procedural cognitive dysfunction after atrial fibrillation ablation. Journal of the American College of Cardiology 62, 531-539.

Meier, B., Blaauw, Y., Khattab, A.A., Lewalter, T., Sievert, H., Tondo, C., Glikson, M., Reviewers, D., Lip, G.Y., Lopez-Minguez, J., 2014. EHRA/EAPCI expert consensus statement on catheter-based left atrial appendage occlusion. Europace 16, 1397-1416.

Melenovsky, V., Hwang, S.-J., Lin, G., Redfield, M.M., Borlaug, B.A., 2014. Right heart dysfunction in heart failure with preserved ejection fraction. European heart journal 35, 3452-3462.

Mitchell-Heggs, L., Lellouche, N., Deal, L., Elbaz, N., Hamdaoui, B., Castanié, J.-B., Dubois-Randé, J.-L., Guéret, P., Lim, P., 2010. Transseptal puncture using minimally invasive echocardiography during atrial fibrillation ablation. Europace 12, 1435-1438.

Miyazaki, S., Shah, A.J., Nault, I., Wright, M., Jadidi, A.S., Forclaz, A., Liu, X., Linton, N., Xhaet, O., Rivard, L., 2011. Impact of patent foramen ovale on left atrial linear lesions in the context of atrial fibrillation ablation. Journal of cardiovascular electrophysiology 22, 846-850.

Moher, D., Liberati, A., Tetzlaff, J., Altman, D.G., Group, P., 2010. Preferred reporting items for systematic reviews and meta-analyses: the PRISMA statement. International journal of surgery 8, 336-341.

Morais, P., Tavares, J.M.R.S., Queirós, S., Veloso, F., D'hooge, J., Vilaça, J.L., 2017a. Development of a patient-specific atrial phantom model for planning and training of inter-atrial interventions. Medical physics 44, 5638-5649.

Morais, P., Vilaça, J.L., Ector, J., D'hooge, J., Tavares, J.M.R.S., 2017b. Novel solutions applied in transseptal puncture: a systematic review. Journal of Medical Devices 11, 010801.

Morais, P., Vilaça, J.L., Queirós, S., Bourier, F., Deisenhofer, I., Tavares, J.M.R.S., D'hooge, J., 2017c. A competitive strategy for atrial and aortic tract segmentation based on deformable models. Medical Image Analysis 42, 102-116.

Morais, P., Vilaça, J.L., Queirós, S., Marchi, A., Bourier, F., Deisenhofer, I., D'hooge, J., Tavares, J.M.R.S., 2018a. Automated segmentation of the atrial region and fossa ovalis towards computer-aided planning of inter-atrial wall interventions. Computer Methods and Programs in Biomedicine 161, 73-84.

Morais, P., Vilaça, J.L., Queirós, S., Rodrigues, P.L., Tavares, J.M.R.S., D'hooge, J., 2018b. A novel interventional guidance framework for transseptal puncture in left atrial interventions, in MICCAI 2018 Workshop on Bio-imaging and Visualization for Patient-Customized Simulations, September 16-20 2018, Granada.

Motiwala, S.R., Delling, F.N., 2015. Assessment of mitral valve disease: a review of imaging modalities. Current treatment options in cardiovascular medicine 17, 30.

Mulder, A.A., Balt, J.C., Wijffels, M.C., Wever, E.F., Boersma, L.V., 2012. Safety of pulmonary vein isolation and left atrial complex fractionated atrial electrograms ablation for atrial fibrillation with phased radiofrequency energy and multi-electrode catheters. Europace 14, 1433-1440.

Murarka, S., Lazkani, M., Moualla, S., Verma, D.R., Pershad, A., 2017. Left atrial anatomy and patient-related factors associated with adverse outcomes with the watchman device—a real world experience. Journal of Interventional Cardiology 30, 163-169.

Nguyen, B., Merino, J., Shachar, Y., Estrada, A., Doiny, D., Castrejon, S., Marx, B., Johnson, D., Marfori, W., Gang, E.S., 2013. Non-fluoroscopic transseptal catheterization during electrophysiology procedures using a remote magnetic navigation system. JAFIB: Journal of Atrial Fibrillation 6, 6-9.

Nijenhuis, V., Alipour, A., Wunderlich, N., Rensing, B., Gijsbers, G., Ten Berg, J., Suttorp, M., Boersma, L., van der Heyden, J., Swaans, M., 2017. Feasibility of multiplane microtransoesophageal echocardiographic guidance in structural heart disease transcatheter interventions in adults. Netherlands Heart Journal 25, 669-674.

Nishimura, T., Fukamizu, S., Matsushita, N., Hojo, R., Hayashi, T., Abe, T., Komiyama, K., Tanabe, Y., Tejima, T., Sakurada, H., 2012. High-risk transseptal puncture in a patient with a “pancake” deformity in the left atrium caused by descending aorta displacement. Journal of Arrhythmia 28, 250-253.

Noble, J.A., Boukerroui, D., 2006. Ultrasound image segmentation: a survey. IEEE Transactions on Medical Imaging 25, 987-1010.

Nucifora, G., Faletra, F.F., Regoli, F., Pasotti, E., Pedrazzini, G., Moccetti, T., Auricchio, A., 2011. Evaluation of the left atrial appendage with real-time 3-dimensional transesophageal echocardiography. Circulation: Cardiovascular Imaging 4, 514-523.

O’Brien, B., Zafar, H., De Freitas, S., Sharif, F., 2017. Transseptal puncture—Review of anatomy, techniques, complications and challenges. International journal of cardiology 233, 12-22.

Okada, T., Linguraru, M.G., Hori, M., Summers, R.M., Tomiyama, N., Sato, Y., 2015. Abdominal multi-organ segmentation from CT images using conditional shape–location and unsupervised intensity priors. Medical Image Analysis 26, 1-18.

Olszewski, R., Trawiński, Z., Wójcik, J., Nowicki, A., 2012. Mathematical and ultrasonographic model of the left ventricle: In vitro studies. Archives of Acoustics 37, 583-595.

Otsu, N., 1975. A threshold selection method from gray-level histograms. Automatica 11, 23-27.

Park, J.W., Bethencourt, A., Sievert, H., Santoro, G., Meier, B., Walsh, K., Lopez-Minquez, J.R., Meerkin, D., Valdés, M., Ormerod, O., 2011. Left atrial appendage closure with Amplatzer cardiac plug in atrial fibrillation: initial European experience. Catheterization and Cardiovascular Interventions 77, 700-706.

Pavlović, N., Reichlin, T., Kühne, M., Knecht, S., Osswald, S., Sticherling, C., 2014. Fluoroscopy-free recrossing of the interatrial septum during left atrial ablation procedures. Journal of Interventional Cardiac Electrophysiology 41, 261-266.

Pedrosa, J., Barbosa, D., Almeida, N., Bernard, O., Bosch, J., D'hooge, J., 2016. Cardiac chamber volumetric assessment using 3d ultrasound-a review. Current pharmaceutical design 22, 105-121.

Pedrosa, J., Barbosa, D., Heyde, B., Schnell, F., Rösner, A., Claus, P., D’hooge, J., 2017. Left Ventricular Myocardial Segmentation in 3-D Ultrasound Recordings: Effect of Different Endocardial and Epicardial Coupling Strategies. IEEE Transactions on Ultrasonics, Ferroelectrics, and Frequency Control 64, 525-536.

Pellegrino, P.L., Fassini, G., Biase, M., Tondo, C., 2016. Left atrial appendage closure guided by 3D printed cardiac reconstruction: emerging directions and future trends. Journal of cardiovascular electrophysiology 27, 768-771.

Preece, D., Williams, S.B., Lam, R., Weller, R., 2013. “Let's get physical”: advantages of a physical model over 3D computer models and textbooks in learning imaging anatomy. Anatomical sciences education 6, 216-224.

Queirós, S., Barbosa, D., Heyde, B., Morais, P., Vilaça, J.L., Friboulet, D., Bernard, O., D’hooge, J., 2014. Fast Automatic Myocardial Segmentation in 4D cine CMR datasets. Medical image analysis 18, 1115-1131.

Queirós, S., Dubois, C., Morais, P., Adriaenssens, T., Fonseca, J.C., Vilaça, J.L., D'hooge, J., 2017. Automatic 3D aortic annulus sizing by computed tomography in the planning of transcatheter aortic valve implantation. Journal of cardiovascular computed tomography 11, 25-32.

Queirós, S., Morais, P., Dubois, C., Voigt, J.-U., Fehske, W., Kuhn, A., Achenbach, T., Fonseca, J.C., Vilaça, J.L., D'hooge, J., 2018. Validation of a Novel Software Tool for Automatic Aortic Annular Sizing in Three-Dimensional Transesophageal

Echocardiographic Images. Journal of the American Society of Echocardiography 31, 515-525. e515.

Queirós, S., Papachristidis, A., Barbosa, D., Theodoropoulos, K.C., Fonseca, J.C., Monaghan, M.J., Vilaça, J.L., D'hooge, J., 2016. Aortic valve tract segmentation from 3D-TEE using shape-based B-spline Explicit Active Surfaces. IEEE Transaction on Medical Imaging 35, 2015-2025.

Queiros, S., Papachristidis, A., Morais, P., Theodoropoulos, K.C., Fonseca, J.C., Monaghan, M.J., Vilaca, J.L., D'hooge, J., 2016. Fully automatic 3D-TEE segmentation for the planning of Transcatheter Aortic Valve Implantation. IEEE Transactions on Biomedical Engineering 64, 1711-1720.

Radinovic, A., Mazzone, P., Landoni, G., Agricola, E., Regazzoli, D., Della Bella, P., 2016. Different transseptal puncture for different procedures: Optimization of left atrial catheterization guided by transesophageal echocardiography. Annals of cardiac anaesthesia 19, 589.

Rajpoot, K., Grau, V., Noble, J.A., 2009. Local-phase based 3D boundary detection using monogenic signal and its application to real-time 3-D echocardiography images, in IEEE International Symposium on Biomedical Imaging: From Nano to Macro, 2009. ISBI'09. IEEE, pp. 783-786.

Rajwani, A., Nelson, A.J., Shirazi, M.G., Disney, P.J., Teo, K.S., Wong, D.T., Young, G.D., Worthley, S.G., 2016. CT sizing for left atrial appendage closure is associated with favourable outcomes for procedural safety. European Heart Journal-Cardiovascular Imaging, jew212.

Rana, B.S., Shapiro, L.M., McCarthy, K.P., Ho, S.Y., 2010. Three-dimensional imaging of the atrial septum and patent foramen ovale anatomy: defining the morphological phenotypes of patent foramen ovale. European Journal of Echocardiography 11, i19-i25.

Reddy, V.Y., Doshi, S.K., Kar, S., Gibson, D.N., Price, M.J., Huber, K., Horton, R.P., Buchbinder, M., Neuzil, P., Gordon, N.T., 2017. 5-Year Outcomes After Left Atrial Appendage Closure: From the PREVAIL and PROTECT AF Trials. Journal of the American College of Cardiology, 24357.

Reddy, V.Y., Holmes, D., Doshi, S.K., Neuzil, P., Kar, S., 2011. Safety of percutaneous left atrial appendage closure results from the watchman left atrial appendage system for embolic protection in patients with AF (PROTECT AF) clinical trial and the continued access registry. Circulation 123, 417-424.

Reig, J., Mirapeix, R., Jornet, A., Petit, M., 1997. Morphologic characteristics of the fossa ovalis as an anatomic basis for transseptal catheterization. Surgical and Radiologic Anatomy 19, 279-282.

Rengier, F., Mehndiratta, A., von Tengg-Kobligk, H., Zechmann, C.M., Unterhinninghofen, R., Kauczor, H.-U., Giesel, F.L., 2010. 3D printing based on imaging data: review of medical applications. International journal of computer assisted radiology and surgery 5, 335-341.

Rettmann, M.E., Holmes III, D.R., Kwartowitz, D.M., Gunawan, M., Johnson, S.B., Camp, J.J., Cameron, B.M., Dalegrave, C., Kolasa, M.W., Packer, D.L., 2014. Quantitative modeling of the accuracy in registering preoperative patient-specific anatomic models into left atrial cardiac ablation procedures. Medical physics 41, 021909.

Rhoades, R.A., Bell, D.R., 2012. Medical phisiology: Principles for clinical medicine. Lippincott Williams & Wilkins.

Richardson, C., Bernard, S., Dinh, V.A., 2015. A Cost-effective, Gelatin-Based Phantom Model for Learning Ultrasound-Guided Fine-Needle Aspiration Procedures of the Head and Neck. Journal of Ultrasound in Medicine 34, 1479-1484.

Rolf, S., Hindricks, G., Sommer, P., Richter, S., Arya, A., Bollmann, A., Kosiuk, J., Koutalas, E., 2014. Electroanatomical mapping of atrial fibrillation: Review of the current techniques and advances. Journal of Atrial Fibrillation 7.

Rosengart, T.K., Feldman, T., Borger, M.A., Vassiliades, T.A., Gillinov, A.M., Hoercher, K.J., Vahanian, A., Bonow, R.O., O'Neill, W., 2008. Percutaneous and Minimally Invasive Valve Procedures A Scientific Statement From the American Heart Association Council on Cardiovascular Surgery and Anesthesia, Council on Clinical Cardiology, Functional Genomics and Translational Biology Interdisciplinary Working Group, and Quality of Care and Outcomes Research Interdisciplinary Working Group. Circulation 117, 1750-1767.

Ross, J., 2008. Transseptal left heart catheterization: a 50-year odyssey. Journal of the American College of Cardiology 51, 2107-2115.

Ruisi, C.P., Brysiewicz, N., Asnes, J.D., Sugeng, L., Marieb, M., Clancy, J., Akar, J.G., 2013. Use of intracardiac echocardiography during atrial fibrillation ablation. Pacing and Clinical Electrophysiology 36, 781-788.

Russo, A.D., Russo, E., Fassini, G., Casella, M., Innocenti, E., Zucchetti, M., Cefalú, C., Solimene, F., Mottola, G., Colombo, D., 2013. Role of Intracardiac Echocardiography in Atrial Fibrillation Ablation. JAFIB: Journal of Atrial Fibrillation 5.

Salghetti, F., Sieira, J., Chierchia, G.-B., Curnis, A., de Asmundis, C., 2017. Recognizing and reacting to complications of trans-septal puncture. Expert review of cardiovascular therapy 15, 905-912.

Saliba, W., Reddy, V.Y., Wazni, O., Cummings, J.E., Burkhardt, J.D., Haissaguerre, M., Kautzner, J., Peichl, P., Neuzil, P., Schibgilla, V., 2008. Atrial fibrillation ablation using a robotic catheter remote control system: initial human experience and long-term follow-up results. Journal of the American College of Cardiology 51, 2407-2411.

Sanchis-Gomar, F., Perez-Quilis, C., Lippi, G., Cervellin, G., Leischik, R., Löllgen, H., Serrano-Ostáriz, E., Lucia, A., 2017. Atrial fibrillation in highly trained endurance athletes—Description of a syndrome. International journal of cardiology 226, 11-20.

Sandoval, Z., Betancur, J., Dillenseger, J.-L., 2013. Multi-atlas-based segmentation of the left atrium and pulmonary veins, in International Workshop on Statistical Atlases and Computational Models of the Heart. Springer, pp. 24-30.

Saw, J., Lempereur, M., 2014. Percutaneous left atrial appendage closure: procedural techniques and outcomes. JACC: Cardiovascular Interventions 7, 1205-1220.

Schernthaner, C., Danmayr, F., Daburger, A., Eichinger, J., Hammerer, M., Strohmer, B., 2013. High incidence of echocardiographic abnormalities of the interatrial septum in patients undergoing ablation for atrial fibrillation. Echocardiography 30, 402-406.

Schroeder, S., Achenbach, S., Bengel, F., Burgstahler, C., Cademartiri, F., de Feyter, P., George, R., Kaufmann, P., Kopp, A.F., Knuuti, J., 2007. Cardiac computed tomography: indications, applications, limitations, and training requirements: report of a Writing Group deployed by the Working Group Nuclear Cardiology and Cardiac CT of the European Society of Cardiology and the European Council of Nuclear Cardiology. European heart journal 29, 531-556.

Schroeder, W.J., Lorensen, B., Martin, K., 2004. The visualization toolkit: an object-oriented approach to 3D graphics. Kitware.

Schwagten, B., Jordaens, L., Rivero-Ayerza, M., Van Belle, Y., Knops, P., Thornton, I., Szili-Torok, T., 2010. A Randomized Comparison of Transseptal and Transaortic Approaches for Magnetically Guided Ablation of Left-Sided Accessory Pathways. Pacing and Clinical Electrophysiology 33, 1298-1303.

Shahzad, R., Bos, D., Budde, R.P., Pellikaan, K., Niessen, W.J., van der Lugt, A., van Walsum, T., 2017. Automatic segmentation and quantification of the cardiac structures from non-contrast-enhanced cardiac CT scans. Physics in Medicine and Biology 62, 3798.

Sharma, G., Singh, G.D., Smith, T.W., Fan, D., Low, R.I., Rogers, J.H., 2017. Accuracy and procedural characteristics of standard needle compared with radiofrequency needle transseptal puncture for structural heart interventions. Catheterization and Cardiovascular Interventions 89.

Shepherd, E.J., Gall, S.A., Furniss, S.S., 2008. Interatrial septal puncture without the use of fluoroscopy—reducing ionizing radiation in left atrial ablation procedures. Journal of Interventional Cardiac Electrophysiology 22, 183-187.

Silverthorn, D.U., Ober, W.C., Garrison, C.W., Silverthorn, A.C., Johnson, B.R., 2009. Human physiology: an integrated approach. Pearson/Benjamin Cummings San Francisco, CA, USA:.

Smelley, M.P., Shah, D.P., Weisberg, I., Kim, S.S., Lin, A.C., Beshai, J.F., Burke, M.C., Knight, B.P., 2010. Initial experience using a radiofrequency powered transseptal needle. Journal of cardiovascular electrophysiology 21, 423-427.

Sodian, R., Weber, S., Markert, M., Rassoulian, D., Kaczmarek, I., Lueth, T.C., Reichart, B., Daebritz, S., 2007. Stereolithographic models for surgical planning in congenital heart surgery. The Annals of thoracic surgery 83, 1854-1857.

Song, H., Zhou, Q., Deng, Q., Chen, J., Zhang, L., Tan, T., Guo, R., 2016. Morphologic Assessment of the Left Atrial Appendage in Patients with Atrial Fibrillation by Gray Values–Inverted Volume-Rendered Imaging of Three-Dimensional Transesophageal Echocardiography: A Comparative Study with Computed Tomography. Journal of the American Society of Echocardiography 29, 1100-1108.

Spottiswoode, B., Van den Heever, D., Chang, Y., Engelhardt, S., Du Plessis, S., Nicolls, F., Hartzenberg, H., Gretschel, A., 2013. Preoperative three-dimensional model creation of magnetic resonance brain images as a tool to assist neurosurgical planning. Stereotactic and functional neurosurgery 91, 162-169.

Squillacote, A.H., Ahrens, J., 2007. The paraview guide. Kitware.

Standring, S., 2008. Gray's Anatomy: The anatomical basis of clinical practice, expert consult. Aubrey Durkin.

Stec, S., Zaborska, B., Sikora-Frąc, M., Kryński, T., Kułakowski, P., 2011. First experience with microprobe transoesophageal echocardiography in non-sedated adults undergoing atrial fibrillation ablation: feasibility study and comparison with intracardiac echocardiography. Europace 13, 51-56.

Stender, B., Blanck, O., Wang, B., Schlaefer, A., 2013. Model-Based Segmentation of the Left Atrium in CT and MRI Scans, International Workshop on Statistical Atlases and Computational Models of the Heart. Springer, pp. 31-41.

Stevanella, M., Maffessanti, F., Conti, C.A., Votta, E., Arnoldi, A., Lombardi, M., Parodi, O., Caiani, E.G., Redaelli, A., 2011. Mitral valve patient-specific finite element modeling from cardiac MRI: application to an annuloplasty procedure. Cardiovascular Engineering and Technology 2, 66-76.

Stone, D., Byrne, T., Pershad, A., 2015. Early results with the LARIAT device for left atrial appendage exclusion in patients with atrial fibrillation at high risk for stroke and anticoagulation. Catheterization and Cardiovascular Interventions 86, 121-127.

Suetens, P., 2017. Fundamentals of medical imaging. Cambridge university press.

Sugand, K., Abrahams, P., Khurana, A., 2010. The anatomy of anatomy: a review for its modernization. Anatomical sciences education 3, 83-93.

Sun, D., Rettmann, M.E., Packer, D., Robb, R.A., Holmes, D.R., Simulated evaluation of an intraoperative surface modeling method for catheter ablation by a real phantom

simulation experiment, in SPIE Medical Imaging 2015: Image-Guided Procedures, Robotic Interventions, and Modeling. International Society for Optics and Photonics, p. 94152N.

Suradi, H., Hijazi, Z., 2017. Left atrial appendage closure: outcomes and challenges. Netherlands Heart Journal 25, 143-151.

Sy, R.W., Klein, G.J., LEONG-SIT, P., Gula, L.J., Yee, R., Krahn, A.D., Skanes, A.C., 2011. Troubleshooting difficult transseptal catheterization. Journal of cardiovascular electrophysiology 22, 723-727.

Tam, M.D., Laycock, S.D., Brown, J.R., Jakeways, M., 2013. 3D printing of an aortic aneurysm to facilitate decision making and device selection for endovascular aneurysm repair in complex neck anatomy. Journal of Endovascular Therapy 20, 863-867.

Tan, T.C., Zeng, X., Jiao, Y., Wang, L., Wei, Q., Thiele, K., Salgo, I., Mehta, V., Andrawes, M., Picard, M.H., 2016. Three-dimensional field optimization method: clinical validation of a novel color Doppler method for quantifying mitral regurgitation. Journal of the American Society of Echocardiography 29, 926-934.

Tang, R.-B., Dong, J.-Z., Long, D.-Y., Yu, R.-H., Liu, X.-P., Cheng, Y.-L., Sang, C.-H., Ning, M., Jiang, C.-X., Avula, U.M.R., 2014. Incidence and clinical characteristics of transient ST-T elevation during transseptal catheterization for atrial fibrillation ablation. Europace, euu278.

Taramasso, M., Maisano, F., Latib, A., Denti, P., Guidotti, A., Sticchi, A., Panoulas, V., Giustino, G., Pozzoli, A., Buzzatti, N., 2014. Conventional surgery and transcatheter closure via surgical transapical approach for paravalvular leak repair in high-risk patients: results from a single-centre experience. European Heart Journal–Cardiovascular Imaging, jeu105.

Thaden, J.J., Sanon, S., Geske, J.B., Eleid, M.F., Nijhof, N., Malouf, J.F., Rihal, C.S., Bruce, C.J., 2016. Echocardiographic and fluoroscopic fusion imaging for procedural guidance: an overview and early clinical experience. Journal of the American Society of Echocardiography 29, 503-512.

Thiagalingam, A., D'Avila, A., Foley, L., Fox, M., Rothe, C., Miller, D., Malchano, Z., Ruskin, J.N., Reddy, V.Y., 2008. Full-Color Direct Visualization of the Atrial Septum to Guide Transseptal Puncture. Journal of cardiovascular electrophysiology 19, 1310-1315.

Tobon-Gomez, C., Geers, A.J., Peters, J., Weese, J., Pinto, K., Karim, R., Ammar, M., Daoudi, A., Margeta, J., Sandoval, Z., 2015. Benchmark for algorithms segmenting the left atrium from 3D CT and MRI datasets. IEEE Transactions on Medical Imaging 34, 1460-1473.

Tomlinson, D.R., Sabharwal, N., Bashir, Y., Betts, T.R., 2008. Interatrial septum thickness and difficulty with transseptal puncture during redo catheter ablation of atrial fibrillation. Pacing and Clinical Electrophysiology 31, 1606-1611.

Torres, H.R., 2016. Kidney Segmentation in 3D Ultrasound Images. University of Minho, Braga, Portugal.

Tzeis, S., Andrikopoulos, G., Deisenhofer, I., Ho, S.Y., Theodorakis, G., 2010. Transseptal catheterization: considerations and caveats. Pacing and Clinical Electrophysiology 33, 231-242.

Uchida, B.T., Pavcnik, D., Shimohira, M., Choi, Y.H., Jeromel, M., Keller, F.S., Rösch, J., 2011. New coaxial transseptal needle for creation of atrial septal defects in adult sheep. Cardiovascular and interventional radiology 34, 620-625.

Unnithan, A.G., Dexter, B.C., Law, I.H., Von Bergen, N.H., 2014. Limiting left-sided catheter dwelling time using 3-D NavX to mark and reaccess the left atrium via prior transseptal puncture site. Journal of Interventional Cardiac Electrophysiology 40, 125-128.

Vahanian, A., Brochet, E., 2017. Transseptal puncture for structural heart intervention: an old technique with new indications. Heart, heartjnl-2016-310483.

Vannelli, C., Moore, J., McLeod, J., Ceh, D., Peters, T., 2015. Dynamic heart phantom with functional mitral and aortic valves, ín SPIE Medical Imaging 2015: Image-Guided Procedures, Robotic Interventions, and Modeling. International Society for Optics and Photonics, p. 941503.

Verma, S., Adler, S., Berman, A., Duran, A., Loar, D., 2011. Localization of fossa ovalis and Brockenbrough needle prior to left atrial ablation using three-dimensional mapping with EnSite Fusion™. Journal of Interventional Cardiac Electrophysiology 30, 37-44.

von Alvensleben, J.C., Dick II, M., Bradley, D.J., LaPage, M.J., 2014. Transseptal access in pediatric and congenital electrophysiology procedures: defining risk. Journal of Interventional Cardiac Electrophysiology 41, 273-277.

Wadehra, V., Buxton, A.E., Antoniadis, A.P., McCready, J.W., Redpath, C.J., Segal, O.R., Rowland, E., Lowe, M.D., Lambiase, P.D., Chow, A.W., 2011. The use of a novel nitinol guidewire to facilitate transseptal puncture and left atrial catheterization for catheter ablation procedures. Europace, eur155.

Wagdi, P., Alkadhi, H., 2012. Can computer tomography help predict feasibility of transseptal puncture after percutaneous closure of an interatrial septal communication? Journal of Interventional Cardiac Electrophysiology 34, 167-172.

Wang, D.D., Eng, M., Kupsky, D., Myers, E., Forbes, M., Rahman, M., Zaidan, M., Parikh, S., Wyman, J., Pantelic, M., 2016a. Application of 3-dimensional computed tomographic image guidance to WATCHMAN implantation and impact on early operator learning curve: single-center experience. JACC: Cardiovascular Interventions 9, 2329-2340.

Wang, L., Feng, J., Jin, C., Lu, J., Zhou, J., 2016b. Left Atrial Appendage Segmentation Based on Ranking 2-D Segmentation Proposals, International Workshop on Statistical Atlases and Computational Models of the Heart. Springer, pp. 21-29.

Wang, Y., Chen, G., Bai, Y., Li, S., Natale, A., Dong, J., Wang, H., Sang, C., Yu, R., Long, D., 2016c. Transseptal puncture by CTP-2 method: Results from cardiac computed tomography analysis and clinical application. Medicine 95.

Wang, Y., Di Biase, L., Horton, R.P., Nguyen, T., Morhanty, P., Natale, A., 2010. Left atrial appendage studied by computed tomography to help planning for appendage closure device placement. Journal of cardiovascular electrophysiology 21, 973-982.

Wang, Y., Xue, Y.M., Mohanty, P., Natale, A., Li, L., Wu, W.F., Zhu, C.M., Liu, H., Zhong, G.Q., Zhu, L.G., 2012. Dilator method and needle method for atrial transseptal puncture: a retrospective study from a cohort of 4443 patients. Europace 14, 1450-1456.

Wasmer, K., Zellerhoff, S., Köbe, J., Mönnig, G., Pott, C., Dechering, D.G., Lange, P.S., Frommeyer, G., Eckardt, L., 2017. Incidence and management of inadvertent puncture and sheath placement in the aorta during attempted transseptal puncture. EP Europace 19, 447-457.

Wieczorek, M., Hoeltgen, R., Akin, E., Salili, A.R., 2010. Use of a novel needle wire in patients undergoing transseptal puncture associated with severe septal tenting. Journal of Interventional Cardiac Electrophysiology 27, 9-13.

Winder, J., Bibb, R., 2005. Medical rapid prototyping technologies: state of the art and current limitations for application in oral and maxillofacial surgery. Journal of oral and maxillofacial surgery 63, 1006-1015.

Winkle, R.A., Mead, R.H., Engel, G., Patrawala, R.A., 2011. The use of a radiofrequency needle improves the safety and efficacy of transseptal puncture for atrial fibrillation ablation. Heart Rhythm 8, 1411-1415.

Wolf, I., Vetter, M., Wegner, I., Böttger, T., Nolden, M., Schöbinger, M., Hastenteufel, M., Kunert, T., Meinzer, H.-P., 2005. The medical imaging interaction toolkit. Medical Image Analysis 9, 594-604.

Wolz, R., Chu, C., Misawa, K., Fujiwara, M., Mori, K., Rueckert, D., 2013. Automated abdominal multi-organ segmentation with subject-specific atlas generation. IEEE Transactions on Medical Imaging 32, 1723-1730.

Wu, T.-G., Wang, L.-X., Chen, S.-W., Lin, Z.-Q., Yan, C.-J., Huang, L.-P., 2008. Value of radiographic esophageal imaging in determining an optimal atrial septal puncture site for percutaneous balloon mitral valvuloplasty. Medical principles and practice: international journal of the Kuwait University, Health Science Centre 17, 280-283.

Wunderlich, N.C., Beigel, R., Swaans, M.J., Ho, S.Y., Siegel, R.J., 2015. Percutaneous interventions for left atrial appendage exclusion: options, assessment, and imaging using 2D and 3D echocardiography. JACC: Cardiovascular Imaging 8, 472-488.

Xu, Z., Burke, R.P., Lee, C.P., Baucom, R.B., Poulose, B.K., Abramson, R.G., Landman, B.A., 2015. Efficient multi-atlas abdominal segmentation on clinically acquired CT with SIMPLE context learning. Medical Image Analysis 24, 18-27.

Yan, P., Shen, W., Kassim, A.A., Shah, M., 2005. Segmentation of neighboring organs in medical image with model competition, in International Conference on Medical Image Computing and Computer-Assisted Intervention. Springer, pp. 270-277.

Yang, J., Staib, L.H., Duncan, J.S., 2004. Neighbor-constrained segmentation with level set based 3-D deformable models. IEEE Transactions on Medical Imaging 23, 940-948.

Yao, Y., Ding, L., Chen, W., Guo, J., Bao, J., Shi, R., Huang, W., Zhang, S., Wong, T., 2013. The training and learning process of transseptal puncture using a modified technique. Europace, eut078.

Yao, Y., Guo, J., Ding, L., Bao, J., Huang, W., Shi, R., Wu, L., Zhang, S., 2012. Improved approach to atrial septum puncture: experience in 539 cases. Chinese medical journal 125, 1179-1181.

Yezzi, A., Tsai, A., Willsky, A., 2002. A fully global approach to image segmentation via coupled curve evolution equations. Journal of Visual Communication and Image Representation 13, 195-216.

Yoshida, S., Suzuki, T., Yoshida, Y., Watanabe, S., Nakamura, K., Sasaki, T., Kawasaki, Y., Ehara, E., Murakami, Y., Kato, T., 2015. Feasibility and safety of transseptal puncture procedures for radiofrequency catheter ablation in small children weighing below 30 kg: single-centre experience. EP Europace 18, 1581-1586.

Yuan, Y., Long, D., Sang, C., Tao, L., Dong, J., Ma, C., 2017. A practical guide for building a highway between atria during transseptal puncture without radiation. Anatolian journal of cardiology 17, 470.

Zellerhoff, S., Daly, M., Lim, H.S., Denis, A., Komatsu, Y., Jesel, L., Derval, N., Sacher, F., Cochet, H., Knecht, S., 2014. Pulmonary vein isolation using a circular, open irrigated mapping and ablation catheter (nMARQ): a report on feasibility and efficacy. Europace, euu133.

Zheng, Y., Barbu, A., Georgescu, B., Scheuering, M., Comaniciu, D., 2008. Four-chamber heart modeling and automatic segmentation for 3-D cardiac CT volumes using marginal space learning and steerable features. IEEE Transactions on Medical Imaging 27, 1668-1681.

Zhou, Y., Bernard, O., Saloux, E., Manrique, A., Allain, P., Makram-Ebeid, S., De Craene, M., 2015. 3D harmonic phase tracking with anatomical regularization. Medical Image Analysis 26, 70-81.

Zhuang, X., Rhode, K.S., Razavi, R.S., Hawkes, D.J., Ourselin, S., 2010. A registration-based propagation framework for automatic whole heart segmentation of cardiac MRI. IEEE Transactions on Medical Imaging 29, 1612-1625.

Zuluaga, M.A., Cardoso, M.J., Modat, M., Ourselin, S., 2013. Multi-atlas propagation whole heart segmentation from MRI and CTA using a local normalised correlation coefficient criterion, in Functional Imaging and Modeling of the Heart. Springer, pp. 174-181.